School of Science
Department of Imaging and Applied Physics

# A Low Frequency Array of Simple Radio Telescopes for the Detection of Solar X-Ray and Radio Flares and the Study of the Ionosphere

Christopher J Lord

This thesis is presented for the Degree of
Master of Philosophy
of
Curtin University

March 2014

**Declaration**

To the best of my knowledge and belief this thesis contains no material previously published by any other person except where due acknowledgment has been made.

This thesis contains no material which has been accepted for the award of any other degree or diploma in any university.

Christopher J Lord

Signature:.....

Date:.....

**Acknowledgements**

Firstly, I am very fortunate that my wife, Heather, does not object to having poles and wires around and over the house and that there have been no complaints from neighbours.

I would like to thank Carol Redford and Donna Vanzetti, the previous owners of Gingin Observatory, for supporting this project and also the new owners, Bella and Hans Wunderlin for continuing to provide space and facilities for the radio observatory. Also a big thank you to all at Gingin Observatory who have helped to keep the computer and radios running.

I am indebted to John Kennewell for giving me the opportunity to work as an analyst at Learmonth Solar Observatory (LSO) for six months and who helped me in many ways during and after my time there. I would also like to thank Owen Giersch for his help finding a suitable PC and in setting up the network connections. Many thanks to Phil Wilkinson and Campbell Thomson at IPS Radio & Space Services for supporting this project and facilitating the data transfer through the IPS network. My thanks go to Alan Brockman for allowing me to modify and use his JOVE Receiver and antenna in this project. And last but not least to all the staff at LSO for making my short time there a memorable and enjoyable experience.

I would also like to thank my supervisors Steven Tingay, Peter Hall and Craig Buckley for their patience in what has been a longer than expected project.

Finally, to all those who I have not mentioned, your help is much appreciated.

**Abstract**

This project, "A Low Frequency Array of Simple Radio Telescopes for the Detection of Solar X-Ray and Radio Flares, and the Study of the Ionosphere", describes the development of antennas, receivers and software for a simple radio telescope (SRT) system that captures data from the 16 to 30 MHz radio spectrum to a personal computer.

The SRT uses an existing system, based on NASA's Radio JOVE Project[1], as a starting point. The Radio JOVE Project is a 'hands on' system and a key requirement of the new SRT system was to improve data reliability under an automated data acquisition system. A significant component of this new SRT system was the design of a receiver with flexible frequency coverage and a computer interface. New software was written to replace the Radio-SkyPipe[2] data acquisition software and directly control the receiver. The antenna, a phased array of two dipoles, was optimised with baluns and a combiner designed for low-frequency use; it has a broad beam (approximately 60 degrees) oriented vertically upwards and scans a strip of sky at zenith as the Earth rotates.

Some solar and other events (e.g. noise from Jupiter) can be detected directly, while other events (e.g. solar X-ray flares) may only be indirectly detected through their effect on the ionosphere. The galactic background noise and other radio emissions such as those from Jupiter and the Sun have to pass through the ionosphere on their way to the antenna. Using the galactic background noise (which varies predictably with sidereal time) as a reference, this research has searched for links between variations in opacity of the ionosphere and solar activity.

[1] http://radiojove.gsfc.nasa.gov/

[2] http://radiosky.com/skypipeishere.html

# Contents

# List of Figures

# List of Tables

# Chapter 1

# Introduction

## 1.1 Project Aims

The aim of this project was to deploy an array of simple radio telescopes based on NASA's Radio JOVE Project, to improve on the Radio JOVE system design, and to make observations of solar, ionospheric and galactic phenomena.

A major part of the research project was to design and develop a new Direct Digital Synthesis (DDS)[1] radio receiver with Universal Serial Bus (USB) connection to a Personal Computer (PC). The receiver design has two input and output channels and power supplied from the USB. Each channel has a wide-band, radio-frequency (RF) amplifier with good dynamic range capable of handling peak input signals in the order of $-40$ dBm. The design of the RF amplifier also minimises output to input coupling, making it less likely that the local oscillator (LO) will produce significant radiation from the antenna. Synchronised tuning of both channels is controlled by a common LO derived from a DDS chip under control of the PC via the USB. A crystal-controlled oscillator provides the reference frequency for the DDS, for good frequency stability. The two audio-frequency outputs, with bandwidths up to 22 kHz, connect to the left and right channels of the PC's audio Line In socket. A receiver of this type provides maximum flexibility for antenna configurations and for Digital Signal Processing (DSP) using the wide dynamic range of the PC's 16 bit digital audio system.

An important project objective was to find ways to minimise and mitigate radio-frequency interference (RFI). Careful design and construction of the an-

[1]Described in the Analog Devices application data as: "DDS technology is an innovative circuit architecture that allows fast and precise manipulation of its output frequency under full digital control. DDS also enables very high resolution in the incremental selection of output frequency; the AD9850 allows an output frequency resolution of 0.0291 Hz with a 125 MHz reference clock applied."

tenna system is essential for maximising the desired astronomical signal and minimising the pick-up of RFI. Care was also needed in the design of the new receiver and the interface to the PC, to avoid generating RFI. Finally, data processing in software plays a part in removing some of the remaining RFI.

The quality of the data collected depends largely on the software used to process it. The objective in writing the software for this project was to have maximum control over the collection, processing, storing and display of the data. Initial software development was associated with data collection and display, using the Radio JOVE receivers. Having established a working system, the software was extended for use with the new DDS receiver.

## 1.2 Background

This project builds on work by Brodrick, Tingay, and Wieringa (2005) that used a pair of Radio JOVE receivers operating at 20.1 MHz to measure the magnitude and timing of a large X-class X-ray solar flare that occurred on 4 November 2003. By recording the 20.1 MHz galactic background radio emission before, during and after the flare and correcting for solar zenith angle, it was possible to measure the absorption of the emission by the ionosphere due to the X-ray flare and from this absorption determine the magnitude and timing of the flare. Brodrick, Tingay, and Wieringa (2005) used the Radio JOVE receivers as riometers (relative ionospheric opacity meter) (Little & Leinbach, 1959), where the diffuse galactic background emission is recorded over time to generate a 'quiet day curve' (QDC) which is then used as a reference for measuring sudden deviations from this norm. Such deviations can occur when the ionospheric opacity increases due to a large solar X-ray flare. The development of the riometer followed work by Mitra and Shain (1953), which showed that absorption of the cosmic background emission occurred mainly in the D region of the ionosphere and could readily be measured using a suitable antenna and standard communications receivers. Prior to this work, the measurement of ionospheric absorption was carried out using active transmission of a radio signal directed vertically upwards and measurements made of the strength and timing of reflected signals. This method is still in use today for measuring a range of parameters of the ionosphere over a range of frequencies; the instrument used is known as an ionosonde. Bibl (1998) describes the evolution of the ionosonde from work by Appleton and Barnett (1925) and Breit and Tuve (1925). However, the ionosonde has limitations at high latitudes during periods of polar blackout (Little & Leinbach, 1959) and is a far more complex and expensive

system compared with that of the passive measurement of cosmic background emission used by the riometer.

Radio JOVE receivers are part of NASA's Radio JOVE Project[2] and, combined with the free version of Radio-SkyPipe[3] software, can be used as a simple low cost riometer. NASA's Radio JOVE Project brings radio astronomy to the classroom by allowing students to build a simple radio receiver and antenna for listening to radio noise from Jupiter and the Sun. The system is supplied as a kit, or ready built (at extra cost), including assembly manuals and software. The receiver is of the direct-conversion type (explained later in this thesis), taking radio-frequency input and producing audio-frequency output for feeding into a personal computer or headphones. The audio output level is adjusted from a front panel control, as is the tuning, which can be adjusted over a small range centred on 20.1 MHz. A 12 Volt power supply is required, which can be either a 12 Volt battery or a plug pack from the AC mains. In this project, additional frequencies of 17 and 28 MHz were used to give a diversity of frequencies when observing solar radio flares and the effects of solar X-ray flares on the ionosphere. The 17 and 28 MHz versions of the Radio JOVE receiver were purchased via a special request to Richard Flagg[4].

Solar radio noise picked up by the JOVE Receiver is of a type known as a Solar Radio Flare (SRF) or Burst. The mechanism that produces this type of radio noise differs from that which produces the broadband solar radio noise of the quiet Sun (Gopalswamy, 2004). The quiet Sun broadband thermal emission is at a level far too weak for the JOVE receiver to detect. However, SRFs have intensities many orders of magnitude greater than the Sun's thermal radio emission and are easily detected. They have been studied for many years and much work has been done to identify their source and to classify the different types (Kundu & Stone, 1984; Pick & Trottet, 1988; Wild, 1969). SRFs or Bursts often accompany sunspot activity, disappearing filaments or X-ray flares. This type of solar radio activity is best observed on a spectrograph (Prestage, Luckhurst, Paterson, Bevins, & Yuile, 1994) or a radioheliograph.

The Culgoora radioheliograph (Sheridan, Labrum, & Payten, 1973) was a complex instrument comprising 96 parabolic dishes of 13.7 m diameter arranged in a 3 km circle, which, with the aid of a computer to synchronise the data from the dishes, displayed a two dimensional contour map of radio emissions from the Sun on a Cathode Ray Tube (CRT). This allowed researchers to observe the

[2] `http://radiojove.gsfc.nasa.gov/`

[3] `http://radiosky.com/softwarehome.html`

[4] Mail to: rf@hawaii.rr.com

source of the emissions emanating from the Sun in real time, much as optical flares are observed on an optical telescope. It was at the cutting edge of solar radio astronomy from 1967 until it was decommissioned in 1984 (Haynes, 1996, p. 285). Since 1984 there has been no solar radio imaging capability in Australia at low frequencies. However, the recently commissioned Murchison Widefield Array (MWA) (Tingay et al., 2013), having similar frequency coverage to the Culgoora radioheliograph, but with modern instrumentation, and located at the Murchison Radio Observatory (MRO) in Western Australia, is now producing good solar science results (Bowman et al., 2013; Oberoi et al., 2011, 2014).

Spectrograph measurements allow the complex nature of the different types of solar radio bursts to be better understood by recording the intensity of radio emission as a function of frequency and time (Prestage, 1995). The solar radio spectrograph (SRS) is still in use as part of the Radio Solar Telescope Network (RSTN) (Castelli, Aarons, Guidice, & Straka, 1973) that operates around the world under the control of the United States Air Force Weather Agency[5] and jointly with IPS Radio and Space Services[6] in Australia . The graphical display of data on the SRS enables the identification of the different types of bursts and the measurement of TypeII shock speeds (Thompson, Kennewell, & Prestage, 1996). These results are then used to predict the likely effect of the solar activity on space-related activities and the approximate arrival time of material ejected during Coronal Mass Ejections (CME) (Gopalswamy, 2004; Kathiravan, Ramesh, & Subramanian, 2002), as indicated by the TypeII shock speed.

Data from the Learmonth Solar Observatory (LSO) SRS (part of the RSTN located near Exmouth in Western Australia) (Thompson et al., 1996) was used to check for correlation of solar events with data recorded by the JOVE Receivers and confirm the timing and types of bursts detected. The JOVE Receiver can only record the intensity vs. time of a solar burst over a very narrow bandwidth. However, the improved DDS receiver described in Chapter 5, is able to record data over a much wider bandwidth with a limited spectrograph display.

Shkarbalyuk, Kosolapenko, and Vasil'ev (2012) describe a system using the WiNRADiO[7] G305e Scanning Receiver linked to a PC using a USB port. This receiver has a very wide tuning range and can be commanded by the PC to avoid frequencies that have high levels of RFI. However, the system is expensive and the receiver suffers from relatively high internal noise levels, requiring the use of an external RF pre-amplifier, as described in their article. Receivers of this type are

[5] http://www.afweather.af.mil/library/factsheets/factsheet.asp?id=16521
[6] http://www.ips.gov.au/World_Data_Centre/2/8/9
[7] http://www.winradio.com/

referred to as a software defined radio (SDR) since they are entirely controlled by software running on the PC. Mostly, these receivers are designed for radio communications applications and are not optimised for radio astronomy. However, Behnke et al. (2013) describe a SDR design that emulates a JOVE Receiver with a bandwidth of 1 MHz and open-source software suitable for radio astronomy. The design is complex with a lot of processing carried out at high frequencies, resulting in high power consumption. The advantage of the JOVE Receiver is its basic simplicity, which keeps internal noise levels and power consumption low, making this system an ideal starting point for development.

Modifications made to the JOVE Receiver as part of this project have increased the audio-frequency bandwidth from 3.5 kHz to 22 kHz on one of the two audio output sockets, and further reduced internal circuit noise. The additional bandwidth allows more effective use of the DSP software written for this project. The temperature stability of the Radio JOVE LO is poor, resulting in the rapid drift of many kHz at an operating frequency of 28 MHz. For the receiver's original purpose, this is not a major problem, since the tuning is easily adjusted to avoid interference and compensate for the drift. However, with an automated recording system operating 24 hours a day, it is not practical to make manual tuning adjustments. In addition to the LO drift, there is significant leakage of the LO back to the antenna. This would have serious implications for other users of a radio quiet location. The use of a DDS based LO in the improved receiver provides flexible tuning and stability, while re-arranging the RF front-end reduces unwanted radiation. Full details of these and other changes are contained in the pages that follow.

Evaluation of the Radio-SkyPipe software used with NASA's Radio JOVE Project showed a lack of DSP capabilities. The only way of 'smoothing' out the data was to increase the time over which samples were averaged. This approach works well for transient RFI but is not effective for longer duration RFI such as persistent carriers. For the purposes of this research, full access to the data samples was required for maximum flexibility in signal processing. Therefore, a major part of this project was to write software for data capture and processing.

## 1.3 Significance

This work shows that the standard JOVE Receiver can be modified to provide a significant increase in bandwidth with reduced internal noise. This will enable existing or prospective owners to maximise the performance of their JOVE

Receivers.

The improved receiver design is aimed more in the direction of a SDR and provides the basis for further hardware and software development. With the receiver tuning accomplished using a computer and USB connection, it is much easier to collect data over a wide range of frequencies. It is hoped that the development of this improved receiver will fill the gap between the JOVE Receiver and more expensive receivers. It is envisaged that the improved receiver will make amateur radio astronomy available to the public at a reasonable cost, in much the same way as modern small optical telescopes have done for optical astronomy.

Understanding solar radio flares and the behaviour of the ionosphere are important factors for terrestrial, satellite and space communications. With a significant amount of solar activity and ionospheric effects occurring at low frequencies, it is important to have good coverage in this area. However, there are relatively few low-frequency observatories such as LOFAR (LOw-Frequency ARray) (Van Haarlem et al., 2013), which can operate down to frequencies comparable with the JOVE Receiver. A large number of amateur radio astronomy observers using the improved receiver developed for this project could make a valuable contribution to science.

## 1.4 Research Method

Galactic background noise, solar and other radio emission data have been collected from three sites located in Western Australia over a significant period of the research program. These sites include the author's home observatory in the northern suburbs of Perth, Gingin Observatory approximately 70 km north of Perth and Learmonth Solar Observatory approximately 1000 km north of Perth. The author's home observatory is equipped with a 28 MHz receiver, Learmonth has a 20 MHz receiver and Gingin has 28 MHz and 17 MHz receivers. The radio telescope PC at each site sends the most recent 24 hours of recorded data daily as an attachment to an e-mail to the author. These data are processed and plotted as a power vs. time graph. By comparing data from all three sites it is possible to identify local RFI at each site and compare the strength and time of solar events. The data are then checked for events that are correlated with observed solar and ionospheric events from other observatories. These observatories include: the High Frequency Active Auroral Research Program (HAARP)[8], which

[8] `http://www.haarp.alaska.edu/haarp/index.html`

has a riometer and other instrumentation based in Alaska; IPS data services[9], Learmonth Solar Observatory, near Exmouth in Western Australia; the Solar and Heliospheric Observatory (SOHO)[10] space observatory; and the National Oceanic and Atmospheric Administration (NOAA)[11] solar and X-Ray observatory.

RFI is expected to be a major limiting factor affecting data quality. With this in mind, the improved receiver makes it easier to identify the presence of RFI and mitigate its effects. By switching rapidly over a range of frequencies in a band, a very wide bandwidth is realised compared to that of the PC audio system. Sampling data from a wide bandwidth avoids much of the narrow-band RFI. An alternative strategy available with the improved receiver is to use DSP to combine the data from the two dipoles instead of the hardware combiner. With this approach, the same data is combined in different ways to minimise RFI. Offringa et al. (2010); Offringa, De Bruyn, and Zaroubi (2012) describe methods for removing RFI from LOFAR data and other interferometric radio telescopes. It may be possible to implement these techniques for real time data processing in the RioMeter program and/or in the RioPlot program for post-processing. Alternatively, a small sensing antenna connected to the second channel of the receiver could be used to pick up local RFI which is then used to cancel the RFI in the astronomy data (Barnbaum & Bradley, 1998).

## 1.5 Thesis Outline

This thesis describes in detail, the development of a new radio telescope based on the Radio JOVE system, but with improved facilities for automated data collection and RFI mitigation.

Chapter 2 examines the design of the antenna system as used by the Radio JOVE Project and shows how it was adapted to this project. Detailed design information for the various components in the antenna system shows how optimum performance was realised in this application. An important consideration was minimising the system's vulnerability to RFI and this is dealt with in some detail.

The JOVE Receiver and its modifications are detailed in Chapter 3. This chapter looks at the building blocks of the receiver and shows how changes to the circuit increased bandwidth and reduced circuit noise. The increased bandwidth

[9] `http://www.ips.gov.au/Solar`
[10] `http://sohowww.nascom.nasa.gov/`
[11] `http://www.n3kl.org/sun/noaa.html`

allows the use of DSP software to significantly reduce some types of human-made RFI.

Described in Chapter 4 is the setup at the three observatory sites. Each site has its own special requirements regarding placement of antennas and measures taken for reducing local RFI.

Chapter 5 presents a prototype design for an improved radio telescope receiver that uses DDS technology to control the receiver tuning. This enables rapid frequency changes to be made in response to RFI detected by the DSP software. A USB connection to the PC provides the power and control interface for the receiver. The prototype receiver developed in this project has a single antenna input and a single audio output. However, the final design will have two antenna inputs and two audio outputs, which utilise the left and right channels of the PC stereo audio system. This allows simultaneous recording of data on the two channels, giving greater flexibility for polarisation measurements and advanced RFI mitigation.

The project software, described in Chapter 6, is in two parts. The first part is the data capture system (RioMeter.exe) that runs on the radio telescope PC. This software provides the user interface for setting up the observatory details, controlling the data display and for e-mail forwarding of the data. The second part (RioPlot.exe) provides facilities for collating and analysing the data from the three sites.

Chapter 7 presents the results of four years of data collected at the three sites. Several types of solar event are shown, along with comparison data from other sources such as the LSO spectrograph and NASA's Geostationary Operational Environment Satellite (GOES) X-ray data.

Appendix A takes a closer look at how the combiner, a component of the antenna system, works.

Appendix B describes the major items of equipment and software used by the author in the development of this project.

# Chapter 2

# Antenna System

## 2.1 General Description

The antenna system closely follows that of NASA's Radio JOVE Project, details of which can be found in the antenna manual available at `http://radiojove.gsfc.nasa.gov/telescope/ant_manual.pdf`.

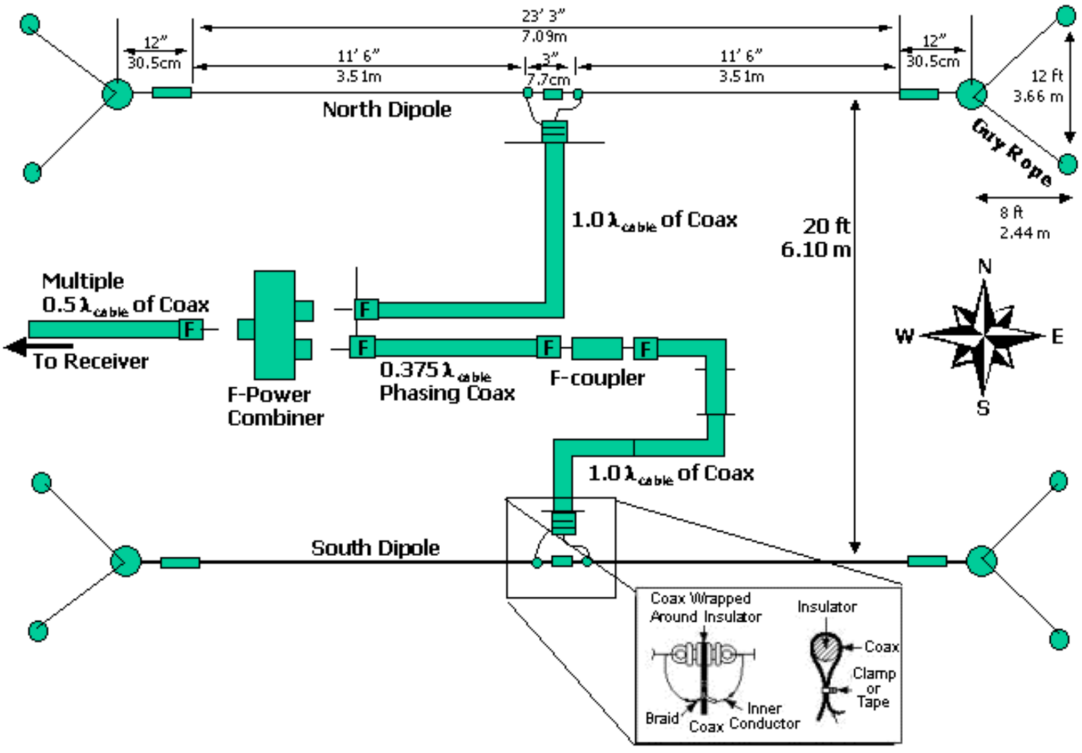


Figure 2.1: Top-view schematic of Radio JOVE dual dipole, Figure 5.2 from the Radio JOVE Antenna Manual. Note that the phasing coax is not required in this application.

The Radio JOVE antenna (Figure 2.1) consists of a pair of horizontal half-

wave dipoles acting as a phased array. Each dipole is coupled, via a balun (implemented with large ferrite[1] beads over the coax at the dipole feed point) and coaxial cable, to a combiner and from the combiner to the receiver. Figure 2.1 shows the antenna layout viewed from above; this schematic includes a length of phasing coax inserted in the southern dipole feeder for steering the antenna beam to the south, which optimises the antenna gain for Jupiter observations from the Northern Hemisphere. Inserting the phasing coax in the northern dipole feeder steers the beam to the north for Southern Hemisphere users. The dimensions shown are for the standard Radio JOVE frequency of 20.1 MHz. Figure 2.2 shows the assembled antenna from the Radio JOVE Antenna Manual. The picture demonstrates two different guying arrangements: one for metal masts (foreground) and one for PVC masts (background).


Figure 2.2: Radio JOVE dual dipole antenna, Figure 7.3c from the Radio JOVE Antenna Manual. This picture shows the different guying arrangements for metal (foreground) and PVC masts.

In this project, a zenith directed antenna beam is required and therefore the

[1]A ceramic material with special magnetic properties used in the manufacture of inductive components. Ferrite cores reduce the physical size of inductors, but material losses result in a lower 'Q'.

phasing coax is not required. This arrangement gives a half power beam width of approximately sixty degrees and uses the Earth's rotation to scan a strip of sky at zenith. Shown in Figure 2.3 is the XLNEC[2] simulated beam pattern of the Radio JOVE antenna without the phasing coax and with dimensions as shown in Figure 2.1. The dipoles are at a height of 3.05 m over sandy ground. This pattern is typical of what can be expected at each of the sites in this project.

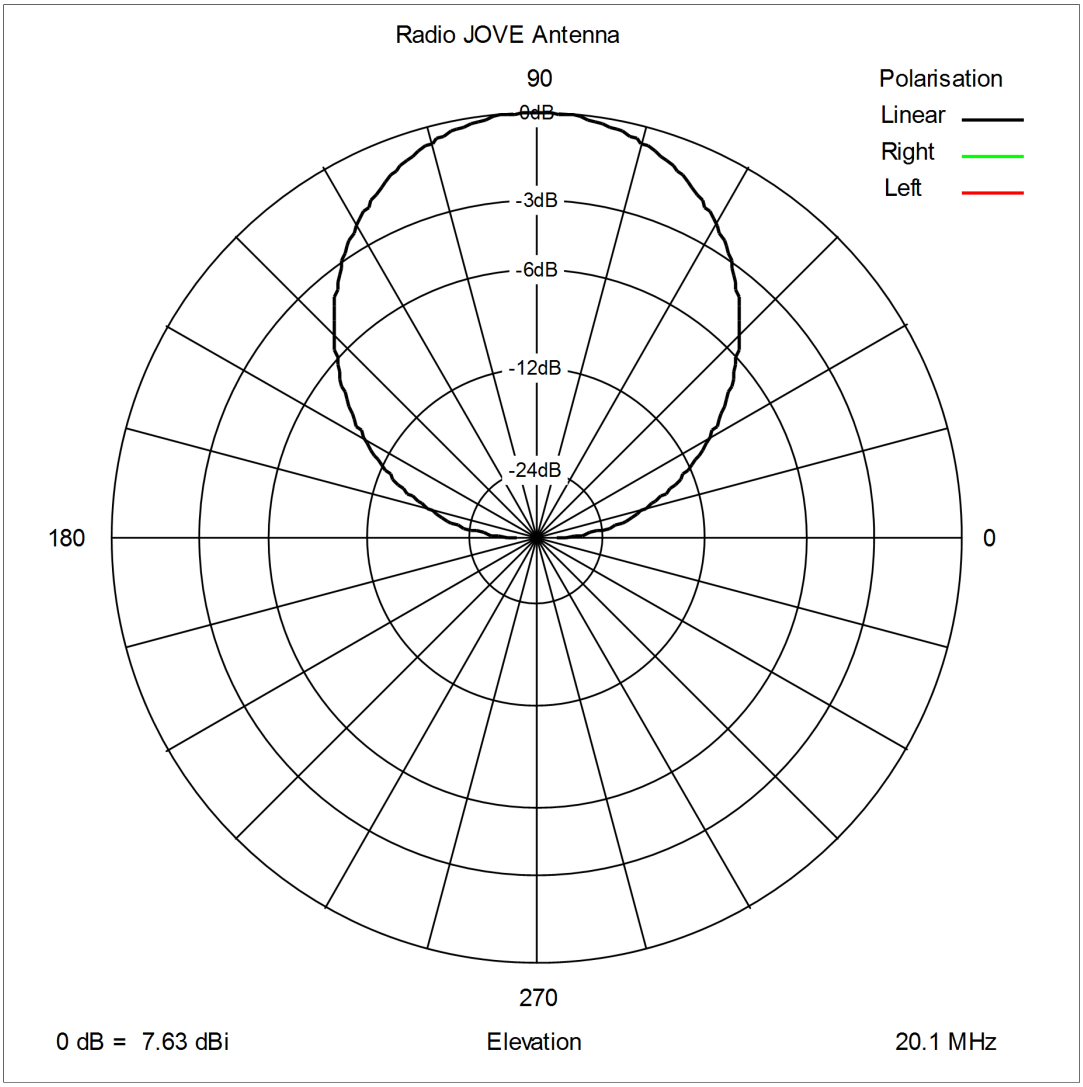


Figure 2.3: XLNEC simulation of the Radio JOVE antenna showing zenith directed beam, without the phasing coax and above sandy ground.

Presented in the pages that follow, is a detailed description of the various components of the antenna system used in this project. The observatories chapter gives specific dimensions and design details for the antennas used at each site.

[2]XLNEC combines Microsoft Excel and the NEC2 engine. For NEC2 details see `http://www.nec2.org/`. The XLNEC software is included on the CD available with this document.

## 2.2 Dipoles

The type of wire used for the dipoles is not critical, but stranded wire, rather than a single solid wire, is less likely to break as the antenna flexes in the wind. Medium or heavy duty insulated wire of 14/0.2 mm or 24/0.2 mm, respectively, is quite suitable.

The dipole length is determined as follows:

$$l = \frac{c}{2f}, \tag{2.1}$$

where:

$l$ = length, m;

$c$ = speed of light $\approx 300 \times 10^6$ m/s;

$f$ = frequency, Hz.

The above formula assumes that the wire is infinitely thin and located in free space. Since the wire is not infinitely thin, is located close to the ground and is supported by insulators at the wire ends, it is necessary to make the wire a little shorter than calculated. The discrepancy between the calculated and actual length to achieve resonance is called 'end effect' and is compensated for by reducing the dipole length by approximately five per cent. See Straw (1994, p. 2-4) for a more detailed explanation of the effects of wire diameter on the calculation of dipole lengths and the influence of the supporting insulators on antenna resonance.

The dipoles are arranged parallel to each other and, if possible, oriented in an east-west direction. This orientation allows for the possibility of changing the beam elevation to favour north-south directions by using an inserted phasing coax (or by reversing the polarity of one of the dipoles). This maximises the signal for solar observations during the winter months when the Sun is low in the sky or when Jupiter lies in the northern sky. The dipoles must have the same polarity for a vertically directed beam, i.e. elements connected to the centre conductor of the coaxial cable should be oriented in the same direction. The spacing between dipoles should be half a wavelength. The Radio JOVE antenna with phasing line has a slightly closer spacing, which lowers the beam elevation. As dipole spacing increases beyond half a wavelength, antenna gain increases and low angle side lobes start to appear. Side lobes should be avoided, since they can introduce signals that are not part of the main beam, such as local RFI. The

dipole height should be approximately 0.2 of a wavelength, depending on soil conditions. Increasing the dipole height tends to spread the beam. Increasing the Radio JOVE antenna height, when using the phasing coax, lowers the beam elevation. Antenna gain is a maximum for a perfectly conducting ground plane and is degraded by sandy dry soils.

The theoretical feed impedance for a single resonant dipole in free space is approximately 73 Ohms (Straw, 1994, p. 2-6). However, the actual feed impedance will differ slightly from this, depending on dipole height, spacing and ground conditions. The dipole length calculated from (2.1), minus the five per cent 'end effect' gives a close approximation to the length required. For optimum performance, it is necessary to measure the dipole impedance using an antenna analyser and adjust the dipole length for resonance at the working frequency. Small hand held antenna analysers such as the RigExpert[3] AA-200 are able to measure the impedance of the antenna and display this information as a graph of impedance vs. frequency or as a ratio of impedance divided by some fixed resistance, usually 50 or 75 Ohms. The ratio of the dipole impedance to the fixed resistance determines the 'voltage standing wave ratio' or VSWR. For the RigExpert AA-200, a fixed resistance of 75 Ohms is selected, since this is the nearest available resistance to the 73 Ohms of the dipole. The antenna is tuned by adjusting the length of each dipole independently for lowest VSWR at the frequency of use. Then, with both dipoles correctly positioned, the VSWR at the output of the combiner is checked and small adjustments made to the dipole lengths as necessary. A simple way to adjust the dipole lengths is to loop the end of the dipole through its insulator and twist about 10 cm of wire back on itself. This is adequate for holding the wire on the insulator and facilitates easy antenna adjustment.

## 2.3 Baluns

The feed point of each dipole should be coupled to the coaxial cable with a suitable balun. The word 'balun' is a contraction of the words balanced and unbalanced, meaning a device to couple a balanced system (dipole) to an unbalanced system (coaxial feeder). Without a balun, electrical currents flowing on the outer screen of the coaxial cable are coupled directly to one leg of the dipole and from there to the other leg of the dipole. This is likely to significantly degrade the signal to noise ratio of the antenna system.

[3]Rig Expert Ukraine Ltd. `http://www.rigexpert.com`

The Radio JOVE antenna uses ferrite beads slipped over the coax at the dipole feed point as a current balun. This is simple and effective but requires several relatively heavy ferrite beads. The weight increases the strain on the dipole causing it to sag in the middle. The ferrite toroid solution used in this project produces good results with far less weight.

There are two types of balun: current and voltage (Straw, 1994, p. 26-10). Current baluns force the outgoing and returning currents in the feeder to be equal. This is often achieved using ferrite components, either as sleeves over the coaxial cable at the dipole feed point, or as a bifilar winding on a ferrite toroid. This type of balun has the advantage of being simple to construct and offers a broadband coupling to the antenna. However, it does not allow impedance transformation between the coaxial cable and the antenna.

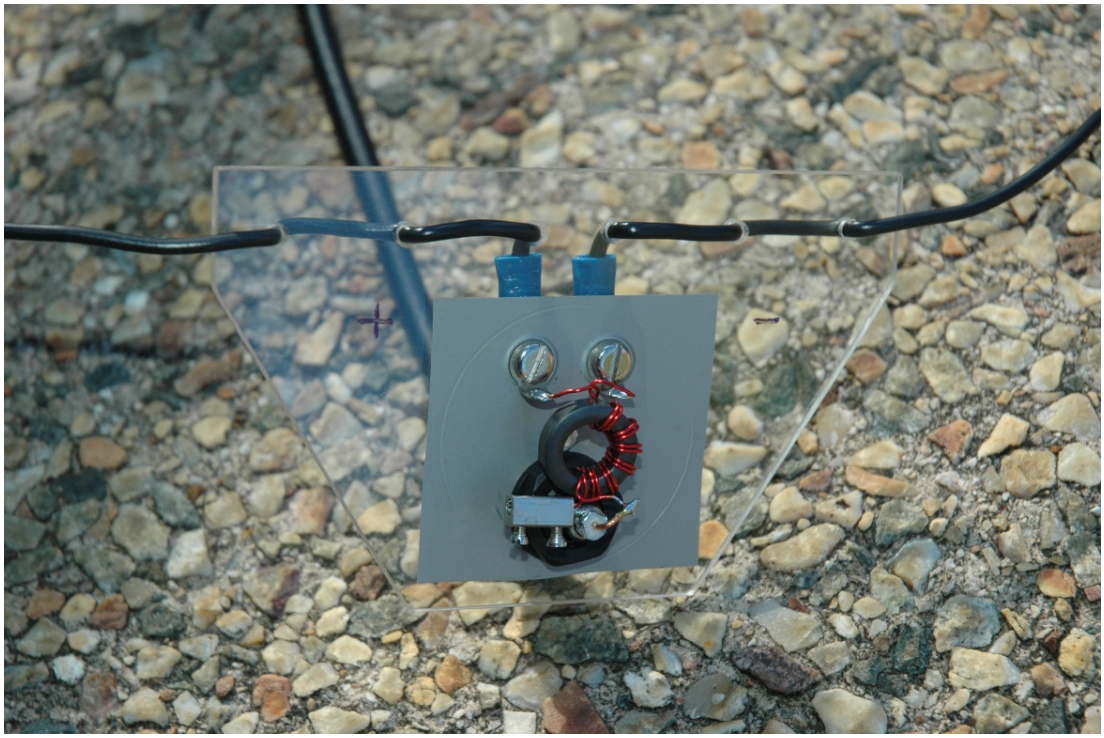

Figure 2.4: The balun assembly (protective cover removed) showing bifilar wound ferrite toroid with dipole wires and coax attached.

The voltage balun forces equal and opposite voltages at the dipole feed point. However, the effectiveness of this depends on the symmetry of the antenna and proximity to nearby objects. The voltage balun is a transformer and is therefore able to make an impedance transformation between the coaxial cable and the dipole if necessary. The bandwidth of this type of balun is less than that of the current balun and dependent on the type of ferrite material used.

For this application, the current balun is used. It consists of seven turns (150 mm) of bifilar wound 0.63 mm diameter enamelled copper wire on a type 43 mix ferrite toroid measuring 16x10x4.5 mm (ODxIDxH). The windings are spaced evenly around 180 degrees of the toroid, see Figure 2.4. This separation between the input and output ends of the winding maximises the isolation of the balun by keeping stray coupling capacitance low. The toroid and exposed connections are fitted with a protective cover (not shown) and the coaxial cable enters through a weather tight cable gland. A piece of clear plastic sheet provides support for the components and strain relief for the dipole wires, which terminate at two M4 nickel-plated brass machine-screws.

The common mode impedance measured (using the RigExpert AA-200) between the ends of one wire of the bifilar pair was greater than 700 Ohms at 28 MHz. This is the minimum impedance seen by currents flowing on the outside of the coaxial cable and significantly reduces their effect on wanted signals picked up by the dipole. The differential impedance measured with a 75 Ohm load was $75 + j4$ Ohms, indicating a slightly inductive load.

In contrast to the above, a large ferrite sleeve (of suitable material), 29 mm in length and 16 mm diameter, has an impedance in the order of 166 Ohms at 28 MHz and 130 Ohms at 20.1 MHz.

## 2.4 Feeders

Three feeders are required, two from the dipoles/baluns to the combiner and one from the combiner to the receiver. Generally, 75 Ohm television (TV) coaxial cable is suitable and has low losses over the HF (3 to 30 MHz) frequency range. This type of coax has a slightly higher than optimum impedance but has the advantage of being easily connected to the combiner and receiver using readily available 'F' type twist on connectors. The small impedance mismatch does not add significantly to the overall loss of the cable.

The two dipole feeder coaxial cables should be identical in length and cut from the same length of coax. This is because coax of the same type e.g. RG59, but from different batches may not have identical characteristics. All three feeders should be cut to some multiple of an electrical half wavelength. The reason for this is two-fold. Firstly, resonant lengths of coax between the receiver and the antenna should be avoided. By making the coax a multiple of an electrical half wavelength, it cannot be resonant at its physical length (since its physical length would need to be a multiple of half a wavelength to be resonant). If

the coax is resonant at the antenna frequency, it can interact with the dipoles causing distortion of the beam pattern and loss of gain. Secondly, the impedance measured at the end of the coax is the same as that of the load (Straw, 1994, p. 24-12). Therefore, the impedance at the combiner is the feed impedance of the dipole. This also makes it easy to check the dipole tuning by measuring the impedance at the combiner end of the feeder using an antenna analyser.

The electrical length of the feeder is calculated as follows:

$$l = \frac{c}{2f} \times VF \times n, \tag{2.2}$$

where:

$l$ = length, m;

$c$ = speed of light $\approx 300 \times 10^6$ m/s;

$f$ = frequency, Hz;

$VF$ = velocity factor of cable;

$n$ = number of half wavelengths.

The velocity factor of coaxial cables lies approximately within the range 0.66 to 0.89 and represents the reduction in speed of propagation of a signal in the cable compared with its propagation in free space. Typical 75 Ohm TV coax such as RG59U (foamed polyethylene dielectric) has a velocity factor of 79 per cent ($VF = 0.79$) and a loss of approximately 4.3 dB per 100m at 20 MHz (Straw, 1994, p. 24-17). A loss of 3 dB in the cable means that half the power from the antenna is lost in the coax. In order to keep losses below this level the cable must be less than 70m in length. Losses can be reduced to around 2 dB per 100m at 20 MHz by using more expensive coaxial cable such as Belden 9913. However, low loss cables such as these are large in diameter and not suitable for use with 'F' type connectors.

Whenever possible, the feeders should be routed at right angles to the dipoles so that stray coupling between feeder and dipole is minimised. Generally, the feeder drops down to ground from the dipole feed point and runs to a central point between the two dipoles, where it is terminated at the combiner. This usually results in the need for at least one full electrical wavelength of cable from each dipole feed to the combiner. The main feeder coaxial cable to the receiver then runs from the combiner, passing between the two dipoles.

Where the coax between the combiner and receiver is long or has to run close to other wiring, such as running through the roof space of a building, ferrite

suppressors fitted over the cable help reduce RFI pick-up. A more expensive coaxial cable such as RG6 Quad Shield reduces the amount of RFI reaching the central core, but suppression of the RFI on the shield is still required. This is because the RFI currents on the outside of the coax shield are connected to the receiver casing and are picked up by components and wiring within the receiver. Putting a ferrite suppressor over the coax at the entry point to the receiver increases the impedance seen by the RFI and reduces the currents flowing through the casing of the receiver. The resistance of the suppressor effectively absorbs the RFI power.

A good ground/earth connection to the threaded stud close to the antenna connector on the receiver also helps to reduce RFI. However, the earthing wire must be short (less than one eighth of a wavelength), of heavy gauge and connected to one or more earth rods. Previously, it was stated that the feeder length should be a multiple of half an electrical wavelength, however, the braid of the coax is connected to the case of the receiver and in turn to the receiver power supply and computer. Therefore, the effective length of the feeder for currents on the outside of the coax includes this ancillary wiring and the total length may become resonant. If the receiver happens to be located at a point of current minimum then a ferrite suppressor over the coax at the antenna input will not be effective. Ferrite suppressors work best at points of current maxima. A good ground connection at the receiver ensures this condition and the ferrite suppressor minimises the total noise current. Such an earthing system is often difficult to realise. Therefore, if noise pick-up on the coax is severe and the distance to the ground rod is greater than one eighth of a wavelength, it may be helpful to use one-half of a wavelength of heavy gauge wire to force a current maximum at the receiver. Another strategy, especially if no earth is available, is to try experimentally one or more ferrite suppressors at different points along the feeder until the noise is minimised.

Another important point to remember about the feeder is that it can act as a conduit for noise generated by electronic devices such as personal computers and transport it out to the antenna. Ferrite suppressors along the feeder will reduce this problem but wherever possible the noise is best suppressed at source.

## 2.5 Combiner

The function of the combiner is to add the signals from the two dipole feeders in such a way as to provide the correct load impedance for each feeder, while

maintaining isolation between the two feeders and also the correct load impedance for the feeder to the receiver. The action of the combiner is power additive: a wave front arriving at the dipoles from directly overhead produces in-phase voltages at both inputs to the combiner and hence double the power of a single dipole at the output. For a wave front arriving horizontally at right angles to the dipoles the voltages at the input to the combiner are 180 degrees out of phase by virtue of the fact that the dipoles are half a wavelength apart. This results in voltage cancellation and the total absorption of the power from both dipoles within the combiner. Hence, no power is available at the output of the combiner. With real world components there are losses and circuit imbalances which cause the performance of the combiner to deviate from this ideal.

From the description above, it can readily be seen how the antenna system as a whole achieves its vertically directed gain and high rejection of low angle signals.

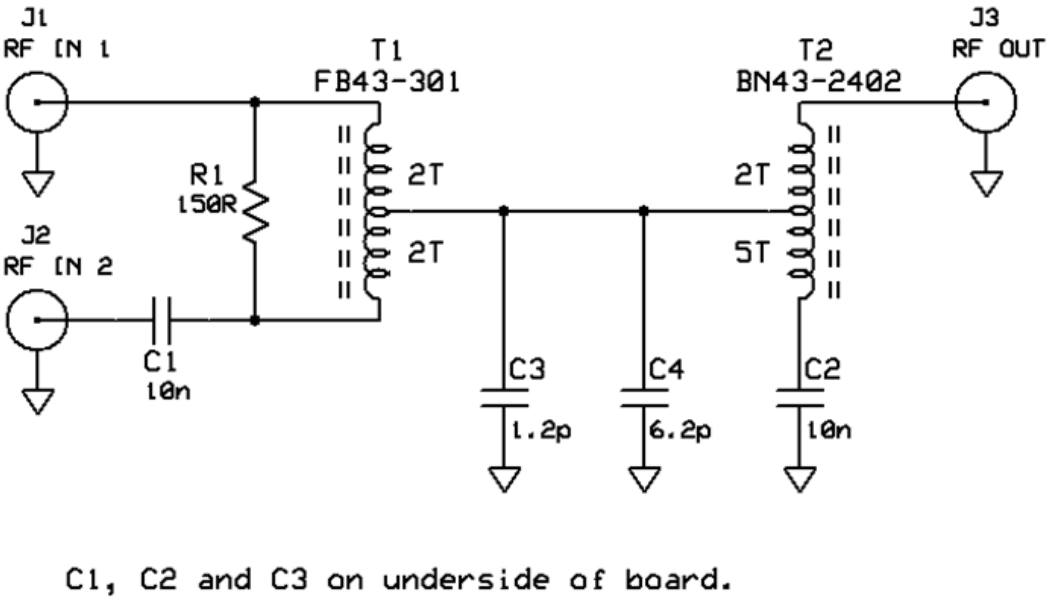


Figure 2.5: Circuit diagram of the modified combiner. T1 and T2 replace the original T1 and T2; R1 and C4 are added components.

An off the shelf television splitter can be used as a combiner. However, although the claimed frequency range is 5 - 1000 MHz, its performance suffers at low frequencies due to the ferrite components being optimised for VHF (Very High Frequency) use. For this application the standard television splitter was modified using ferrite components suited to frequencies in the HF range. As shown in Figure 2.5, C1, C2 and C3 are the existing capacitors located on the underside of the circuit board and are inaccessible without removing the circuit board from its

housing. C1 and C2 are not required in this application but can be left in circuit without detrimental effect. The required increase in the value of C3 is achieved by adding C4 in parallel on the topside of the circuit board. The resistor R1, also on the topside of the circuit board, is added across T1. See Figure 2.6. For more information on splitters and combiners, see Schetgen (1996, p. 17-7, p. 26-37) and `http://www.minicircuits.com/applications/applications_notes.htm`.

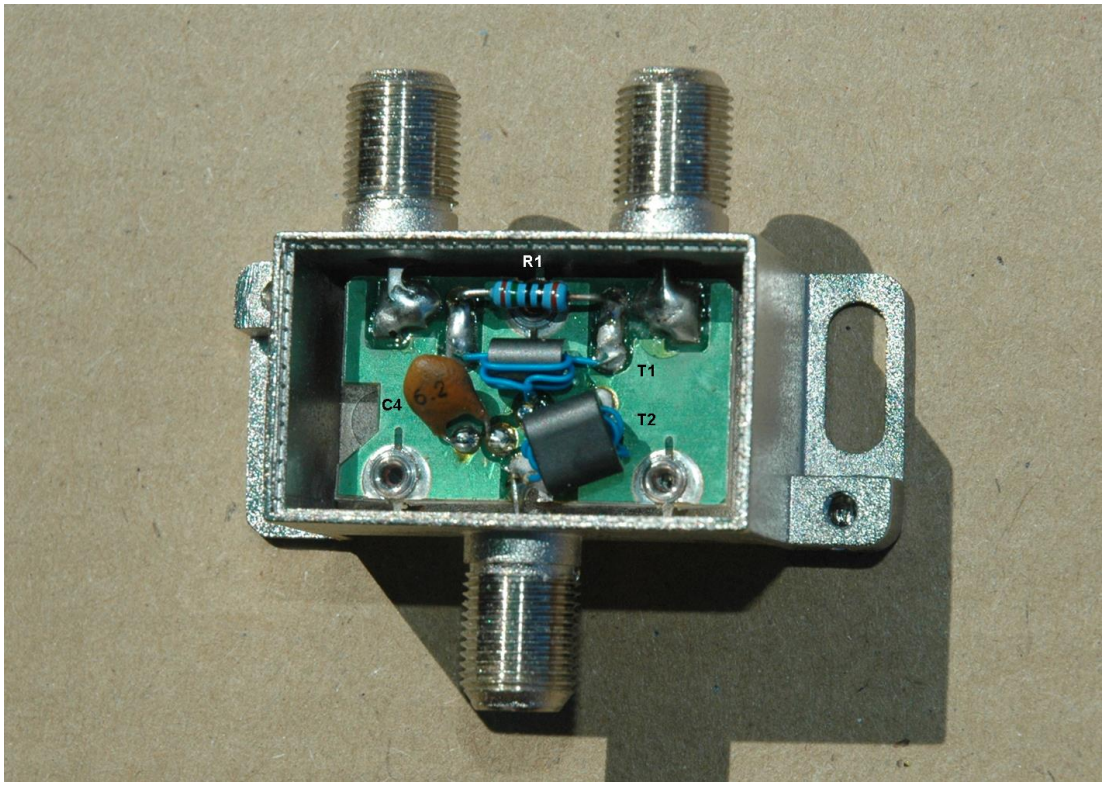


Figure 2.6: The modified combiner with cover removed showing added components R1 and C4 and replacement ferrite components T1 and T2.

A small amount of the signal power is lost within the combiner. This 'insertion loss' was measured by connecting two combiners as shown in Figure 2.7. Using the RigExpert AA-200 as a signal generator, the signal is split and re-combined by the two combiners before being applied to the matching network and the switched attenuator. The matching network increases the impedance seen by the second combiner to the necessary 75 Ohms for a correct match. The switched attenuator provides selectable attenuation of the signal in the range 0 to 100 dB in 1 dB steps whilst maintaining a constant 50 Ohm load for the input and output[4].

The attenuated signal is applied to the receiver (Yaesu FT101E) antenna input and the switched attenuator adjusted for an S-Meter reading of as close

[4]This may not hold true for attenuations of less than 10 dB when input and/or output impedances are not 50 Ohms.

to S5 as possible. The RF Gain control on the receiver is used to adjust the S-Meter reading to exactly S5. The S-Meter on the FT101E is an analogue meter which makes it possible to see changes in signal strength of less than one S-point. The more modern receivers available to the author use a digital bar graph with a resolution of two dots per S-point and it is therefore not possible to see intermediate signal strengths.

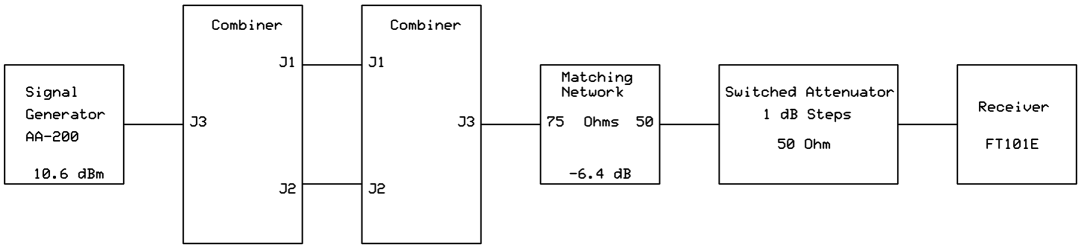


Figure 2.7: Insertion loss measurement of two combiners connected back-to-back.

The S-Meter displays signal strength in S-units, where each S-unit or S-point represents a doubling or halving of input voltage. For Yaesu receivers, S9 corresponds to an input signal of 50 microvolts RMS into 50 Ohms. Therefore, S9 in dB referenced to 1 mW is:

$$\begin{aligned} P_{in} &= 10 \times \log\left(\frac{v^2}{R} \times 1000\right) \\ &= 10 \times \log\left(\frac{(50 \times 10^{-6})^2}{50} \times 1000\right) \\ &= -73.0 \text{ dBm}. \end{aligned} \tag{2.3}$$

For signal strengths greater than S9, the S-Meter is calibrated in dB over S9 up to a full-scale deflection of 60 dB. S5 is approximately one quarter of full scale and is most suitable for comparative measurements.

The following insertion loss test procedure was used:

1. Connect the AA-200 to the matching network and adjust the switched attenuator for S5 on the FT101E S-Meter. Note the number of dB attenuation required to achieve this signal strength.

2. Insert the back to back connected combiners between the AA-200 and the matching network and adjust the switched attenuator for S5 on the FT101E S-Meter.

3. Subtract the number of dB recorded in step 2 from the number in step 1 and divide by two. This is the insertion loss for each combiner in dB.

The insertion loss for both combiners together was less than 1 dB; therefore, each combiner has an insertion loss of less than 0.5 dB. This result compares reasonably with commercial units having insertion losses in the order of 0.2 to 0.3 dB. E.g. Mini-Circuits ZFSC-2-1W-75+.

Another important function of the combiner is to provide isolation between port 1 (J1) and port 2 (J2). This reduces coupling of signals from one dipole to the other via the feeder and degradation of the antenna performance as a whole.

The following combiner isolation test procedure was used:

1. Connect the AA-200 to the matching network and adjust the switched attenuator for S5 on the FT101E S-Meter. Note the number of dB attenuation required to achieve this signal strength.

2. Connect a 75 Ohm terminating resistor to port 3 (J3), then connect the AA-200 to port 1 (J1) of the combiner and port 2 (J2) to the matching network. Adjust the switched attenuator for S5.

3. Subtract the number of dB recorded in step 2 from the number in step 1 to obtain the isolation in dB.

The resultant isolation was found to be 26 dB. This compares reasonably well with commercially available units costing four or five times as much. For example, a combiner with a 5 – 600 MHz frequency range available from Mini-Circuits[5] has an insertion loss of 0.2 dB and an isolation of 34.2 dB at 20 MHz. Commercial combiners designed specifically for low-frequency use, such as the Mini-Circuits ZSC-2-2-75+, achieve much better results with isolations of 36 dB at 17 MHz. Consistent with the philosophy of bringing radio astronomy equipment to the general public, an emphasis on low cost components is maintained here.

The above measurement results using the FT101E receiver have been confirmed using a more recently acquired Tektronix 2465B oscilloscope. However, measurements of the TV splitter (which does not have the resistor R1 fitted) showed that isolation, when used as a combiner, was better without R1 than with R1. It had been assumed that the TV splitter did not need R1 since it is normally used to divide the signal from a single antenna between two televisions and isolation between the two TVs is not an issue. This result calls into question the function of R1 as described in the Mini-Circuits applications guide (`http://www.minicircuits.com/applications/applications_notes.htm`) and also the ARRL Handbook (Schetgen, 1996, p. 17-7, p. 26-37). It seems that the ferrite

[5] `www.minicircuits.com/pdfs/ZFSC-2-1W-75+.pdf`

components in the TV splitter are manufactured such that the resistor is not required. A more detailed description of the splitter/combiner function is presented in Appendix A.

## 2.6 Antenna Performance

Performance measurements of the antenna system are limited to the voltage standing wave ratio (VSWR - commonly abbreviated to SWR). Measurements of the antenna gain and half power beam width are outside the scope of this thesis. The SWR performance of the LSO antenna system, which is representative of all three observatories' antennas, is shown in Figure 2.8.

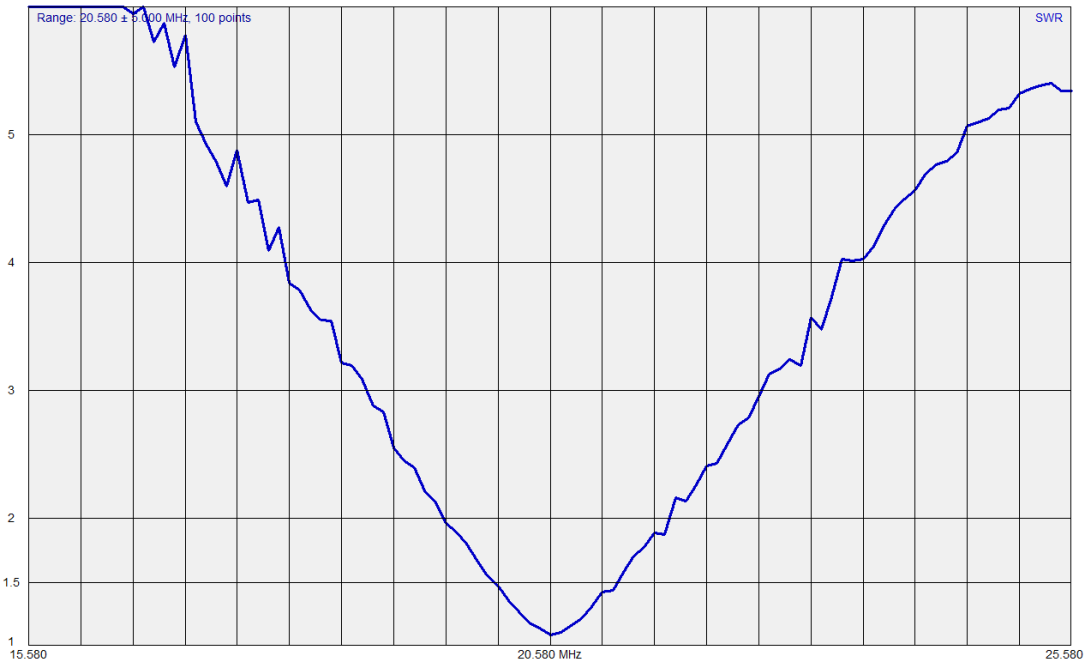


Figure 2.8: LSO antenna SWR measured at the combiner with the AA-200 antenna analyser.

The SWR is a measure of how well the antenna matches into a given transmission line impedance $Z_0$, in this case 75Ω and is determined by (Straw, 1994):

$$SWR = \frac{1 + |\rho|}{1 - |\rho|} \ , \tag{2.4}$$

where:

$$\text{reflection coefficient} = |\rho| = \frac{Z_L - Z_0}{Z_L + Z_0} \ , \tag{2.5}$$

and $Z_L =$ antenna impedance.

For a perfect match the ratio of the antenna impedance to the transmission line impedance is 1:1 and therefore the SWR = 1:1.

The antenna impedance was measured using the AA-200 antenna analyser with $Z_0 = 75\Omega$ selected for the transmission line impedance. From Figure 2.8 it can be seen that the lowest SWR calculated by the AA-200 is less than 1.1:1 at 20.58 MHz. The optimum SWR is above the required frequency of 20.1 MHz due to the dipoles being slightly too short. The dipoles, which were part of the Radio JOVE kit at LSO, had been constructed in a way that made it difficult to extend their length and due to time constraints were left unchanged. However, the SWR is still less than 1.5:1 at 20.1 MHz and transmission line losses associated with this amount of mismatch are negligible (Straw, 1994).

## 2.7 Summary

The Radio JOVE antenna with its phasing line is designed specifically for Jupiter observations and therefore has its gain optimised for the lower angles required for that application. In this project, the galactic background noise after it has passed through the ionosphere is of interest and for this an antenna with a beam optimised towards zenith is required. In this chapter, the general design requirements for such an antenna system were determined.

Locally generated RFI/noise was a major problem at all three sites used in this project. Unfortunately, there are no simple solutions. Some RFI/noise mitigation strategies were presented and more specific sources and solutions are covered in the observatories chapter. Every site has its own challenges, which take time and patience to resolve. A large bag of ferrite suppressors is usually required!

The function of the combiner within the antenna system was examined and a basic analysis of how it works presented in Appendix A. The standard TV splitter/combiner is adequate for most installations. However, the modified combiner did appear to give slightly improved results in the presence of RFI. If cost is not an issue, then a commercial combiner is the best option for the ultimate in performance.

The antenna system has proven to be reliable and the clearly visible diurnal cycle of the galactic background noise in the results of observations, presented later, suggest that the antenna gain must be close to that determined by simulation earlier in this chapter. The antenna system at the author's home observatory has been in constant use for over four years and has only required the replacement of the support cords.

# Chapter 3

# JOVE Receiver

Presented in this chapter is an overview of the JOVE Receiver (Figure 3.1) functional blocks and a description of some modifications to improve its performance for this application.


Figure 3.1: The Radio JOVE receiver as shown in the kit assembly manual.

The JOVE Receiver is a simple radio astronomy receiver designed by Richard Flagg and provided in kit form, or ready built, through NASA's Radio JOVE project[1]. Richard Flagg's kit assembly manual[2] provides full details of how to

[1]Radio JOVE Kits order form available at `http://radiojove.gsfc.nasa.gov/office/order_form.pdf`

[2]`http://radiojove.gsfc.nasa.gov/telescope/rcvr_manual.pdf`

assemble and test the receiver as well as a brief description of how the receiver works.

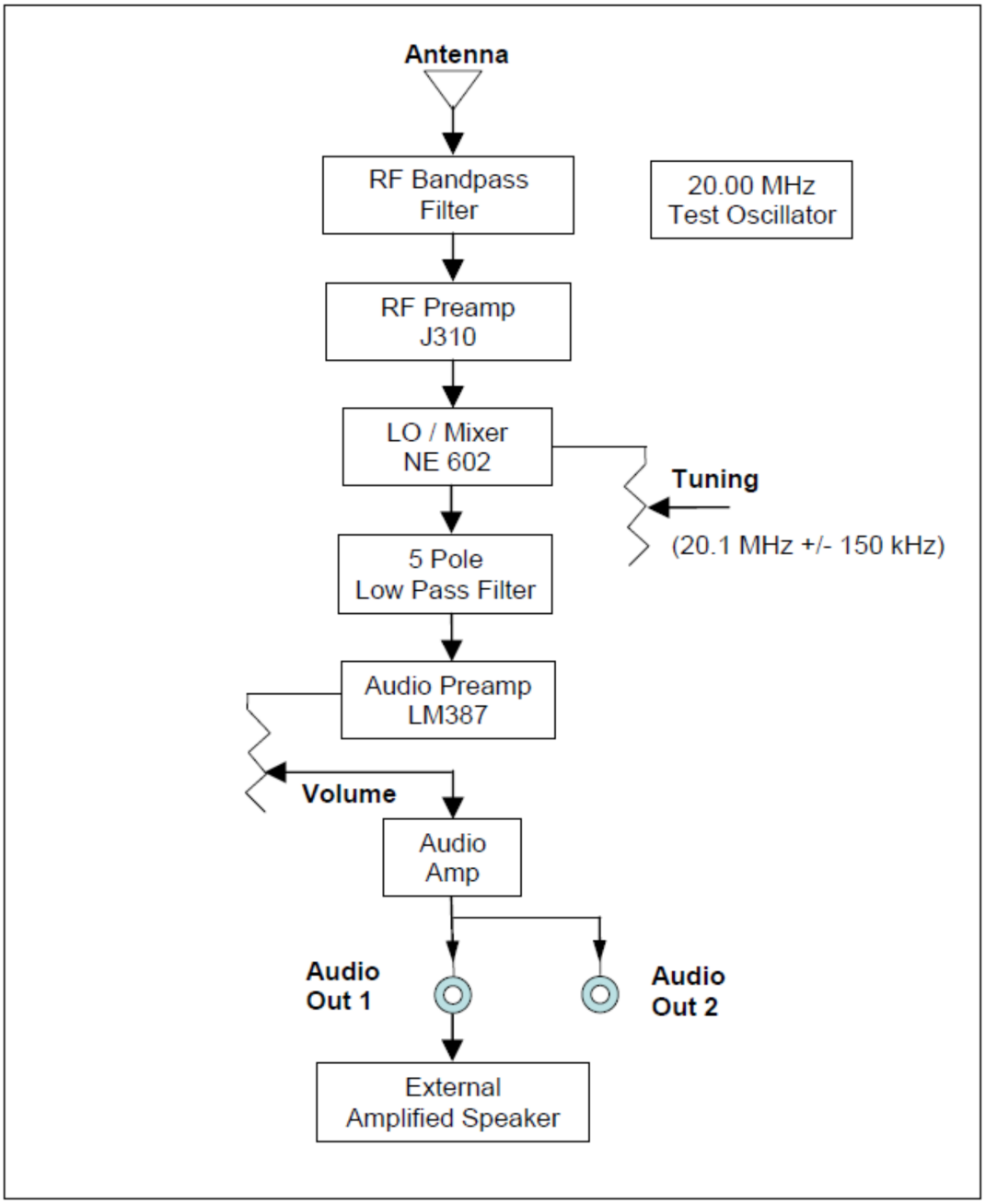


Figure 3.2: JOVE Receiver block diagram (Figure 1 from the kit assembly manual) showing the sequence of signal processing between the antenna and external speaker.

For ease of comparison between unmodified and modified JOVE Receivers, reproduced here are the block and circuit diagrams from the kit assembly manual, see Figures 3.2 and 3.3. Some modifications are common to all four receivers used in this project, while other modifications are specific to the observatory where the

receiver is used. Discussed in this section are the common modifications, leaving observatory-specific modifications for consideration in the Observatories chapter.

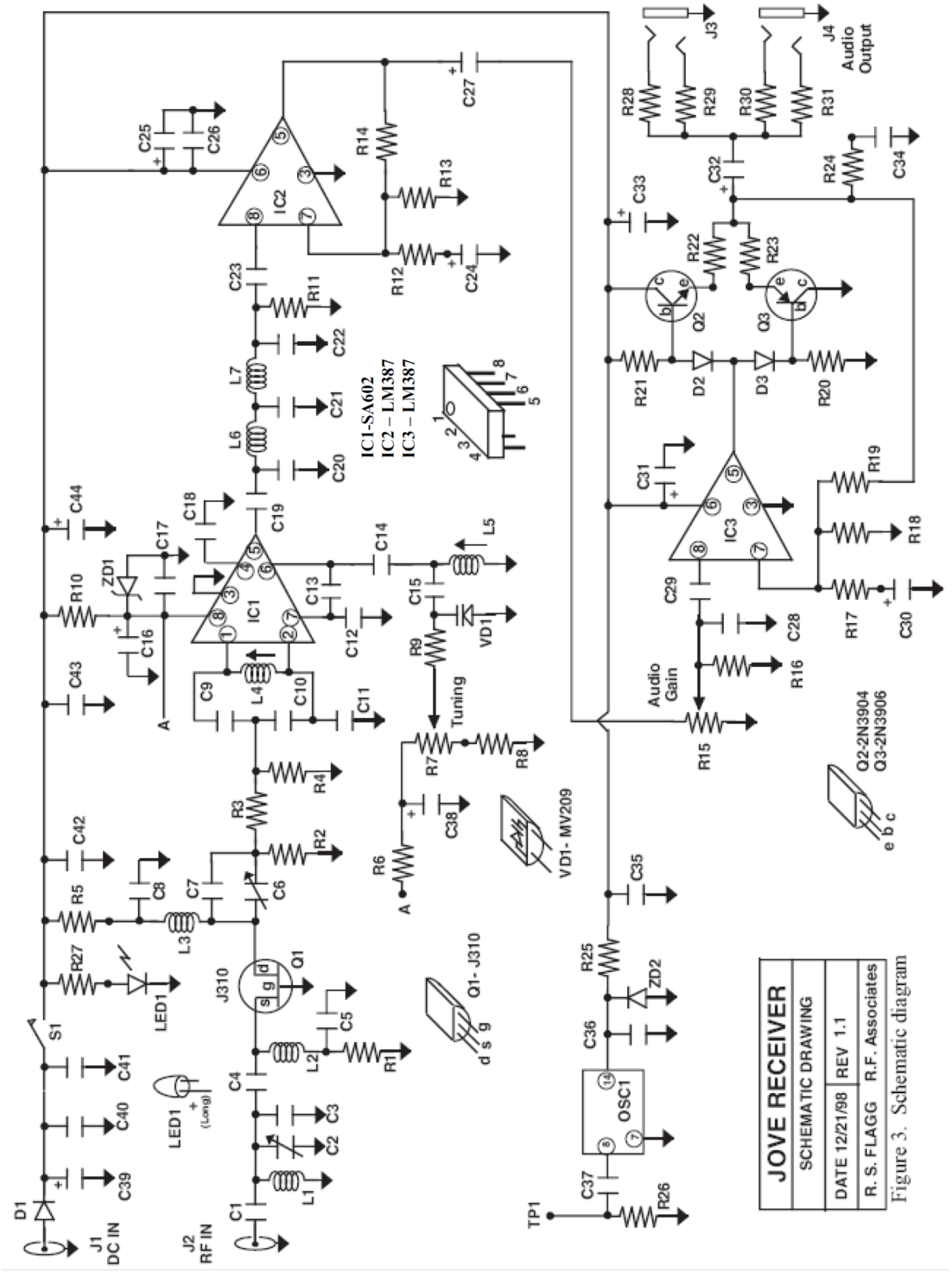

Figure 3. Schematic diagram

Figure 3.3: JOVE Receiver circuit diagram (Figure 3 from the kit assembly manual) showing the component implementation of the signal processing blocks of Figure 3.2.

## 3.1 General Description

The following is a general description of the functional blocks that make up the JOVE Receiver (refer to the receiver block diagram Figure 3.2) and describes the issues encountered within each block. The modifications section later in this chapter will show how improvements in each of the blocks delivered an overall improvement in performance.

### 3.1.1 Band-pass Filter

The first stage in the receiver is the 'RF Bandpass Filter'; its function is to exclude all signals outside of the narrow tuning range of the receiver and to match the antenna impedance to the radio-frequency (RF) pre-amplifier (RF Preamp J310) that follows. The tuning range of the JOVE Receiver is approximately $\pm$150 kHz and whilst it is possible to build a band-pass filter (BPF) that has a suitably sharp cut-off outside this range, the filter would be complex and expensive. The filter used here is simple, inexpensive and performs adequately under most circumstances. However, problems arise when there are strong signals from broadcast stations just outside of the $\pm$150 kHz tuning range of the receiver. The simple band-pass filter is unable to attenuate these signals sufficiently to prevent them from overloading the stages that follow. The mixer is particularly vulnerable, producing unwanted output from the audio amplifier and hence erroneous data output. A detailed analysis of the BPF is provided in the 'modifications' section that follows.

Another form of this large-signal, out-of-band overload, is where the wanted 'in-band' signal is suppressed, with the result that the wanted data are diminished or completely lost. In both these cases it is impossible to tell if the effect seen in the data is due to natural phenomena (e.g. a solar radio burst or an ionospheric fade out due to an intense solar X-ray flare) or due to radio-frequency interference (RFI).

The 28 MHz JOVE Receiver used at the author's home observatory was particularly susceptible to interference from the 27 MHz citizens band (CB) and the local shipping frequencies, which extend up to 28 MHz.

### 3.1.2 RF Pre-amplifier

Following the 'RF Bandpass Filter' is the 'RF Preamp J310'. This stage amplifies the signals from the antenna, provides additional band-pass filtering and matches the antenna impedance to the following stage, the 'LO/Mixer NE 602'. The

circuit configuration of the JFET (Junction Field Effect Transistor) gives good performance in its primary task of coupling signals from the 'RF Bandpass Filter' to the 'LO/Mixer NE 602' stage, but its performance in the reverse direction is poor. It is required that the leakage signal of the local oscillator (LO), from the NE 602 mixer, is suppressed and does not find its way to the antenna. Any radiation from the antenna is undesirable, but the extent to which it is a problem depends on the proximity of the antenna to other sensitive services. For most locations, e.g. home or school observatories, the radiation from the antenna is unlikely to be a problem. However, the JOVE Receiver is unlikely to be suitable for installation at a radio observatory, or in a radio quiet location, where other sensitive equipment will monitor at its frequency of operation.

No changes were made to the JFET circuit configuration, since the antenna radiation is unlikely to present a problem at the chosen sites.

### 3.1.3 Mixer

As stated in Richard Flagg's kit assembly manual (Flag, 2012), the 'LO/Mixer NE 602' stage performs the important function of converting the RF signal to an audio-frequency (AF) signal. The mixer combines the signal generated by the LO with the input RF signal to produce arithmetic sum and difference signals at the mixer output. The sum component is then easily removed using a low-pass filter (LPF), since it is well outside the frequency band of interest, leaving just the difference signal.

This type of direct conversion from RF to AF gives these receivers their name of 'direct conversion' or DC receivers (Tiuri & Raisanen, 1986, p. 7-3), with the AF output often referred to as 'baseband' (Schetgen, 1996, p. 12.1; p.18.14).

Consider the following example: the standard JOVE Receiver has the LO set to 20.1 MHz, with a small manual tuning range of approximately ±150 kHz. Therefore, for a desired tuning frequency of 21.1 MHz, the mixer output consists of the difference (baseband) signal at 0 Hz and the sum at 42.2 MHz. The JOVE Receiver has a LPF bandwidth of 3.5 kHz and therefore signals at 21.1 MHz ±3.5 kHz (a receiver bandwidth of 7 kHz) pass through to the AF amplifier but the signal at 42.2 MHz is blocked.

Unfortunately, real world mixers are not ideal and generate a number of other, undesirable products, many of which appear within the passband of the receiver. Further discussion of the many types of mixer is beyond the scope of this work. For a summary of different mixer types and their performance, see Everard (2002)

and Schetgen (1996, pp. 15.1-15.35) for a more detailed discussion of mixers and applications.

The mixer in the NE 602 is a 'Gilbert Cell'[3] double balanced transistor mixer. This mixer has the advantage of significant gain, in the order of 10 to 20 dB, but performs poorly in the presence of strong signals (Schetgen, 1996, p. 15.31). Strong out-of-band RF signals cause a disproportionate increase in intermodulation distortion (Everard, 2002, p. 245), resulting in unwanted output within the passband. It is for this reason that the input BPF ('RF Bandpass Filter' and 'RF Preamp. J310') must have adequate attenuation of out-of-band signals.

### 3.1.4 Local Oscillator (LO)

The LO component of the 'LO/Mixer NE 602' stage is a free running oscillator where frequency is determined by the L (inductance) and C (capacitance) of the circuit components. Temperature variation on these components (especially capacitors) causes significant changes in LO frequency. Since the receiver's bandwidth is relatively narrow at 7 kHz, man-made narrow-band signals can drift right through the receiver passband as temperature changes. This results in an erroneous peak (often with a central dip, as the signal passes through zero Hertz) in the recorded data. Temperature drift and other issues are dealt with in the 'modifications' section that follows.

### 3.1.5 Low-pass Filter

The '5 Pole Low Pass Filter' (LPF) has a bandwidth of 3.5 kHz and feeds the filtered signal to the 'Audio Preamp LM387'. The receiver is a 'hands on' receiver whereby the operator adjusts the tuning, to avoid man-made interference such as broadcast stations. However, for continuous recording of data, this is not practical and software can remove much of the interference, given sufficient bandwidth. Unfortunately, the receiver bandwidth is too narrow for this to be effective. For this application, digital signal processing (DSP) is used to reduce the effects of RFI. Imposing a 3.5 kHz bandwidth limitation on the personal computer (PC) audio system's 22 kHz of bandwidth does not make best use of available resources. A 22 kHz LPF is described in the 'modifications' section.

[3]First described by Barrie Gilbert in 1967, see Schetgen (1996) and `http://en.wikipedia.org/wiki/Gilbert_Cell`.

### 3.1.6 Audio Amplifier

Consistent with this 'hands on' approach, the receiver has an adjustable 'volume' control knob on the front panel, for setting the sound level when using headphones or an external speaker. There is no independent, fixed gain output for recording the audio on a PC or other recording device. Therefore, any change of the volume control setting makes it difficult, or impossible, to compare the magnitude of signals recorded at different times. This problem is overcome by using a second pre-amplifier, which is independent of the volume control and described in the 'modifications' section.

## 3.2 Modifications

The following describes, in detail, the modifications made to overcome the various problems identified in the previous section.

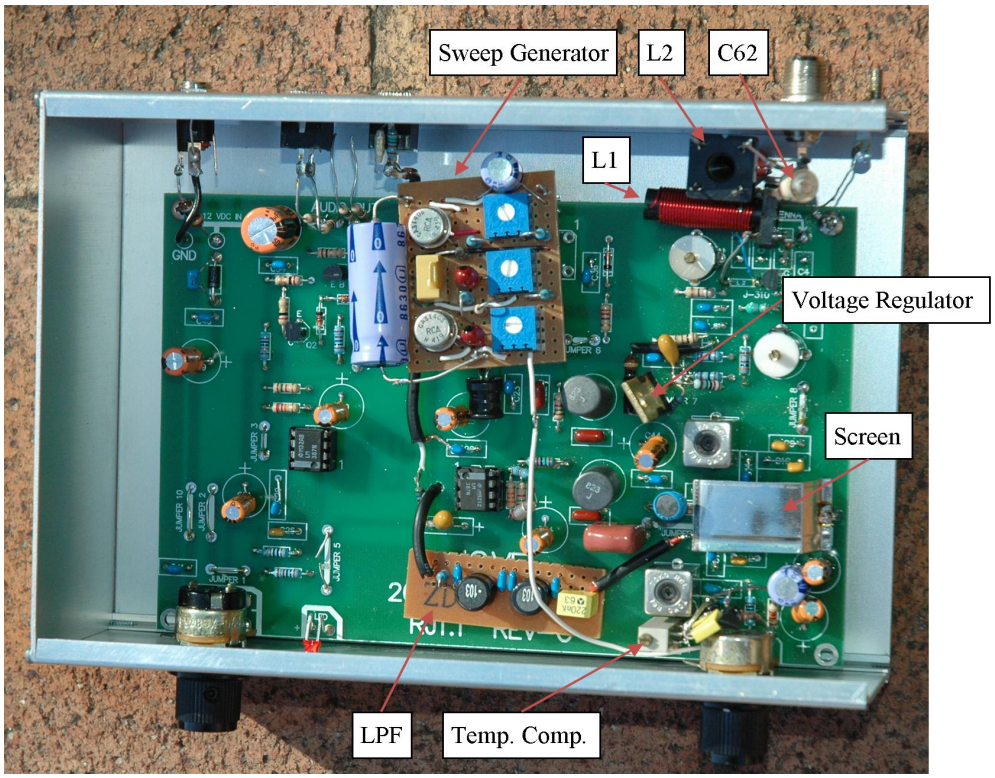


Figure 3.4: The author's home observatory 28 MHz JOVE Receiver showing modifications.

Shown in Figure 3.4 and Figure 3.5 are the modifications made to the author's home observatory 28 MHz JOVE Receiver. The block and circuit diagrams are shown in Figure 3.6 and Figure 3.7, respectively.

The JOVE Receivers at the other sites (Gingin and LSO) have most, but not all, of these modifications, details of which are presented in the Observatories chapter.

In general, all the modified JOVE Receivers conform to the arrangement shown in Figure 3.7 and differ only in minor detail.

When first considering these modifications, it was hoped that a wide-band output of several hundred kilohertz could be made available from IC2/b (see Figure 3.7). This output could be used in conjunction with a spectrum analyser or a PC sound card with a much higher sampling frequency than the standard audio system. However, early tests showed that the strong local signals overloaded the amplifier causing limiting. This in turn generates a wide range of harmonics that render the entire bandwidth useless. Reducing the gain to accommodate these signals would make it impossible to see low-level signals like the diurnal galactic background noise.

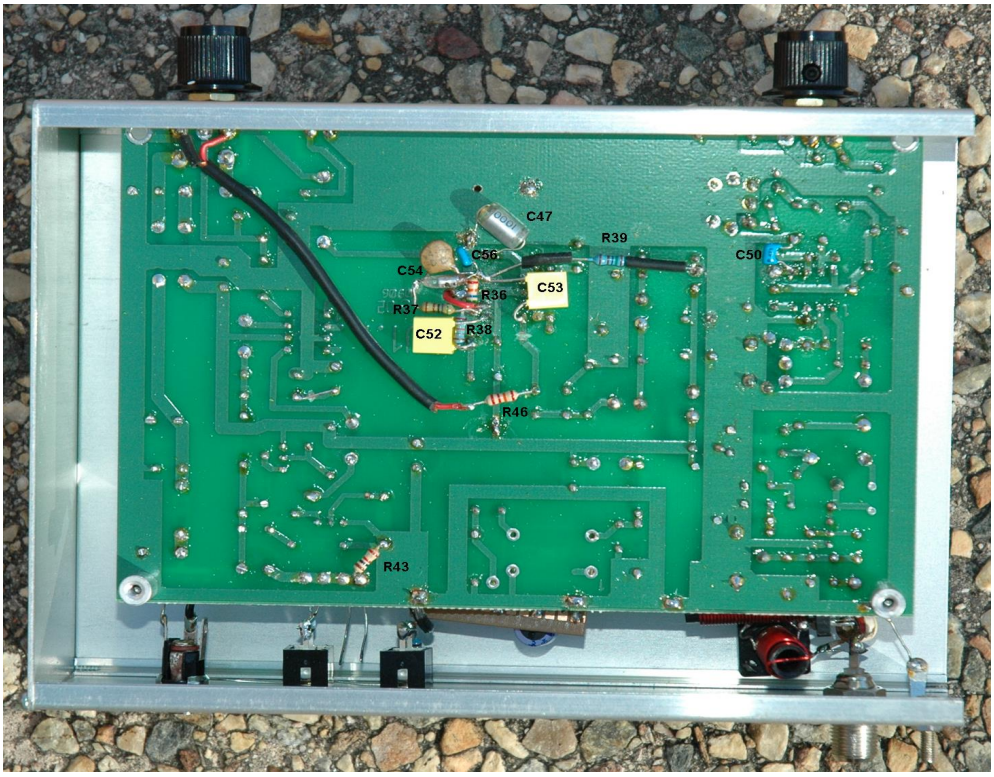


Figure 3.5: The author's home observatory 28 MHz JOVE Receiver showing printed circuit board (PCB) underside modifications.

The addition of bandwidth-limiting components (amplifier gain is reduced as frequency increases) solved the local interference problem but another problem soon became evident. During testing on the author's home PC, signals were

seen on the spectrograph display that had not been apparent on the laptop PC normally used with the JOVE Receiver.

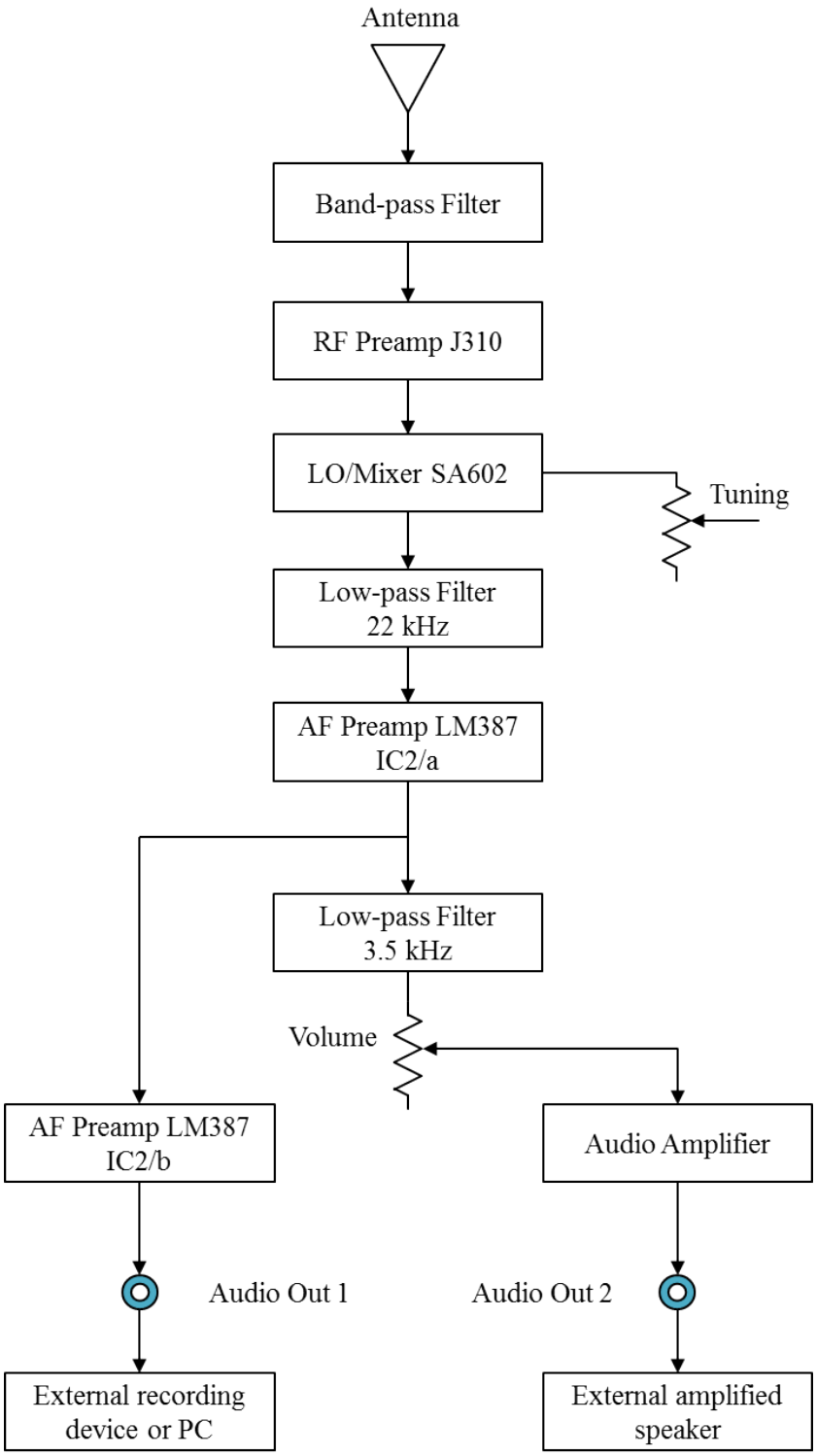


Figure 3.6: Modified JOVE Receiver block diagram showing the additional 22 kHz low-pass filter and AF preamp. IC2/b. Derived from the original JOVE Receiver block diagram.

These signals turned out to be aliased products (Proakis & Manolakis, 1996, p. 276) of input signals outside the 22 kHz bandwidth of the author's home PC audio system and extended out 300 kHz either side of the tuning frequency. Because the PC audio system analogue to digital converter (A/D) samples at 44.1 kHz, input signals must be limited to 22.05 kHz to avoid aliasing.

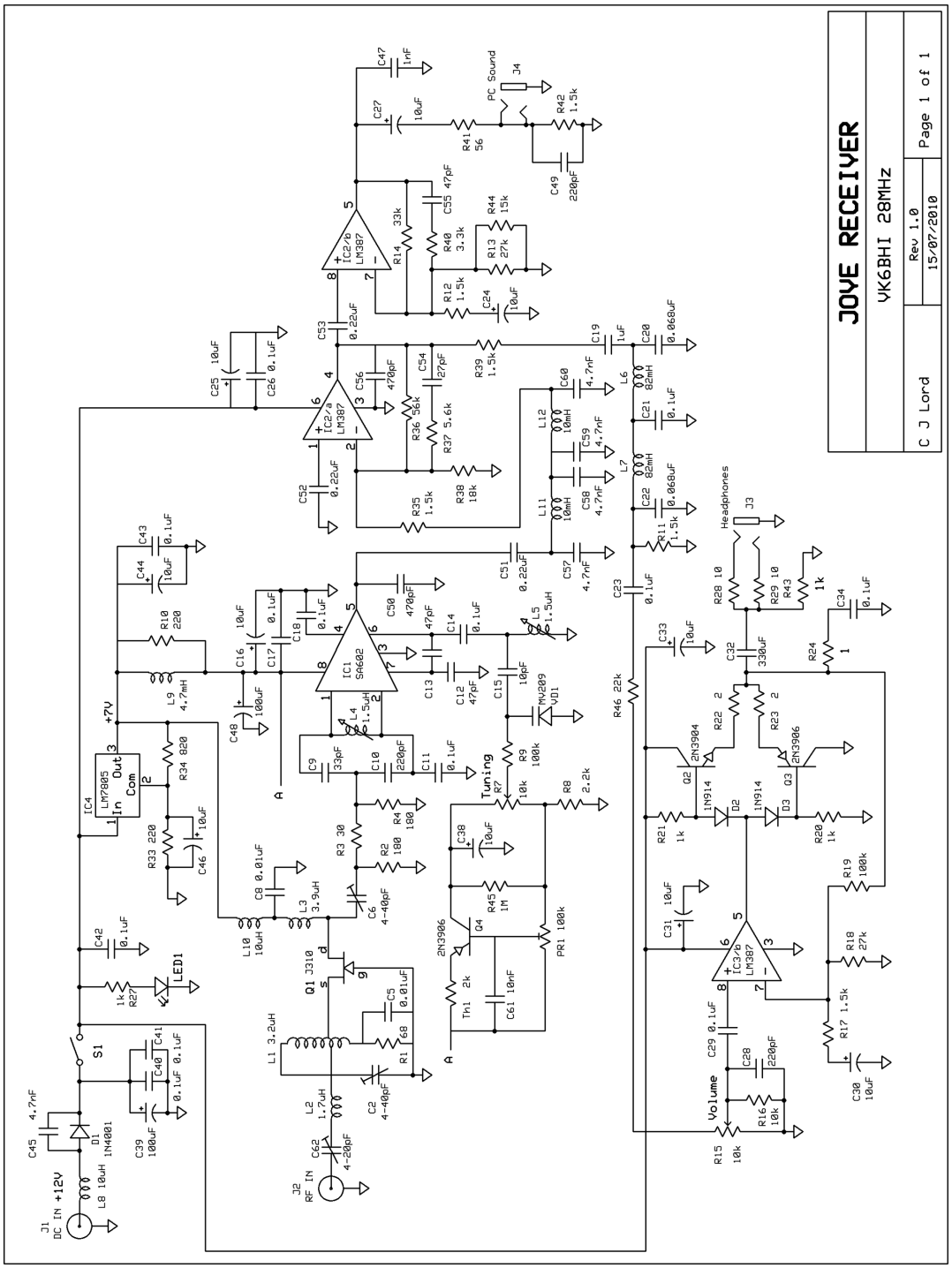


Figure 3.7: The author's modified home observatory 28 MHz JOVE Receiver circuit diagram. Derived from the original JOVE Receiver circuit diagram.

It was decided therefore, to abandon the idea of a wide-band output and build in a LPF (described later) with a sufficiently sharp cut off to avoid the potential aliasing problems and allowing reliable use with a range of PCs.

### 3.2.1 Selectivity

As stated earlier, the receiver was easily overloaded by strong CB radio and shipping channels. Obtaining the required selectivity to avoid these problems comes at the cost of a more complex tuned circuit in the RF band-pass filter, specifically the inductor L1. The original L1 was removed along with L2, C3 and C4 (see Figure 3.3) and a new L1 wound with additional tapping points, as shown in Figure 3.7. L1 and C2 now form the new input tuned circuit. This circuit arrangement (Chow et al., 1963, p. 167) allows correct impedance matching between the antenna and the RF amplifier transistor Q1, with increased selectivity.

To maximise the Q (quality factor) and hence the selectivity of the tuned circuit, both L1 and L2 were wound with 0.63mm enamelled copper wire on 7mm diameter plastic formers, without using ferrite cores. L1 has 29 turns tapped at 4.7 turns and 5.1 turns and L2 has 23 turns. Additional selectivity results from using a series tuned circuit comprising the newly wound L2 and C62, between the antenna and the receiver input, as shown in Figures 3.4 and 3.7.

### 3.2.2 Mixer SA602

In the original JOVE Receiver circuit, the power supply for the NE602 (IC1 – SA602 in Figure 3.7) is derived from a 6.2 Volt zener diode (ZD1 in Figure 3.3) and resistor, supplied from the main 12 Volt DC (direct current) supply. The SA602 mixer output has a 1.5 k Ohm internal resistor pull up to its supply pin, through which any noise on the supply finds its way to the output of the mixer. The zener diode is also a source of noise and although it appears well decoupled by several capacitors, low-frequency noise was still a problem. There was also a small amount of 100 Hz ripple from the power pack supplying the 12 VDC to the receiver, from the AC (alternating current) mains supply. Voltage regulator IC4 (LM7805 in Figure 3.7) overcomes these problems and supplies both the SA602 and the RF amplifier Q1. The addition of R33, R34 and C46 increases the output voltage of the regulator to 7 Volts, to maximise the performance of the SA602. Fitting a small, grounded, tin plate screen, over the SA602 also helps reduce noise. See Figure 3.4.

### 3.2.3 22 kHz Low-pass Filter

The 22 kHz LPF helps to prevent aliasing in the PC audio system. Most PCs should have adequate filters built in, but the author found that this is not always the case. If frequencies higher than 22 kHz enter the PC audio system and filtering is inadequate, then the sampling process produces erroneous outputs known as aliased products. These aliased products appear in addition to the wanted signals, increasing noise levels and interference from out-of-band signals.

The basic design for the LPF (see Figure 3.8) is a five pole Butterworth filter (Huelsman, 1993, p. 34), but with components optimised using a SPICE[4] circuit simulation program. With only a limited range of component values available, it is usually not possible to construct a filter that conforms exactly to the calculated values for the components. Therefore, a compromise was made between component values and performance. In this case, flatness of passband was sacrificed for a slightly sharper cut off at the band edge. This had the advantage of increased attenuation for out-of-band signals, with only a minor variation of magnitude across the passband.

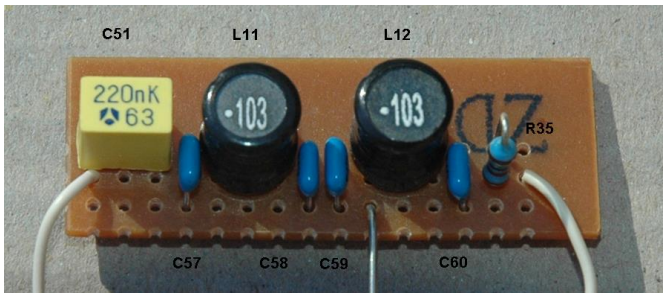


Figure 3.8: 22 kHz LPF components layout.

Figure 3.9 below shows the magnitude response as measured for the LPF, compared to a SPICE simulation using component values as calculated. Calculating component values (Huelsman, 1993, pp. 434,435) for an upper passband frequency of 30 kHz ensures a sufficiently flat response over the range 0 to 22 kHz. Since the filter does not immediately cut off signals beyond 22 kHz, the receiver tuning is adjusted to ensure that strong RFI falls sufficiently far outside the filter passband that it is attenuated to an acceptable level. The DSP software removes weaker RFI within the passband.

[4]The author used B2Spice_v5 `http://www.beigebag.com/v5_features`, but there are also versions available for free download such as LTSpice `http://www.linear.com/ltspice` by Linear Technology. General information about SPICE can be found at `http://en.wikipedia.org/wiki/SPICE`.

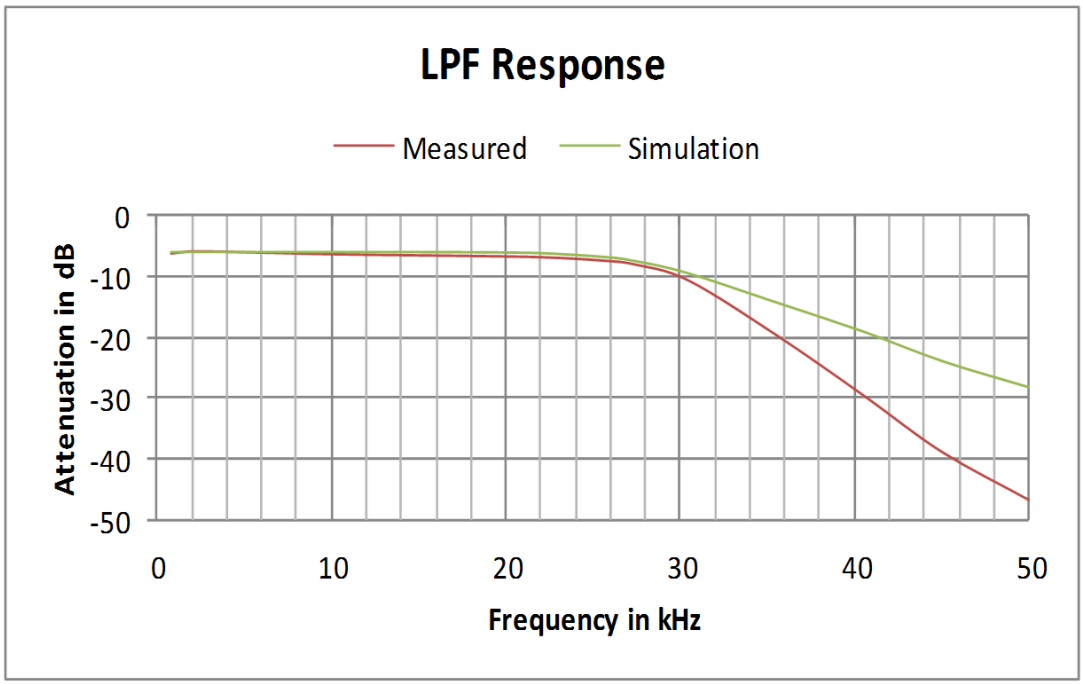


Figure 3.9: 22 kHz LPF Magnitude Response vs. Frequency. The measured response is with components optimised for greater out-of-band attenuation whereas the simulation used ideal components for a maximally flat Butterworth response.

### 3.2.4 LM387 Pre-amplifier

The original JOVE Receiver uses two LM387, low noise, wide-bandwidth amplifier ICs (IC2 and IC3). IC2 is the audio pre-amplifier and IC3 forms part of the audio amplifier that drives Audio Out1 and Audio Out2. However, the LM387 is a dual amplifier consisting of two identical amplifiers 'a' and 'b'; only the 'b' amplifier is used from each package. Using IC2/a, a new pre-amplifier was built to provide a wide-bandwidth output to drive the original IC2/b pre-amplifier and the original LPF. The original IC2/b pre-amplifier is now used to provide a low power output from Audio Out1, for connection to a recording device or PC. The original LPF connects to the volume control, audio amplifier and Audio Out2, as in the original circuit. Components for pre-amplifier IC2/a are mounted on the underside of the JOVE Receiver PCB as shown in Figure 3.5.

The circuit configuration of IC2/a was chosen to minimise the noise contribution of the amplifier, by grounding the non-inverting input of the amplifier for AC and feeding the output from the 22 kHz LPF to the inverting input. Low noise in this amplifier is particularly important since the noise is subject to the gain of the following stages. R35 provides the correct load impedance for the LPF,

due to the very high open loop gain of the LM387 and the negative feedback resistor R36. The addition of R37, C54 and C56 reduces the gain-bandwidth of the amplifier, which gives an extra margin of safety against strong out-of-band signals.

IC2/b has the same bandwidth restriction applied with R40, C55 and C47. The addition of R44 shifts the DC output of IC2/b, such that its AC output voltage swing is maximised before clipping occurs. It is important that strong signals do not cause clipping, since this produces high levels of wide-bandwidth harmonic distortion, making it impossible for the DSP software to recover the wanted signals.

It was found that high-frequency noise could be transferred from the PC, to the interior of the receiver via the Audio Out1 connection. To prevent this, C49 was added across Audio Out1 to chassis and a ferrite suppressor fitted to the PC end of the audio lead.

## 3.3 Performance

The following describes measurements made on the author's unmodified and modified JOVE Receivers, to determine how successful the modifications have been in improving selectivity and noise factor.

These measurements were accomplished using a signal generator (RigExpert AA-200), fixed and switched attenuators, oscilloscope (Tektronix 2465B) and digital voltmeter (Fluke 8060A).

### 3.3.1 Band-pass Filter

The band-pass filter (BPF) comprises all of the tuned circuits up to and including the input to the mixer. The following measurements were made to determine how much effect the high Q antenna coupling tuned circuit has had on the bandwidth of the BPF as a whole.

The BPF response test setup is shown in Figure 3.10. The mixer output was temporarily disconnected from the LPF and connected instead to an equivalent 1.5 k Ohm load resistor. This allowed the complete range of outputs from the mixer to be observed without loading effects due to the LPF and following stages. To minimise loading effects on the mixer output, measurements were made with a high impedance probe connected to channel 2 of the 2465B oscilloscope. Channel 2 has an output that was used to drive channel 1, giving up to 10 times amplification of the signal. Unwanted mixer products and LO feed through were

filtered out using a 6.5 MHz LPF interposed between channel 2 out and channel 1 input. The characteristics of this filter were taken into account when calculating the BPF response. The signal level at the mixer output was measured over a range of frequencies either side of the centre-frequency to which the receiver was tuned. With measurements taken from both the modified and unmodified receivers, it was possible to compare graphically the input characteristics of both receivers.

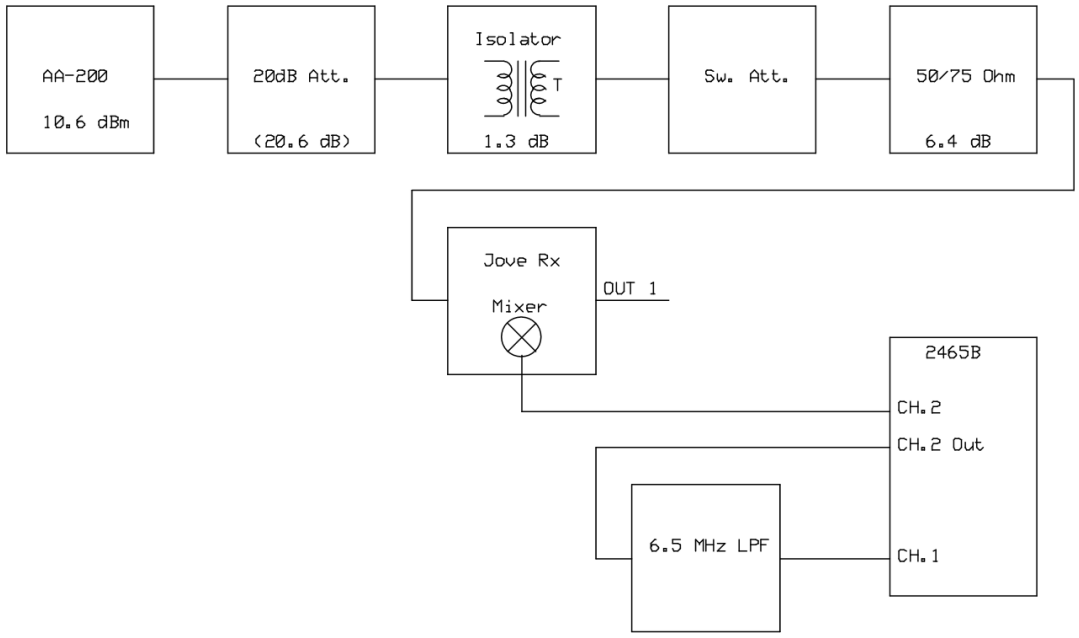


Figure 3.10: Test setup for BPF measurements showing the JOVE Receiver mixer output connected directly to the 2465B oscilloscope.

Since the BPF attenuation increases as signals move further away from the centre-frequency, signal levels from the mixer would very soon become impossible to measure with the equipment available. To overcome this problem, a reference level at the mixer output was established, which produced maximum output from the receiver at the centre-frequency and the switched attenuator used to maintain this level for each test frequency.

The centre-frequency is the frequency as set by the tuning knob (the LO frequency) and the frequency to which all of the tuned circuits comprising the BPF have been aligned.

With the centre-frequency reference level established, the number of decibels (dB) indicated on the switched attenuator was noted. Next, the signal generator was adjusted away from the centre-frequency, the switched attenuator adjusted to restore the reference level and the number of dB on the switched attenuator

recorded. This process was repeated either side of the centre-frequency to a sufficient extent to cover the usable width of the BPF. The graph in Figure 3.11 plots the dB data recorded in this fashion and normalised to the reference dB at the centre-frequency of 28.126 MHz. This frequency places the receiver tuning range within the 28.0 to 28.3 MHz Morse code and digital modes allocation, within the 28.0 to 29.7 MHz Amateur Radio band. Morse code and Amateur digital modes are narrow-band, and easily removed with DSP software.

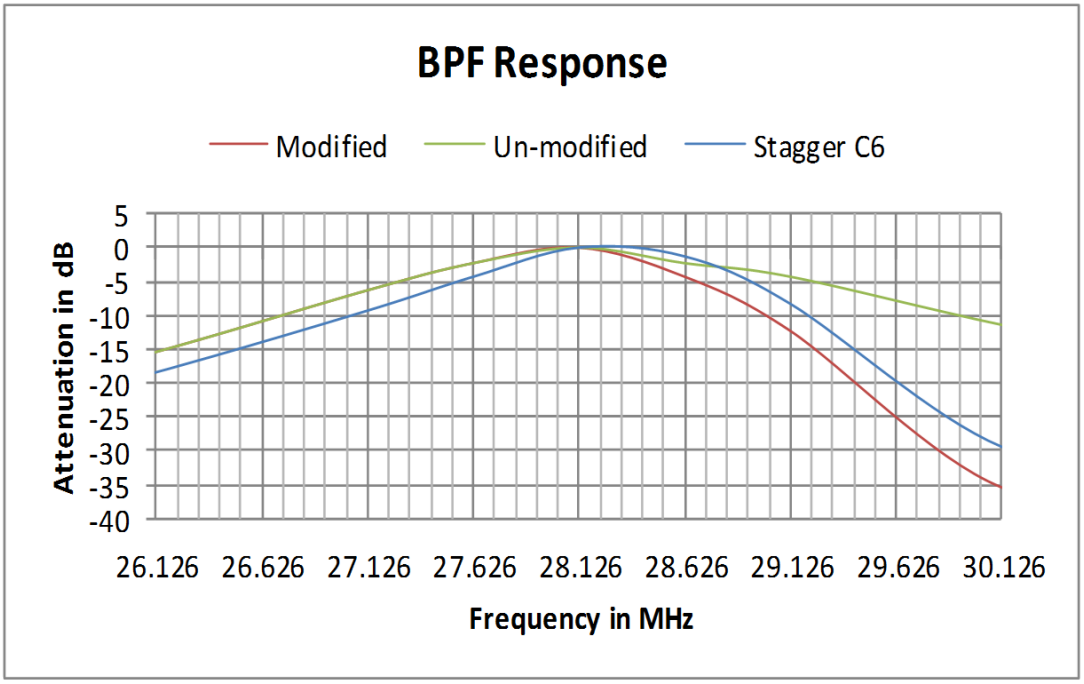


Figure 3.11: Comparison of modified and unmodified receiver BPF response.

Figure 3.11 shows that the modified BPF response has a much greater rejection of frequencies above the centre-frequency than the unmodified version. However, it is to the low-frequency side of the centre-frequency where most of the problems of RFI occur and there was no improvement in this area. Some improvement was made by re-tuning C6 (in the 'RF Preamp J310' output tuned circuit) to 28.626 MHz, as indicated by the 'stagger C6' data plot. This 'stagger' tuning gives approximately 3 dB extra attenuation on the low side of the centre-frequency at the expense of the high side. An additional benefit is a broader peak, giving more consistent gain over a wider range of frequencies, with a loss of only about 1 dB in total sensitivity. These improvements are very marginal and it was not considered worthwhile implementing them at other than the author's home installation. Post mixer filtering was successful in eliminating the local interference and aliasing problems, so these modifications were implemented on the other receivers. The

extent to which intermodulation distortion (IMD), due to strong signals being applied to the mixer, may be affecting the receiver is unknown. No clear evidence for this was found with the author's receiver and IMD measurements are beyond the scope of this work.

### 3.3.2 Noise Factor

In order to determine how effective the modifications to the JOVE Receiver have been, a method is required for measuring how good the receiver is. If the receiver were perfect, it would convert the signal at the antenna input, to the required output signal, without adding any noise of its own. Since receivers are not perfect, there is a small amount of noise power at the output attributed to components within the receiver. A measure of this noise power is the Noise Factor, which when expressed in dB is called the Noise Figure (Everard, 2002, p. 117) for the receiver.

Noise appearing at the output of the receiver, with the antenna input connected to a dummy load, is expressed by the following equation (Tiuri & Raisanen, 1986, p. 7-24), (Schetgen, 1996, p. 17.4):

$$N_o = kTBFG, \tag{3.1}$$

where:

$N_o$ = Noise output, W;

$k$ = Boltzmann's constant, J/K;

$T$ = Temperature, K;

$B$ = Bandwidth, Hz;

$F$ = Noise Factor, dimensionless;

$G$ = Power gain, dimensionless.

For a perfect receiver, the Noise Factor $F = 1$ and the noise output is a function of the thermal noise at the antenna input multiplied by the bandwidth and gain of the receiver. Re-arranging (3.1), the noise factor can be determined as:

$$F = \frac{N_o}{kTBG}. \tag{3.2}$$

The numerical values for this equation cover a wide range and therefore it is simpler to work in dB. The noise factor is then expressed as a noise figure as follows:

$$F = N_o(\text{dB}) - (kT(\text{dB}) + B(\text{dB}) + G(\text{dB}))\ \text{dB}. \tag{3.3}$$

Next, the gain of the receiver in dB needs to be determined. This is achieved by first measuring the signal to noise ratio of the receiver, which is also an indication of the sensitivity of the receiver. Using a digital volt meter (DVM) such as the Fluke 8060A, with the facility of measuring directly in dB with a 'relative' (REL button) measurement capability, greatly simplifies these measurements. The test setup is shown in Figure 3.12.

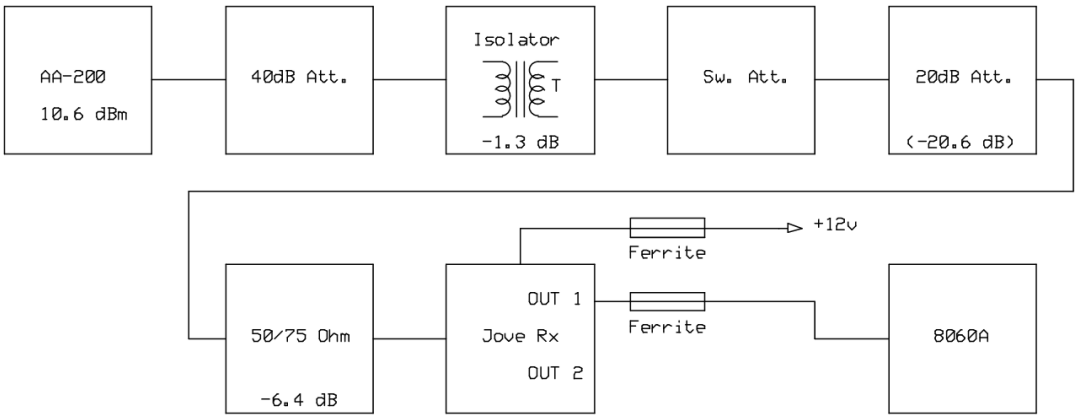


Figure 3.12: Test setup for noise figure measurements using the 8060A DVM.

If a signal generator attached to the antenna input is adjusted such that the signal plus noise voltage at the receiver output increases by 10 dB then (Schetgen, 1996, p. 17.5),

$$20 \times \log\left[\frac{\text{signal} + \text{noise}}{\text{noise}}\right] = 10 \text{ dB} \tag{3.4}$$

and the signal output voltage is

$$S_{Vo} = \text{noise} \times \left(10^{\frac{10}{20}} - 1\right) = 2.162 \times \text{noise}. \tag{3.5}$$

The 'signal in' power was determined from the signal power available from the AA-200 and the amount of attenuation applied by the attenuator switch settings. The signal output of the AA-200 at the centre-frequency of 28.126 MHz was measured to be 2.14 V p-p into 50 Ohms. This results in a signal power of:

$$10 \times \log\left(\frac{V_{RMS}^2}{50} \times 1000\right) = 10.6 \text{ dBm}. \tag{3.6}$$

The total fixed attenuation is 68.3 dB. Therefore, the maximum input power available before adding switched attenuation is $10.6 - 68.3 = -57.7$ dBm.

If, for a 10 dB signal to noise ratio, it is necessary to add $A_{sw}$ dB of switched attenuation, then the signal input power is:

$$S_{Pi} = -57.7 - A_{sw} \text{ dBm}, \tag{3.7}$$

which, in terms of signal voltage at the receiver input is:

$$S_{Vi} = \sqrt{\left(\frac{10^{\frac{S_{Pi}}{10}}}{1000} \times R\right)} \text{ Volts,} \tag{3.8}$$

where $R$ = receiver input impedance = 75Ω.

The gain of the receiver is then:

$$G = 20 \times \log\left(\frac{S_{Vo}}{S_{Vi}}\right) \text{ dB.} \tag{3.9}$$

The output noise voltage $N_{Vo}$ was measured using the 8060A DVM and the signal output voltage $S_{Vo}$ found from (3.5). The gain of the receiver can now be determined from (3.9).

The signal output was measured with the receiver tuned 1.5 kHz off the centre-frequency. This gave a signal output of 1.5 kHz and put the signal approximately mid-band in the unmodified receiver's LPF.

The noise output $N_{Vo}$ of the modified receiver was measured to be 15.4 mV RMS (root mean square) using the 8060A DVM and the switched attenuator setting $A_{sw}$ was 55 dB for a 10 dB signal plus noise to noise ratio. Therefore, from (3.5) the signal output is:

$$S_{Vo} = 2.162 \times 15.4 = 33.295 \text{ mV.} \tag{3.10}$$

From (3.7) the signal input power (sensitivity) is:

$$S_{Pi} = -57.7 - A_{sw} = -57.7 - 55 = -112.7 \text{ dBm} \tag{3.11}$$

and the signal input voltage:

$$S_{Vi} = \sqrt{\left(\frac{10^{\frac{-112.7}{10}}}{1000} \times 75\right)} = 6.346 \times 10^{-7} \text{ Volts,} \tag{3.12}$$

giving a receiver gain of:

$$G = 20 \times \log\left(\frac{S_{Vo}}{S_{Vi}}\right) = 94.4 \text{ dB.} \tag{3.13}$$

The bandwidth of the receiver is determined by the bandwidth of the LPF. However, the bandwidth $B$ used in (3.2) needs to be twice the receiver bandwidth for this type of receiver, a two channel receiver (Tiuri & Raisanen, 1986, p. 7-2). The bandwidth is then expressed in dB as follows:

$$B = 10 \times \log\big(2 \times \text{ receiver bandwidth (Hz)}\big) \text{ dB} \tag{3.14}$$

and for the modified receiver with bandwidth equal to 30 kHz,

$$B = 47.8 \text{ dB}. \tag{3.15}$$

The value of $kT$ expressed in dBm for an absolute temperature of 290 K is

$$kT = -174 \text{ dBm}. \tag{3.16}$$

The noise output $N_o$ of the receiver can be measured directly in dBm on the 8060A. However, this requires a conversion factor to be programmed into the DVM via the REL button. It is simpler to calculate the noise power using a load resistance equal to the input impedance of the receiver, as follows:

$$N_o = 10 \times \log\left(\frac{N_{Vo}^2}{R} \times 1000\right) \text{ dBm}, \tag{3.17}$$

where $R$ = receiver input impedance = 75Ω.
For the modified receiver,

$$N_o = -25.0 \text{ dBm}. \tag{3.18}$$

The noise figure for the modified receiver can now be found as follows:

$$\begin{aligned} F &= N_o(\text{dB}) - (kT(\text{dB}) + B(\text{dB}) + G(\text{dB})) \text{ dB} \\ &= -25.0 - (-174 + 47.8 + 94.4) \\ &= 6.8 \text{ dB}. \end{aligned} \tag{3.19}$$

Table 3.1: Modified and unmodified JOVE Receiver performance comparisons.

| Parameter | | Modified | Unmodified |
|---|---|---|---|
| Noise output voltage | $N_{Vo}$ | 15.4 mV | 1.4 mV |
| Noise output power | $N_o$ | −25 dBm | −45.8 dBm |
| Signal output voltage | $S_{Vo}$ | 33.295 mV | 3.027 mV |
| Signal input voltage | $S_{Vi}$ | $6.346 \times 10^{-7}$ V | $3.038 \times 10^{-7}$ V |
| Signal input power | $S_{Pi}$ | −112.7 dBm | −119.1 dBm |
| Bandwidth | $B$ | 47.8 dB | 38.5 dB |
| Gain | $G$ | 94.4 dB | 80 dB |
| Noise Figure | $F$ | 6.8 dB | 9.7 dB |

## 3.4 Summary

Figure 3.11 shows that the high Q tuned circuit has not significantly improved the BPF response below the centre-frequency, where most of the problems from local RFI have occurred. However, it does show that improvements could be made to the receiver front-end selectivity, which would lead to a higher IMD immunity in the presence of strong signals.

The ideal of having a very wide-band output was not realisable due to lack of dynamic range in the receiver and the risk of aliasing problems with PC audio systems. Limiting the bandwidth of the audio amplifiers in the receiver and adding the 22 kHz LPF did, however, cure the local interference problem and reduce the risk of aliasing in unfiltered PC audio systems.

The noise figure $F$ has improved from 9.7 dB for the unmodified receiver, to 6.8 dB for the modified version. So, how much better is the noise performance of the modified receiver?

Substituting the unmodified receiver's noise figure into equation (3.1) gives a noise output of:

$$\begin{aligned} N_o &= -kT(\text{dB}) + B(\text{dB}) + F(\text{dB}) + G(\text{dB}) \\ &= -174 + 47.8 + 9.7 + 94.4 \\ &= -22.1 \text{ dBm}. \end{aligned} \tag{3.20}$$

This is equivalent to a noise output voltage of:

$$N_{Vo} = \sqrt{\left(\frac{10^{\frac{-22.1}{10}}}{1000} \times 75\right)} = 21.5 \text{ mV}. \tag{3.21}$$

From this result, it can see that there has been a significant 28% reduction in noise output voltage from the modified receiver, compared to what would have been achieved, by simply increasing the bandwidth and gain of the unmodified receiver.

# Chapter 4

# Observatories

The three observatory sites were established over a period of two years, starting with the author's home observatory vk6bhi[1]. After eight months of development of the JOVE Receiver and software, the receivers at Gingin Observatory were modified, the Radio-SkyPipe software replaced with the RioMeter software and repairs carried out to the antenna system. Eighteen months after starting the project the author established a third radio telescope at the Learmonth Solar Observatory (LSO) during a six month working contract at that site.

By comparing the data from each of the three sites, it is possible to separate natural phenomena from local interference. The radio telescope PC clock at each site is synchronised to internet time, so the error in timekeeping between sites is expected to be less than the average sampling time of six seconds.

Each observatory has a different set up in terms of frequencies covered and antenna system layout. LSO has a JOVE Receiver with tuning centred on 20.1 MHz which is the standard frequency for JOVE Receivers, whereas Gingin Observatory has JOVE Receivers tuned to 17 and 28 MHz and vk6bhi observatory has a single JOVE Receiver tuned to 28 MHz. The choice of 17 and 28 MHz has no special significance other than to give a diversity of frequency coverage. This has the advantage that a broad spread of data are gathered and therefore a greater likelihood of picking up interesting phenomena, but has the disadvantage that data cannot be directly compared between sites. It was hoped that the galactic background signal would provide a source of calibration for the data. However, broadband RFI pushes up the noise floor and this needs to be taken into account when determining the galactic background signal level.

[1]VK6BHI is the author's Australian Amateur Radio station call sign. The author also holds the United Kingdom call sign G3YUU.

## 4.1 Observatory VK6BHI

The observatory radio telescope consists of a modified 28 MHz JOVE Receiver connected to a laptop PC running the Microsoft Windows XP operating system. An internet connection is provided for transfer of data to the author's e-mail address. This maintains consistency with the other sites and provides backup for the data. The antenna system, JOVE Receiver and laptop PC were installed in October 2008 and after identifying and suppressing the major sources of RFI, the first data were recorded using Radio Sky-pipe in November 2008. Over the next few months modifications were made to the receiver to improve its performance. More sources of RFI were identified and suppressed while work continued on the development of the RioMeter and RioPlot software that would replace Radio Sky-pipe (see Chapter 6). By October 2009 the major modifications to the JOVE Receiver had been completed, compiled versions of the RioMeter and RioPlot software had been installed on the laptop PC and work was under way on the upgrade to the Gingin Observatory system. The most recent upgrade to the RioMeter software occurred in January 2011 and experimental work commenced on an improved receiver design as described in Chapter 5.

Figure 4.1: The author's 28 MHz antenna over salt water swimming pool 'ground plane' on 26$^{th}$ February 2009.

### 4.1.1 Antenna System

Figure 4.1 shows the 28 MHz antenna system erected over a salt water swimming pool at the author's home. Due to space constraints in a suburban environment, the dipoles are aligned approximately north/south rather than the preferred orientation of east/west. The salt water of the swimming pool acts as a ground plane and gives the antenna an improved gain compared with an antenna erected over sand.

The design of the baluns and combiner is as described earlier in Chapter 2. However, the dimensions differ from those of the Radio JOVE antenna because of the increased operating frequency. The dimensions for this antenna system are as follows: dipole length 4.84 m; height 2.30 m; and spacing 5.34 m.

The feeders for this installation use RG6 Quad Shield coaxial cable to reduce RFI picked up from the house wiring where the feeder to the receiver passes through the roof space. The length of the feeder from the combiner to the receiver is a multiple of half wavelengths. The surplus is wound into a coil approximately 200 mm in diameter, held together with cable ties and positioned close to the receiver. This acts as a choke balun[2], increasing the impedance for RFI on the coax braid. In addition to this, a ferrite suppressor is placed over the coax just before it enters the coil.

### 4.1.2 SA602 LO Temperature Stability

An attempt was made to stabilise the local oscillator (LO) frequency of the JOVE Receiver using a temperature dependent resistor (Th1 in Figure 3.7) in the voltage controlled oscillator (VCO) circuit. However, the amount of frequency drift was too great for this simple solution and a more complex circuit was not considered a practical modification for the receiver. Instead, the sweep generator (Figure 4.2) described in the next section, provides a more general solution to the temperature and RFI problems.

### 4.1.3 Sweep Generator

The sweep generator sub-assembly is shown in Figure 4.2 and fits on the main receiver board over the crystal calibrator circuit. Refer to Figure 3.4 in Chapter 3. L1 in Figure 4.3 is not shown in Figure 4.2 since it fits between the main board and the sweep generator sub-assembly. L1 and C6 had to be added later, due to

[2]A choke balun is essentially a current balun, details of which can be found in the Antenna System chapter.

higher than expected noise coupling from the receiver +12 VDC supply and the components of the sweep generator and were therefore not part of the original component layout. C1 and C2 are located on the underside of the circuit board.

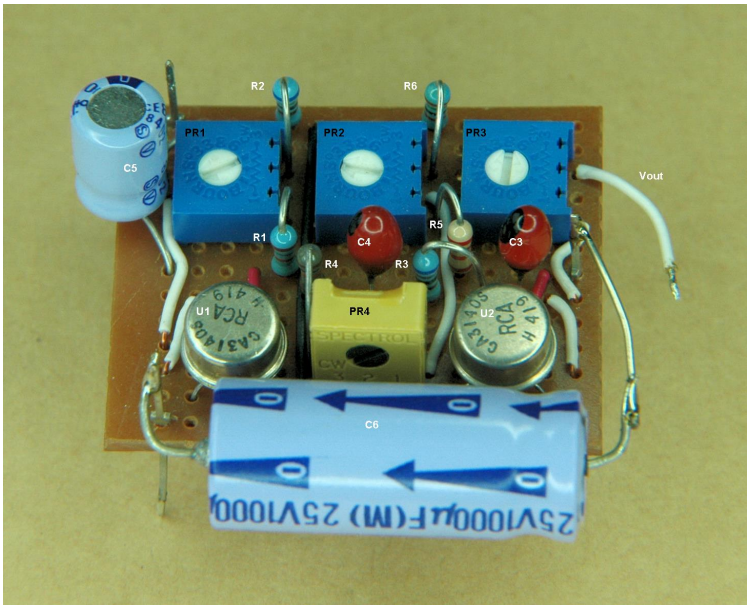


Figure 4.2: Sweep Generator sub-assembly.

The purpose of the sweep generator is to scan the receiver frequency over a wide band of frequencies compared to the bandwidth of the receiver. The sweep generator output voltage (Vout in Figure 4.3) rises and falls linearly with time and is connected to the wiper of the tuning potentiometer (R7 In Figure 3.7 of Chapter 3). For correct operation the tuning potentiometer needs to be set midway in its range. The span control (PR3 in Figure 4.3) is used to adjust the range of frequencies scanned, in the same way as the manual tuning control changes the frequency when turned by hand. Using PR4 in Figure 4.3, the sweep period is adjusted to be approximately equal to that of the averaged sampling period of the software. The software takes a number of samples of the receiver output over the sampling period and saves the average signal level as a data sample. During the sampling period, the sweep generator causes the receiver frequency to traverse twice over its tuning range. It is expected that the swept range of the receiver will be mostly free from RFI and therefore only a few of the samples will be contaminated. When all the samples are averaged over the sampling period, the contribution from RFI should be small. Since the receiver frequency is swept over a wide range of approximately ten times the receiver bandwidth, a few kilohertz of drift in the receiver LO is not going to be significant.

In practice the sweep generator works well for certain types of RFI but does

cause the base noise level to be higher. The type of RFI that this system is effective against is the relatively wide-bandwidth audio and data communications from broadcast stations. Where greater than half of the receiver bandwidth is occupied by this type of RFI, it is difficult for the digital signal processing software (DSP) to remove it and still recover a stable average for the remainder of the bandwidth. The base noise level is higher since variations in magnitude of the strong broadcast stations cause a significant increase in average background noise. However, this is still a better result than would have been the case if broadband RFI had been permanently within the receiver bandwidth. A disadvantage of the swept system is that the DSP software is not able to remove the narrow-band RFI in the normal way because several samples at the same frequency are required. Normally, two sets of data are recorded, one being the average time domain magnitude and the other being the average frequency domain magnitude after narrow-band RFI has been removed. By comparing these two sets of data it is usually clear which data are due to RFI and which are due to wide-band natural phenomena such as solar radio bursts. With the swept system there is effectively only one set of data: the average time domain data.

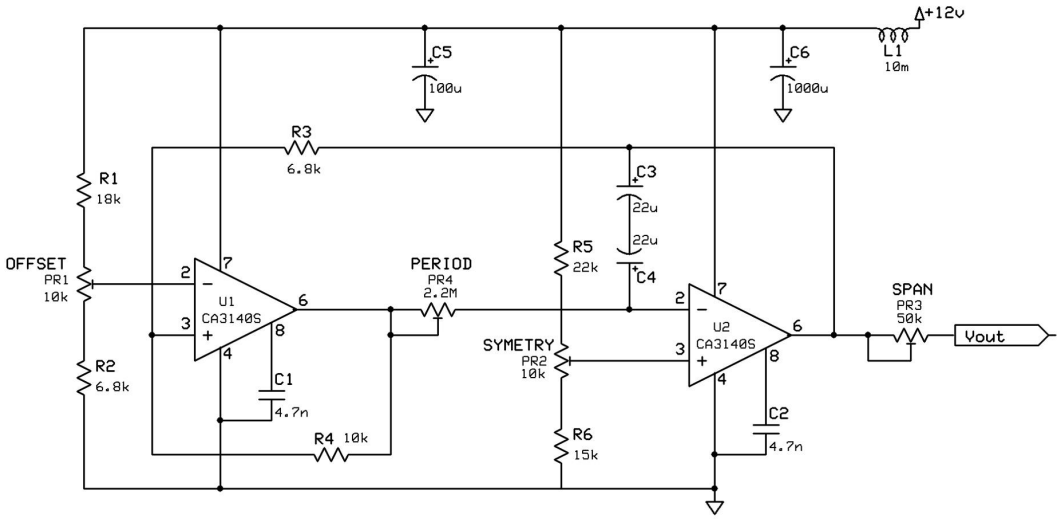


Figure 4.3: Sweep Generator ciruit diagram.

The swept system was installed on 4th September 2009 and did significantly improve the quality of the data recorded. However, this interference has since disappeared and the sweep generator was removed on 31st December 2012. Since the nature of the interference at the other sites was different from this site, it was concluded that there would be no significant advantage in installing the sweep generator at those sites.

### 4.1.4 RFI Sources

Local RFI sources were identified by associating the jumps in detected RFI with activities within the household. E.g. it was noticed that RFI levels increased abruptly when picking up the telephone handset or turning on the TV. The phone/fax/answering machine required three ferrite suppressors, two on the handset cable where it exits the machine and one on the mains lead. Several ferrite suppressors were required on the TV and digital cable TV box. The laptop computer used to record the data radiated RFI from its screen. This was suppressed by connecting the laptop chassis to ground. A ferrite suppressor was needed on the audio lead to the JOVE Receiver where it exits the laptop and also on the 12 VDC power lead at the receiver. However, an older analogue computer monitor and a sewing machine could not be satisfactorily suppressed. Fortunately, these items are rarely used. By far the biggest source of RFI is the air conditioning unit which is of the inverter[3] type and produces broadband interference of such magnitude that conventional ferrite suppressors are of little use. All but the very strongest of solar radio bursts are completely swamped by this RFI. Efforts to find a solution from the manufacturers were unsuccessful. The only solution would appear to be the re-wiring of the unit to the mains supply adding commercial in-line suppressors. This would be expensive and with no guarantee of success.

RFI emanating from sources beyond the author's property was frequently observed. It is likely that some of this came from neighbour's properties and from overhead power lines. Tests using the Yaesu FT100D receiver, which can have its frequency changed by the PC, showed that some RFI was present simultaneously on the 14 and 28 MHz Amateur Radio bands. This broadband signal followed an on/off pattern common to both frequencies and it is possible that these signals were harmonically related, but this could not be determined. The magnitude of these signals was similar to that of the galactic background at its peak. The full extent of the bandwidth of this RFI is not known, but its extent is sufficient to pose a significant problem for its removal.

During periods of enhanced ionospheric propagation, considerable interference is experienced from distant and overseas radio stations. A lot of this interference could be avoided by having a receiver that can adjust its tuning frequency to avoid channels with persistent RFI. It is, in part, this aspect of RFI mitigation that has motivated the design of an improved receiver using digital frequency synthesis and described in Chapter 5.

[3]Inverter air conditioners use variable speed motors to regulate heat transfer and it is the switching power control circuits for these motors that produce the RFI.

## 4.2 Gingin Observatory

Gingin Observatory[4] is a privately owned and operated business where the public have access to a wide range of optical telescopes. Located approximately 70 kilometres north of Perth, they have dark skies and relatively low RFI. One of the white antenna poles can be seen at the left of the picture (Figure 4.4) at the rear of the building.


Figure 4.4: Gingin Observatory on 25th August 2011.

The observatory hosts two JOVE Receivers, one tuned to 17 MHz and the other to 28 MHz, and a dedicated desktop PC with an internet connection for sending the received data to the author's e-mail address. Power for the two receivers is supplied from a single, regulated 12 VDC plug pack that has had an extra 12 VDC connector added to its output lead. The power consumption of the two receivers is very low so there is no danger in doing this. A special lead was made up that combines the audio output from the two receivers into a single 3.5mm stereo jack plug for connection to the PC audio input. The 17 MHz receiver is allocated to the left stereo channel.

In March 2010 a UPS (uninterruptable power supply) was installed to smooth out power glitches which were causing frequent shutdowns of the PC and resultant corruption of data. The PC was slow and installing the upgrade to Windows XP

[4] `http://www.ginginobservatory.com`

service pack 3 did not improve its performance. So, in April 2010 a new PC was installed running the Microsoft Windows 7 Professional operating system. The other sites use the Windows XP operating system.

In September 2012 the remote access program TeamViewer[5] was installed on the PC. This enables a remote computer to access the PC via the internet using an encrypted and password protected connection. This makes it easy to fix problems with the software and also see the output of the RioMeter program in real time. Since then, a change of internet service provider (ISP) at the observatory and the creation of a new e-mail account for the PC has resulted in a much more reliable internet connection and data transfer.

### 4.2.1 Antenna System

Figure 4.5 shows the original antenna system located at the rear of the observatory. The Leaning Tower of Gingin[6] can be seen beyond the retractable domed roof of the observatory. This picture was taken on 31$^{st}$ July 2009 and shows the condition of the antennas at the start of this project. Both the 17 and 28 MHz antennas have sagged well below their optimum height and one 17 MHz and one 28 MHz dipole are attached to the same pair of poles in the foreground.

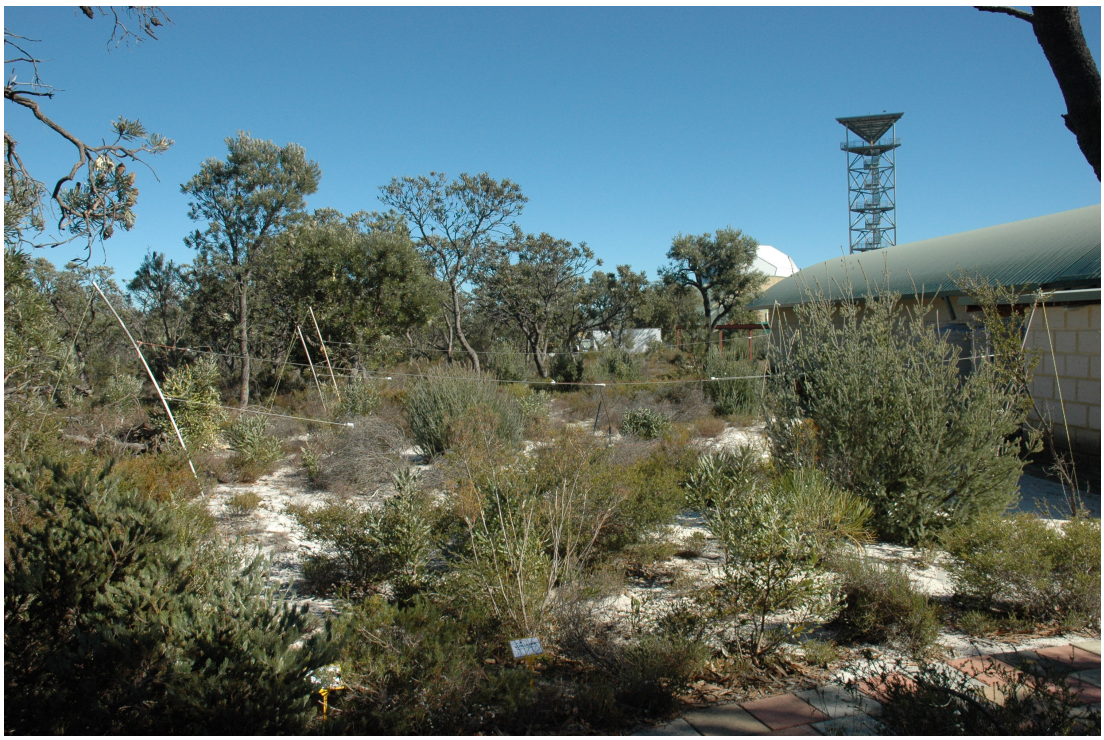

Figure 4.5: Original Gingin Observatory antennas on 31$^{st}$ July 2009.

[5]See http://www.teamviewer.com/en/index.aspx.
[6]Part of the Gravity Discovery Centre. See http://www.gravitycentre.com.au/.

Interaction between these two dipoles was significant and the overall performance of the antenna system was very poor. New 28 MHz dipoles and baluns were installed in July 2009 but performance did not improve significantly and the entire antenna system was re-arranged in November 2009. The antenna support cords were moved to the top of the poles and the 28 MHz dipoles rotated 90 degrees with respect to the 17 MHz dipoles. This re-arrangement of the antennas and the application of ferrite suppressors to various cables and equipment in the observatory, showed significant improvement in the quality of data for February 2010. The antenna system remained in this format until August 2011 when the original poles finally succumbed to termite attack and had to be replaced.

Figure 4.6: Gingin Observatory antennas with new support poles on 25$^{th}$ August 2011.

Figure 4.6 shows the new antenna system as of the 25$^{th}$ August 2011. The 17 MHz dipoles are attached to the top of the support poles and one dipole can be seen in the foreground silhouetted against the sky. The 28 MHz dipoles run parallel with the building and are supported with cords attached to the poles at the lower set of guys. Since the 17 and 28 MHz dipoles are at right angles to each other, interactions between the antennas are minimised. This antenna layout was adopted to make maximum use of the space available, but it does mean that one pair of dipoles is oriented in the less favoured direction of north/south. The support poles are made from plastic irrigation pipe with oak dowels sealed inside

to increase stiffness.

The dimensions for the 17 MHz antenna are: dipole length 8.10 m; height 3.50 m; and spacing 8.80 m. The baluns shown in Figure 4.7 differ slightly in construction from the 28 MHz baluns described in Chapter 2. Here the same type of toroid is used but with 11 turns (210 mm) of bifilar wound 0.63 mm enamelled copper wire instead of 7 turns. The extra turns are required to maintain the same high level of isolation as the 28 MHz balun but at the lower frequency of 17 MHz. The feeder terminates at an 'F' type connector instead of entering the balun through a cable gland. This approach to terminating the feeder was adopted after difficulty was experienced in making a soldered connection to certain types of coax braid. Also, with this approach it is easier to change the lengths of feeders as required. The connector is then bound with self-amalgamating tape for weather proofing, once the feeder has been attached. The completed dipole is shown in Figure 4.8.

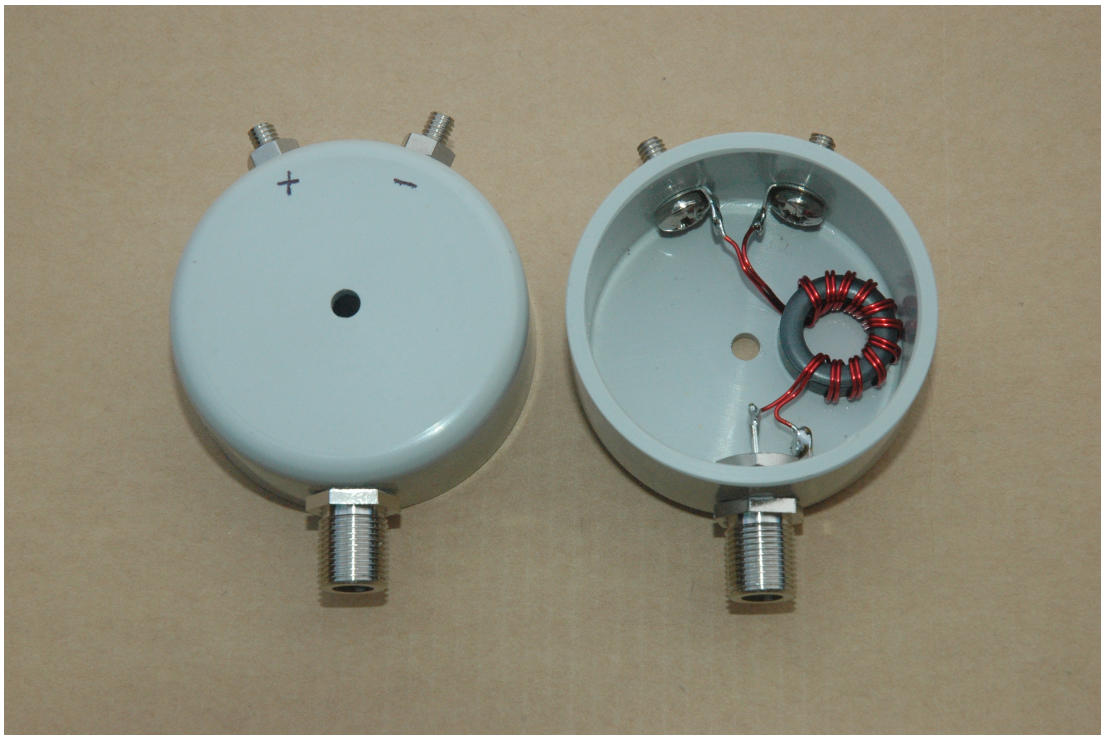


Figure 4.7: Gingin 17 MHz Balun, showing the toroidal core with bifilar windings, terminating screws for the dipole and 'F' connector termination for the feeder .

The dimensions for the 28 MHz antenna are: dipole length 4.84 m; height 2.30 m; and spacing 5.40 m. The baluns and combiner are as described in Chapter 2. Modified combiners were fitted to both antennas in October 2009.

The ground is white, fine grained sand which does not make a good reflector

for radio waves. Therefore, the gain of the antennas is expected to be less than that achieved by the vk6bhi system erected over a salt water swimming pool. Also, some variability of gain may be expected between summer and winter due to increased moisture retained in the sand during the winter months.

Figure 4.8: Gingin 17 MHz Dipole assembly. The clear acrylic backing of the balun assembly provides strain relief for the dipole wires and weather protection using a rubber gasket.

### 4.2.2 17 MHz JOVE Receiver

This receiver has all of the modifications described in the modifications section of Chapter 3 with the exception that it does not have the temperature compensation circuit or the high 'Q' RF band-pass filter. The temperature compensation and high 'Q' RF band-pass filter were shown to be insufficiently effective on the author's 28 MHz JOVE Receiver to justify their inclusion in the other JOVE Receivers. However, three additional resistors R45, R46 and R47 (Figure 4.9) were added internally at the antenna connector to reduce the signal strength arriving at the RF amplifier. This attenuation was necessary to prevent overload in later stages of the receiver caused by very strong broadcast stations close to 17 MHz. The circuit diagram for the 17 MHz receiver is shown in Figure 4.9.

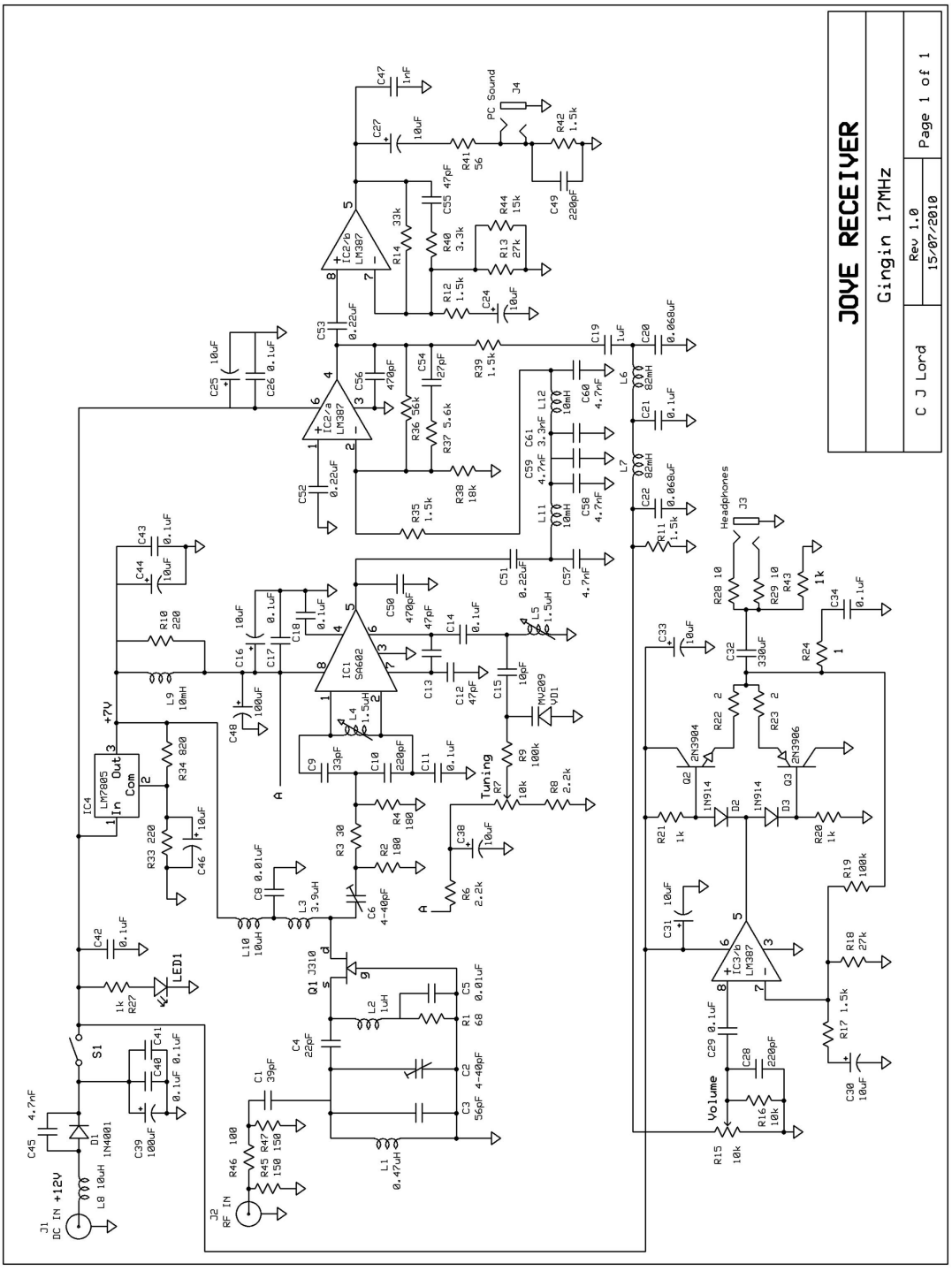


Figure 4.9: Gingin modified 17 MHz JOVE Receiver circuit diagram. Derived from the original JOVE Receiver circuit diagram.

### 4.2.3 28 MHz JOVE Receiver

This receiver has all of the modifications described in the modifications section of Chapter 3 with the exception that it does not have the temperature compensation

circuit or the high 'Q' RF band-pass filter (for the same reason as described for the 17 MHz JOVE Receiver). Since there are no strong broadcast stations near 28 MHz the antenna attenuator of the 17 MHz receiver is not required. The circuit diagram for the 28 MHz receiver is shown in Figure 4.10.

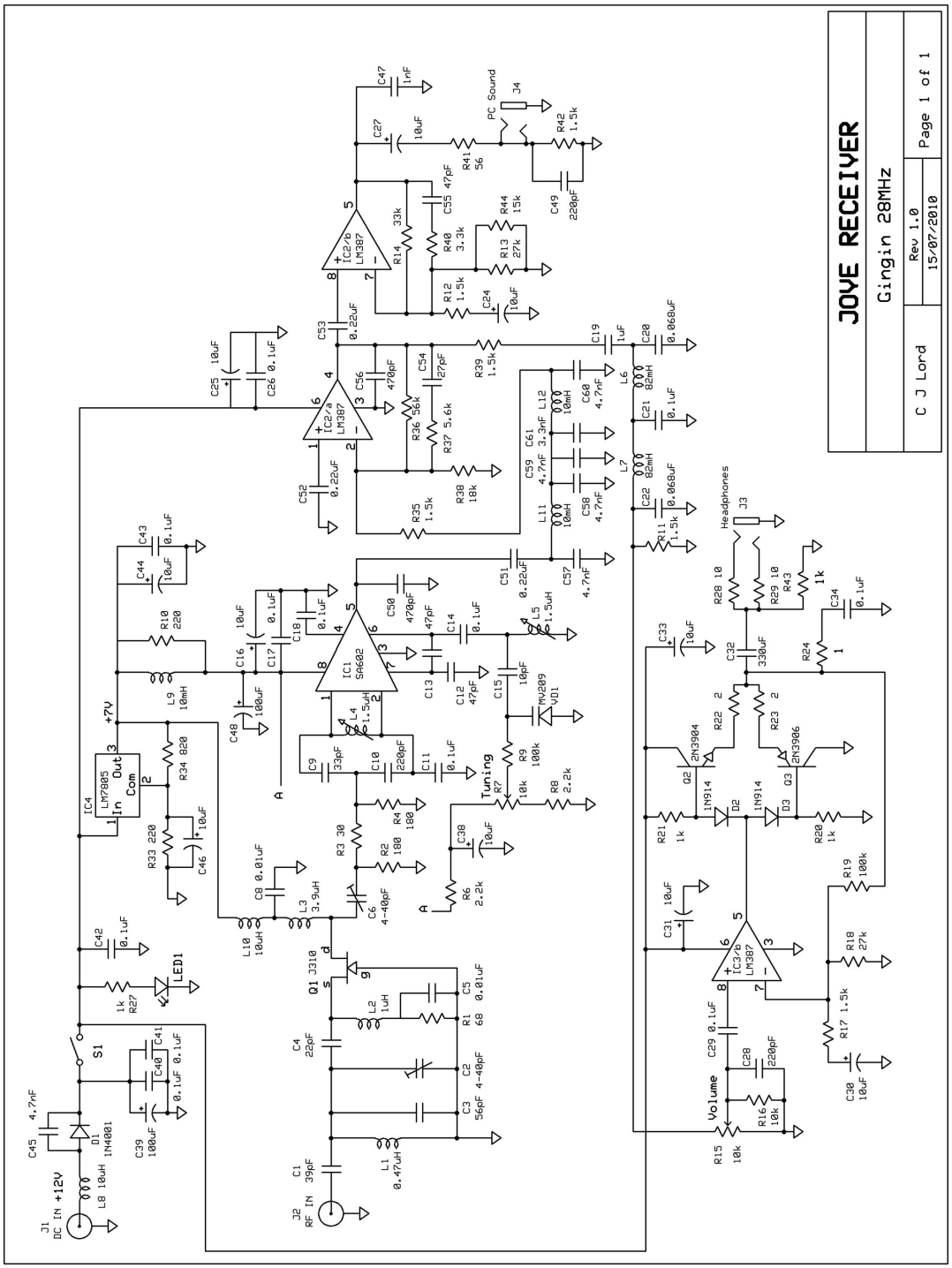


Figure 4.10: Gingin modified 28 MHz JOVE Receiver circuit diagram. Derived from the original JOVE Receiver circuit diagram.

### 4.2.4 Watchdog

Due to its remote location, Gingin Observatory's power and internet connections have not been very reliable. Power glitches and software problems often caused the PC to crash. Frequently the PC could not send its data for several days due to internet connection problems and so several days could pass before it was realised that the PC had in fact crashed. The Watchdog performs a reset of the PC if the data recording program (RioMeter.exe) stops running. A switch is provided on the panel to turn off the Watchdog when it is not required, e.g. during RioMeter software upgrades. The Watchdog assembly fits into an expansion slot at the back of the PC and the flying leads, shown in Figure 4.11, terminate in connectors that plug into the PC mother board and power supply.

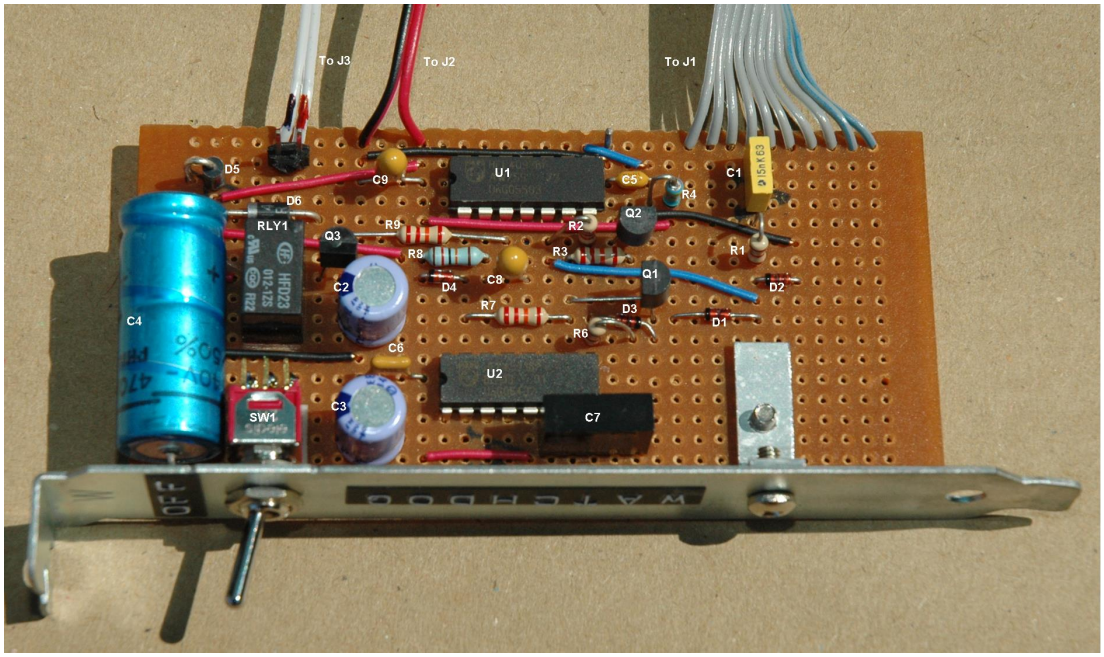


Figure 4.11: Gingin Watchdog assembly showing the components layout and mounting bracket for assembly into a standard PC expansion slot.

A reset occurs approximately four minutes after the stimulus from the RioMeter program via the request to send (RTS) line of ComA ceases, see Figure 4.12. If the RioMeter program fails to start, a second reset occurs after approximately a further eight minutes. This gives sufficient time for Microsoft Windows automatic updates to install and re-start the computer.

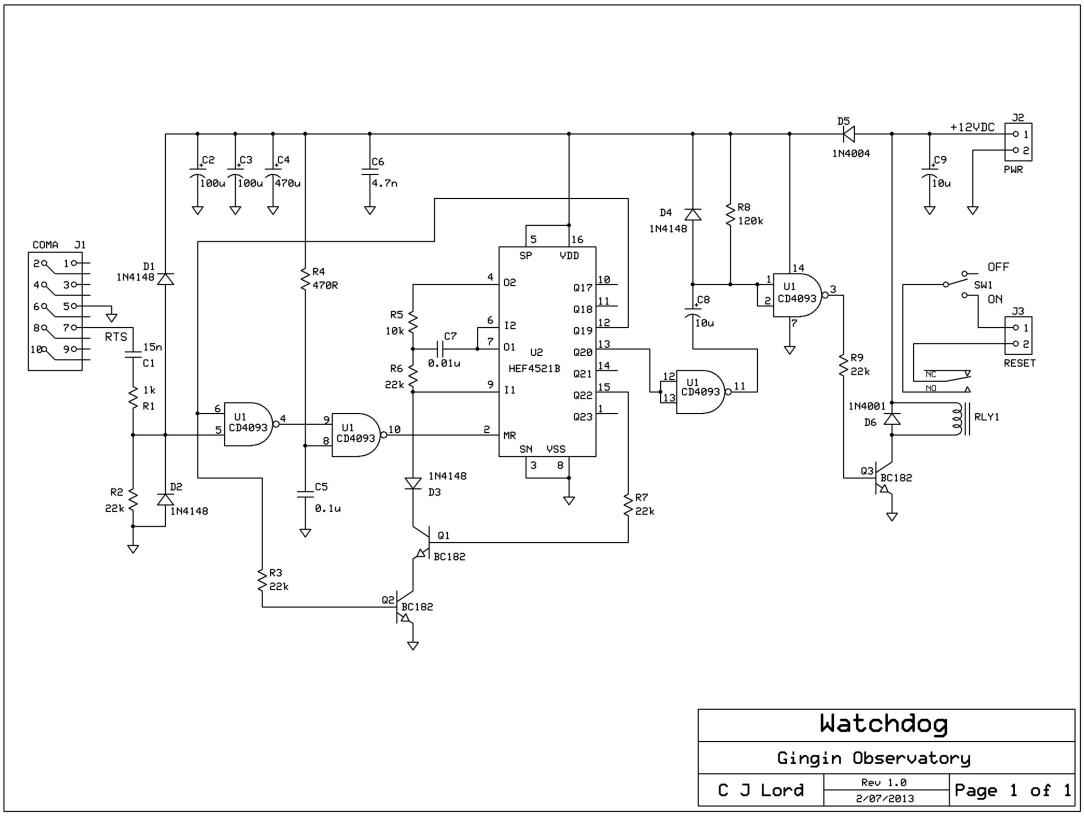


Figure 4.12: Gingin Watchdog circuit diagram.

### 4.2.5 RFI Sources

A major source of RFI at Gingin Observatory is the roof motor controller. This produces broadband RFI while it is turned on, even when the roof motors are not running. Fitting several ferrite suppressors over the cables to the controller and motors reduced the RFI but did not remove it. Eventually, an isolating switch was installed between the AC mains supply and the controller. This eliminates the RFI except for periods when the roof is open.

Other sources of RFI from the observatory computers and communications cables have been suppressed to an acceptable level. A further reduction in RFI may be gained from suppressing the AC mains supply where it enters the building from underground.

## 4.3 Learmonth Solar Observatory

Learmonth Solar Observatory (LSO) is jointly operated by IPS Radio and Space Services[7] and the US Air Force[8]. Located approximately 1000 kilometres north of Perth and 35 kilometres south of Exmouth in Western Australia, LSO keeps watch on solar activity in both the optical and radio wavebands. Solar activity can present a hazard to astronauts, satellites and to terrestrial power and communications systems. If potentially hazardous solar activity can be predicted or observed early enough, then warnings can be issued and action taken to mitigate the effects.

Figure 4.13: The Radio Solar Telescope Network (RSTN) building and antennas at Learmonth Solar Observatory at sunset on 12$^{th}$ October 2010.

Seen in the foreground of Figure 4.13 are the 8 and 3 feet diameter dishes for the ultra high frequency (UHF) receivers and beyond the radio building, where the JOVE Receiver was also housed, is the 28 feet diameter dish for very high frequencies (VHF). The optical observatory is out of view to the left of the picture.

The author was fortunate to find on arrival at LSO, a JOVE Receiver and antenna in storage, that could be modified and put into service for this project.

[7] http://www.ips.gov.au/Solar/3/1

[8] http://www.afweather.af.mil/units/airforceweatheragency/2ndweathersquadron.asp

After a few weeks the system was assembled along with a spare PC found on site and connected to the internet for data transfer.

### 4.3.1 Antenna System

The 20 MHz antenna (Figure 4.14) is located approximately 100 metres to the east of the observatory in a fenced off area previously occupied by an observatory antenna that was destroyed by cyclone Vance in March 1999. Fortunately the underground run of HELIAX[9] coaxial cable to the radio operations room was still in good condition and was used to connect the antenna to the JOVE Receiver.

Figure 4.14: LSO 20 MHz Antenna on 14$^{th}$ October 2010. The short white poles are all that remains of a previous antenna destroyed by cyclone Vance.

The antenna was first erected on 12$^{th}$ July 2010 using the plastic poles that were part of the JOVE Receiver kit. These poles were not very substantial and gave a dipole height of 2.3 m instead of the required 3.3 m. Some data were recorded with this system before the poles were replaced on 23$^{rd}$ September 2010. The new poles (Figure 4.14) for the antenna are 3.5 m long by 55 mm diameter plastic conduit pipe and better able to withstand the strong winds encountered in this region. The antenna was not expected to withstand cyclone strength winds, but its structure is simple and the antenna was easily re-erected once the wind

[9]HELIAX is a semi-rigid low loss coaxial cable. See `http://www.commscope.com/catalog/andrew/product_details.aspx?id=1329` for detailed specifications.

had abated. The antenna blew down on several occasions and the author is very grateful to the IPS staff on site for re-erecting it.

The 20 MHz antenna details are: dipole length 6.97 m; height 3.30 m; spacing 7.50 m and dipoles oriented east/west. There was not sufficient time to make new baluns, as described in Chapter 2, so the baluns for this antenna consist of three large ferrite sleeves over the coax at the dipole feed point. The combiner is the modified version as described in Chapter 2.

### 4.3.2 20.1 MHz JOVE Receiver

Some additional modifications were made to the 20.1 MHz JOVE Receiver to reduce RFI coupled from the PC via the audio lead and to counter problems with the 12 VDC connector. The additional components C61, C62, C64 and L13 associated with these modifications are labelled in Figure 4.15 and can be found in the associated circuit diagram Figure 4.16. C63 is located on the underside of the PCB.


Figure 4.15: LSO modified 20.1 MHz JOVE Receiver showing additional components C61, C62, C64 and L13.

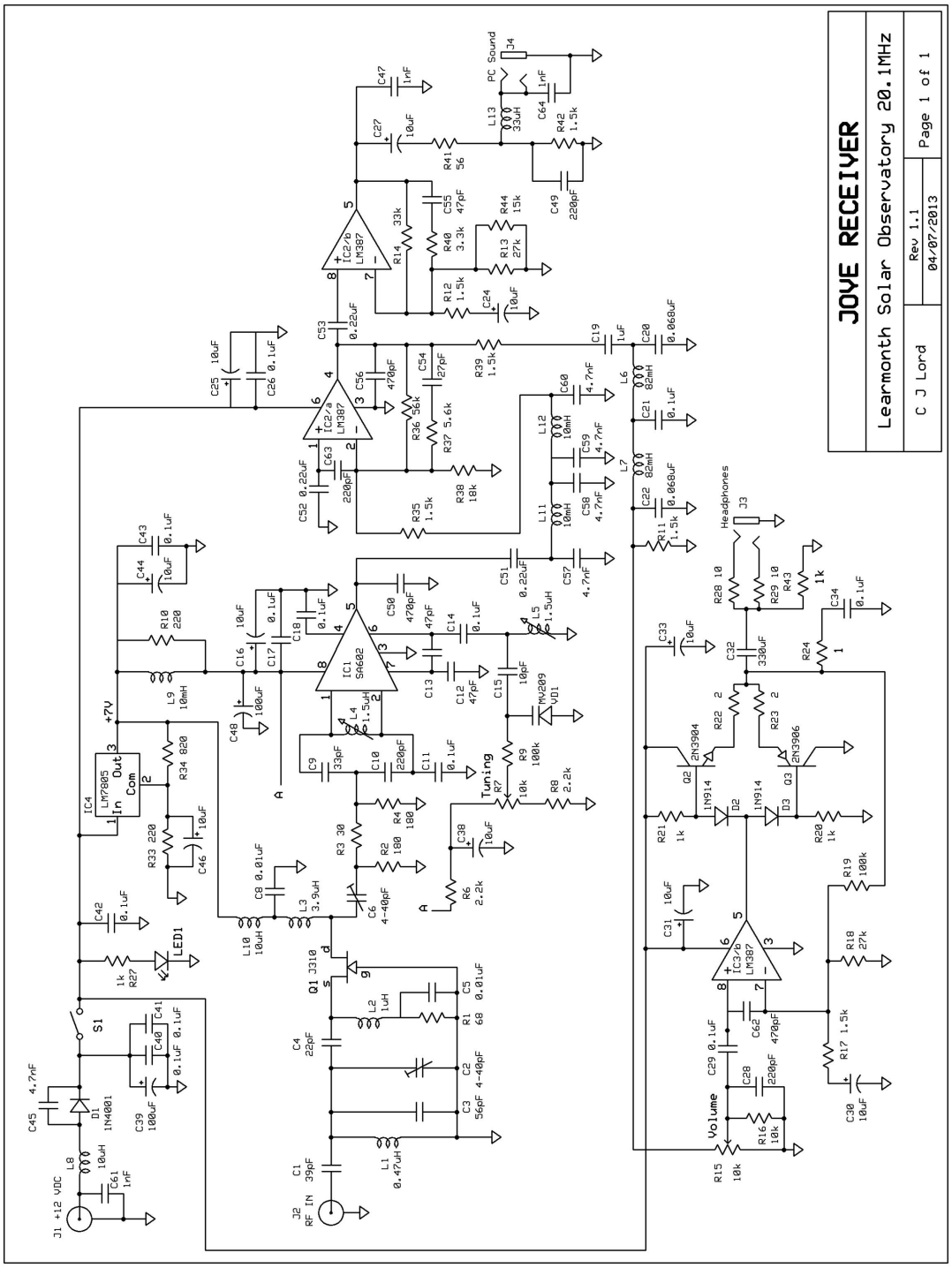


Figure 4.16: LSO modified 20.1 MHz JOVE Receiver circuit diagram. Derived from the original JOVE Receiver circuit diagram.

### 4.3.3 RFI Sources

During the author's time at LSO (April to October 2010), locally generated RFI was low and so too was RFI from broadcast stations. Some RFI (from the various

computers and control systems within the radio building) was picked up on the coax feeder that runs from the underground HELIAX where it enters the building, to the receiver. This was suppressed with three suppressors over the feeder at the receiver. At this time the Sun was just emerging from a long minimum in the solar sunspot cycle and ionospheric propagation was low. Since then RFI has increased along with solar activity. Some increase in locally generated RFI may be attributed to new air conditioning systems installed at the site. Due to the distance of LSO from the author's home in Perth and the cost of travel, it has not been possible to evaluate the RFI situation on site and take remedial action.

## 4.4 Summary

Overall, performance of the systems at all three sites was good. Data loss due to power glitches and internet problems was small in proportion to the total data collected. The antennas have stood up well to the weather: only requiring minor maintenance. If any improvement could be made, it would be to replace the sash cord guys with more expensive Kevlar cords that do not stretch in wet weather and are longer lasting. The sash cord stretches a lot in wet weather causing the antennas to sag and lasts about three years before breaking.

A note of caution to anyone considering venturing into the Australian bush to put up antennas (or any other activity) is in order. The author was well aware of the dangers from snakes and spiders but not of the nuisance caused by kangaroo tics. These little beasties (some as small as a pin head) attack from the ground and from overhanging foliage. They are not deterred by insect repellents or sprays and will find any small gaps in clothing to gain access to and attach themselves to ones body, usually where they can not be seen. Once attached they are difficult to remove, a hot shower is no good and care has to be taken to avoid leaving parts of the tic embedded in the skin. In the author's experience a cotton wool pad soaked in alcohol applied at the doctor's surgery worked best. However, the toxins left by the tics continued to cause irritation for several months and was only cured by a trip to the dermatologist to freeze the affected areas. The author now wears a cover all one piece suit with elasticated seals at the ankles, wrists and face. This has been successful so far but is rather uncomfortable in summer when temperatures are in the high thirties.

# Chapter 5

# Improved Receiver Development

In Chapter 3 it was shown that the JOVE Receiver suffers from a number of deficiencies. Some improvements were made which included increased bandwidth lower internal noise levels. However, nothing could be done to improve the temperature stability of the receiver or reduce the radiated signal originating from the local oscillator (LO). Also the receiver design fixes the standard JOVE Receiver frequency at 20.1 MHz and only a small range of tuning is available using the tuning control. Larger changes in tuning frequency can only be achieved by changing the band-pass tuning components and it was by changing these components that it was possible to have JOVE Receivers tuned to 17 and 28 MHz. Many frequencies are affected by radio-frequency interference (RFI) which can only be avoided by manually adjusting the tuning of the receiver using the tuning control. This is not practical for remote, 24 hour a day operation and some method of controlling the receiver frequency by software is desirable.

The JOVE Receiver requires a 12 V DC power supply, which is normally in the form of a plug pack powered by the AC mains supply. It would be convenient if the receiver derived its power from the PC that it is connected to.

Many of the deficiencies in the JOVE Receiver are due to its simple design. However, this simplicity also has its advantages: low power consumption; low circuit noise through simple radio-frequency (RF) and mixer circuits; and reduced construction and parts costs. The objective of the improved receiver is to keep the simplicity of the RF and mixer circuitry, albeit with a different circuit configuration, while providing flexible frequency control from the host PC. This is achieved by using a direct digital synthesiser (DDS), to generate the LO frequency, under control of a programmable interface controller (PIC) linked to the PC via the USB port.

The target areas for the improved receiver development are:

- Easy to adjust tuning over a wide frequency range;
- Stable operating frequency;
- Wide bandwidth;
- Low re-radiated signal;
- Dual channel;
- Software controlled via USB port;
- Power from USB port.

The following gives a brief outline of the functionality of the improved receiver. A detailed description of the component parts follows later in this chapter.

The improved receiver design, shown in Figure 5.1, utilises a DDS which can generate a LO frequency in the range 1 to 40 MHz. This gives the receiver the potential to tune to any frequency in the range of the LO. For the design described here the tuning range is limited to 16 to 30 MHz, in order to simplify the filtering requirements. Since the DDS clock is derived from a crystal oscillator, the operating frequency is much less affected by temperature variations than the LC oscillator of the JOVE Receiver.

The RF amplifier (RF Amp. in Figure 5.1) is a broadband design using a dual gate Metal Oxide Silicon Field Effect Transistor (MOSFET). This design minimises feedback from the LO to the antenna input and allows automatic gain control (AGC) to be applied to gate two of the device. The RF amplifier is coupled to a high level double-balanced mixer via a 30 MHz low-pass filter (LPF).

The mixer performs a direct conversion from radio-frequency (RF) to audio-frequency (AF) and its output is buffered by a dual, low-noise, audio operational amplifier (op-amp). This dual op-amp provides most of the gain of the audio system and two AF filters, with a bandwidth of 22 kHz, deliver high out-of-band rejection. These filters have a sharper cut-off than those used in the modified JOVE Receiver, providing better protection against aliasing in the PC audio system.

The final AF amplifier provides a voltage gain of 20 dB and 'rail to rail' voltage output capability for driving the computer audio input. This output is also used to generate the AGC voltage which is fed back to the RF amplifier.

The PIC built into the receiver provides the USB interface to the PC, generates the command signals to the DDS and selects the signal source between antenna

and internal calibrator. Calibration parameters are stored in the PIC to allow consistent calibration when the receiver is used on different PCs.

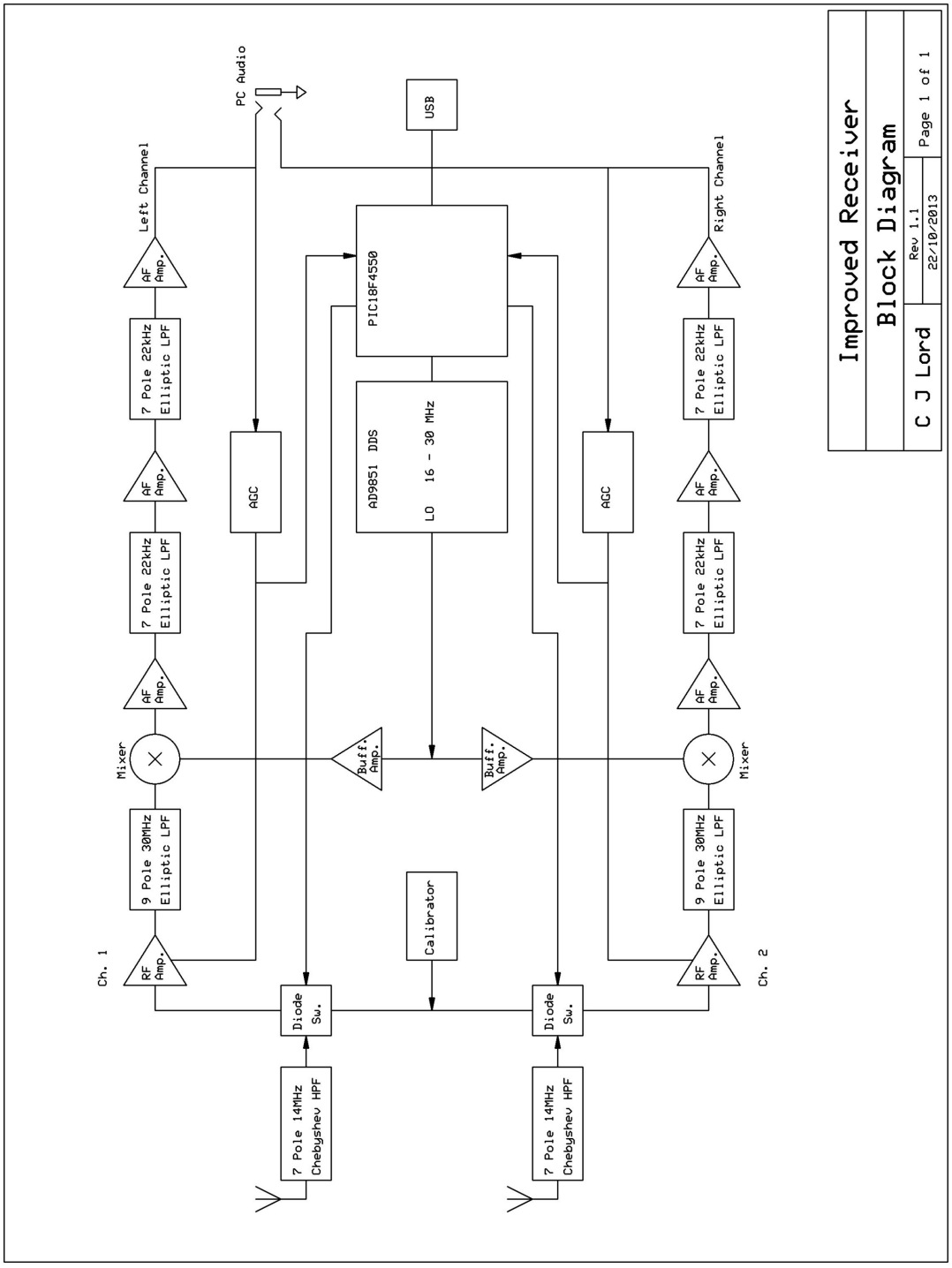


Figure 5.1: Improved receiver block diagram showing the general arrangement of the two channel system controlled by a PIC.

It is proposed that the receiver will have two RF/AF channels providing simultaneous data to the left and right channels of the PC audio system, as shown in

the block diagram of Figure 5.1. The prototype receiver only has a single channel. With two channels it is possible to implement a simple beam forming scheme in software, rather than using a coaxial phasing line. This allows the antenna gain to be optimised for Solar or Jovian data collection throughout the year. There is also the possibility of using the second channel for advanced RFI mitigation. The prototype improved receiver is seen in Figure 5.2 and the arrangement of its sub-assemblies in Figure 5.3.

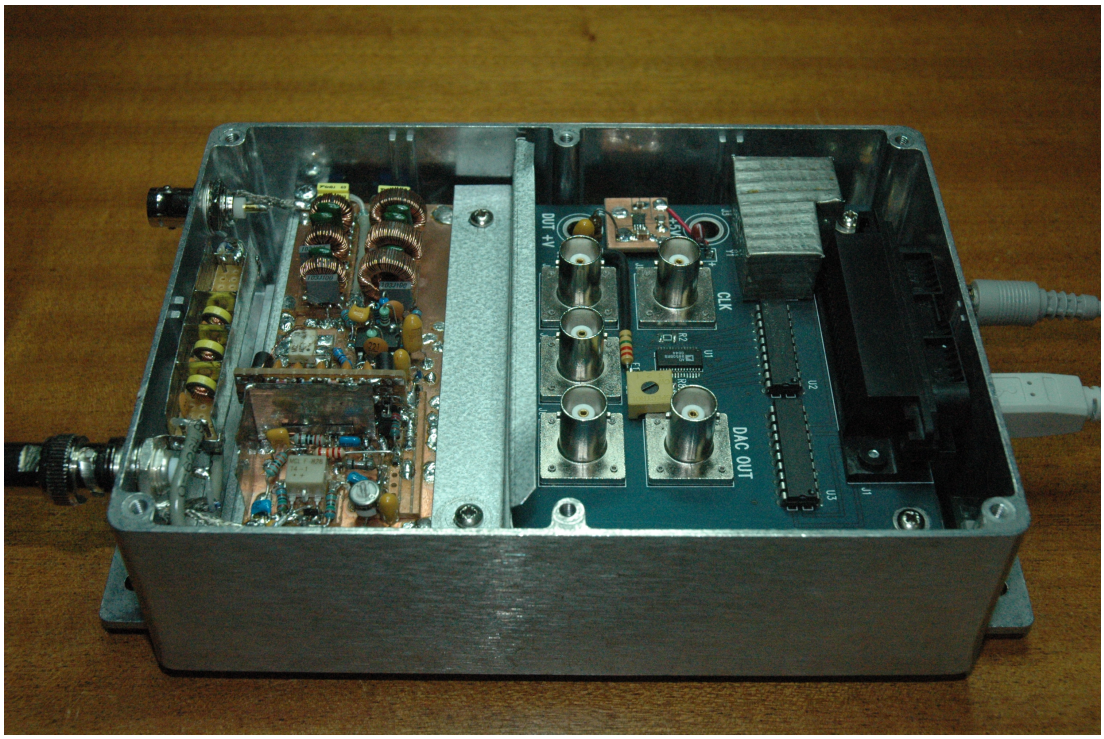


Figure 5.2: Prototype improved receiver with top cover removed. The antenna input enters the RF/AF board on the left and the DDS board is on the right. Also on the right are the USB and audio cables.

The RioMeter software (see Chapter 6) running on the host PC collects and processes the receiver data from the PC audio system. This software determines the best frequencies to use (within a specified range) to avoid as much human-made radio-frequency interference (RFI) as possible. A system for doing this was tested using the FT100D communications receiver in version 2 of the RioMeter software. Primary and secondary arrays of five frequencies within the same band and separated by 20 kHz, were established. Using a serial port connection from the PC to the FT100D, the frequency of the FT100D was stepped through the primary frequencies and data sampled from each frequency, taking a total time of approximately six seconds. The frequency with the lowest noise level was used

as the data sample and saved. The frequency with the highest noise level was then swapped for the next sequential frequency in the secondary frequency array and the data sampling process repeated. By this process, the most RFI affected frequencies gravitate to the secondary frequency array but get periodically sampled and brought back into use if the RFI levels fall. These tests were carried out in both the 17 and 28 MHz bands with encouraging results. The software routines for doing this were removed from the RioMeter software in version 3, since the JOVE Receiver has no means of having its frequency set from the PC. With the improved receiver, frequencies can be changed extremely rapidly via the USB port and PIC. Therefore, it is possible to collect data from many different frequencies almost simultaneously.

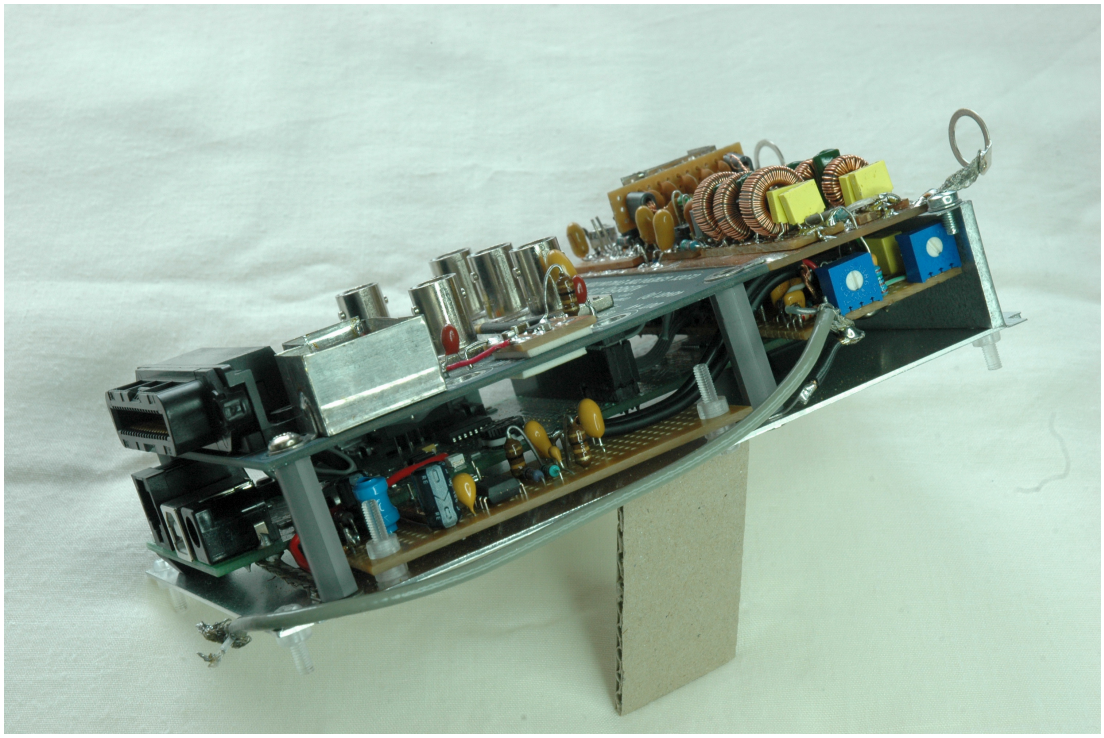

Figure 5.3: Prototype improved receiver showing sub-assemblies. On the lower level at the front is the plus and minus 5 Volt regulator board and behind is the PIC board. The interface board is at the intermediate level on the right.

## 5.1 RF System

Figure 5.4 shows the circuit diagram for a single channel from the receiver. The antenna input passes through a high-pass filter (HPF) to a diode switching network. The HPF (Figure 5.5) progressively attenuates all frequencies below approximately 14 MHz, reaching a measured attenuation of greater than 100 dB

at 4 MHz. The main purpose of this filter is to remove the strong signals found in the AM broadcast band. The author lives only a few km from very powerful transmitters used in this band and that caused serious overloading of the receiver.

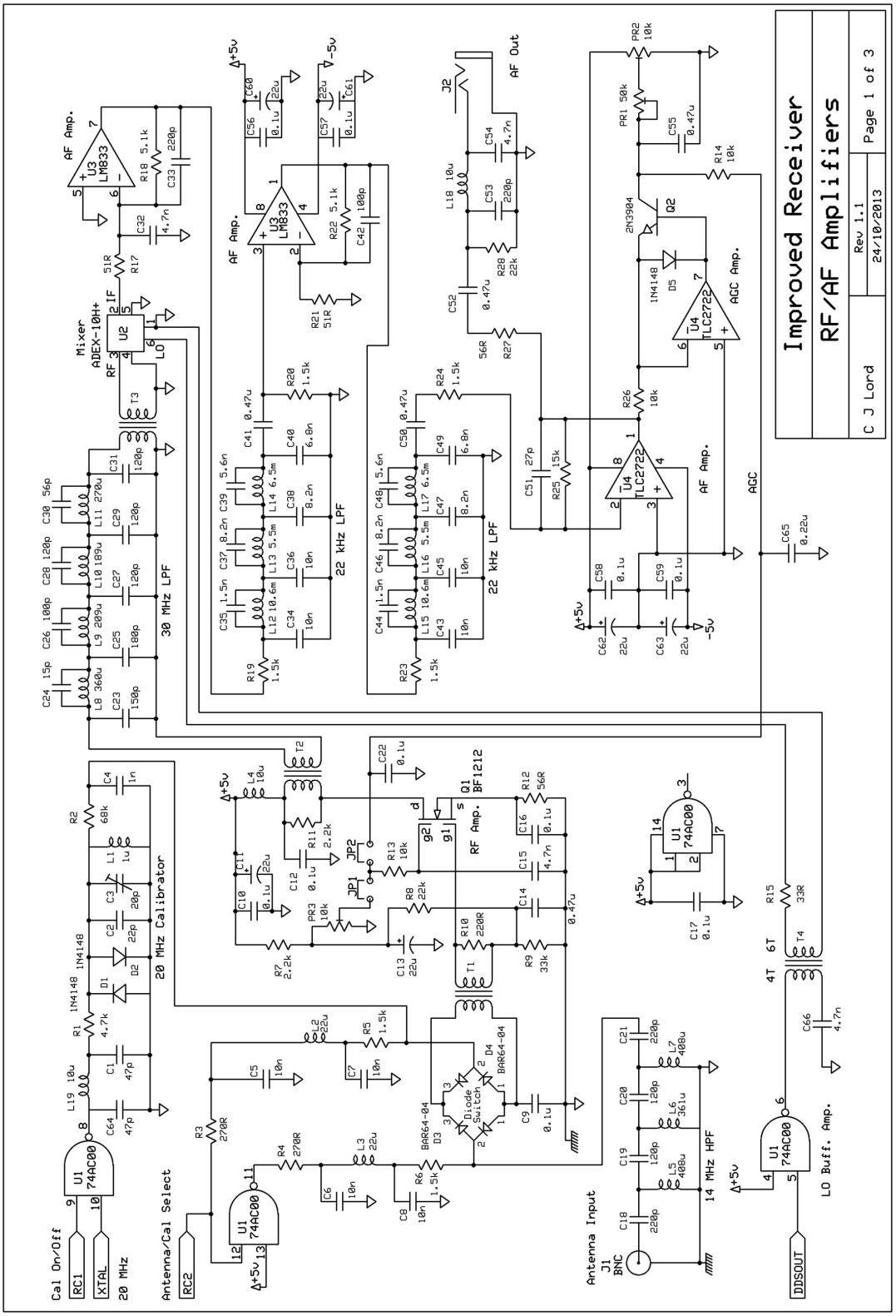


Figure 5.4: RF and AF system circuit diagram.

Normally, a selective band-pass filter (BPF) such as that used on the JOVE Receiver is used to attenuate out-of-band signals. However, for this improved receiver design a wide-band RF amplifier is used to enable access to frequencies in the range 16 to 30 MHz. A limitation of the JOVE Receiver is that its tuning frequency is restricted to the range determined by the RF BPF. Traditionally the tuning of the RF BPF is linked to the LO tuning which determines the frequency of reception, with mechanically coupled tuning capacitors in the BPF and LO, requiring careful mechanical and electrical alignment. Modern receiver designs use more complex circuits to achieve this result, without the mechanical components. However, this increased circuit complexity can lead to higher noise levels. The improved receiver relies on advanced mixer design to limit intermodulation distortion to an acceptable level for signal levels normally found in the 16 to 30 MHz range.

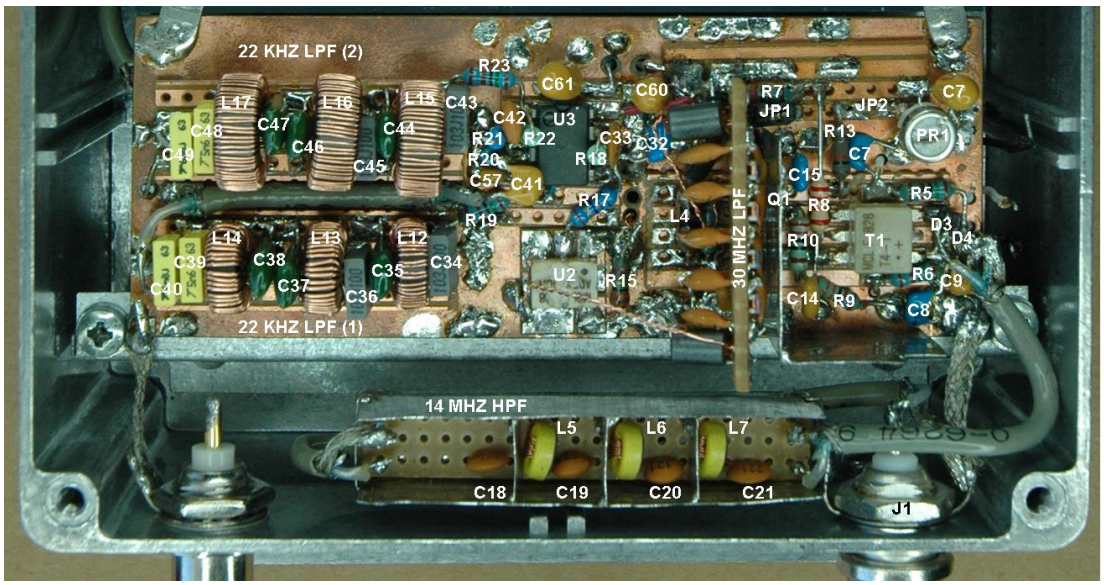


Figure 5.5: RF/AF System Board and 14 MHz HPF.

The diode switching network allows the input to the RF amplifier to be switched between the antenna and a calibration reference signal. This reference signal is derived from the 20 MHz crystal clock generator used by the PIC and is used to check the gain and frequency calibration of the receiver. During receiver calibration, using an accurate signal generator, the reference level and gain vs. frequency profile for the receiver is saved in the PIC and used periodically by the software (RioMeter.exe) to check and adjust the overall system calibration. Once calibrated, the receiver can be used with any suitable PC running the RioMeter software and the system will self-calibrate.

The output from the diode switching network is coupled to the input of the RF amplifier. The gain of the RF amplifier is controlled by the AGC which prevents overload in the following stages when strong signals are present. The output of the RF amplifier is transformer coupled to the RF low-pass filter (LPF) for impedance matching. The LPF has a sharp cut-off beyond 30 MHz to remove second and higher order harmonics of the tuning frequency. A second transformer is used to couple and match the LPF to the mixer.

### 5.1.1 14 MHz High-pass Filter

The HPF is a seven-pole Chebyshev filter (Huelsman, 1993), see Figure 5.5. The component values for this filter were optimised using the SVC filter design program (Tonne, 2013). Attenuation increases rapidly below the cut-off frequency of 14 MHz and continues to increase as frequency falls. Figure 5.6 shows the attenuation vs. frequency characteristics of the filter. It can be seen that the attenuation at 1 MHz and below is significant and the problem AM broadcast stations are removed from the input signal.

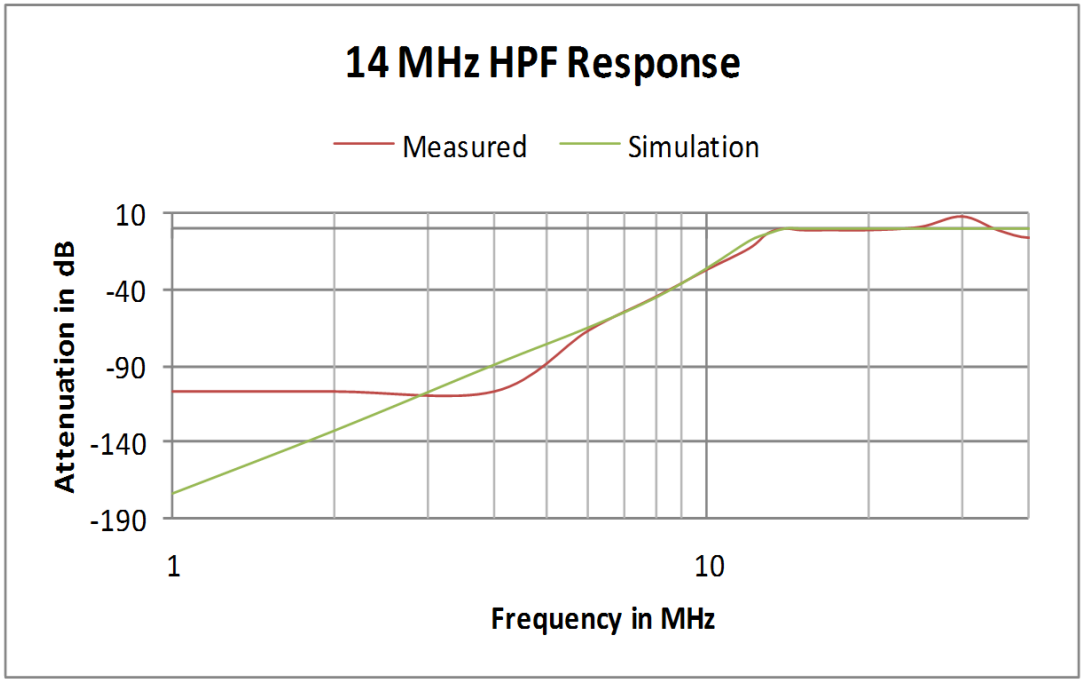


Figure 5.6: 14 MHz HPF Attenuation vs. Frequency. The maximum measured attenuation was limited to 107 dB by the FT100D used for the measurements.

The filter response was determined using a signal generator (AA-200), a combination of fixed and switched attenuators and a communications receiver (FT100D). The FT100D receiver was used because of its extended frequency cov-

erage. However, the signal strength meter (S meter) is of the bar graph type and has poor resolution. In order to overcome this limitation the transition from signal strength 'S1' to 'S2' was used when determining the total number of dBs of attenuation. Starting with a large amount of attenuation and no filter between the signal generator and the FT100D, the attenuation was reduced until the S meter registered S1. The attenuation was then reduced in 1 dB steps until the S meter just registered S2 (it is this transition from S1 to S2 that is important, since one S point covers a range of 6 dB). The total number of dBs of attenuation was recorded and the HPF inserted between the attenuator and the FT100D. Insertion of the HPF causes the signal strength to drop, so some attenuation was removed until the S meter registers S1. Once again, the attenuation was reduced in 1 dB steps until the S meter just registered S2 and the total attenuation recorded. The attenuation of the filter is then the difference between the two total dB values recorded. The limit of sensitivity with this method was $-107$ dBm for low frequencies, as indicated on the graph.

The inductors were wound on small iron powder toroid cores to achieve small size and high quality factor 'Q'. The result is a fairly close approximation to the simulated performance, seen in Figure 5.6

### 5.1.2 30 MHz Low-pass Filter

The LPF is a nine-pole elliptic filter (Huelsman, 1993). Attenuation increases very rapidly above the cut-off frequency of 30 MHz, which maximises the usable tuning range of the receiver. With the receiver tuning set to 16 MHz or above, the second harmonic of the LO falls outside the filter passband where there are no signals for it to mix with and hence there is no output from the mixer. This filter also, therefore, determines the upper tuning range of the receiver at 30 MHz. The elliptic filter does have a certain amount of ripple in both the passband and stop-band. Variation of receiver gain with frequency due to the passband ripple can be accounted for during the calibration process.

As seen in Figure 5.7, the performance of the filter in terms of its cut-off frequency and stop-band depth, is not as good as the simulation. The problem with real world components is that they are not available in all the values required, so the nearest 'preferred' values are chosen. These components also have manufacturing tolerances typically in the order of $\pm 5\%$. In addition to these problems there is the quality factor or 'Q' of the manufactured component to take into account. The 'Q' of the component is a measure of how far the component deviates from an ideal inductance or capacitance (Schetgen, 1996, p. 6.1, p. 10.8). 'Q' is

reduced by the resistance of the wire used to wind the inductor, the core material used, and by dielectric losses in capacitors.

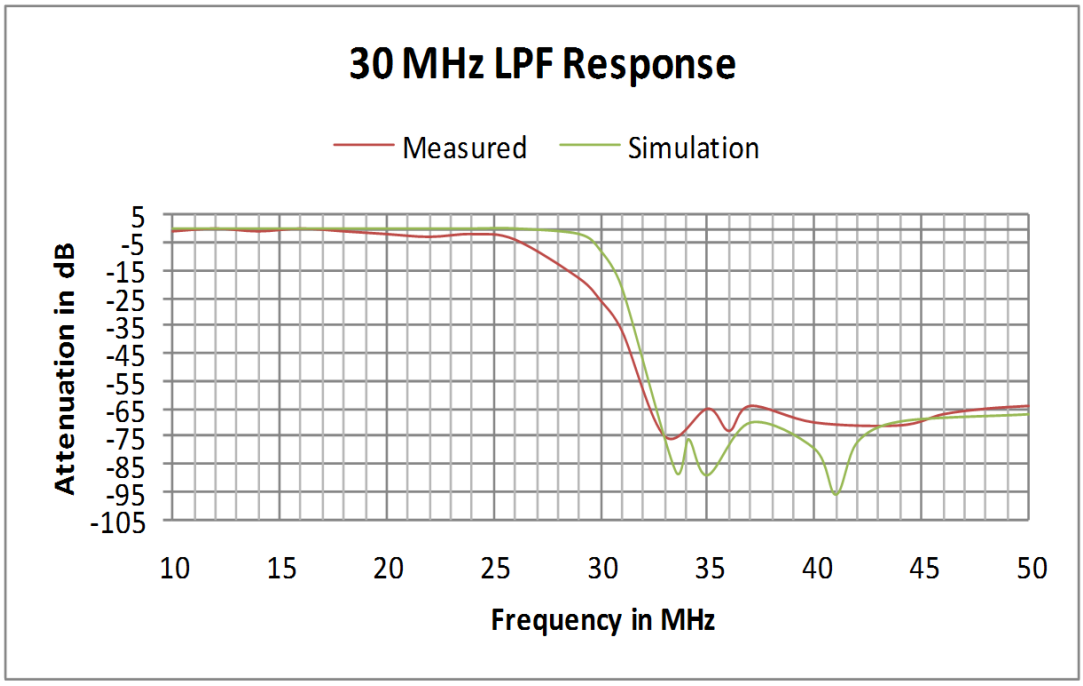


Figure 5.7: 30 MHz LPF Attenuation vs. Frequency. The measured response shows the effects of component tolerances, low 'Q' and the construction method.

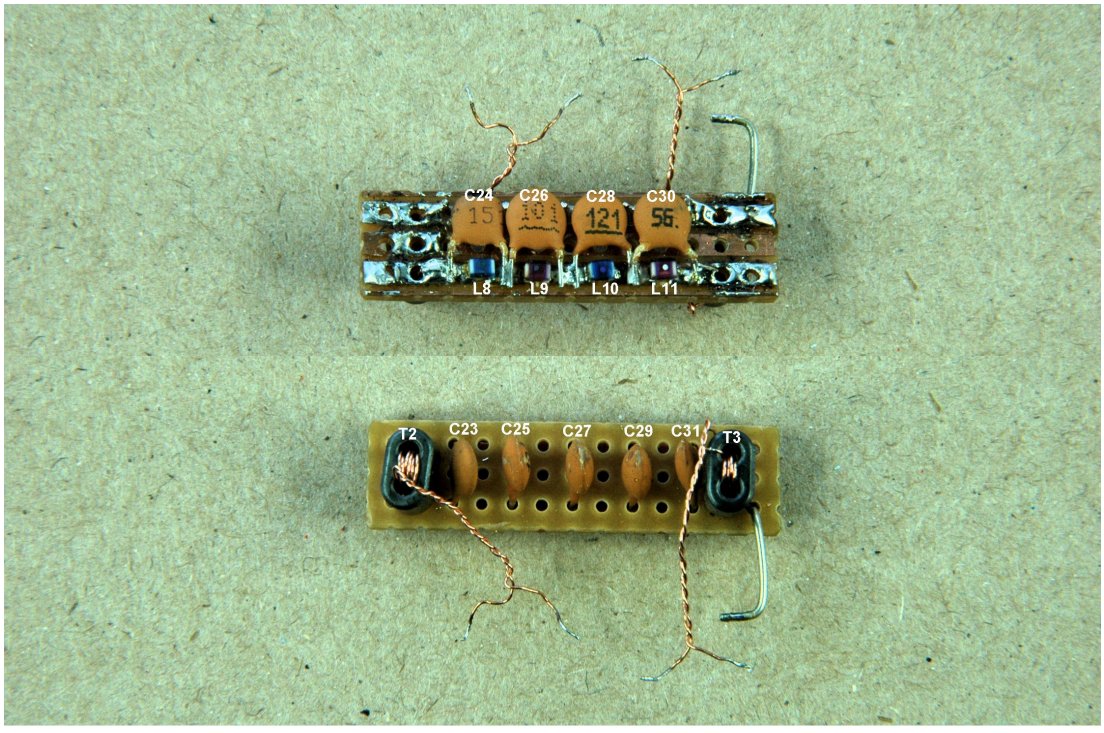


Figure 5.8: 30 MHz Low-Pass Filter showing upper and lower components.

For this filter the main problem is finding suitably close tolerance inductors. Small surface mount inductors were used to save space (see Figure 5.8), instead of winding the inductors on iron powder toroids, as was done for the 14 MHz HPF. The use of small adjustable inductors may be the answer, though these are more expensive than fixed value inductors. The construction of the prototype filter is also not ideal. A printed circuit arrangement on a ground plane with surface mount capacitors would likely give superior results. The test set up and procedure for measuring the filter performance was the same as for the 14 MHz HPF.

### 5.1.3 RF Amplifier

The RF amplifier utilises a dual gate MOSFET in grounded source configuration (Everard, 2002, p. 45, p. 115). Gate 1 is the signal input and presents a very high impedance and low capacitance. Advantage is taken of this high input impedance by using a 1:4 impedance ratio transformer and shunting the secondary winding with a resistor which sets the antenna input impedance to approximately 50 Ohms and provides a 2:1 voltage step up for the signal. The transformer primary also provides the DC path for biasing the diode switching network. Increasing the input impedance seen by the MOSFET can result in higher noise levels. However, over the working frequency range of the receiver, antenna noise is the significant factor.

The diode switching network enables the input to the RF amplifier to be selected between the antenna and the calibrator, under control of the PIC. This enables checking of the gain and frequency calibration of the receiver during operation.

Gate 2 is used to control the gain of the transistor by varying the DC bias voltage and this is where the AGC is applied. Under conditions of full bias, a gain in excess of 10 dB can be expected, falling to less than $-40$ dB with zero AGC voltage. This affords significant protection against receiver overload in the presence of strong signals. In the prototype receiver the gate 2 voltage can be selected, using jumpers JP1 and JP2, between an adjustable value determined by potentiometer PR3 or the AGC voltage from the AGC amplifier.

The output impedance of the amplifier is relatively high, requiring the use of a coupling transformer into the 30 MHz LPF. Isolation between the MOSFET output and gate 1 is very good due to the low drain to gate capacitance and the decoupling associated with gate 2. Therefore, the LO signal finds it difficult to pass from the mixer circuit back through the RF amplifier to the antenna.

### 5.1.4 Direct Digital Synthesiser (DDS)

The Analog Devices AD9850/CGPCB DDS evaluation board[1] (Figure 5.9), originally designed for use with a PC parallel printer port, has been adapted to use connections to the PIC in the prototype receiver.

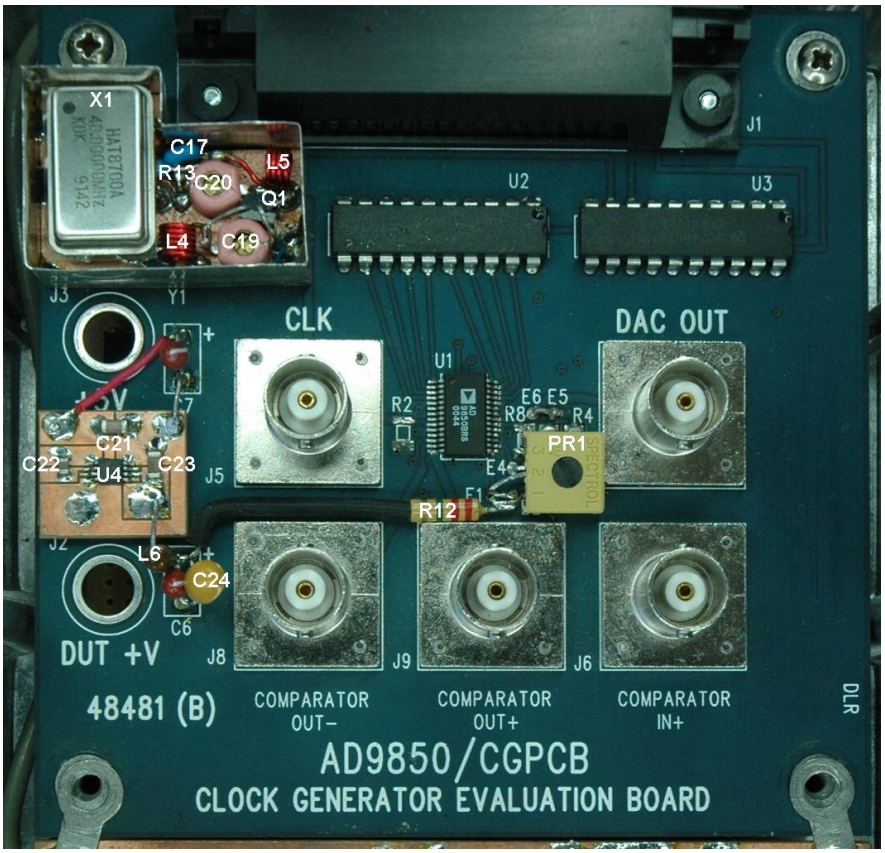


Figure 5.9: The DDS circuit board with added clock multiplier module (top left) and voltage regulator module (centre left).

The output frequency of the DDS is determined by a 32 bit control word sent by the PIC and by the frequency of the reference clock. The reference clock can be provided by an optional plug in crystal module (Y1) or externally via a BNC (J5) socket (see Figures 5.9 and 5.10). Here a plug-in frequency multiplier module (described later) is used as the reference clock (Y1) and increases the clock frequency from a standard 40 MHz crystal oscillator module (X1) to 120 MHz. This extends the operating frequency range of the DDS to at least 40 MHz and helps reduce unwanted 'spurs' in the output. A 'symmetry' potentiometer (PR1) has been added which enables the symmetry of the output waveform to be precisely adjusted to minimise harmonic content. The DDS output to the interface board and ribbon cable connection to the PIC can be seen in Figure 5.11.

[1]See `http://www.analog.com/static/imported-files/data_sheets/AD9850.pdf`

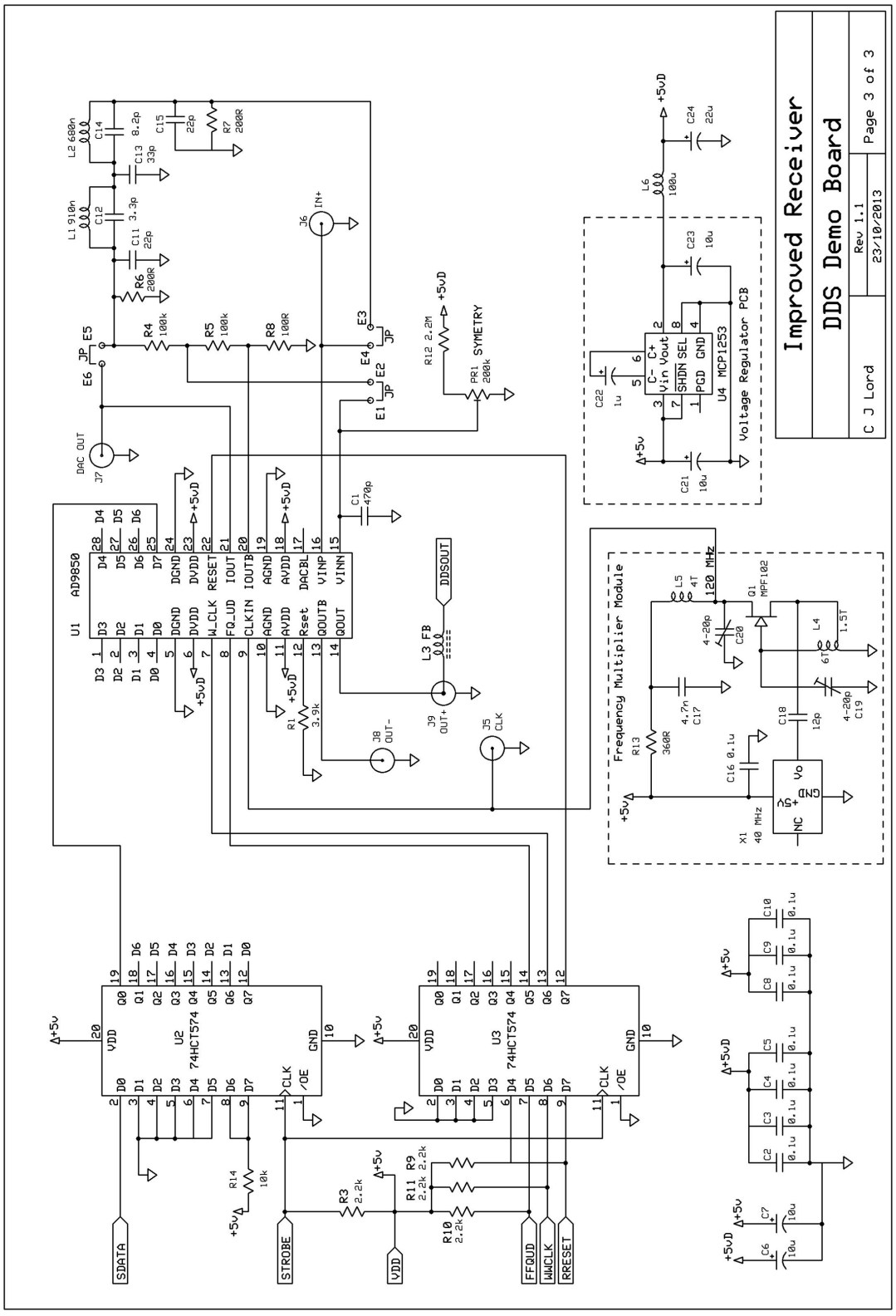


Figure 5.10: The DDS system circuit diagram showing the added Frequency Multiplier and Voltage Regulator modules. Derived from the Analog Devices AD9850 data sheet.

Also added to the original demonstration board is a 5 Volt regulator module. This ensures that the 5 Volt supply, which is derived from the USB port, remains stable under varying load conditions. Variations in the 5 Volt supply to the DDS results in higher noise levels in the receiver.

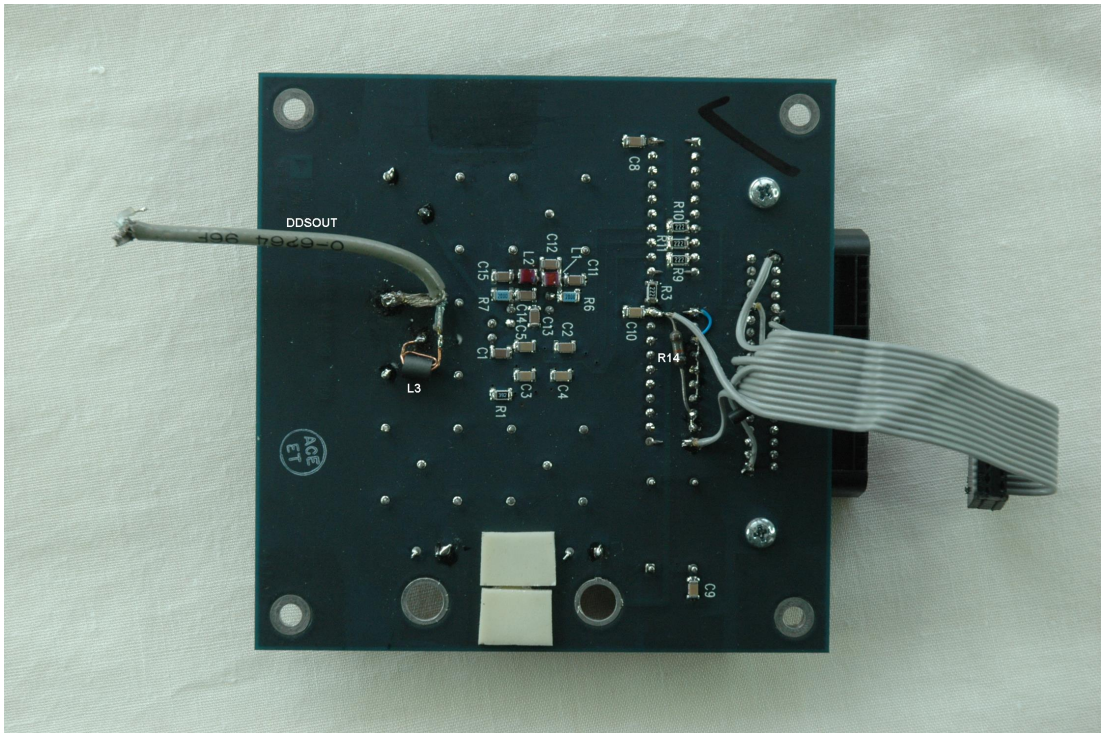


Figure 5.11: The DDS circuit board underside showing the DDS output to the interface board (left) and ribbon cable to the PIC board (right).

### 5.1.5 Crystal Oscillator Multiplier

The crystal oscillator (X1) (Figures 5.10 and 5.9) is a 40 MHz module from a PC. The output from the module drives a field effect transistor (FET) tuned to the third harmonic. The resulting output from the FET is a 120 MHz sine wave with sufficient amplitude to drive the DDS reference clock input.

### 5.1.6 Mixer

The mixer (refer to Figure 5.4) is a high-level, double-balanced mixer which offers good intermodulation distortion (IMD) performance in the presence of strong signals. The output of the DDS is buffered by a logic gate and coupled to the LO input of the mixer by a matching transformer. This combination of logic gate and transformer provides the high LO drive signal required by the mixer. The signal input to the mixer is via a 50 Ohm matching transformer from the 30 MHz

LPF. This transformer also provides isolation and minimises ground currents. Output from the mixer drives the first audio amplifier which has a 50 Ohm input impedance. This ensures mixer performance is maximised by maintaining a fixed 50 Ohm load resistance over a wide frequency range and by keeping reactive loads low.

## 5.2 AF System

The AF output from the mixer is buffered and amplified using a dual, wide bandwidth, high-gain, low-noise operational amplifier (op-amp) before being fed to the first of two AF LPFs. The LPFs have a sharp cut-off after 22 kHz to prevent strong out-of-band signals reaching the PC, which may result in aliasing. The second low-noise op-amp provides further amplification of the output from the first LPF before passing the signal through the second LPF. The final stage of amplification provides high-level output suitable for driving the PC audio system and the automatic gain control circuit (AGC).

The AGC circuit generates a DC voltage inversely proportional to the signal output voltage, which is used to control the gain of the RF amplifier via the MOSFET's gate 2. The AGC voltage is monitored by the PIC so that the overall gain of the receiver can be established. This enables the true strength of the RF input to be determined. The advantage of the AGC system is that the dynamic range of the receiver is significantly increased. This allows both the weak galactic background emission and the sometimes very strong solar radio flares to be observed without receiver overload and loss of peak intensities.

### 5.2.1 Low-pass Filters

The LPFs are seven-pole elliptic filters (Huelsman, 1993) with a cut-off frequency of 22 kHz. These filters determine the bandwidth of the receiver and it is important that they have a sharp cut-off beyond 22 kHz in order to minimise the chance of aliasing in the PC audio system. The attenuation vs. frequency of the filter is shown in Figure 5.12.

The test set-up for the 22 kHz LPFs is the same as that for the previous filters, except that an AF signal generator (TG230) is used instead of the AA-200 and a digital Volt meter (DVM) replaces the FT100D. The test method is also the same as before, except that the reference level is 0.1 mV RMS instead of the S1 – S2 transition.

Figure 5.12 shows that there is a significant performance difference between LPF(1) and LPF(2) and the transition from passband to stop-band is approximately 2.5 kHz higher in frequency than for the simulation. The performance difference between LPF(1) and LPF(2) can be accounted for mostly in the larger ferrite toroidal cores used for LPF(2), although some differences are due to component value tolerance variations. Larger toroids were used in LPF(2) to see how an increase in inductor Q might affect the performance of the filter.

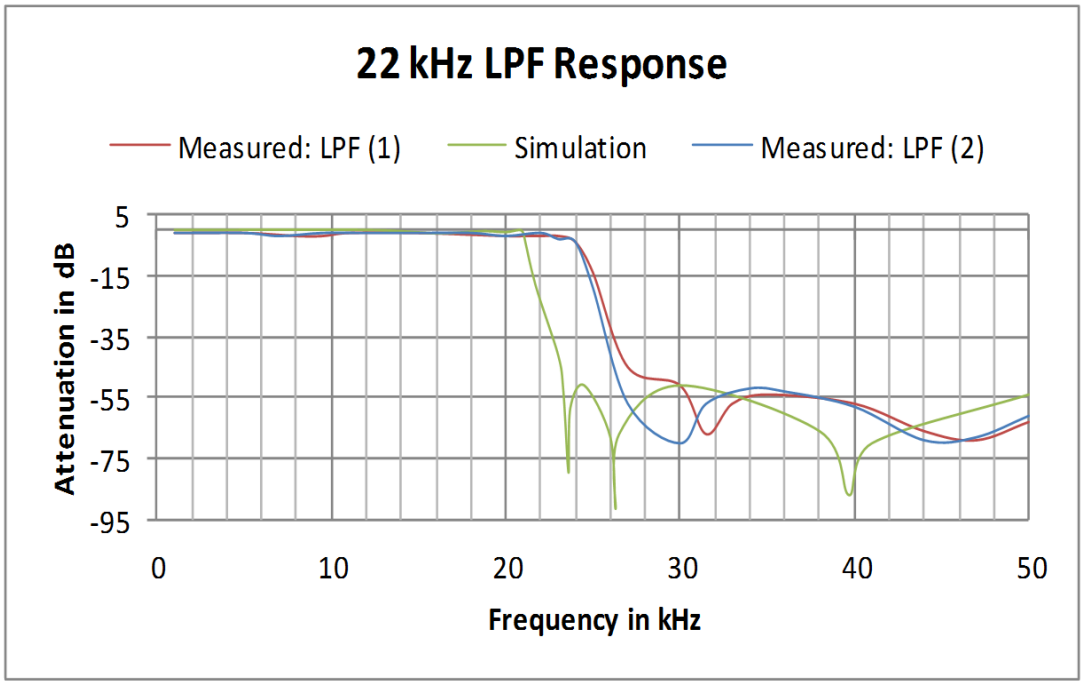


Figure 5.12: 22 kHz LPF Attenuation vs. Frequency. LPF(2) has larger toroids than LPF(1) and the simulation does not take into account the properties of the toroids.

It seems clear that the higher inductor Q has led to a significant improvement in performance in the critical region of the transition from passband to stop-band. The author's simulation program (B2Spice[2]) does not have a model for inductors wound on ferrite toroids, therefore ideal inductors were used which have an infinite Q. Real inductors can be approximated by adding series resistance, which models the wire resistance and lowers the Q, and overall parallel capacitance to model the inter-winding capacitance, but there is no simple way to model the effects of the ferrite core. In the simulation, modelling real inductors in this way did not replicate the measured response. Ideal inductors were, therefore, kept for the reference response. The author used an Agilent U1732C LCR meter to measure the inductor values and its highest frequency for measurements is 10 kHz. The

[2] `http://www.beigebag.com`

2.5 kHz discrepancy in the transition from passband to stop-band is accounted for if the real inductors are approximately 20% lower in inductance at 22 kHz than their measured value at 10 kHz. If this is the case, then it is most likely due to the properties of the ferrite toroid. Further investigations into the properties of ferrite toroids and the availability of spice models were outside the time frame for this project.

### 5.2.2 AF Amplifiers

The first two stages of the audio amplifier system use high performance op-amps (LM833) specifically designed for low-noise high-fidelity audio systems. It is particularly important to keep noise levels low in the early stages, since this noise is subject to the gain of all the following stages. The third and final stage (TLC2722) was chosen for its wide output voltage drive capability (close to the plus and minus five Volt supply) when connected to the PC audio system. It is not designed for use with headphones, although no harm will result from their use. The audio output to the PC is via a phono (RCA) socket on the prototype receiver.

### 5.2.3 Automatic Gain Control (AGC)

The AGC amplifier produces a positive voltage which decreases as the received signal strength increases. This voltage, when applied to the RF amplifier MOSFET gate 2, causes the gain of the amplifier to decrease as the signal level input to the receiver increases. PR2 (see Figure 5.4) sets the maximum gain of the RF stage with no signal present while PR1 sets the RF gain for a specified input signal level. Figure 5.13 shows how the AF output of the receiver stays below the maximum output voltage of 1V RMS over a much wider range of input power compared with the output without AGC.

PR3 provides a means of manually setting the RF gain, for the purposes of testing, and is brought into operation by jumpers JP1 and JP2. Using PR3, the voltage at gate 2 of the MOSFET can be adjusted over the range 0 to 3.9 Volts. A graph of gain vs. gate 2 voltage is shown in Figure 5.14.

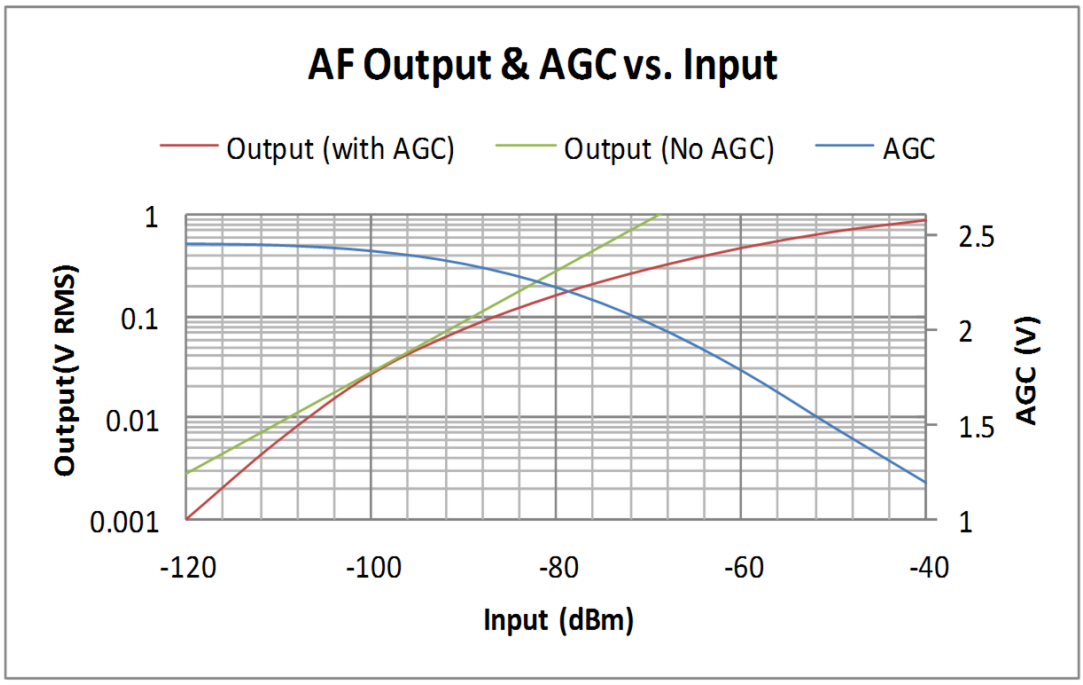


Figure 5.13: AF output and AGC voltage vs. receiver input power. The red trace demonstrates the improved strong signal capability of the receiver when AGC is used.

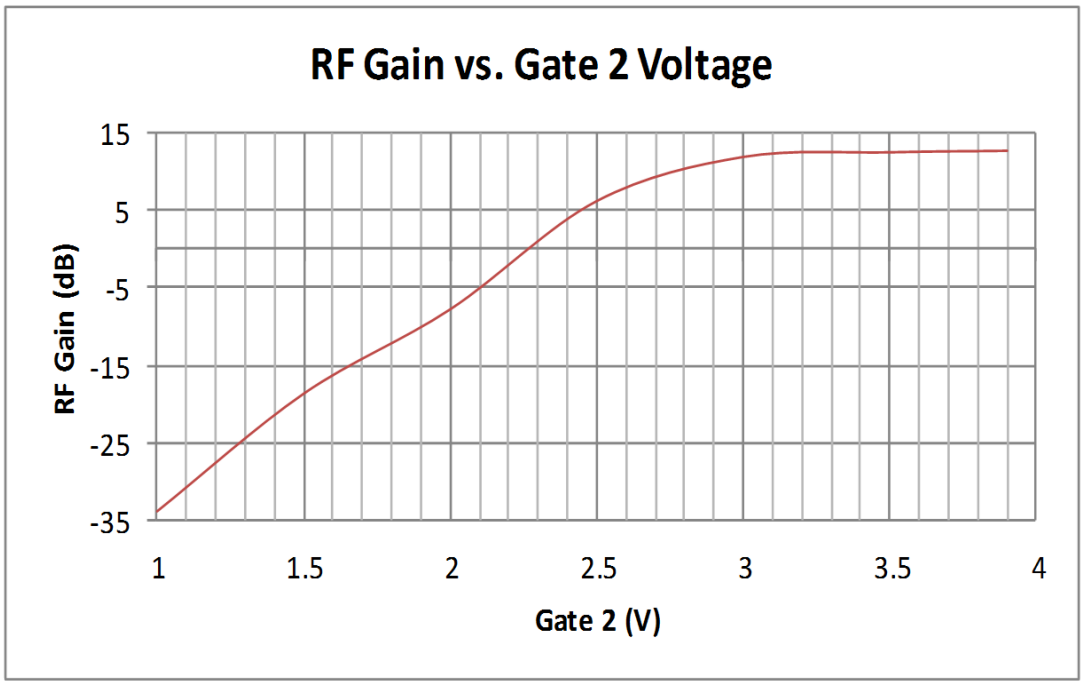


Figure 5.14: RF Gain vs. Gate 2 Voltage. The RF gain is close to linear in dB for gate voltages between 1 and 2.5 Volts and this relationship simplifies receiver calibration.

## 5.3 Programmable Interface Controller (PIC)

The PIC provides the control interface between the PC USB port, the DDS and receiver control circuits. In the prototype receiver, the PIC is implemented with the Microchip PICDEM FSUSB Demo Board seen in Figure 5.15. Also shown in Figure 5.15 is the voltage regulator board which is mounted alongside the PICDEM board and provides regulated ±5 Volt supplies to the receiver circuits. Figure 5.16 shows details of the circuit connections on the underside of the voltage regulator board. The circuit diagram, Figure 5.17, only shows those parts of the PICDEM board which are relevant to the receiver application. Full details of the PICDEM board can be found from the Microchip website[3].

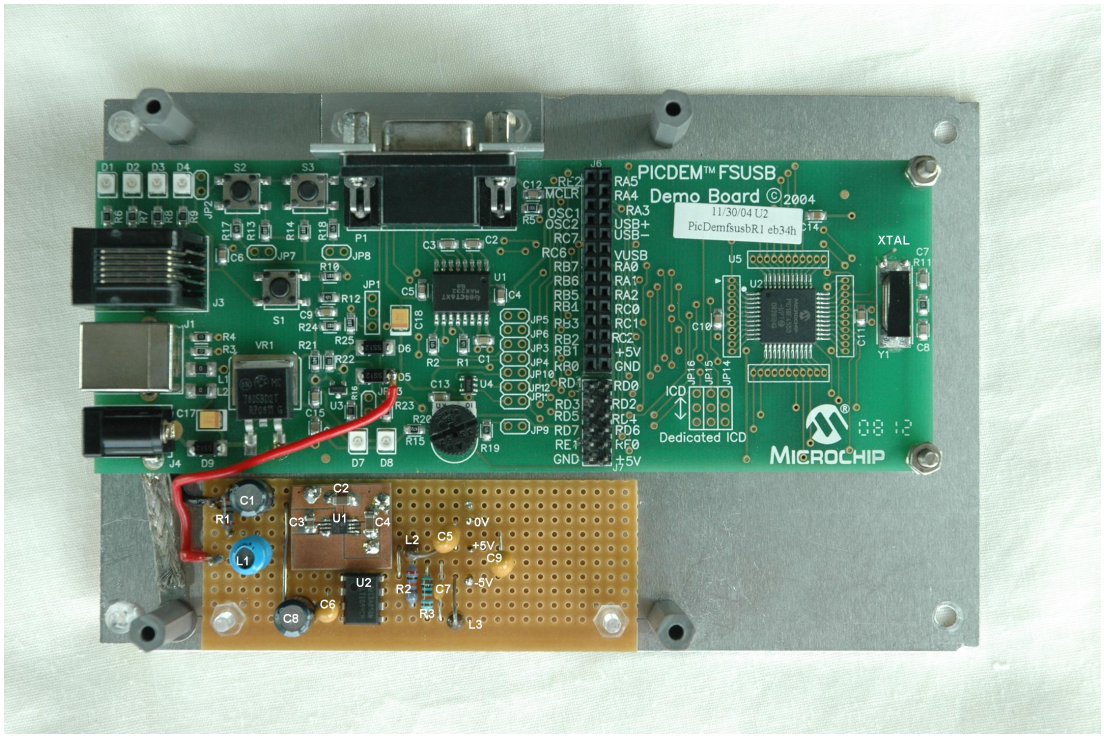


Figure 5.15: The PICDEM FSUSB Demo Board and ±5 Volt Regulator Board.

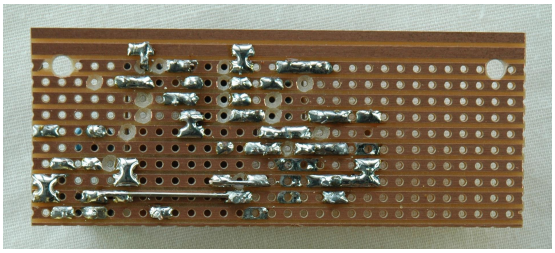

Figure 5.16: Voltage Regulator Board underside.

[3] http://www.microchipdirect.com/productsearch.aspx?keywords=DM163025

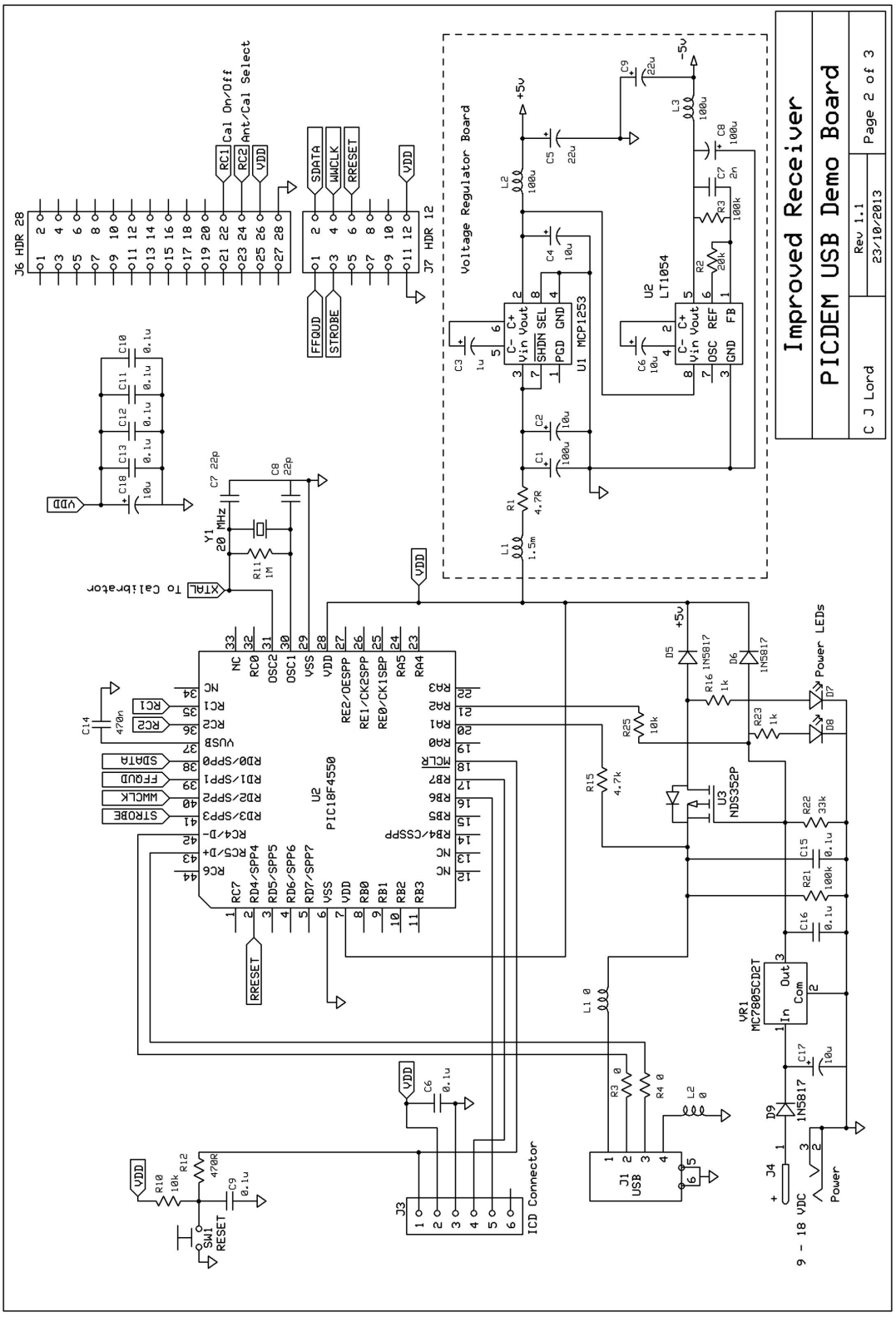


Figure 5.17: PIC system circuit diagram with inset Voltage Regulator Board. Derived from the Microchip PICDEM FSUSB Demo Board users manual.

### 5.3.1 Receiver Control Interface

Connections to the DDS are implemented through the PIC input/output (I/O) ports associated with connectors J6 and J7 (refer to Figure 5.17). Frequency data from the PC is converted to a 40 bit serial-load control word by the PIC, the first 32 bits contain frequency data and the remaining 8 bits contain phase data and control functions. The control word is then clocked serially into the DDS via the I/O ports.

The interface board (see Figures 5.18 and 5.19) contains the final AF amplifier, AGC amplifier, 20 MHz calibrator, mixer LO driver and receiver control logic. Connections to the RF/AF board that sits above the interface board are made via wire links that pass through the ground-plane of the RF/AF board.

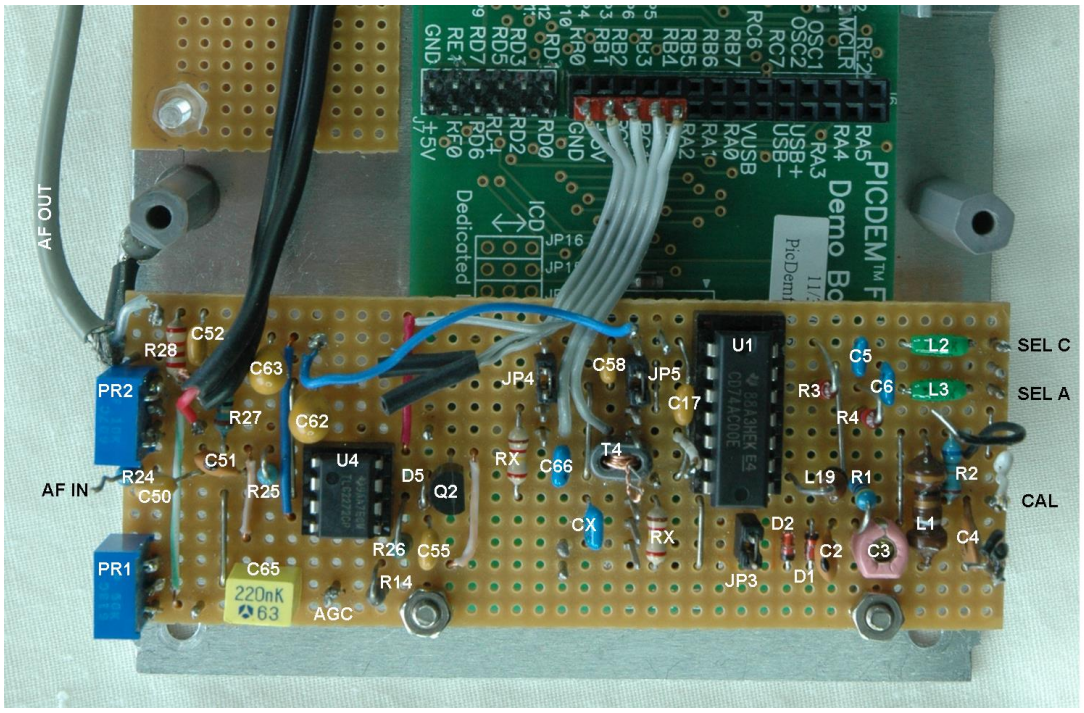


Figure 5.18: The Interface Board which provides functional connectivity between the PIC, DDS and RF/AF Boards.

The 20 MHz calibrator input comes from the 20 MHz crystal clock reference for the PIC, via a logic gate which is part of U1. This logic gate, under the control of the PIC, determines whether the calibrator is active or not. The calibrator circuit attenuates and filters the 20 MHz signal before connecting it to the diode selector circuit on the RF/AF board. The calibrator signal is de-activated when not in use in order to reduce the possibility of it being picked up during normal receiver operation.

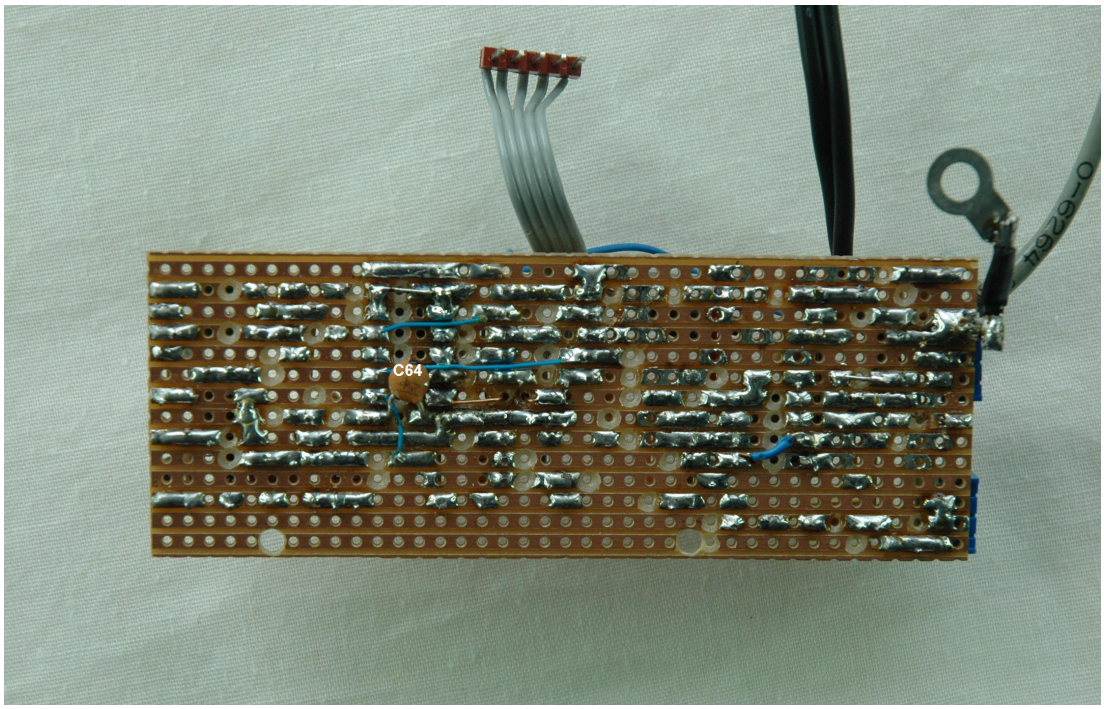


Figure 5.19: The Interface Board underside interconnections.

### 5.3.2 USB Interface

The USB interface provides power and control functions for the receiver. 5 Volts DC at 500 mA is available from the host PC. However, if a USB hub is used with the PC, an additional power source to the hub may be required. Ferrite suppressors are necessary on the USB lead to minimise RFI. The RioMeter software on the PC communicates with the PIC via the USB to transfer frequency and control data between the receiver and the PC. No audio data are transferred over the USB.

### 5.3.3 Voltage Regulators

The voltage regulator board provides stable plus and minus 5 Volt supplies for the RF/AF and Interface boards. The plus 5 Volt supply from the USB can have significant voltage fluctuations and transient spikes which tend to increase noise levels in the receiver generally. The voltage regulators ensure that variations in supply voltage from the USB do not affect the receiver performance, even when moving the receiver between PCs that may have differing USB voltages, or when longer leads are used. Because of its relatively high power demand, and the need to isolate the DDS circuitry from other systems, the DDS board has its own regulator.

### 5.3.4 Firmware

The PIC contains a pre-loaded 'boot' loader which enables the receiver application firmware to be loaded from the host PC over the USB interface. This makes it a simple matter to upgrade the receiver firmware as the receiver development progresses. The prototype receiver firmware is written in the C language using Microchip MPLAB[4] and is kept very simple, most of the work being done by the PC receiver software (RioMeter.exe) which is written using Matlab[5]. The PC operating system uses generic files available from Microchip that interface the USB port to the RioMeter software. These interface programs are written in the C and C++ languages and are linked into the RioMeter software during the compilation process.

Calibration accuracy of the receiver can be improved if necessary by saving look-up tables, in non-volatile memory, for both the RF and AF gain response vs. frequency. This allows receiver gain corrections to be made in the RioMeter software for the passband ripple in both the RF and AF filters.

## 5.4 Performance

### 5.4.1 RF Gain vs. Frequency

The sensitivity of the receiver was measured using the 10 dB signal to noise (S/N) ratio at the audio output. The test frequency was set 5 kHz higher than the LO frequency, thus maintaining a constant 5 kHz AF signal at the audio output. A digital volt meter (DVM) was used to measure the signal level in dB relative to the noise when no signal was present. A switched attenuator between the signal generator (AA-200) and the receiver enabled the signal level to be adjusted to maintain the 10 dB S/N ratio at the output. The attenuation recorded at each test frequency, combined with the known output of the AA-200, was used to determine the input to the receiver in decibels per milli Watt (dBm).

Figure 5.20 shows that signals below 14 MHz are attenuated progressively by the HPF giving good RFI protection from broadcast stations in this part of the spectrum. Above 28 MHz the LPF starts to take effect and signals are attenuated sharply, reaching maximum attenuation at 33 MHz. This reflects the performance of the 30 MHz LPF which is not quite as good as desired. However, the receiver still has a good working frequency range of 16.5 to 28.5 MHz. Below

[4] `http://www.microchip.com/stellent/idcplg?IdcService=SS_GET_PAGE&nodeId=1406&dDocName=en019469&part=SW007002`

[5] `http://www.mathworks.com.au/`

16.5 MHz the second harmonic of the LO progressively adds signals appearing at that frequency into the passband, while signals at the fundamental are attenuated by the 14 MHz HPF.

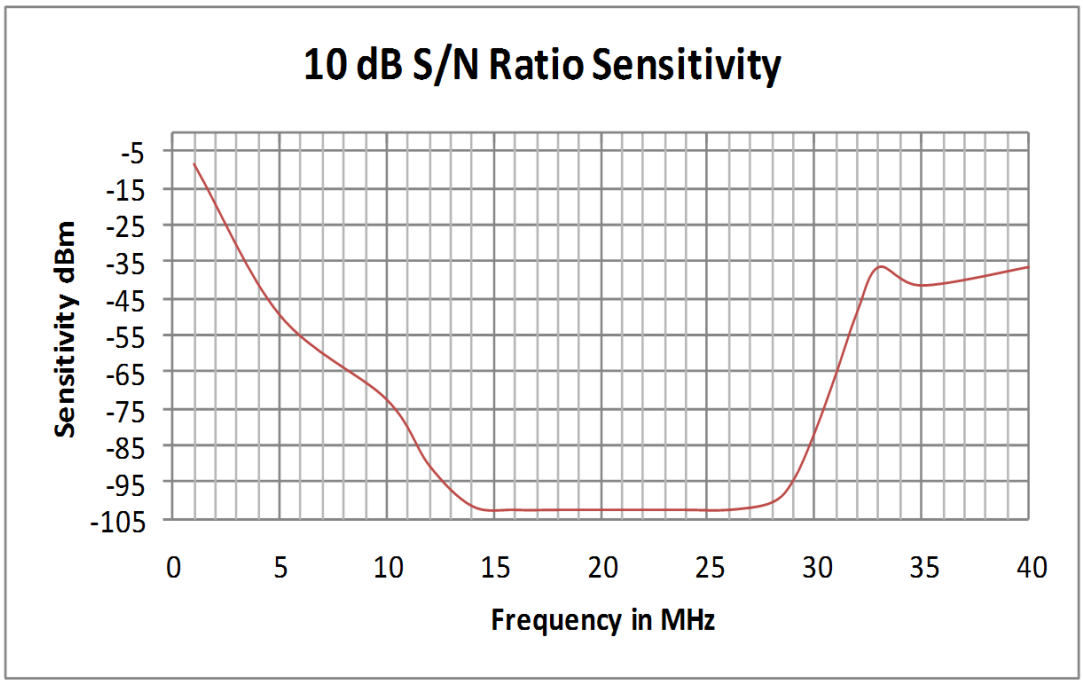


Figure 5.20: The improved receiver RF Sensitivity vs. Frequency showing the effect of the 14 MHz HPF on frequencies below 14 MHz and the 30 MHz LPF on frequencies above 28 MHz.

### 5.4.2 AF Gain vs. Frequency

The same arrangement of test equipment used for the RF sensitivity was used for the AF sensitivity, except that the LO frequency was held constant at 21 MHz and the AA-200 frequency varied between 21 MHz and 21.040 MHz. The choice of LO frequency is not critical and can be anywhere within the flat portion of the receiver's tuning range. The results of the AF sensitivity measurements are shown in Figure 5.21. The lower limit of the passband is designed to roll off by -3 dB at 500 Hz. However, the AA-200 has a minimum frequency step of 1 kHz so this is not shown in Figure 5.21. The upper limit of the passband is determined by the AF LPFs and was designed to be -3 dB at 22 kHz. Due to component tolerances the actual -3 dB point is nearer 23.5 kHz and the attenuation beyond this point is not quite as steep or deep as wanted.

The -3 dB points of the AF LPFs determine the AF bandwidth of the receiver, so the AF bandwidth is 23 kHz. Remembering that this is a dual channel

receiver, like the JOVE Receiver, the receiver RF bandwidth ($B$) is twice the AF bandwidth. Therefore $B = 46$ kHz and from (3.14):

$$\begin{aligned} B &= 10 \times \log\big(2 \times 23 \text{ kHz}\big) \text{ dB} \\ &= 46.6 \text{ dB}. \end{aligned} \tag{5.1}$$

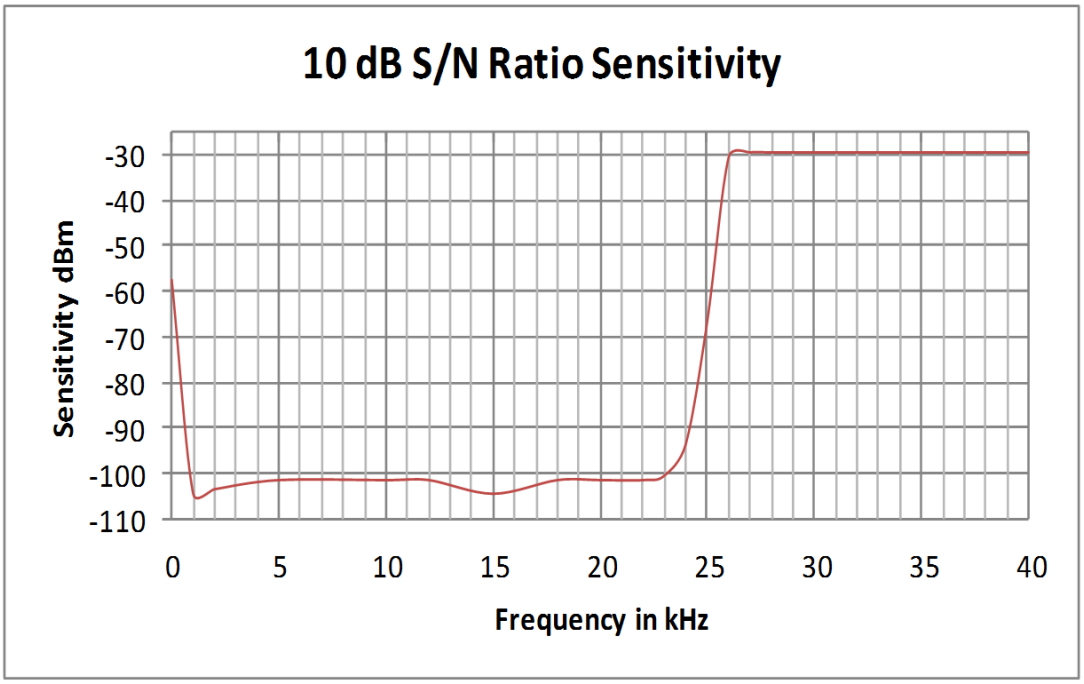


Figure 5.21: The improved receiver AF Sensitivity vs. Frequency showing the upper limit of the passband determined by the AF LPFs.

### 5.4.3 Receiver Sensitivity and Noise Figure

From Figure 5.20 it can be seen that the mid-band sensitivity is approximately -102 dBm for a 10 dB S/N ratio measured at the audio output. From (3.8) the input signal voltage is calculated as follows:

$$\begin{aligned} S_{Vi} &= \sqrt{\left(\frac{10^{\frac{-102}{10}}}{1000} \times R\right)} \text{ Volts RMS} \\ &= 1.8 \text{ micro Volts RMS}, \end{aligned} \tag{5.2}$$

where $R$ = receiver input impedance = 50Ω.

From (3.5) it was shown that the signal output voltage is 2.162 times the noise voltage. Therefore, the signal output voltage for a 10 mV RMS noise output is:

$$S_{Vo} = 2.162 \times 10 = 21.62 \text{ mV RMS.} \tag{5.3}$$

The gain ($G$) of the receiver can now be determined from (3.9) as follows:

$$\begin{aligned} G &= 20 \times \log\left(\frac{S_{Vo}}{S_{Vi}}\right) \text{ dB} \\ &= 81.6 \text{ dB.} \end{aligned} \tag{5.4}$$

From (3.17) the noise output power is calculated as follows:

$$\begin{aligned} N_o &= 10 \times \log\left(\frac{0.01^2}{R} \times 1000\right) \text{ dBm} \\ &= -27 \text{ dBm,} \end{aligned} \tag{5.5}$$

where $R$ = receiver input impedance = 50Ω.

In Chapter 3 (3.19) it was shown that the noise factor of the receiver can be expressed as a noise figure in dB. Substituting values from above gives a noise figure of:

$$\begin{aligned} F &= N_o(\text{dB}) - (kT(\text{dB}) + B(\text{dB}) + G(\text{dB})) \text{ dB} \\ &= -27 - (-174 + 46.6 + 81.6) \\ &= 18.8 \text{ dB.} \end{aligned} \tag{5.6}$$

## 5.5 Summary

The improved receiver development was successful in most of the target areas set out at the start of this chapter. Software on the PC, in conjunction with firmware in the PIC, delivers a useful operating frequency range of 16.5 to 28.5 MHz with good stability. The requirement for the receiver to be fully powered from the USB interface has also been met, with sufficient spare capacity for the implementation of the second channel in a future development. The bandwidth at 23.5 kHz is a little wider than the 22 kHz specified, but tests with an antenna connected show good rejection of strong out-of-band signals. Also the AGC works well, increasing the dynamic range by around 30 dB. The functionality of this receiver represents a significant improvement over that of the JOVE Receiver.

The performance of the LPFs was not as good as expected. The performance of filters depends on the quality and precision of the components used, and at higher frequencies, the layout of the components becomes increasingly important. For the 14 MHz HPF, iron powder toroids and tin plate screens were used to good effect. However, the filter is physically large, so this method of construction was not used for the 30 MHz LPF. For this filter, small surface mount inductors kept the size small but their 'Q' is not as high as the iron powder toroids. Also, no screening was employed between filter stages. The combined effect of this construction method was loss of sharpness of cut-off frequency and loss of depth in the stop-band.

Sensitivity and noise figure measurements were made using a fixed AGC voltage of 2.5 Volts, resulting in a lower than maximum RF gain. The AGC voltage can be increased, and with 3.9 Volts yielded approximately 4 dB of extra RF gain. Although noise levels increased slightly, there was a net improvement in noise figure. The choice of 2.5 Volts for the AGC results from observations that the RF gain changes in a close to logarithmic fashion as AGC voltage decreases. This simplifies considerably the process of calibrating the input signal power to the AGC voltage. Above 2.5 Volts the logarithmic relationship is lost and it is necessary to create a lookup table for the AGC voltage to input signal power relationship. High noise levels from the mixer/LO system are a major contributor to the poor noise figure. This noise appears to be phase noise from the frequency multiplier reference clock. Performance can be improved by the use of a more recent DDS chip, which incorporates a low phase noise reference clock multiplier, and integration of the receiver onto a single PCB with a good ground plane.

The complexity of the improved receiver is significantly greater than that of the JOVE Receiver resulting in increased cost as well as greater flexibility. Also, because of its greater complexity the improved receiver is not suitable for kit assembly. The improved receiver is not intended to be a replacement for the JOVE Receiver, rather, it is an upgrade path for amateur radio astronomers wanting greater flexibility of antenna systems, frequencies and DSP capabilities. Although there are other more highly specified SDR systems available, such as the universal software radio peripheral (USRP)[6] they are expensive, consume a lot more power and are probably too big a jump in complexity from the JOVE Receiver. Many other SDR systems are designed as communications receivers which have different requirements in terms of bandwidth and DSP filtering from radio astronomy receivers.

[6]See Ettus Research `http://www.ettus.com/`

# Chapter 6

# Software

There are two main software components required to run the simple radio telescope: the RioMeter program which is the 'real time' data acquisition and recording component; and the RioPlot program for post-processing and displaying the recorded data. A third software component is the USBtest program which is the working title for the program that controls the USB interface between the PC and the programmable interface controller (PIC) in the improved receiver. This program has yet to be incorporated into the RioMeter program to control the receiver frequency and other functions. These software elements can be used with either the JOVE Receiver or the improved receiver systems.

The RioMeter, RioPlot and USBtest programs were written using the Matlab[1] integrated development environment (IDE). This enables programs to be tested before being compiled into an executable (.exe) file. The RioMeter software, written in Matlab (source code .m files) and compiled under the Microsoft Windows XP operating system, should run on any machine running Microsoft Windows XP or later. There may be compatibility issues with later operating systems and some PCs, however Gingin Observatory has been running the RioMeter software with Microsoft Windows 7 without problems. More recently the RioPlot software, compiled with Matlab under the Microsoft Windows 7 operating system, was tested under both Microsoft Windows 7 and Microsoft Windows XP.

Matlab is a high level language which greatly simplifies the writing of data processing software by providing a large number of built-in mathematical and digital signal processing (DSP) functions. Other features simplify the creation of graphics for display windows and graphical user interfaces (GUI).

The software has a hierarchical structure which calls subroutines and functions as required. This format makes the programs simple to understand and easy

[1] www.themathworks.com

to maintain. The source code generally has sufficient comments throughout to enable the reader to follow the program flow. There are also sections of unused code in comment form and other commented code that has been moved to other locations. The source code files and a copy of the Deploy directory containing the executable binary files are contained on the companion DVD.

## 6.1 RioMeter

The RioMeter program (RioMeter.exe) controls data acquisition from the receiver and performs digital signal processing (DSP) on the data to reduce radio-frequency interference (RFI), explained later in function 'scav', before saving the data to hard disk. Other functions of the RioMeter program include recording the observatory configuration details such as observatory name, location coordinates, receiver frequency and data recording period. Facilities are also provided for e-mailing data at the end of data recording periods or on demand by the user, and selectable filtering of displayed data.

The following flow charts show the major components of the system and the sequence of operations.

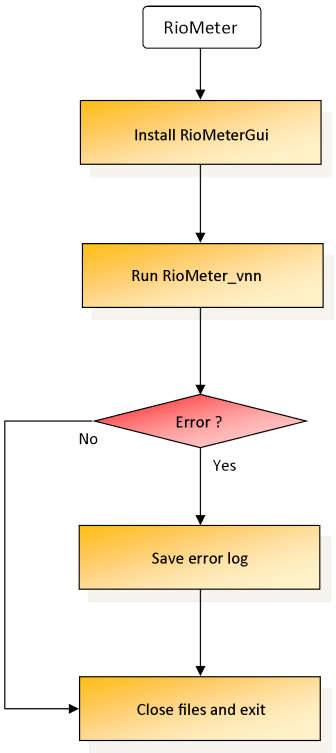


Figure 6.1: RioMeter flow chart for the top level showing program start-up, shut-down and error-handling.

Referring to Figure 6.1, the RioMeter GUI is installed prior to running the main program RioMeter_vnn (where _vnn is currently _v4b) which continues to run until terminated by the user or a fatal error occurs. Errors are recorded to a log file which is saved in the current data directory[2] and sent with the data, if data mailing is activated. Finally, all files are closed and the program exits.

On entering the main program, RioMeter_vnn (shown in Figure 6.2), the program defaults are set and the observatory configuration screen is presented. If the program is being run for the first time, then the observatory configuration data must be entered before the program can continue. Otherwise, a ten second countdown is initiated during which time the user may interrupt to change an existing configuration. At the end of the ten second countdown the program continues using the existing configuration. Observatory configuration is described later in this chapter.

After recovering the GUI settings from a previous session (or the default settings in the case of this being the first run), the display windows are set up to receive data and a data file is created with a file name derived from the current date and time. The data are recovered from the PC audio system and processed by the 'scav' function, described in more detail later. These data represent one sample (currently six seconds duration) and are saved to the data file just created and displayed in the display window.

If the end of the recording period has been reached, the data are sent by e-mail (if enabled) and a new data file created. Otherwise, the timing loop is adjusted using function 'feedback' to maintain the current six second average sampling period and if necessary adjust the number of iterations performed during function 'scav'. Since execution time of the program loop is variable, depending on paths taken at lower levels, computation variability and operating system multitasking delays, an independent timer is used as a reference for adjusting the timing loop. This ensures that the average loop time for a data recording period of 24 hours results in less than one sample of timing error over the period.

As a check on the performance of the computer and specifically its real time clock (RTC), the elapsed time from the start of the data recording period (derived from the RTC in seconds) to the end of the current sample, is saved with the data as a time stamp. The 'TStamp' data shows up any adjustments made to the RTC from the internet time correction facility, or increases in loop time due to interruptions from the operating system. Using this information, it may

[2]Here 'directory' is used rather than 'folder' since it better describes the structure used for saving programs and data.

be possible to change the schedule for the internet time check to minimise the size of time corrections and, to correct errors in the timing of recorded data.

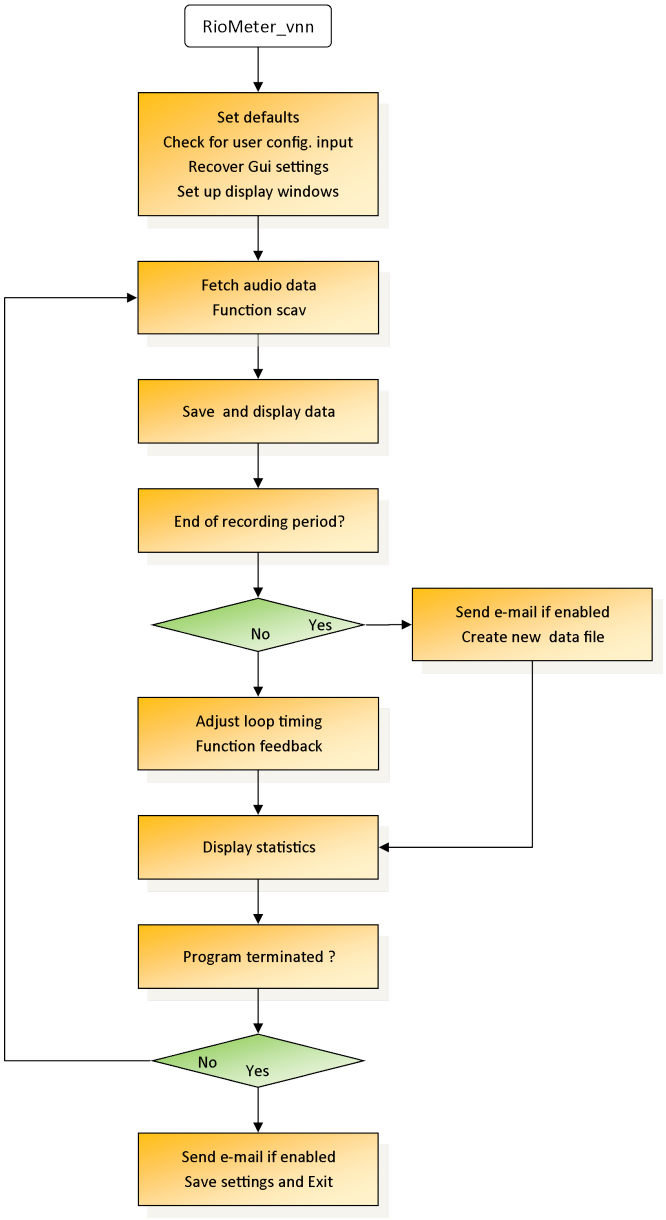


Figure 6.2: Flow chart of the main program loop RioMeter_vnn. Data are processed, saved to hard disk and displayed on screen until the program is terminated.

Next the RioMeter statistics are displayed and the loop continues to fetch and process data unless the program is terminated by the user. When terminated, the current data are sent by e-mail (if enabled), the GUI settings saved and the RioMeter_vnn subroutine returns to the main RioMeter program where the display windows and files are closed before exiting. If e-mailing is enabled, but for some reason fails to send, then another attempt is made when the program next

starts up, and again at the end of the next time period and repeated thereafter as necessary.

### 6.1.1 Data Capture and RFI Mitigation

The following describes the functions used to capture data and the methods used for RFI mitigation. The removal of RFI is a multi-step process that takes place in both the time domain and frequency domain. Not all RFI can be removed by the methods described, but a considerable improvement in data quality can be achieved. RFI is a growing problem in radio astronomy and many papers have been published describing types of RFI and methods for its excision (Fridman, 2001; Fridman & Baan, 2001; Kesteven et al., 2005; Offringa et al., 2010, 2012). Many of these methods rely on having multiple antennas (LOFAR, WSRT, MWA etc.) where RFI is detected by its temporal and spatial relationship to the wanted astronomical signal. Other methods use one or more secondary antennas directed at the source of RFI and an adaptive system that subtracts the RFI component from the astronomical signal (Barnbaum & Bradley, 1998) which can work well for single dish antennas. However, most of these methods have algorithms that are complex and not easily applied to a simple radio telescope. The JOVE Receiver has only one antenna input and although the modified version has an increased bandwidth, it is still very narrow compared with the types of radio telescopes to which the above RFI mitigation methods have been applied.

There are two major forms of RFI that the need to be removed: short duration electric discharge pulses from lightning and vehicle ignition systems; and narrow bandwidth long duration signals from broadcast stations. The methods used to reduce these types of RFI are discussed in the function descriptions that follow. Other broadband RFI from domestic appliances was discussed previously and there is very little that can be done with the JOVE Receiver and software to reduce the effects of this type of interference.

Referring to Figure 6.3, the 'scav' function distributes data sampling evenly over the average six second sampling period using a loop timer and pause, and calculates the averages for the data samples returned by functions 'scc' and 'scfft_1'. The number of iterations (currently 18) of the loop and the loop timer are set from parameters received from the RioMeter_vnn program and are used to maintain the six second average sampling period for the duration of the recording time.

Data samples from the PC audio system are captured by function 'scc'. A total of 4096 samples are captured from each of the left and right channels at a sampling rate of 44.1 kHz. These samples are then processed by function 'ImpulseFilt'

where any large transients caused by lightning static or vehicle ignition noise are removed and replaced with a random noise level close to the surrounding noise levels. These impulses are of short duration compared with the time taken to gather the 4096 samples (approx. 0.093 seconds) and are detected with a threshold based on the average noise level of the 4096 samples.

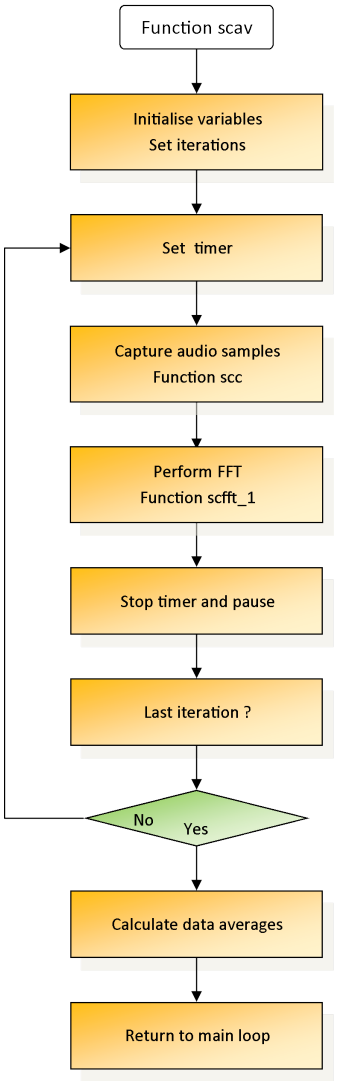


Figure 6.3: Flow chart of the function scav. Data samples are captured, processed and averaged in a loop before being returned to the main program.

The impulse filtering was optimised using simulated data containing random noise data and high level impulses. It was found that a threshold of three times the average noise level was suitable for detecting the leading edge of the pulse and two times the average noise for the trailing edge. This hysteresis give a clean pulse detection and avoids jitter or repeated triggering. Since detection of the pulse occurs after the start of the pulse, when the threshold is reached, an estimate is made of the number of samples that occurred before detection and

these are added to the start of the pulse. The pulse is deemed to have ended if the noise level is rising and is less than two times the average noise level. Having detected the samples where the pulse starts and ends, these samples are replaced in the data by random noise which is scaled to match the average noise level. This method was found to be highly effective in removing lightning static and little or no evidence of this kind of RFI was found in the RioMeter data, even when high levels of contamination were evident in data recorded by the Learmonth SRS.

The method of thresholding is simple and effective. However, it has the disadvantage that it may falsely detect fast transient events that are not RFI and does not remove RFI transients when the average noise level is high, due to dynamic range limitations of the A/D converter in the PC. A more flexible alternative to the current method of thresholding may be to use the rate of change of noise level with time as a means of detection, instead of the absolute noise level. This makes it possible to determine what is rejected based on the type of observation being made. E.g. for galactic background observations where noise levels change very slowly, the detection rate of change is set low, whereas for solar radio flare observations the rate is set much higher. The rate of change method also allows detection over a greater range of average noise levels. Due to time constraints, this method has not been pursued in this work.

Following impulse filtering, the Matlab band-pass filter function is applied to remove frequencies below 500 Hz and above 21 kHz. Removing the low frequencies reduces the effect of mains born interference at 50 Hz and 100 Hz while removing the higher frequencies gives uniformity to the upper roll off of the PC audio filter and removes high-frequency components of any random noise inserted to replace transients. A single RMS value for each channel is now computed from the filtered samples. The RMS and filtered samples from the left and right channels are now returned to function 'scav' for further processing by function 'scfft_1' .

Function 'scfft_1' processes the time domain data into the frequency domain using the combination of a Hanning window (Ingle & Proakis, 2000, p.249) and a FFT (Ingle & Proakis, 2000, p.167), (both Matlab functions) to generate the FFT data. The windowed FFT data provides 2048 frequencies over the range 0 to 22 kHz, representing the signal distribution within the bandwidth of the receiver. These data are then filtered, to reduce artefacts of the windowing process, using the Matlab FILTFILT function, a zero-phase, forward and reverse averaging, finite impulse response (FIR) filter (Carlson, 1998; Oppenheim, Willsky, & Hamid Newab, 1997). This filtering affects only the magnitude of the signals and does not shift the signals on the frequency axis. The extremes of the data

are removed with the Matlab TRIMMEAN[3] function to yield the average FFT for the iteration. Since it is the background noise that is of interest, a value of 80 is used for the PERCENT value. This results in a large percentage of the FFT data due to narrow-band interference being discarded. What is left is the noise level between the interfering signals. Also discarded are the low values of FFT data due to the response of the band-pass filter, for frequencies less than 500 Hz and greater than 21 kHz. This filtering process is effective in removing the narrow-band, human-made signals from the receiver bandwidth.

The loop timer is now stopped and the amount of pause time for the remaining iterations calculated. After the pause, if this is not the last iteration, the loop timer is re-set and a new set of data samples are captured and processed by the functions 'scc' and 'scfft_1'. When all iterations are complete, the data averages for the iterations are calculated using TRIMMEAN with PERCENT equal to 70 for the average FFT data and the mean of just the lower half of the total iterations for the average RMS data. These data are returned to the RioMeter_vnn loop for saving to hard disk and display.

The fact that so much data are discarded in the filtering process could mean that some scientific data are discarded and this is a liability. However, if the data are not discarded then a large amount of the scientific data are lost due to RFI. It is believed that a suitable balance between the retained and discarded data has been found, and that this is demonstrated in the results that are presented in Chapter 7.

### 6.1.2 RioMeter Installation and Configuration

For Microsoft Windows systems, create the RioMeter directory and sub directories under the 'C' drive as follows: C:\RioMeter\Deploy and copy the distribution files into the \Deploy directory. Installation help is available by directing a browser to the installation disk and selecting RioMeterHelp. The screen shots (from the RioMeterHelp file) were created using the Microsoft Windows XP operating system. The RioMeterHelp file also gives detailed set-up information to enable the RioMeter program to self-start in the event of a power failure or after a re-start due to Windows updates being installed. Those instructions are not repeated here.

[3] M = TRIMMEAN(X,PERCENT) calculates the trimmed mean of the values in X. For a vector input, M is the mean of X, excluding the highest and lowest (PERCENT/2)% of the data.

Double click the MCRInstaller.exe file to install the Matlab runtime environment and follow the on-screen prompts. Once the runtime environment has been installed (which may take several minutes), run the RioMeter program by double clicking the RioMeter.exe file. This also may take several minutes to load.

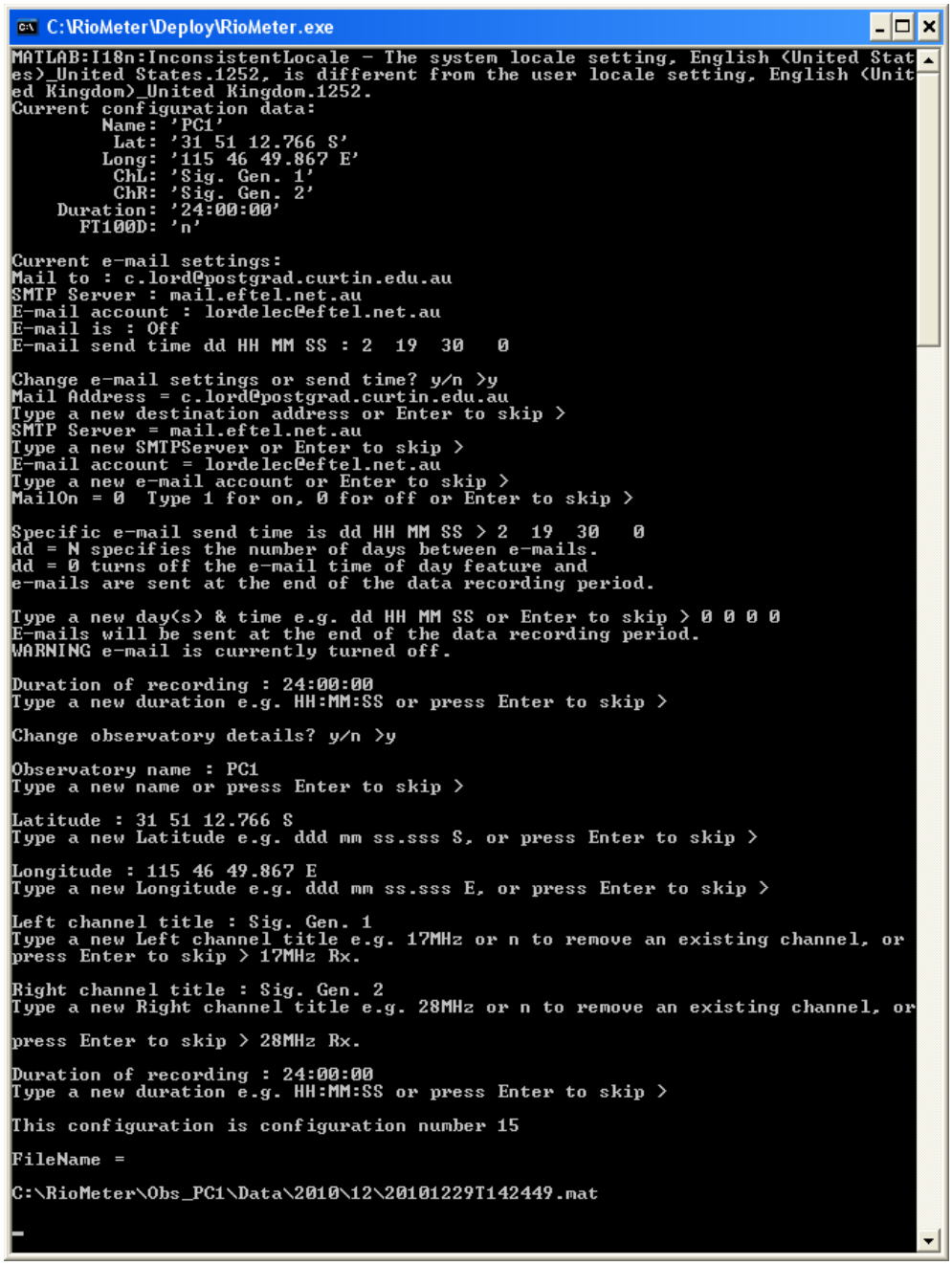


Figure 6.4: The RioMeter start-up configuration screen showing data entry for observatory details, e-mail settings and recording duration.

On first running of the program the user is prompted to enter the configuration data for the observatory. A typical data entry screen is shown in Figure 6.4. Configuration data take the form of an observatory name and some details that

identify the location of the observatory, how many data channels (one or two) are to be used and labels to identify the channels when the data are displayed. The configuration data entry is via a command prompt and yes/no confirmation which can be repeated until the information entered is correct. When the configuration process is complete, a sub directory structure for the observatory is created and the configuration data are saved, together with the configuration reference number to the ConfigData.mat file in the Config directory and the RioMeter program starts. The configuration can now only be changed by closing the program and re-starting it. Once the program is running, help is available from the 'Help' menu item in the RioMeter GUI.

The observatory name should be kept as short as practicable and consist of only upper and lower case letters or numbers. If multiple words can not be avoided then they should be separated by an underscore '_' character, not a space. This is necessary because the observatory name is incorporated into the directory structure where data are saved by the RioMeter program and some operating systems do not like spaces between directory or file names. It should also be born in mind that the RioMeter and RioPlot programs prepend the word 'Observatory' to the observatory name when naming display windows on screen and data plots. See Figures 6.6 and 6.13 for examples of directory structure file names and Figures 6.7 and 6.15 for examples of data screen and plot naming.

The latitude (Lat) and longitude (Long) information in the observatory configuration data is important because it is used to determine the sunrise and sunset times and the local mean sidereal time (LMST) in the RioPlot program. If these data are missing then the default time of UT+8 hours, Western Australia time, is used.

The 'Duration' entry in the observatory configuration data determines the time period for data files. Shorter time periods mean more data files and more frequent e-mailing of data (if enabled). It also means that fewer data are lost if a file becomes corrupted due to a power failure etc.

Sometimes it is helpful to have the data files e-mailed at a specific time of day e.g. after sunset for solar observations, or during the night when there is less demand on local internet services. This facility can be set up through the 'Specific e-mail send time' feature, an example is shown in Figure 6.4

The observatory configuration data are saved to a Matlab data file named ConfigData.mat in the C:\RioMeter\Obs_Name\Config directory (where 'Name' is the observatory name) and any changes to the configuration are added to this file as a new configuration. The configuration reference number is updated

and saved with the data. This ensures that the data are always linked to the configuration that they were recorded under. If e-mailing is enabled, then the ConfigData file is added to the file list and sent in the zip file at the next data mailing time, or when the RioMeter program is closed (or if the program ends unexpectedly, e.g. due to a power cut, the zip file is sent when the program re-starts). When the zipped data files are received and extracted to the data directory, it is important to remember to transfer any ConfigData.mat file to the Config directory. If this is not done, the RioPlot program (described later) does not find the correct configuration for the data and an error occurs. Figure 6.5 shows a normal start-up screen after the configuration data have been saved.

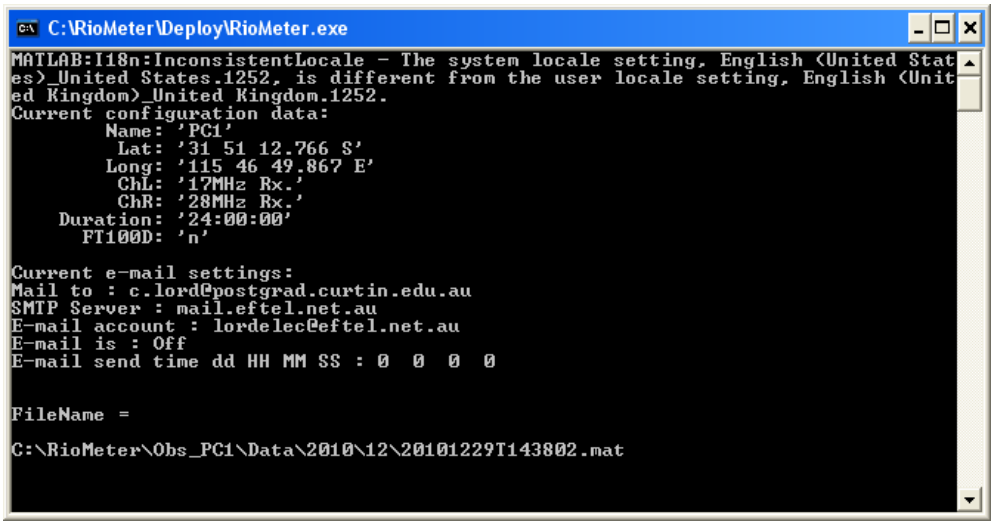


Figure 6.5: RioMeter start-up screen showing observatory configuration details and current data file.

### 6.1.3 Directory Structure

The observatory directory and sub directories are created automatically by the RioMeter software as shown in Figure 6.6. New year and month directories are created as required. The processed data are saved as Matlab data (.mat) files with the filename determined by the date and time as follows: yyyymmddThhmmss.mat.

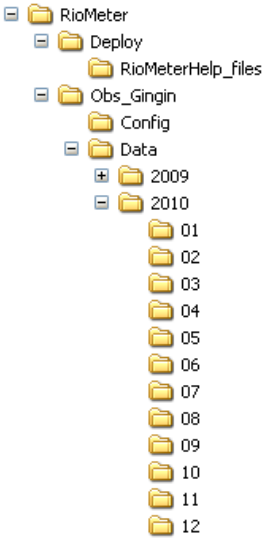


Figure 6.6: RioMeter file directory structure.

### 6.1.4 Data Display Window

The data display window (two windows when two channels are used) shows the time domain data in the upper panel and frequency domain (spectrograph) data in the lower panel. See Figure 6.7. The heading at the top of the window identifies the data channel from the observatory configuration data, as set up during program start-up.

The time domain data display shows data covering the time period selected from the RioMeter GUI with the most recent data on the right. The X-axis graduations show time and date while the Y-axis shows relative magnitude (power) of the received signal. The Y-axis values relate to the numerical value of the analogue to digital conversion and have arbitrary units. Two sets of data are plotted: averaged RMS signal power (green) and the averaged FFT (red). The FFT data are scaled to match the RMS data such that they sit close together in the display under conditions of broadband noise. Narrow-band RFI causes the RMS value to increase ahead of the FFT value, which only becomes affected when the RFI occupies a significant portion of the receiver bandwidth. Increasing levels of broadband noise however, cause the FFT value to increase ahead of the RMS value. This provides a convenient marker for identifying potential solar bursts evidenced by a red tip at the peak of the data.

The spectrograph shows the band-pass filtered data samples which are part of the set of data returned from the scfft_1 function. These data have not had the trimmean function applied and therefore show any peaks in the bandwidth

due to narrow-band signals. The X-axis is calibrated in kHz and the Y-axis to the same scale as used for the Y-axis time domain display.

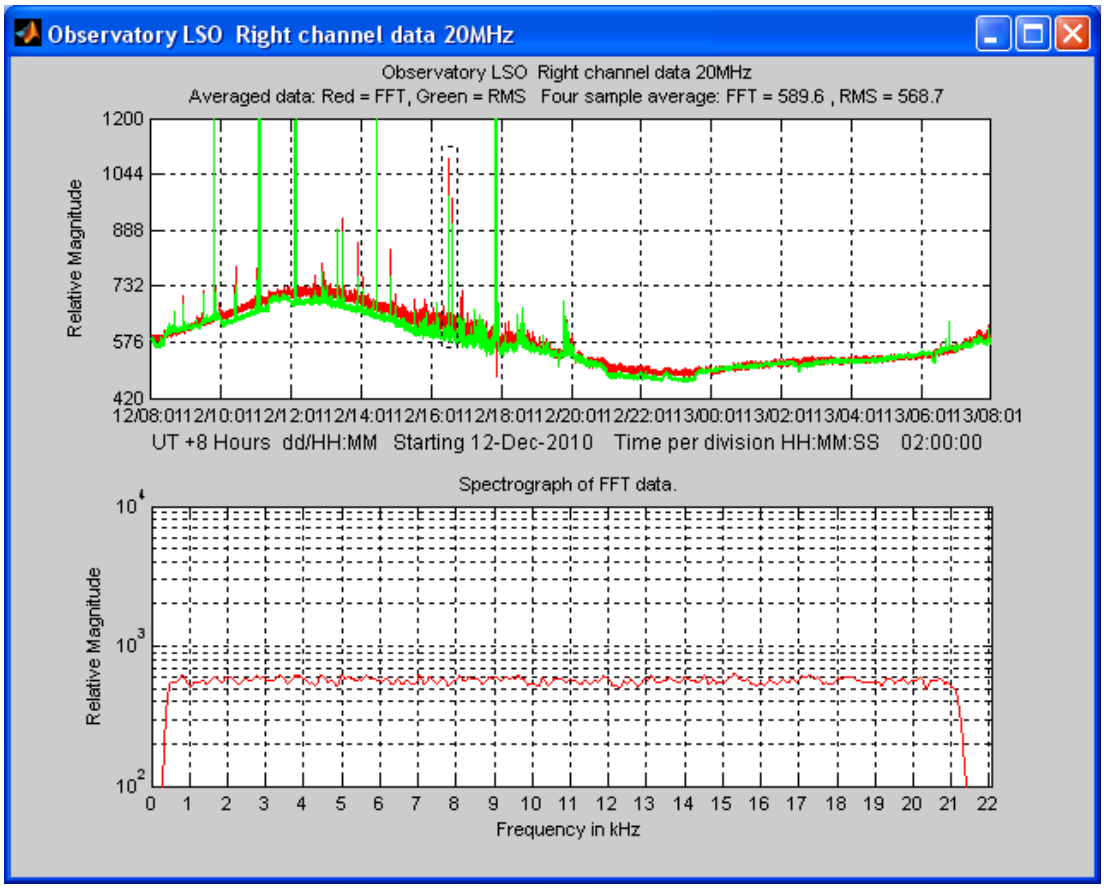


Figure 6.7: RioMeter data display window showing time domain (upper) and frequency domain (lower) data.

### 6.1.5 Statistics Window

The RioMeter statistics window (Figure 6.8) shows the current sample number, sample time, average sample time, iterations, iteration number and pause time.

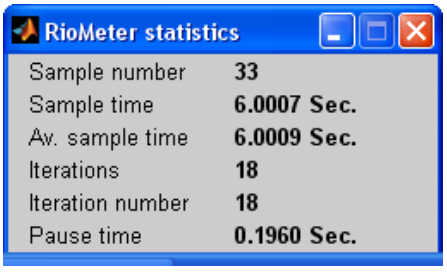


Figure 6.8: RioMeter statistics display window.

Where sample time is the measured time taken for the most recent data sample and iterations is the actual number of sampling iterations used for the sample. The iteration number is the target number of iterations and reduces for slow computers. The pause time is the amount of time that the program is paused per iteration to maintain the average sample time.

### 6.1.6 Display Zoom and Capture

The display zoom feature applies to the time domain display only (either left or right channel, for two channel systems), however, the spectrograph is also captured and displayed.

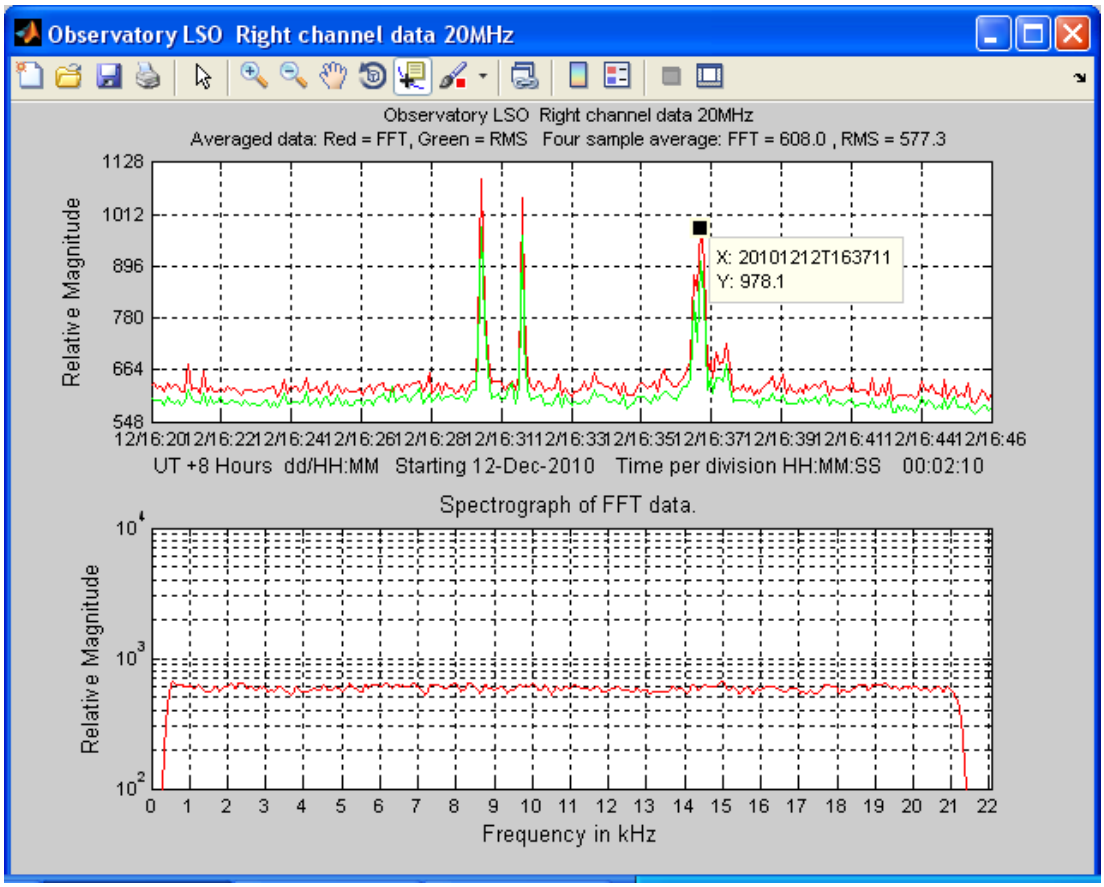


Figure 6.9: RioMeter display zoom window showing the use of the 'data tip' tool to locate the exact coordinates of a data peak .

By positioning the mouse pointer in the window and dragging a box around selected data, while holding down the left mouse button, the data are captured to a new window at the lower right of the screen when the mouse button is released. Figure 6.9 shows zoom data from the dotted region in Figure 6.7 with the data tip tool selected from the tool bar. However, the spectrograph shows data at the time

the zoom was captured since the spectrograph data are not saved. This makes it possible to zoom in to any features that may be unclear in the main window, or lost from the left hand edge of the window when a shorter time interval is selected from the RioMeter GUI. Simply clicking the left mouse button with the pointer in the data display window (either left or right, for two channel systems) captures the entire window to a new window. In both cases the new window is fixed and does not update with the main window. A tool bar at the top of the window provides facilities for labelling data points, and zooming in and out etc.

## 6.2 RioMeterGui

The RioMeter Gui (Figure 6.10) is a separate window for setting up various features in the RioMeter program and can be minimised when not in use.

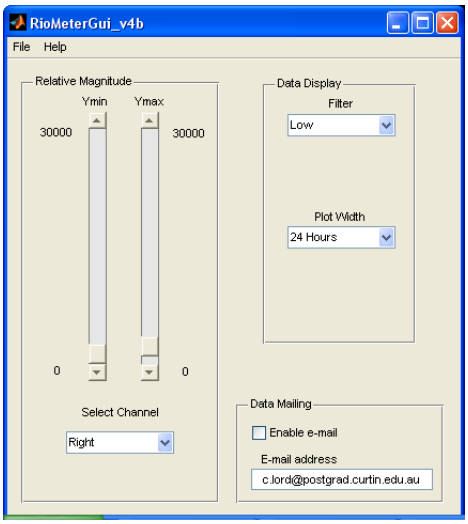


Figure 6.10: The RioMeter GUI is the control centre for the RioMeter program.

### 6.2.1 Relative Magnitude Sliders

These two slider controls are used to set the minimum and maximum values for the Y-axis in the time domain display. If two channel operation is in use, first select the correct channel from the drop down menu below the sliders. The sliders can be dragged up and down by locating the mouse pointer on the slider control and with the left mouse button held down, drag the slider, then release the mouse button. Alternatively, use the up and down arrows at the top and bottom of the slider to make small changes in position.

### 6.2.2 Filter

The filter drop down menu offers three levels of filtering: low, medium and high. The applied filter smooths the displayed data, reducing the effects of noise, without affecting the recorded data. The filter method uses the Matlab function FILTFILT, where the value of low, medium or high and the amount of data to display determines the averaging period of the filter. Averaging varies from 2 data points for 1 hour of data and low filter, to 35 data points for 48 hours of data and high filter. These values were chosen for the best visual interpretation of the data on the PC screen. Since the filter performs zero-phase, forward and reverse digital filtering, there is no shift in the data along the time axis. Filtering is especially useful when looking for trends in data over longer time periods. E.g. When looking at the galactic background noise over 48 hours.

### 6.2.3 Plot Width

The plot width drop down menu offers five ranges of display times: 1, 8, 24, 32 and 48 hours for the time domain display window. Display data are recalled for display if the RioMeter is closed down for a period of less than 48 hours and then re-started. Once re-started, data recording and display resumes, leaving a gap for the period of time that the RioMeter was not running.

### 6.2.4 Data Mailing

When the 'Enable e-mail' check box is ticked, data are sent by e-mail to the address shown in the 'E-mail Address' panel, provided that the necessary e-mail configuration was set up when the RioMeter program was started.

### 6.2.5 File Menu Options

#### 6.2.5.1 Watchdog

Ticking the watchdog option enables the watchdog hardware, if it is installed. This feature is normally enabled by default, but can be disabled if a conflict occurs with the serial port COM1. Watchdog hardware has only been installed at the Gingin Observatory where there were persistent problems with power glitches and internet connections which caused the PC to stop running. The hardware watchdog detects that the RioMeter software has stopped running and performs a reset of the PC.

#### 6.2.5.2 Send Data Now

The send data now option sends all accumulated data since the last data send operation. This is a convenient way of checking that the send data function is working correctly and for sending important event data for analysis without having to wait until the allotted send time.

#### 6.2.5.3 Exit RioMeter

This option exits the RioMeter program and sends any accumulated data since the last send data operation, if e-mailing is enabled.

### 6.2.6 Help Menu Options

#### 6.2.6.1 RioMeter Help

The RioMeter help file (RioMeterHelp.htm) provides set up and general information about the RioMeter program.

#### 6.2.6.2 Help About

Selecting this option displays the version number of the RioMeter program.

## 6.3 USB Interface

The USB program (USBtest.exe) is only used with the improved receiver and has to be run from the C:\RioMeter\Deploy folder by double clicking USBtest.exe. Once opened, the USB connection is enabled by clicking the 'Connect' button. The receiver frequency is set by typing the required frequency into the data entry window and clicking 'Set Frequency'. Other features of the USB program are only used for testing connectivity and function of the PIC. Before unplugging the USB lead, click the 'Connect' button to disconnect the USB port from the PC operating system. Note that power is applied to the receiver all the time the USB lead is plugged in and the 'Connect' button only controls the software status of the connection.

As mentioned earlier, the receiver control element of the USB program has yet to be integrated with the RioMeter program. When this is done, an improved method of setting the receiver frequency will be made available and connection with the receiver will be automatic. USBtest.exe is compiled from USBtest.m,

the high level component, and USBPort.cpp the C++ component which connects with the computer operating system and communicates with the PIC.

### 6.3.1 PIC Firmware

The PIC firmware was developed using the Microchip[4] MPLAB IDE. This software is available for free download and includes numerous examples of applications for the PICDEM USB Demo Board. The firmware for the PIC is written in the 'C' language and compiled and loaded into the PIC from the MPLAB IDE.

## 6.4 RioPlot

The RioPlot program (RioPlot.exe) displays selected data recorded by the RioMeter program. Using this program it is possible to display data from any observatory or observatories over any selected time period. The screen shots show the RioPlot program running under the Microsoft Windows 7 operating system.

The following flow charts show the major components of the system and the sequence of operations.

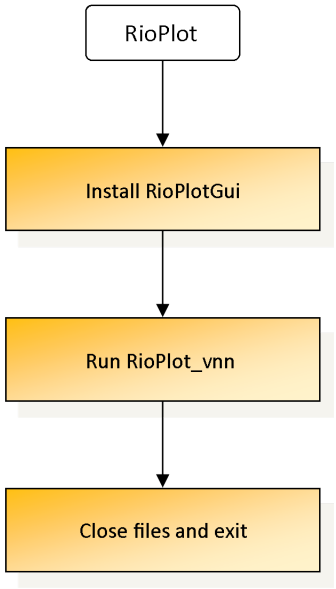


Figure 6.11: RioPlot main program flow chart.

The RioPlot program (see Figure 6.11) is the top level program which installs the RioPlot GUI and runs the RioPlot_vnn program, the current version being RioPlot_v4d. The RioPlot_vnn program continues to run until closed from the

[4]www.microchip.com

GUI. Control then returns to the RioPlot program where all files are closed and the program exits.

At the start of the RioPlot_vnn program (see Figure 6.12) the default variables and RioPlot GUI are set up, with the 'First iteration' flag set to false, before entering the program loop. When a single or multiple observatory plot is selected from the GUI 'Plot' menu, the 'First iteration' flag is set to true and the observatory selection box is presented. This enables the user to make a selection from the available observatories and recorded data facilitated by the GetDataFiles function. Having made the selection, the data files are read using function GetData. From these data the maxima and minima are determined and the GUI sliders set.

The function GetDN returns the latitude (Lat) and longitude (Long) of the observatory from the configuration data file and also the data for the sunrise and sunset times. To do this it calls on three functions: SunRADec which returns the Right Ascension (RA) and Declination (Dec) of the Sun for a particular date in UT; Julian which returns the Julian day (JD) (Meeus, 1991, p. 59); and SunRiseSet which uses the previously determined date, RA, Dec, Lat and Long to determine the sunrise and sunset times. The methods used in these functions are derived from the US Navy Astronomical Information Center[5], Kraus (1986) and Meeus (1991).

Next, the display windows are created, either one or two, depending on the number of channels in use at the observatory. Or, if multiple observatories are being displayed a single window is created. The data are then displayed, including shading for night time periods. If the quiet day curve (QDC) option has been selected from the GUI plot menu, then the QDC is plotted for each channel for single observatory plots. QDC plots are not generated for multiple observatory plots. The 'First iteration' flag is now set to false and the program loop waits for input from the GUI. If the sliders are adjusted, or filter level changed, then a re-plot request is generated and the data are re-plotted. Selecting a new single or multiple observatory from the GUI plot menu generates a new observatory request by setting the 'First iteration' flag to true, then the observatory and data selection boxes are once again presented. Closing the RioPlot GUI window, or using the End Program button, exits the RioPlot_vnn program and control is returned to the RioPlot program, where all files are closed and the program exits. However, the plot windows that were created using RioPlot_vnn remain open and must be closed manually in the normal way.

[5] `http://aa.usno.navy.mil/faq/`

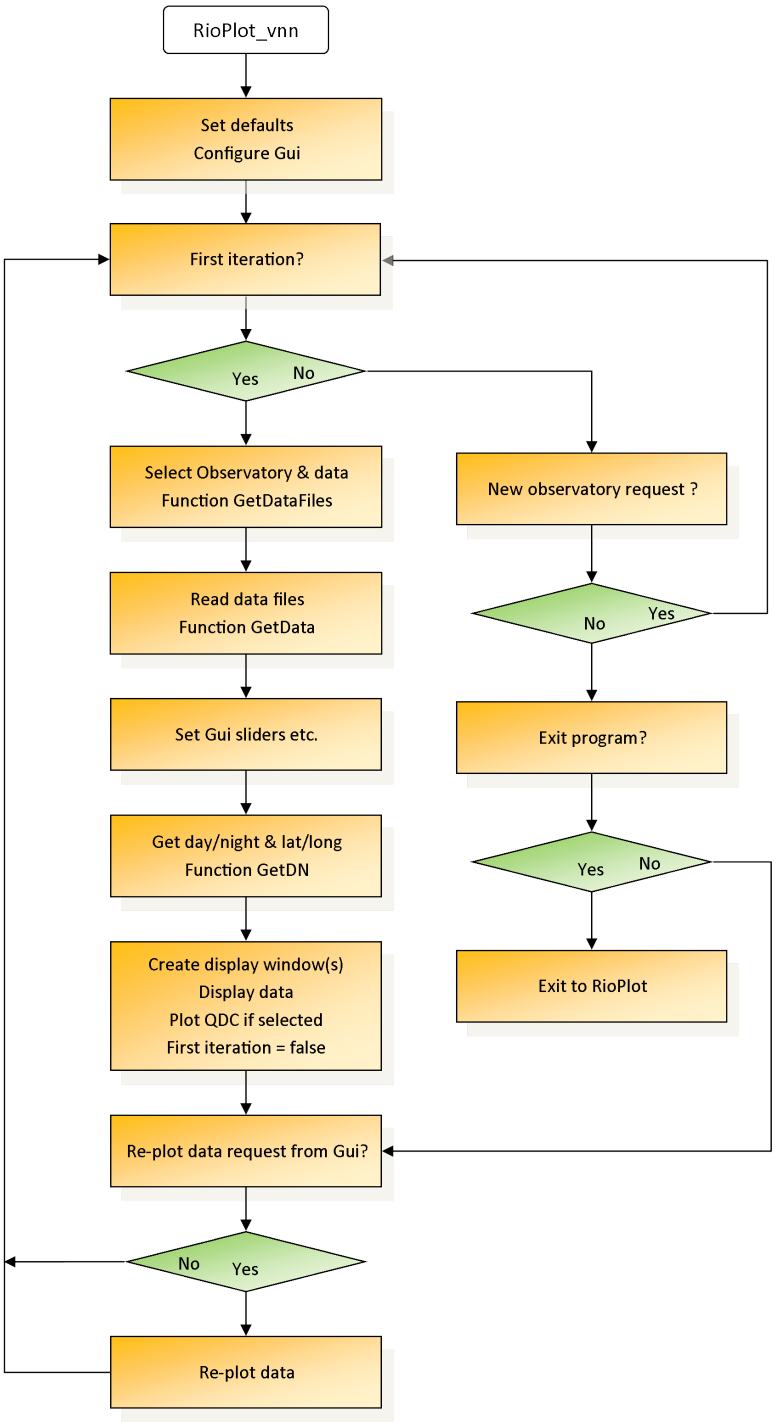


Figure 6.12: RioPlot_vnn flow chart showing observatory and data selection program loops.

### 6.4.1 RioPlot Installation

Installation follows the same format as for the RioMeter program. If the RioPlot program is to be run on the same machine as the RioMeter program, it is only necessary to copy the distribution files to the C:\RioMeter\Deploy directory and double click the RioPlot.exe file to run the program. Otherwise, it is necessary

to create the directories C:\RioMeter\Deploy, copy the distribution files to the Deploy directory and double click the MCRInstaller.exe file to install the runtime environment before running the RioPlot program.

### 6.4.2 Directory Structure

The directory structure is the same as that used for the RioMeter program. However, if data have been sent by e-mail from a remote observatory, it is convenient to save the zip file attachments to a 'zip' directory under the 'Data' directory as shown in Figure 6.13

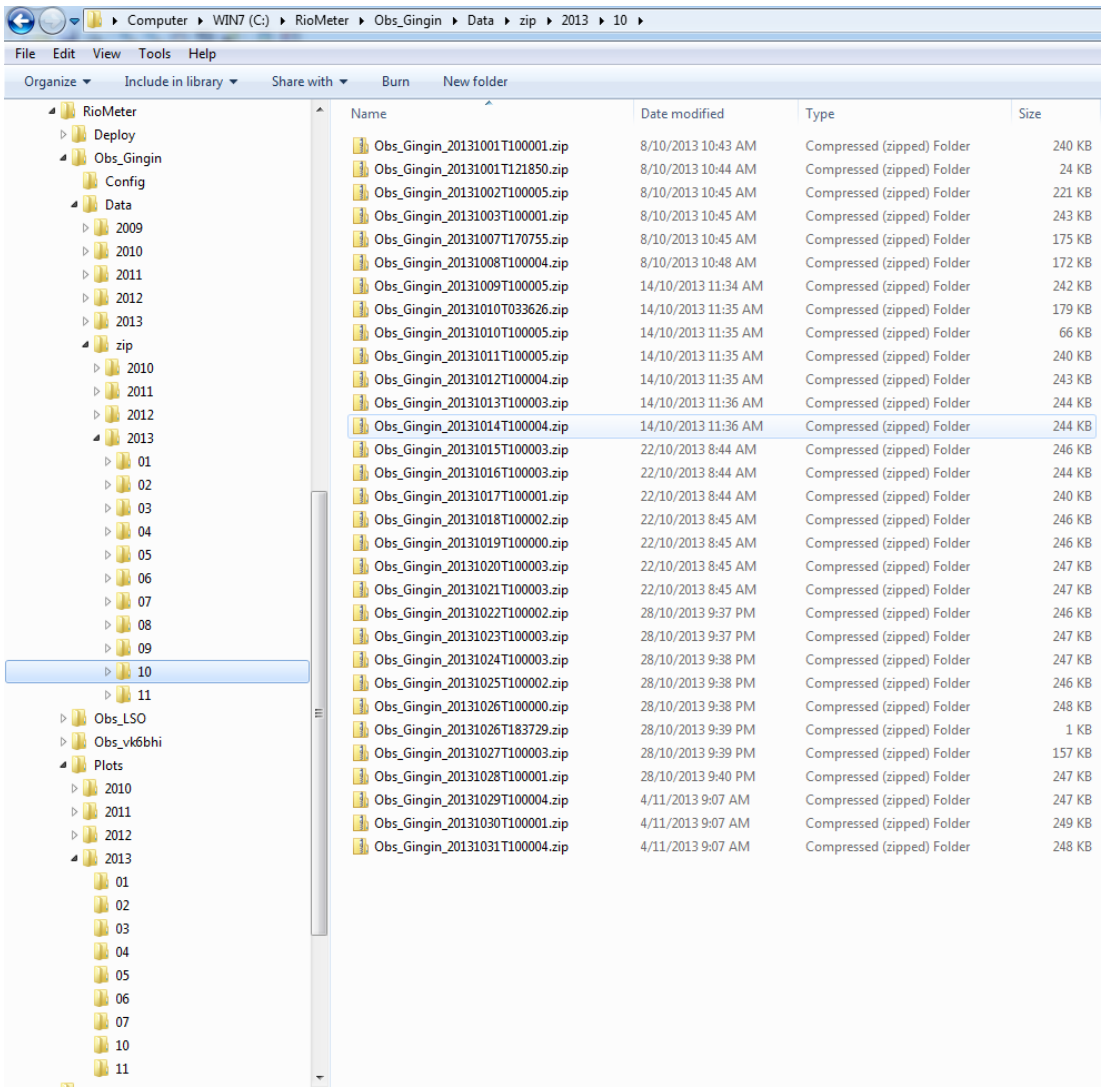


Figure 6.13: RioPlot directory structure showing 'zip' directories and directories for other observatories and saved plots.

Copying of the zip attachments from an e-mail program and extracting the data to the data directory has to be done manually.

The transfer and saving of data from remote observatories could possibly be done more efficiently using ftp (file transfer protocol), however, for this project it was simpler to set up the e-mail facility within the Matlab environment.

### 6.4.3 Single Observatory Data Display

From the RioPlot GUI plot menu, select 'Single Observatory' to display a list of the available observatories, click on the observatory required and click 'Ok'. A list of years follows and having selected a year, a list of months is displayed. Selecting a month displays a list of all the data files for that month. Single or multiple data files can then be selected for display.

Depending on whether the chosen observatory is recording data on one or two channels, the RioPlot_vnn program creates one or two windows to display the data. The X-axis shows the date and time in UT (Universal Time) and UT +8 hours for the top graph. The Y-axis is scaled automatically for best data fit. The scaling can be changed using sliders in the RioPlot GUI. The plot window(s) appear minimised at the top of the screen with the RioPlot GUI in the bottom left corner, as shown in Figure 6.14

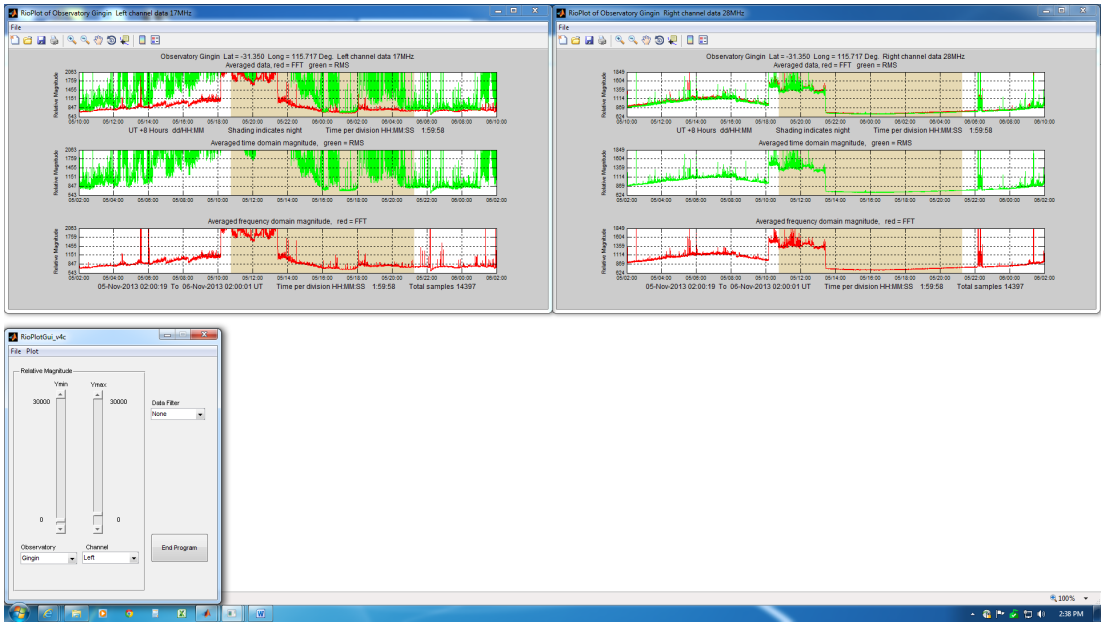

Figure 6.14: RioPlot of two channels and GUI.

The display window contains three graphs with the observatory name and channel identification at the top. The top graph shows both the RMS (green) and the FFT (red) data. These two sets of data normally follow each other closely, except under conditions of strong RFI, where the RMS value can greatly exceed

that of the FFT data. This display is useful for recognising potential solar radio bursts, where a red tip can be seen rising slightly above the green RMS data.

The lower two graphs display the RMS (green) data and FFT (red) data respectively. This is useful when the data are complicated by RFI and it is difficult to determine what is happening in the upper display.

All three displays have shaded areas which indicate night time. The shaded areas are calculated from the geographic coordinates of the observatory and the sunrise and sunset times for the date and location.

### 6.4.4 Multiple Observatory Data Display

The multiple observatory data display enables data from multiple observatories to be displayed in a single window using the same date and time period for each X-axis. This simplifies the visual comparison of the timing and magnitude of events such as HF fade outs and solar radio flares. An example solar radio flare is shown in Figure 6.15. As for the single observatory display, night time is indicated by shaded areas.

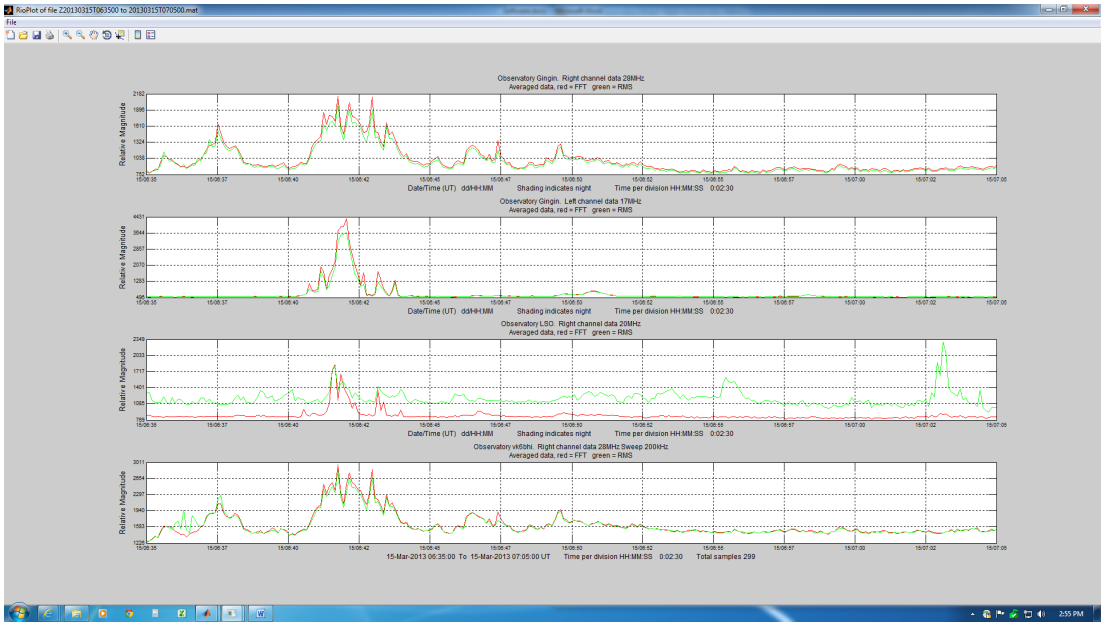

Figure 6.15: RioPlot of multiple observatories showing a solar radio flare recorded simultaneously on all four systems.

Before data can be displayed, two steps are required: step one is to run the 'Collate Data' utility from the GUI File menu which organises the data into monthly files; in step two, using 'Select Data' from the GUI File menu, enter the begin and end times for the data period required. A data file prefixed with a 'Z'

is created and placed in the relevant data directory for each observatory that has data for the period.

From the RioPlot GUI select 'Multiple Observatory' from the 'Plot' menu. As for the single observatory, a list of observatories is displayed, from which the required observatories are selected using the normal Windows methods of Shift plus click or Ctrl plus click. After selecting the year and month for the data period from the selection boxes, a list of data files is presented. The multiple observatory data period prefixed with a 'Z' can now be selected.

The multiple observatory data are displayed in a window with a heading and graph for each observatory. Only the combined RMS (green) and FFT (red) data are displayed, there being two graphs if the observatory has two channels (as in the case of Gingin Observatory, see Figure 6.15). The data are scaled automatically for best fit, but can be changed using the RioPlot GUI.

### 6.4.5 Quiet Day Curve

If the quiet day curve (see Chapter 7) option is ticked, by selecting and clicking the quiet day curve option from the RioPlot GUI plot menu, the QDC is plotted in a separate window for each channel, for the data selected. At least 72 hours of data must be selected before QDC plots are generated. For two channels, the plot windows overlay each other and must be dragged into a suitable position on the screen for viewing.

Function QDC generates the average QDC data by accumulating the data for each sidereal day (Kraus, 1986, p. 2-36) of the data period and dividing by the number of whole sidereal days. The mean start time for each sidereal day of the data is then calculated and returned with the data. Function PlotQDC then plots the averaged sidereal day data vs. right ascension (RA), found from the date, mean start time and the longitude of the observatory, using function Julian (see Kraus 1986, p. 2-27 to 2-29, p. 2-36). Function Julian returns the Julian day (JD), Greenwich mean sidereal time (GMST) and also the local mean sidereal time (LMST) given a date and time in UT and an optional longitude in degrees (positive east) for the LMST. The computations for Julian day and GMST are made using the US Navy formulae from the USNO[6] Astronomical Information Center.

The plot window shows two graphs, the QDC in the upper half of the window and in the lower half, the averaged FFT data, for the time period. Figure 6.16 shows the QDC generated from one month's data, when solar activity and RFI

[6] `http://aa.usno.navy.mil/faq/`

were relatively low. The Y-axis shows relative magnitude with the same scale as for the RMS and FFT data plots. The minimum and maximum points on the QDC are denoted by a black dot and labelled with the local mean time (LMT) at which they occur and the associated RA.

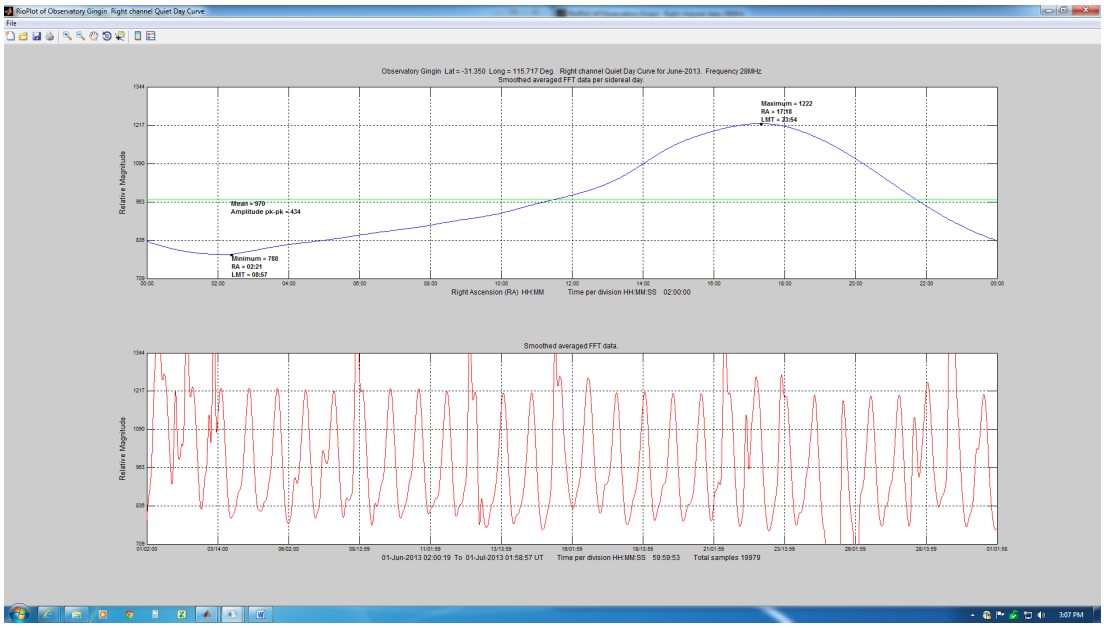


Figure 6.16: RioPlot of the Quiet Day Curve (upper graph) plotted over one sidereal day and derived from the averaged galactic background (lower graph) for the recorded period.

### 6.4.6 Display Features

From the upper graph of the single observatory data display, Figure 6.14, it is possible to zoom in to any part of the data by dragging a box round the data with the left mouse button held down. On releasing the button, a new window opens in the bottom right hand corner of the screen with a plot of the selected data. The zoomed window in Figure 6.17 shows an HF fade out at 22:12 UT on 5 November 2013 due to an X3 class solar X-ray flare which is only just visible in the main display.

Other features, which are part of the Matlab plot environment, are available from the tool bar at the top of the window. Some of these features are not fully functional, e.g. panning does not pan beyond the boundary of the data selected for plotting, however, panning can be useful in conjunction with the Matlab tool bar zoom, as distinct from the zoom feature described above. The data tip item has been customised to show the magnitude and time of selected data points.

This makes measuring the peak intensity and time of a solar radio flare, or the dip in data due to an HF fadeout, a simple matter.

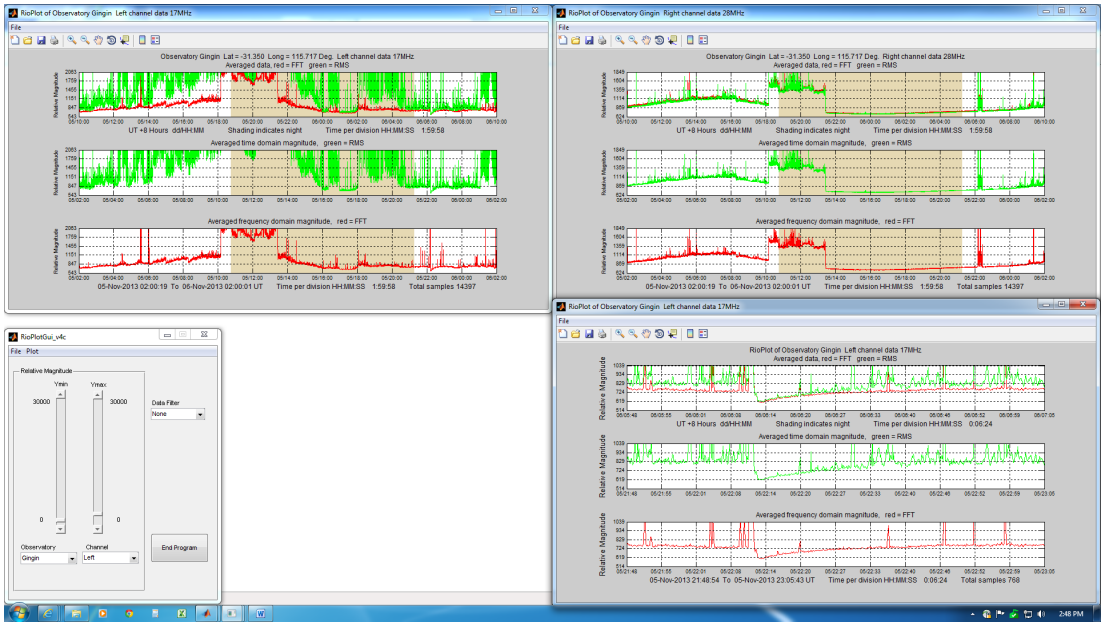

Figure 6.17: Two channel RioPlot wth zoom window (lower right).

## 6.5 RioPlotGui

Like the RioMeter GUI, the RioPlot GUI (Figure 6.18) has sliders to adjust the minimum and maximum values for the Y-axis. Below the sliders are drop down menus for selecting the observatory for multiple observatory displays and the channel (left or right).

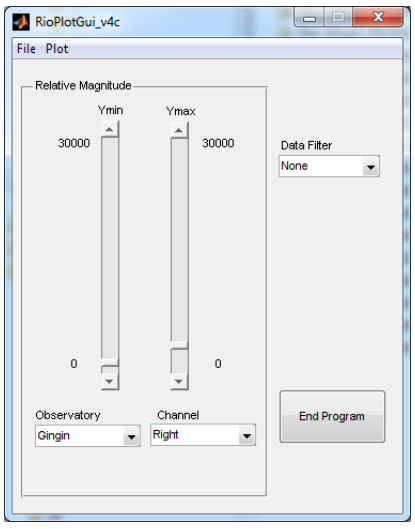


Figure 6.18: The RioPlot GUI.

A filter drop down menu allows the selection of high, medium or low filtering as described for the RioMeterGui. Caution should be exercised when evaluating filtered data, since some spreading of the edges of transients occurs.

### 6.5.1 File Menu Options

#### 6.5.1.1 Collate Data

When selected, this option scans through all the data from all observatories and organises it into a single file for each month for each observatory. No additional user input is required, however the process may take several minutes to complete for large data sets. Having the data organised into a single file for each month simplifies the process of data selection (for multiple observatory plots) where the original data may be in many files, spanning monthly or yearly boundaries and with the possibility that some data are missing.

#### 6.5.1.2 Select Data Period

Having run the collate data procedure above, it is now possible to create a file containing data for any selected time period. The 'Select data period' option produces a prompt window to enter the start/end dates and times as shown in Figure 6.19.

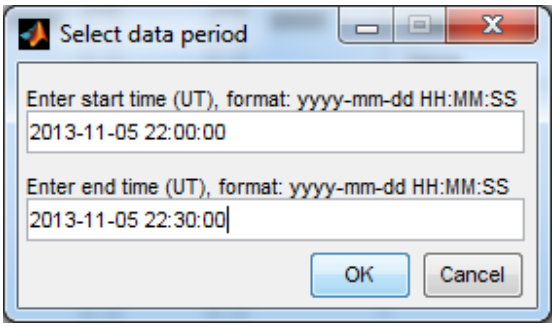


Figure 6.19: Select data period from the RioPlot GUI.

Any data for each observatory, for the time period, is written to a file with the name 'Zyyyymmddhhmmss to yyyymmddhhmmss.mat'. The file is plotted using either the single or multiple observatory options shown above. The 'Z' prefix forces the file to the end of the file list for easier identification.

#### 6.5.1.3 Exit RioPlot

This option closes the RioPlot program, as does the 'End Program' button in the RioPlot GUI. However, in both cases the plot windows have to be closed individually.

### 6.5.2 Plot Menu Options

#### 6.5.2.1 Single Observatory

Plot the data for a single observatory, as described above.

#### 6.5.2.2 Multiple Observatories

Plot the data for multiple observatories, as described above.

#### 6.5.2.3 Quiet Day Curve

Plot the quiet day curve (QDC), as described above.

## 6.6 Summary

The RioMeter software has been running reliably (power and internet connection failures excepted) at all three sites for several years and since the installation of the latest version (January/February 2011), timing issues have been largely resolved. The software now compensates for timing variability in the program loop, however, there are still occasional jumps in timing. These jumps appear to be due to corrections made to the real time clock by the internet time synchronisation utility in Windows, or by the operating system taking excessive time out servicing other tasks. This problem appears worse for older PCs (using Windows XP) in use at the LSO and vk6bhi observatories. Gingin Observatory has a relatively new PC and uses the Windows 7 operating system. More frequent time corrections via the internet may help, but it appears to be impossible to set up the operating system for shorter periods than its current setting of once per week.

Future versions of the RioMeter program may need to take a different approach to time keeping. The current version only saves the full date and time for the start and end of the data recording period. The 'TStamp', in seconds from the start time, is saved with each data sample. The audio data and TStamp are saved in single precision to keep data files as small as possible, whereas the full date and time requires double precision. Double precision requires an extra four

bytes of data which amounts to an extra 57.6 kB of file space over a 24 hour period. This may not sound like much extra space, however, the original concept was to record the RMS and FFT data in single precision resulting in 115.2 kB. Adding the full date and time for each data sample would double this figure. In hindsight and given that at least the time of day needs to be recorded with each data sample, it would have been better to have saved the time of day as the 'TStamp' data instead of the elapsed time since the start of the data period. This is because it is more likely that the date is correct at any instant than the time of day.

Further development of the RioMeter software is required to integrate frequency control for the improved receiver into the RioMeter Gui, but this is beyond the scope of the current project.

The RioPlot software works well for most situations. However, some choices in selection boxes do not behave as expected, so some tidying up of the user interface is required. These defects do not affect the viability of the data, but will take longer to resolve than the time available. Although the 'TStamp' data are now available, there has not been time to incorporate them into the RioPlot program to enable corrections to be made automatically to the data timing.

# Chapter 7

# Results of Observational Programs

In this chapter are presented the results of more than four years of observations. Data are available from all three observatories over most of this period. Some early data may be compromised by timing issues in the earlier version of the RioMeter program, as discussed in chapter 6. Problems with antennas, power and internet connections have also resulted in some data being lost and other data being degraded. These issues are expected as part of developing and commissioning new hardware and software systems.

This chapter starts with a section on RFI (section 7.1) which unfortunately constitutes a large proportion of the recorded data. It is, therefore, useful to categorise the common types of RFI that appear in the data plots of the sections that follow. Section 7.1 includes some examples of RFI and discusses the format of the RioPlot data plots.

The observational results fall into three categories: diffuse galactic background; solar radio flares; and solar X-ray flares. Each category is described separately in the sections that follow.

## 7.1 Radio-Frequency Interference (RFI)

Figure 7.1 shows low-level propagated RFI at 28 MHz. The signals from distant radio stations are propagated by the ionosphere as it is energised by the Sun (Schetgen, 1996, p. 21.11). These signals begin shortly after sunrise, reach a peak during the afternoon and fade away after sunset. This type of RFI is common and is more of a problem at lower frequencies and at times of high solar activity. The diffuse galactic background (DGB) emission, seen in Figure 7.1(a)[1], rises to a peak just before sunrise.

The green Root Mean Square (RMS) (Schetgen, 1996, p. 6.6) trace in the plots show the maximum power of any signals in the receiver bandwidth at any given instant. This green trace shows the presence of one or more narrow-band signals in Figure 7.1(b). These narrow-band signals could be as narrow as a single carrier or maybe as wide as several kHz for voice communications. It can be seen that there are many peaks in the green RMS data that do not appear in the red FFT data. This demonstrates the effectiveness of the DSP filter in the RioMeter software which has removed the narrow-band signals from the receiver bandwidth. The DSP filter is able to do this because the RMS data have been separated out into their various frequency components within the receiver bandwidth by the FFT software. However, as the receiver bandwidth becomes filled with narrow-band signals the DSP filter becomes less effective and the general noise level rises, as can be seen in Figure 7.1(c).

Figure 7.2(b) shows a more extreme case of narrow-band signals with strengths much greater than the DGB indicated at Figure 7.2(d). The frequencies around 17 MHz are heavily populated with commercial broadcasting stations and their signals are propagated strongly by the ionosphere, even under conditions of relatively low solar activity. It can be seen that RFI is starting to build up even before sunrise, as the upper layers of the ionosphere are exposed to ionising radiation from the Sun, and continues for over an hour after sunset.

At 0915UT in Figure 7.2(c) there is a sudden jump in the general noise level indicated by the red FFT plot. This is broadband RFI generated by Gingin Observatory's roof motors and controller. The observatory opens the roof several times per week for the public to view the night sky using the observatory telescopes. Despite efforts to remove the RFI using ferrite suppressors on the motors and control system wiring, a very high noise level remains. It is not possible for the DSP filter to remove this RFI since it fills the entire receiver bandwidth.

[1]The letter in parenthesis following a figure reference refers to an annotation in the plot, explained in the figure caption.

The green RMS trace during this time continues to show the narrow-band signal strength and gradually falls to the same level as the red FFT noise later in the night.

Shown in Figure 7.2(a), at 0200UT, is a short dip in the signal strength to zero. This is the time that the radio PC at Gingin Observatory sends its data, often causing the loss of a few samples of data. Other events such as power failures and times when Windows installs updates and requires a restart of the PC also records zero for the data. Under normal circumstances the receiver output is never zero. Even if the antenna is disconnected, there is still a measurable noise output. Therefore, any zero data indicates that the system is not in operation.

Broadband RFI often starts and ends abruptly and maintains a relatively constant amplitude for its duration. Solar radio flares, on the other hand, tend to start abruptly and rise rapidly to a peak before decaying more slowly, particularly in the latter stages of the event. Figure 7.3(c) shows an extended period of solar activity detected at all three sites followed by a rectangular block of RFI late in the day at the vk6bhi observatory caused by the air conditioner Figure 7.3(e). Other narrow-band local (Figure 7.3(f)) and propagated RFI can be seen in the Gingin Observatory and LSO data , where the green trace exceeds the red. Local RFI is not affected by the ionosphere and therefore persists throughout the day and night.

A recent development at the author's home observatory (vk6bhi) is daily RFI which starts abruptly in the early morning and ends, also often abruptly, during the late afternoon, or as in the example in Figure 7.4(c), late at night. This RFI must be local to vk6bhi since it is broadband at 28 MHz and does not appear in the 28 MHz data for Gingin. The short peak in the Gingin data in Figure 7.4(a) is broadband local RFI since it does not appear in the vk6bhi data. It can also be seen that there is only RFI at the other observatories during this period, since there is no correlation between their data sets.

Broadband RFI occurring at night was investigated in case it was Jupiter noise. However, in most cases no correlation between the data from the three observatories was found and therefore these events were assumed to be local RFI. Those cases which occur shortly after sunset or before sunrise need further investigation to determine whether they are propagated solar emissions or Jupiter noise.

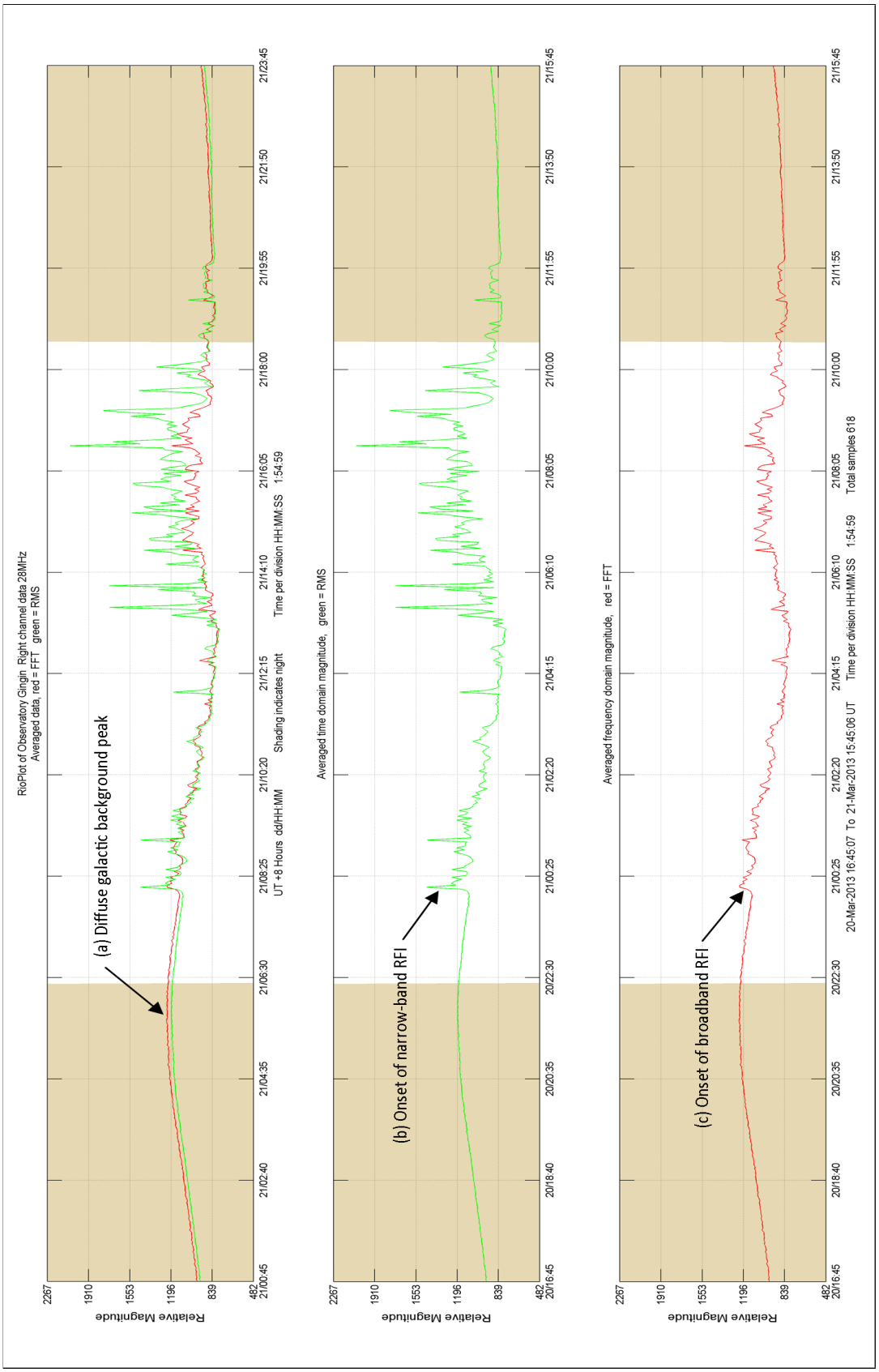


Figure 7.1: 28 MHz narrow-band (green) and broadband (red) propagated RFI. (a) The DGB diurnal cycle peaks; (b) A late onset of narrow-band RFI; (c) Broadband RFI.

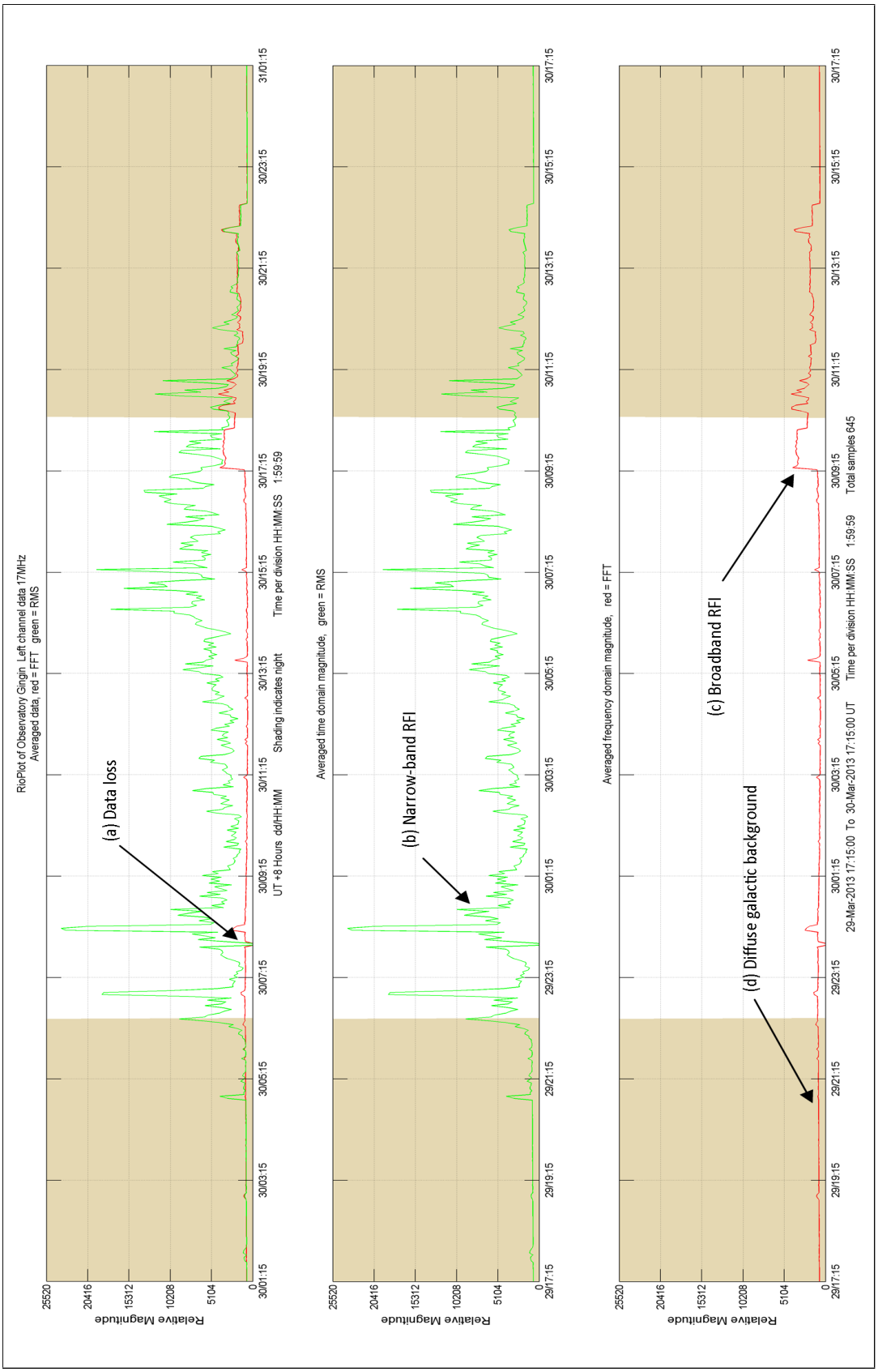


Figure 7.2: 17 MHz narrow-band (green) propagated, and local broadband (red) RFI. (a) Data lost during internet data transfer; (b) Propagated narrow-band RFI; (c) Local broadband RFI from the observatory roof motors; (d) The diffuse galactic background.

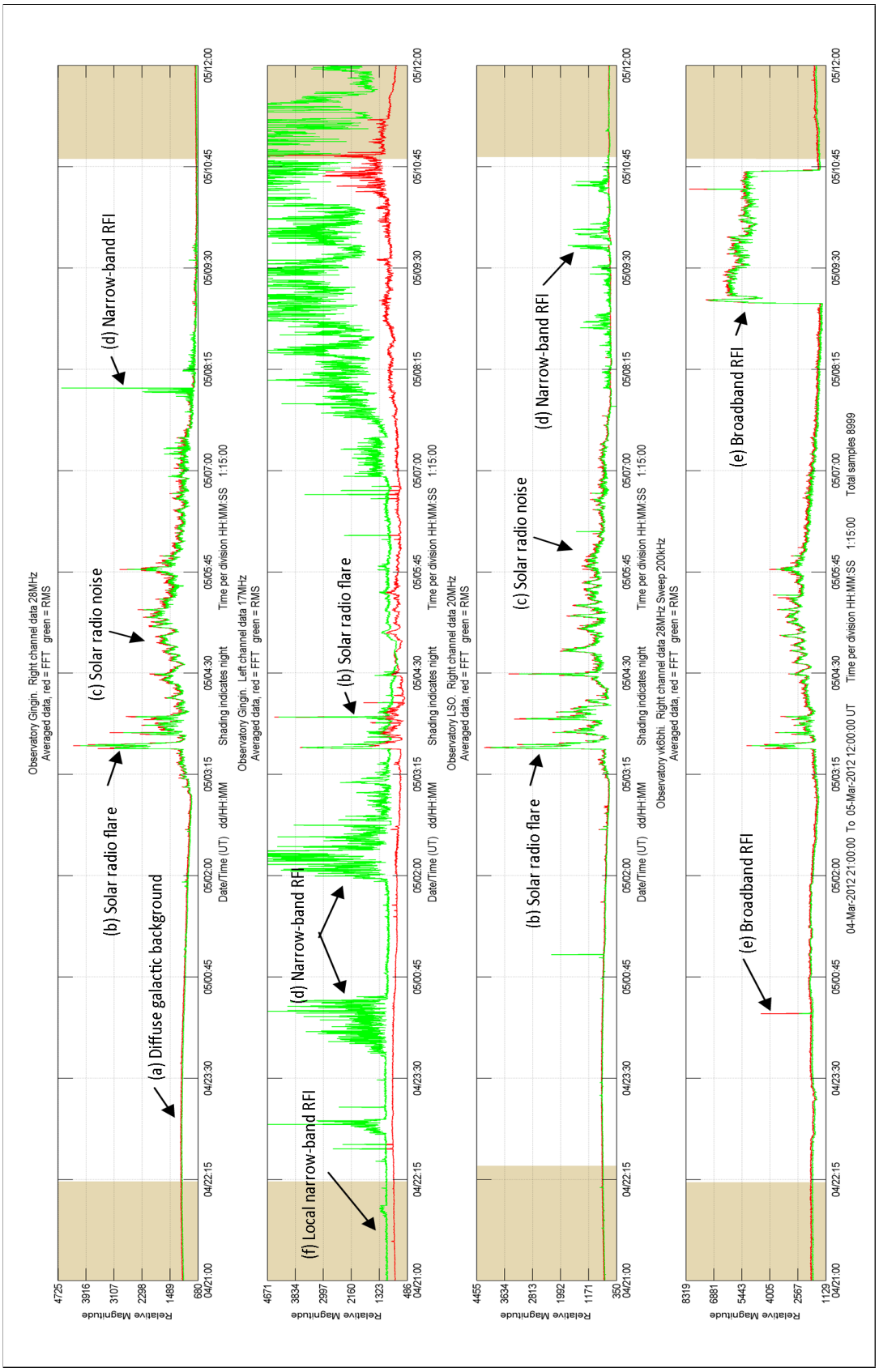


Figure 7.3: Examples of RFI and solar activity. (a) Diffuse galactic background; (b) Solar radio flares showing the typical red tip; (c) Broadband solar radio noise; (d) Narrow-band RFI which does not have the red tip; (e) Broadband RFI which starts and ends abruptly; (f) Persistent local narrow-band RFI.

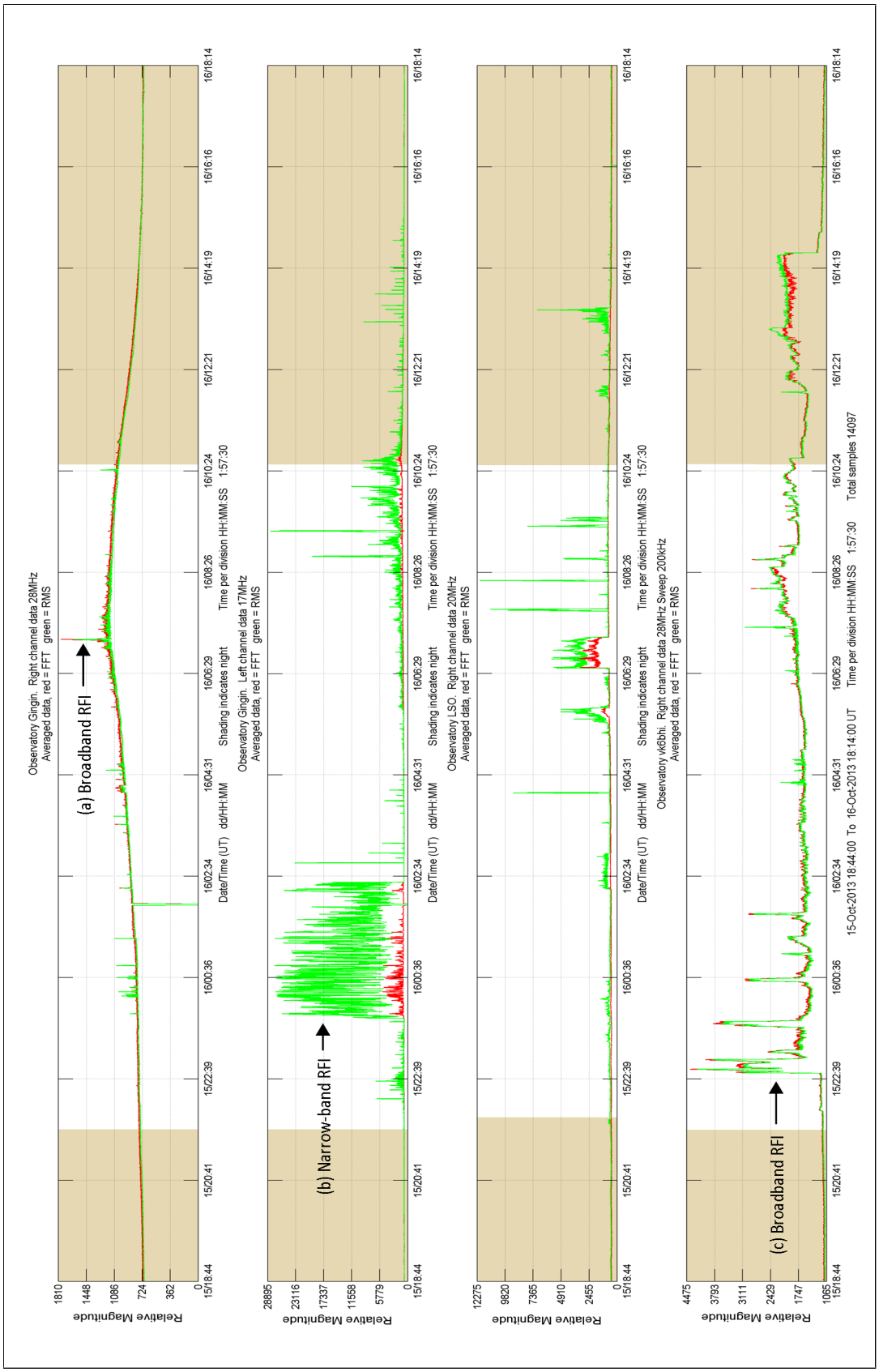


Figure 7.4: Narrow and broadband RFI for all observatories. (a) Broadband RFI local to Gingin; (b) Narrow-band RFI; (c) Broadband RFI local to vk6bhi.

## 7.2 The Diffuse Galactic Background (DGB)

The diffuse galactic background (DGB) can be detected most of the time and is only blocked from view to a greater or lesser extent by changes in the ionosphere. The DGB consists of the sum total of all the emissions from all the many radio sources in our galaxy and beyond. Due to the wide field of view of the simple radio telescope' (SRT) antenna ($\approx 60°$) it is not possible to identify any particular individual source. However, it was found that the DGB varies in intensity in a diurnal cycle which is synchronous with the sidereal day. The peak in DGB occurs when the galactic centre (declination $\approx -28°$) is overhead the antennas located at latitude $\approx -22°$ and $\approx -32°$. The null in DGB occurs in a direction generally away from the galactic centre but not exactly 180° away.

The strength of the received DGB varies depending on the amount of absorption in the ionosphere and is therefore dependant on solar activity. During periods of high solar activity it may be difficult to detect the DGB, especially at low frequencies where propagated RFI can be a problem. Under these conditions a true representation of the DGB is not received and the curve traced by the DGB strength (power) vs. sidereal time becomes distorted. To get a true representation of the DGB the curve needs to be plotted when solar activity is low, i.e. when the Sun is quiet. This curve is, therefore, referred to as a 'quiet day curve' (QDC) and this topic is covered in more detail later in this chapter.

Figure 7.5 shows several days of data recorded at all three sites where the diurnal cycle of the DGB is clearly visible, but affected by propagated RFI during the daylight hours and local RFI during night time. It can be seen that the propagated RFI is more significant at 17 MHz than at 28 MHz. These data were recorded a little over a year after the start of cycle 24, while solar activity was still low. At this time the Gingin Observatory antennas had not been upgraded and more local RFI suppression was required, so the DGB is not as clear as it could be. The LSO system, however, had just been completed with good results. The DGB during a period of low solar activity near the peak of cycle 24 is shown in Figure 7.6. Unfortunately by this time the LSO antenna system and local RFI had deteriorated from its best performance early in the cycle and during 2011. However, the Gingin Observatory antenna system had been upgraded and an isolator switch fitted, which cuts the AC power to the roof motor drive system and prevents the generation of RFI when the retractable roof is not in use. Observatory vk6bhi is affected by suburban RFI and, in particular, air conditioning systems.

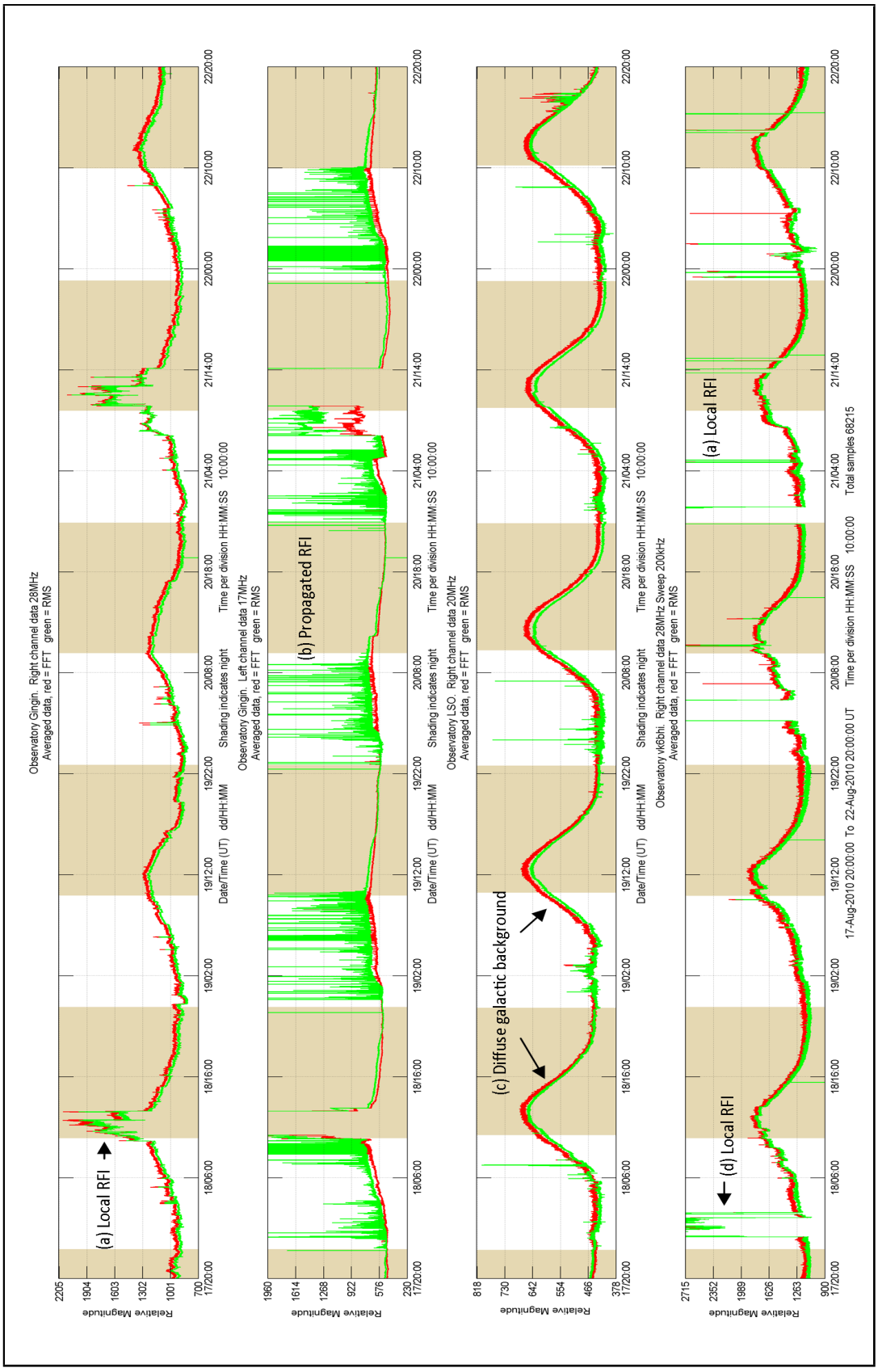


Figure 7.5: The diurnal cycle of the DGB early in solar cycle 24. (a) RFI from roof motor drive system; (b) Narrow-band propagated RFI; (c) The diurnal cycle of the DGB; (d) RFI from air conditioning.

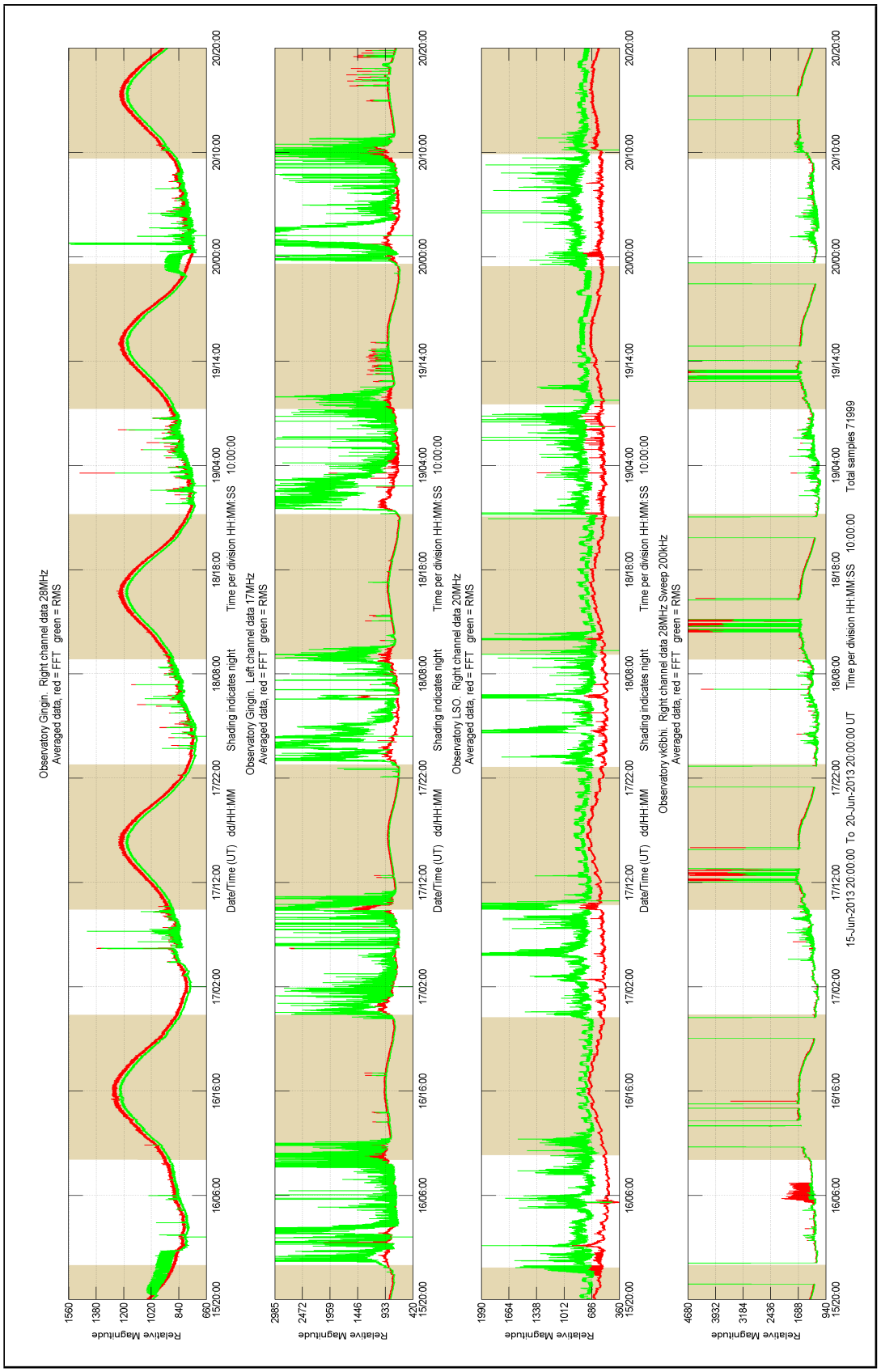


Figure 7.6: The diurnal cycle of the DGB mid solar cycle 24 is clearly visible in the Gingin 28 MHz data. Gingin 17 MHz and LSO data are heavily affected by propagated RFI (green) during daylight hours and vk6bhi data are affected by broadband air conditioner RFI during night time.

### 7.2.1 The Quiet Day Curve (QDC)

The QDC is a plot of the power of the diffuse galactic background emission vs. right ascension (RA). In the plots, the signal power is not calibrated and is therefore shown as a relative magnitude. At least three days of data must be selected, which are then averaged and filtered to remove RFI, to create the QDC. From the time that the data were recorded and the location of the observatory, it is possible to plot the data in RA. The maximum and minimum of RA in hours and minutes and the local mean time (LMT) are then annotated on the plot. The LMT is the mean time of the data period used to create the QDC and also the time used when determining the RA. The LMT shows the local time of day in hours and minutes for the maximum and minimum of the DGB emission. Also plotted is the mean of the QDC and the magnitude of the peak relative to the minimum.

Figures 7.7, 7.8 and 7.9 show the QDCs, using the best data available, for each of the sites. Ideally, the data used to create the QDC would have no solar emission or RFI, local or propagated, and would consist of the diffuse galactic background only. The nearest to this ideal that can be achieved is to use data from a period when the Sun is quiet (a solar minimum) and when the maximum of the DGB occurs at night. Choosing a period when the DGB peaks at night ensures that the solar and ionospheric effects are at a minimum and therefore the peak DGB should be most accurately represented. Unfortunately the night time data in June for vk6bhi observatory is spoiled by air conditioner RFI and the best data that could be found is from September 2010. The galactic centre is overhead during the early evening at this time of year and therefore the data are likely to have been affected by propagated RFI and distortion due to the ionosphere.

All three plots show a strong peak in DGB. For Gingin Observatory this occurs at RA equal to 17 hours 18 minutes and for LSO and vk6bhi close to 18 hours. This peak in emission matches quite closely with the galactic centre and Sagittarius A at RA 17 hours 42.9 minutes (declination $-28°$ 50 minutes) shown in the California Institute of Technology list B (CTB) from Kraus (1986, p. A-15). The minimum of the QDC is quite shallow and occurs close to RA 03 hours 16 minutes for LSO and vk6bhi. The observed minimum for Gingin Observatory is at RA 02 hours and 33 minutes which, as for the peak, is approximately 42 minutes ahead of the other two sites. The observed minimum is not diametrically opposite the maximum on the sky which suggests some other source or sources of emission are present in that direction. From the California Institute of Technology list A (CTA) and list B (CTB) (Kraus, 1986, p. A13 - A14) there are two potential

candidates: Centaurus A and Vela X, both of which have very high flux densities and are well within the field of view of the antennas at approximately $-45°$ declination. However, some distortion of the QDC could be caused by RFI which occurs daily at the same time of day. To test this the QDC was plotted for the time of year when that part of the sky falls during the night. Figure 7.10 shows the QDC when RA 10 hours falls around midnight local time at Gingin Observatory. No significant change in magnitude of the QDC around RA 10 hours can be seen. Therefore, it is concluded that the higher than expected emission background is due to a celestial radio source or sources, rather than RFI.

From the appearance of the radio sky brightness map at 30 MHz (Mathewson, Broten, & Cole, 1965) and 250 MHz (Kraus, 1986, p. 8.3), it can be seen that the brightness distribution of the galactic centre is elliptical in nature with brightness peaking earlier in RA for lower declinations than for higher declinations. The peak in RA occurs at approximately 17 hours 40 minutes for a declination of $-31°$ and approximately 18 hours for a declination of $-22°$. Since the observatory latitudes are $-31.85°$, $-31.35°$, and $-22.22°$, for vk6bhi, Gingin and LSO respectively, it is expected, therefore, that the vk6bhi and Gingin data would peak earlier than the LSO data. Assuming a similar brightness distribution to that at 30 MHz for 17, 20 and 28 MHz and allowing for the difference in declination of antenna pointing (due to the difference in physical location of the observatories) accounts for most of the differences in the observed data. The remaining discrepancies for the observed variation in RA for the galactic background peak at the three sites are most likely explained by RFI affected data, distortion of the antenna radiation pattern caused by the close proximity of metal objects, errors in alignment of the dipoles or in the case of Gingin Observatory, interaction between the 17 and 28 MHz antennas. However, these errors in RA are relatively small, being approximately $+1$ minute for LSO, $-22$ minutes for Gingin and $+21$ minutes for vk6bhi which equate to 0.25, 5.5 and 5.25 degrees of antenna pointing respectively. Or in terms of beam width 0.4%, 9.2% and 8.8%. These results are perhaps, not surprising, since the antenna at LSO is on open ground well away from buildings whereas at Gingin the antennas are in close proximity to the observatory building and for vk6bhi the house guttering and a metal garage.

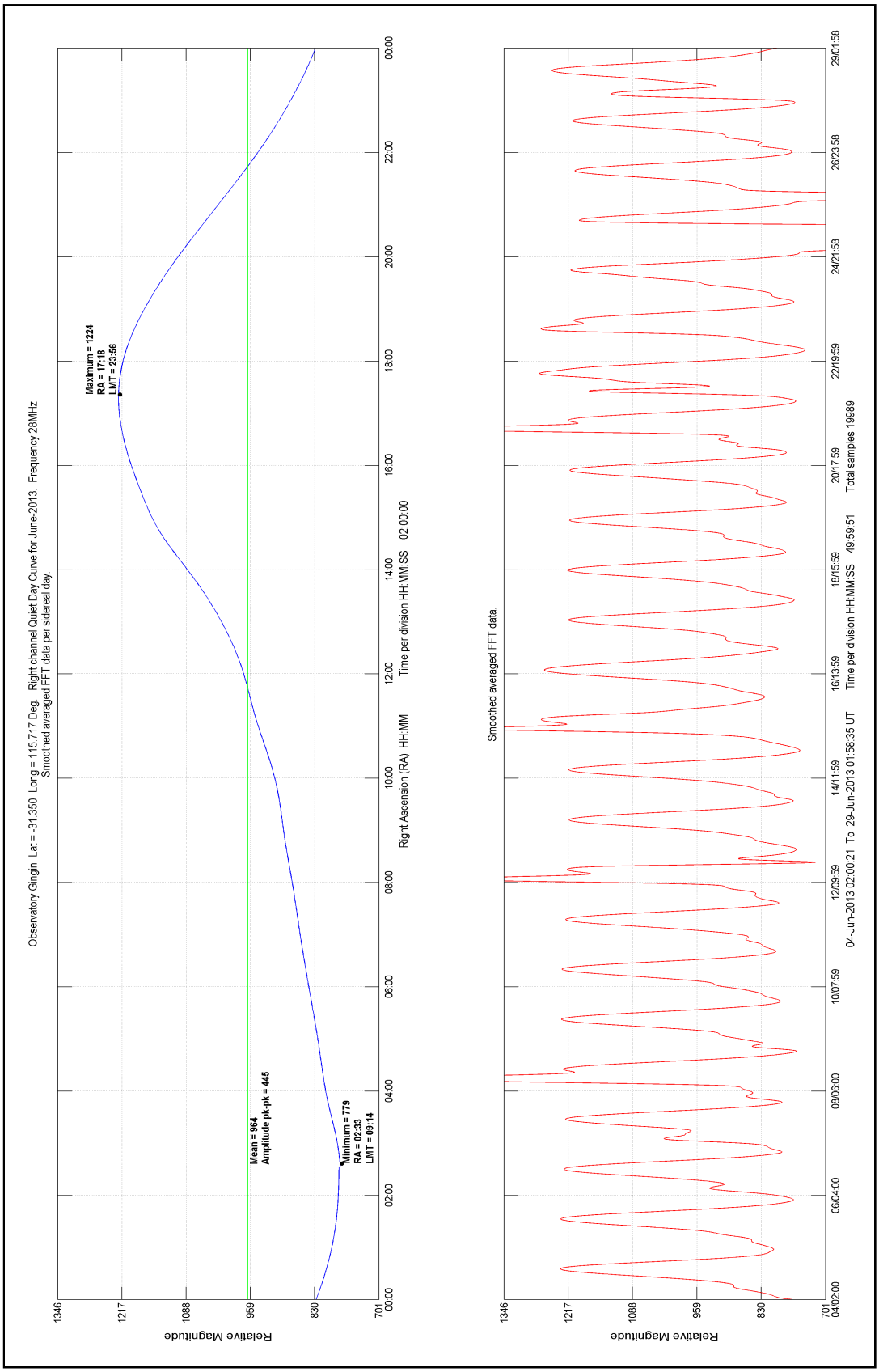


Figure 7.7: Gingin Observatory QDC (blue) and the smoothed diurnal cycle of the DGB (red) for June 2013. The mean maximum of the DGB occurs at RA 17 hours 18 minutes and the mean minimum at RA 2 hours 33 minutes.

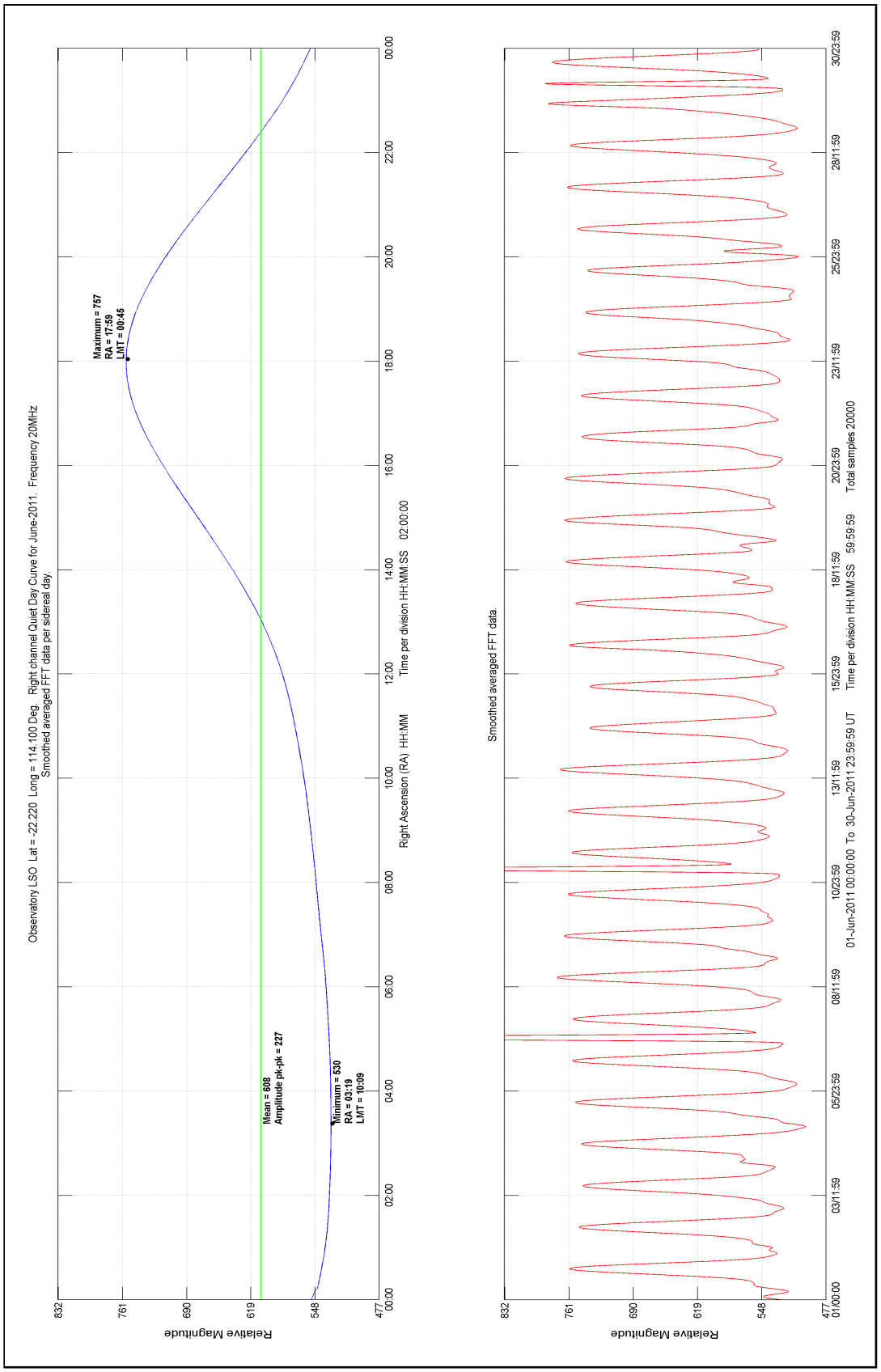


Figure 7.8: Learmonth Solar Observatory QDC (blue) and the smoothed diurnal cycle of the DGB (red) for June 2013. The mean maximum of the DGB occurs at RA 17 hours 59 minutes and the mean minimum at RA 3 hours 19 minutes.

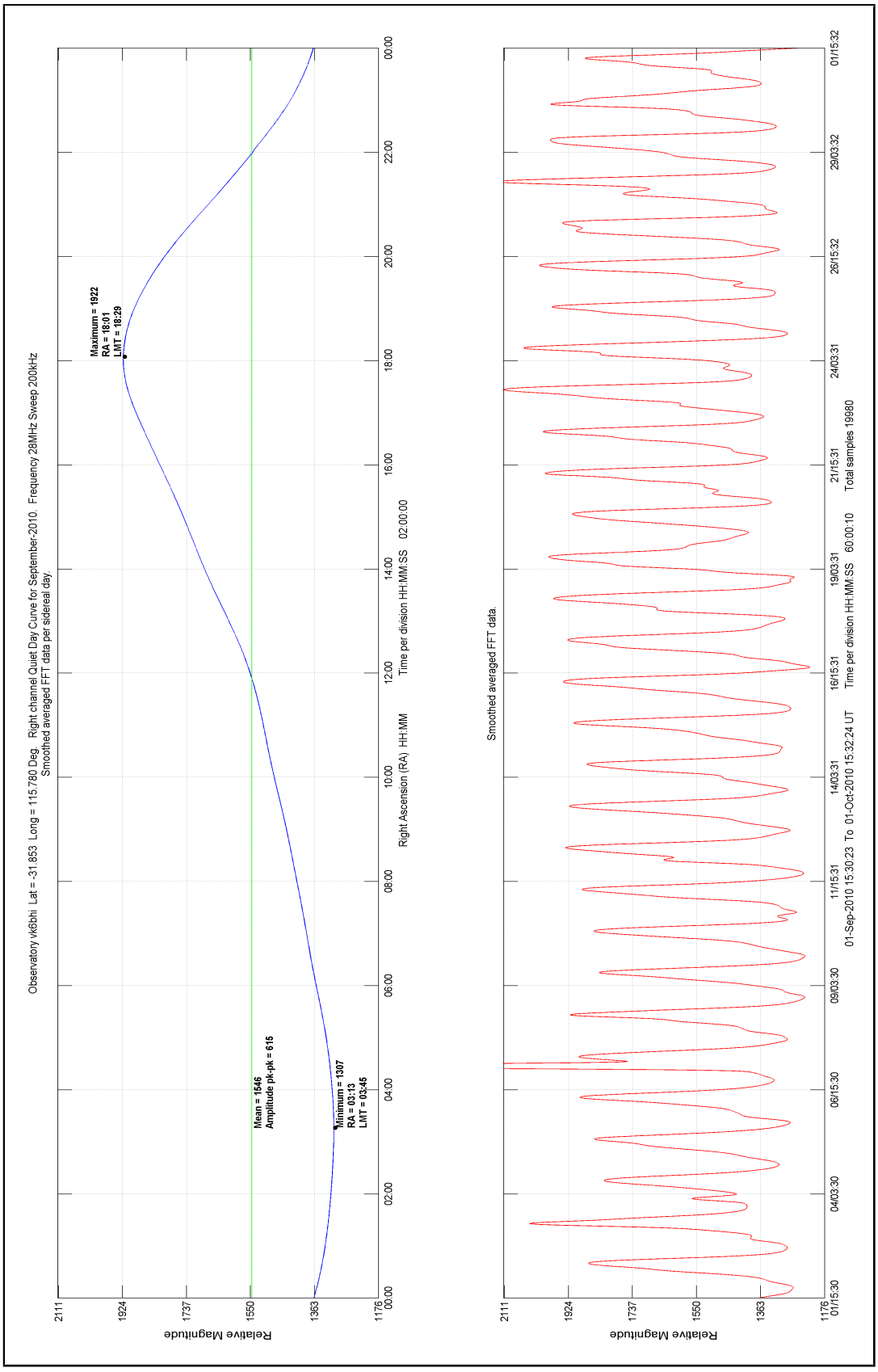


Figure 7.9: VK6BHI observatory QDC (blue) and the smoothed diurnal cycle of the DGB (red) for September 2010. The mean maximum of the DGB occurs at RA 18 hours 1 minute and the mean minimum at RA 3 hours 13 minutes.

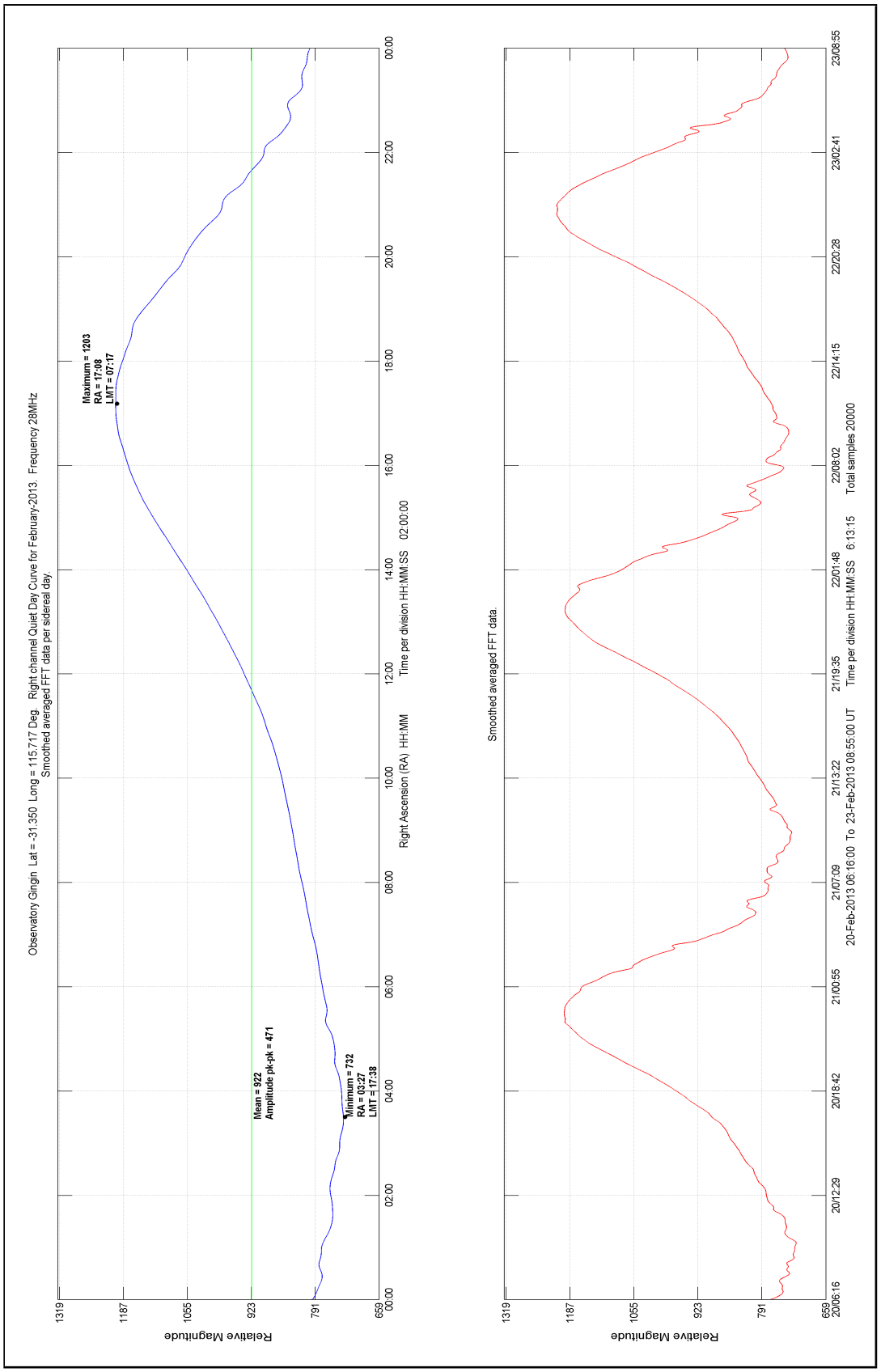


Figure 7.10: Gingin Observatory QDC (blue) and the DGB (red) for RA 10 hours occurring around midnight in February 2013. The magnitude of the QDC at RA 10 hours is not significantly different from the QDC at RA 10 hours in Figures 7.7, 7.8 and 7.9.

## 7.3 Solar Radio Flares (SRF)

Solar radio flares, or 'bursts' as they are often referred to (Gopalswamy, 2004), are by far the most frequent form of solar emission detected by the simple radio telescopes (SRTs). They usually only last between half a minute and two to three minutes and are characterised by a rapid rise and slow decay in intensity. The radio emission is a broadband noise often extending over a frequency range of 25 to 180 MHz, as indicated on the Learmonth Solar Observatory's (LSO) solar radio spectrograph (SRS), and down to 17 MHz as shown in the Gingin data. The frequency range of individual SRFs is quite variable, such that a strong emission between 25 and 70 MHz does not show up in the 17 and 20 MHz data and fades quickly in the SRS data beyond 70 MHz. The signal strength of these emissions is also very variable and are classified at LSO as minor, significant or major and indicated by yellow, red and green respectively on a blue background in the SRS data. More precise calibration is not attempted due to the variability of absorption in the ionosphere at these frequencies. The SRTs have detected SRFs with signal strengths a small fraction of the peak diffuse galactic background emission strength to many times this strength.

SRFs are non-thermal radio emissions (e.g. gyrosynchrotron, cyclotron maser or hybrid-wave emission (Pick & Trottet, 1988)) from the Sun, generated by the interaction of electrons with magnetic fields in the solar plasma and are usually associated with sunspots and filaments (Gopalswamy, 2004; Wild, 1969). A detailed description of the complex mechanisms that generate SRFs is outside the scope of this work and the reader is directed to the many papers published on this subject (Dulk, Leblanc, & Bougeret, 1999; Gopalswamy, 2003, 2004; Kundu & Stone, 1984; Pick & Trottet, 1988; Sheridan et al., 1973; Thompson et al., 1996; Van Haarlem et al., 2013; Wild, 1969; Wild & Smerd, 1972) and references therein. There are several types of SRF, usually designated as TypeII, TypeIII, TypeV etc. The general features of the common types of SRF are summarised below:

**TypeI** are short duration bursts that make up noise storms when superposed on a continuum emission and are typically not associated with any eruption (Gopalswamy, 2004).

**TypeII** bursts are associated with suprathermal electrons accelerated at magnetohydrodynamic shocks to speeds of 400-2000 km $s^{-1}$ (Bowman et al., 2013). They are characterised by their gradual drift from high to low frequencies, a harmonic at twice the fundamental frequency that is almost

always stronger than the fundamental (Thompson et al., 1996) and are generally accompanied by a large flare (Wild & Smerd, 1972).

**TypeIII** are the most common and are due to bursts of electrons moving at speeds of the order of one-third of the speed of light, produced in magnetic reconnection sites during solar flares (Bowman et al., 2013); are characterised by their brief duration and rapid drift from high to low frequencies (Wild & Smerd, 1972).

**TypeIV** long-lasting continuum emissions are produced by non-thermal electrons trapped in moving or stationary structures (Gopalswamy, 2004). Moving TypeIV bursts are emitted from sources of meter-wave continuum radiation and their spectrum is often featureless and confused with other emissions (Wild, 1969; Wild & Smerd, 1972). The emission is broadband and results from trapped electron populations (Cane, Erickson, & Prestage, 2002).

**TypeV** is a continuum emission that often follows intense TypeIII bursts and dominates the decay phase (Cane et al., 2002; Cane & Reames, 1990; Pick & Trottet, 1988).

TypeII and/or TypeIV radio emissions are associated with filaments and coronal mass ejections (CME)(Pick & Trottet, 1988). Filaments are formed from material supported by magnetic fields and these magnetic fields eventually become unstable and the material either collapses onto the surface of the Sun or is hurled through the Sun's atmosphere and escapes the Sun's gravity to become a CME (Gopalswamy, 2003). In the case of a CME, the progress of the magnetic field and material through the Sun's atmosphere produces TypeII electromagnetic radiation which decreases in frequency with altitude (Gopalswamy, 2004). By measuring the rate of change of the frequency, it is possible to estimate the velocity of propagation of the CME.[2] This information can be used to predict the likely arrival time for Earth directed CMEs.

The types of burst most readily identifiable with the SRT and described in the following pages are TypeII, TypeIII and TypeV SRFs. TypeI bursts are not readily detected by the SRT, due to their duration being less than the averaged sample time of the RioMeter software, unless they occur in large numbers as part of a noise storm within the frequency range of the SRT. Also, TypeIV contin-

[2]See the TypeII tool at `http://www.ips.gov.au/Solar/4/3`

uum emissions generally occur at frequencies above the range of the SRT and, therefore, are not detected.

Figure 7.11 shows the simultaneous recording of several TypeIII flares at all observatories and Figure 7.12 shows the same flares as they were recorded on the Learmonth SRS. The more intense of the TypeIIIs in Figure 7.11 exhibit a sharp rise in intensity followed by a more gradual decay. This is a characteristic observed for many examples of this type of flare recorded in the SRTs' data.

Less common than the TypeIII, but still often observed is the TypeV shown in Figure 7.13 and also on the Learmonth SRS as shown in Figure 7.14. The identification of both the TypeIII and TypeV are confirmed from similar spectrograph data obtained by Prestage et al. (1994). The TypeV is characterised by an extended period of activity (continuum) after the initial burst (Prestage et al., 1994). This extended activity is confined mainly to the lower frequencies, as can be clearly seen in the Learmonth SRS data of Figure 7.14. The SRTs' data show that this type of flare has a similarly sharp rise in intensity as the TypeIII but the decay is slower, starting from the peak, and continuing through to the lower frequencies, as can be seen in Figure 7.14.

TypeII solar radio flares most usually occur at times of solar maximum and the examples shown in Figures 7.15 and 7.16[3] are no exception. Although the current solar maximum (cycle 24) is weaker than predicted. The identifying features of the TypeII are its second harmonic and the decrease in frequency over a period of several minutes (Gopalswamy, 2004; Prestage, 1995). Figure 7.16 shows several TypeIIIs and a TypeV preceding the onset of the TypeII at approximately 0507UT. It is not until 0510UT that the TypeII starts to show up in the SRTs' data (Figure 7.15) on 28 MHz and reaches a peak at approximately 0513UT. Figure 7.16 shows that there are two major bands of active frequencies during the 0507UT to 0515UT time period. The upper frequency group is the second harmonic of the lower group and both groups decrease in frequency substantially over the time period. In Figure 7.15, the data for LSO at 20 MHz is showing a peak around 0517UT and a faint trace of the second harmonic at 40 MHz is visible in the SRS data. Then, referring to the Gingin data at 17 MHz, also in Figure 7.15 there appears to be a slight increase in noise (red FFT data) at 0519UT and this corresponds with 34 MHz for the second harmonic, which can also be seen in the SRS data.

[3]Sensitivity of the LSO SRS is reduced over the range 25 to 75 MHz to prevent RFI overload and this leads to the apparent discontinuity at 75 MHz in Figure 7.16.

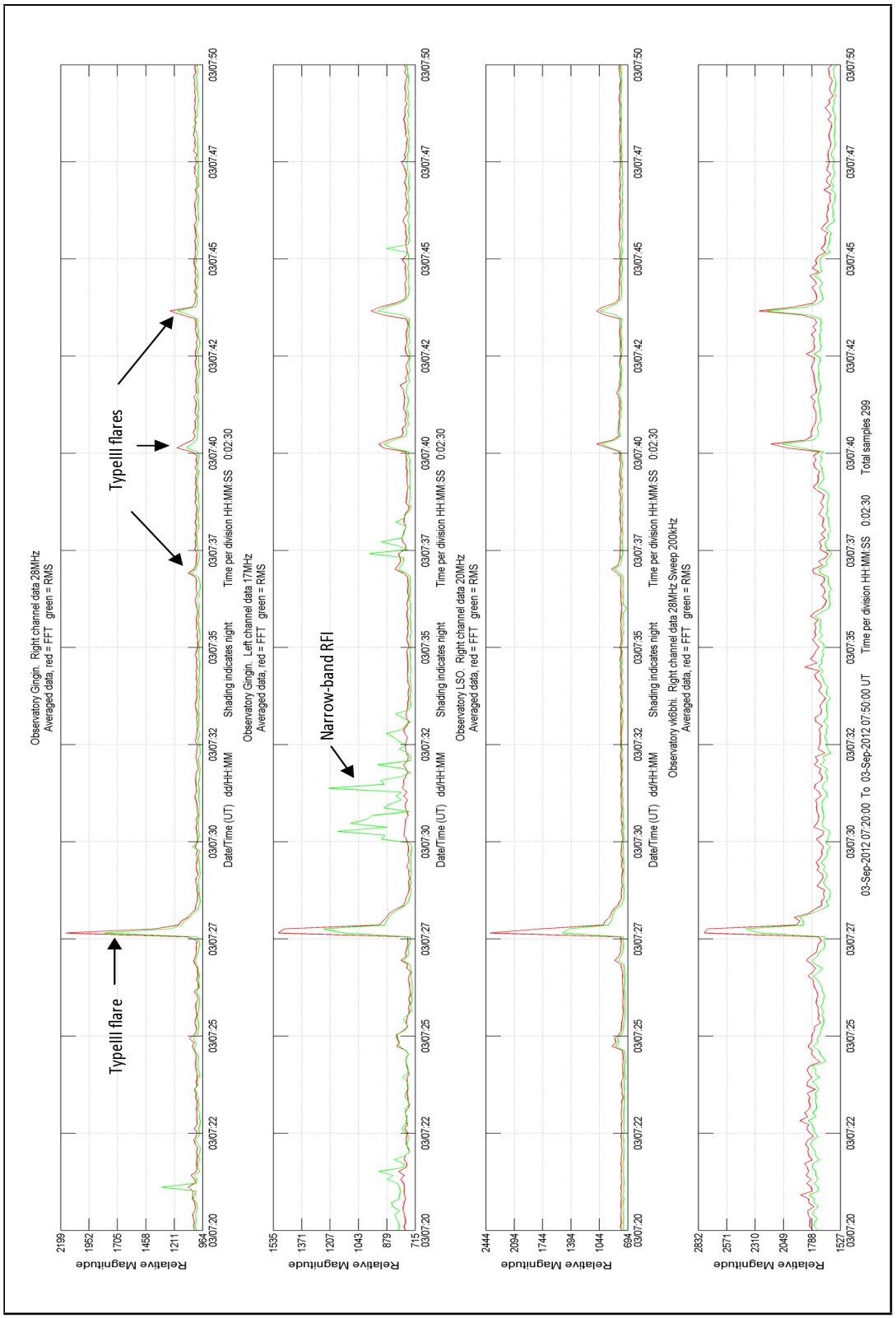


Figure 7.11: Simultaneous TypeIII solar radio flares at all three observatories. Note the sharp rise and more gradual decay of the stronger flare at 0727UT.

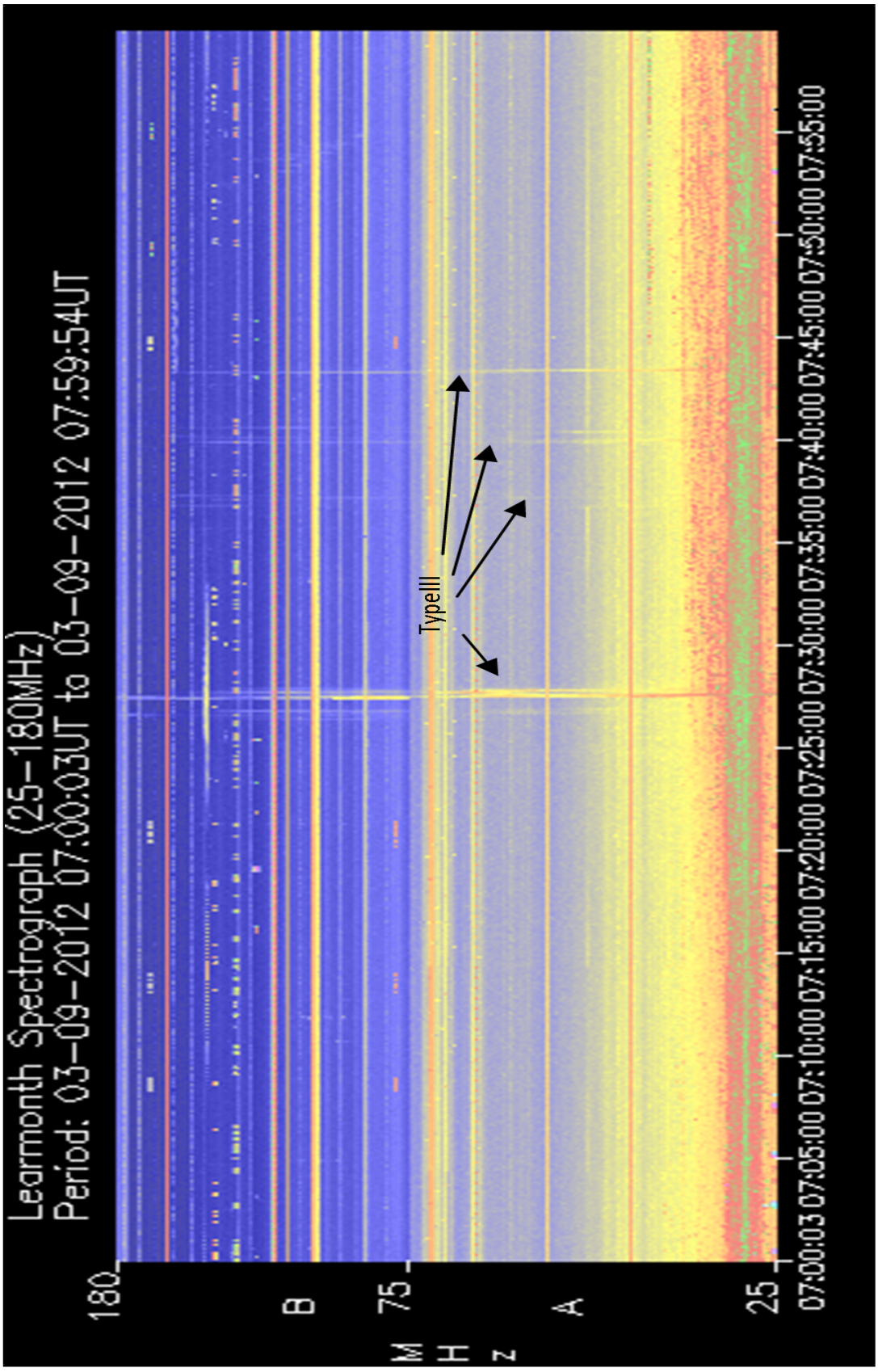


Figure 7.12: LSO SRS display of TypeIII solar radio flares. The main TypeIII flare at 0728UT is preceded by a faint TypeIII at 0727UT and followed by a further three TypeIIIs at 0737UT, 0740UT and 0744UT.

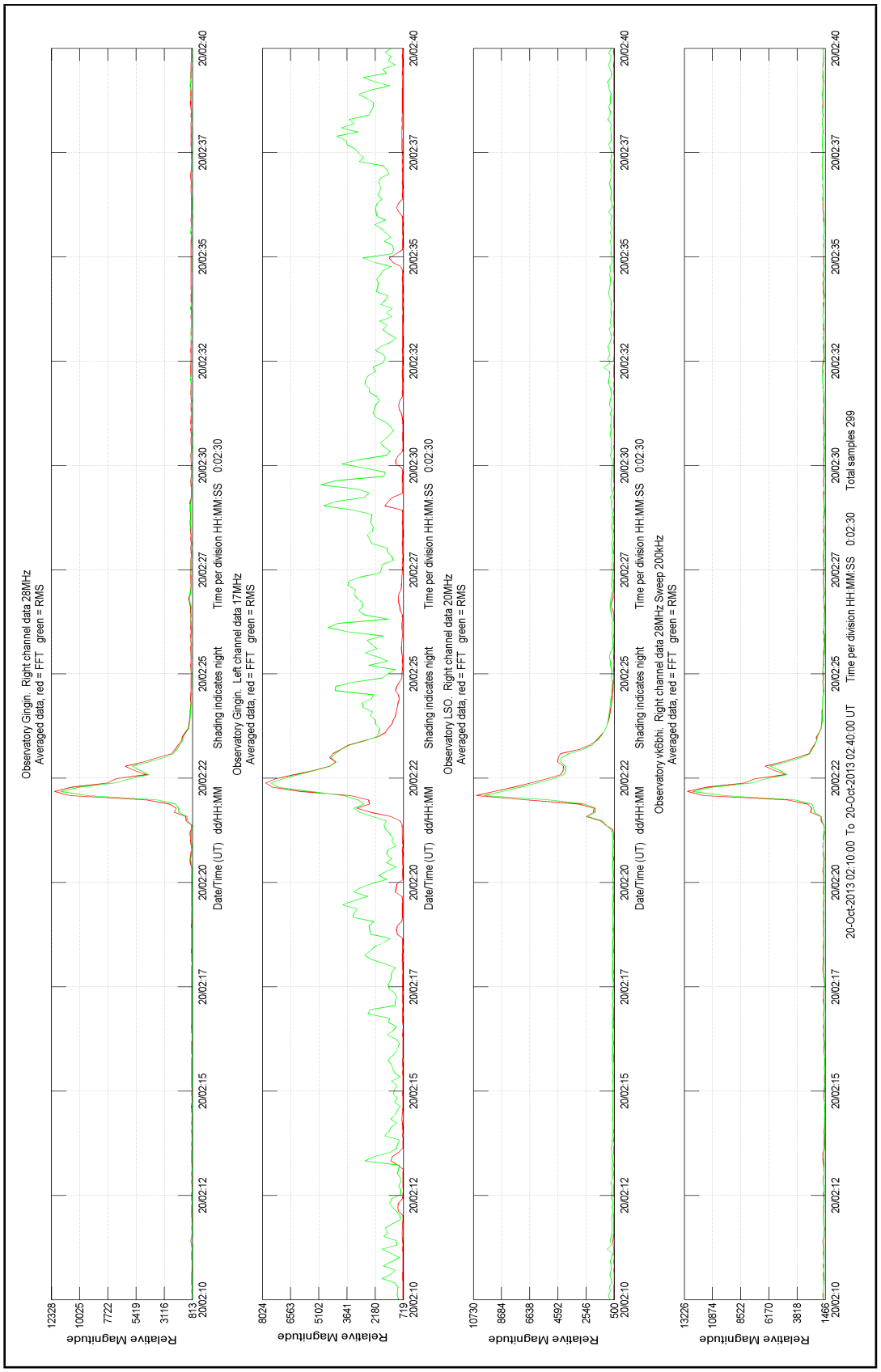


Figure 7.13: A TypeV solar radio flare showing the broad continuum characteristic of this type of flare. It can also be seen that the flare continues for longer at the lower frequencies of 20 MHz (LSO) and 17 MHz (Gingin).

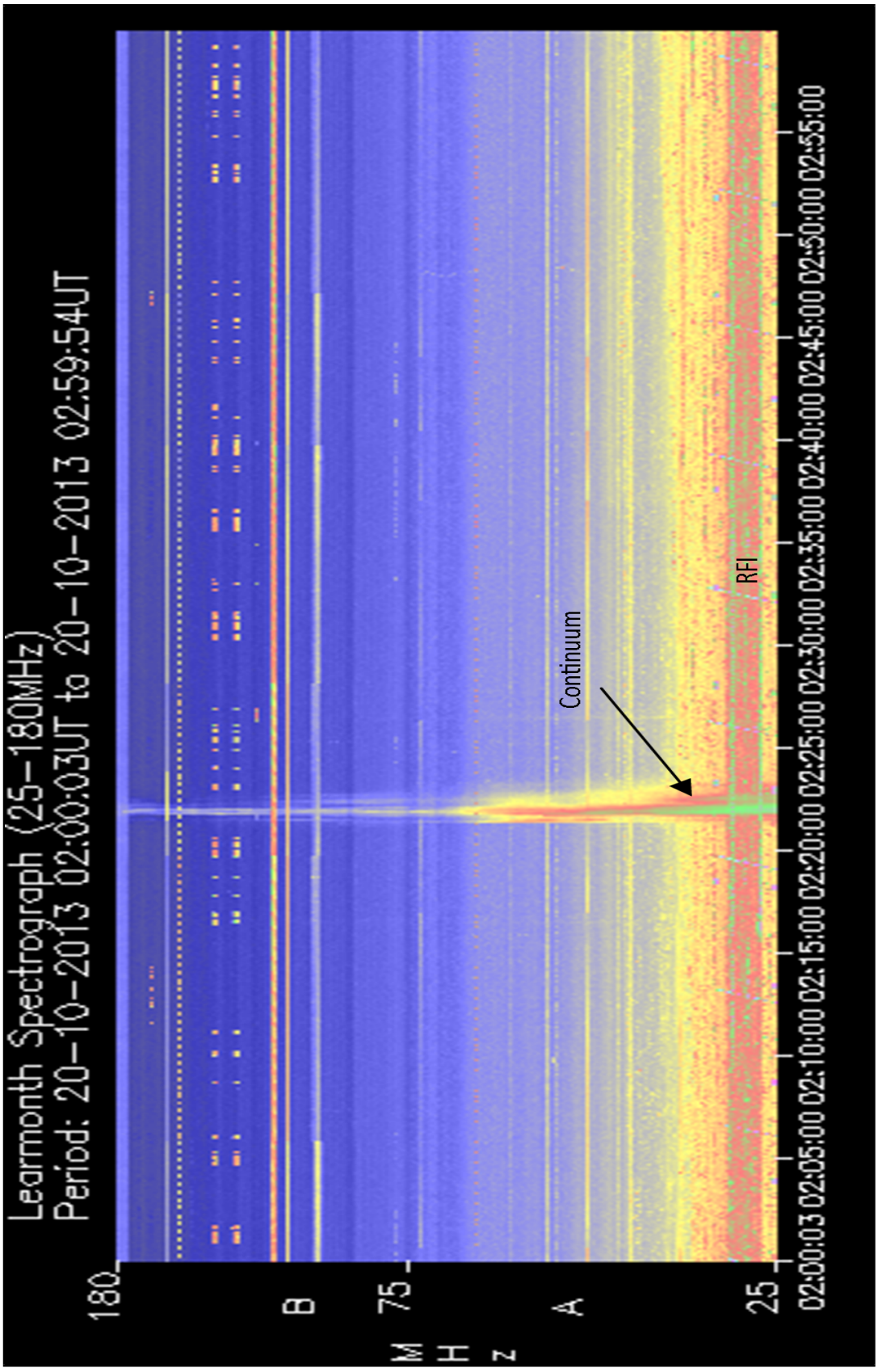


Figure 7.14: LSO SRS display of a TypeV solar radio flare showing a broad continuum lasting approximately two minutes at the lower frequencies.

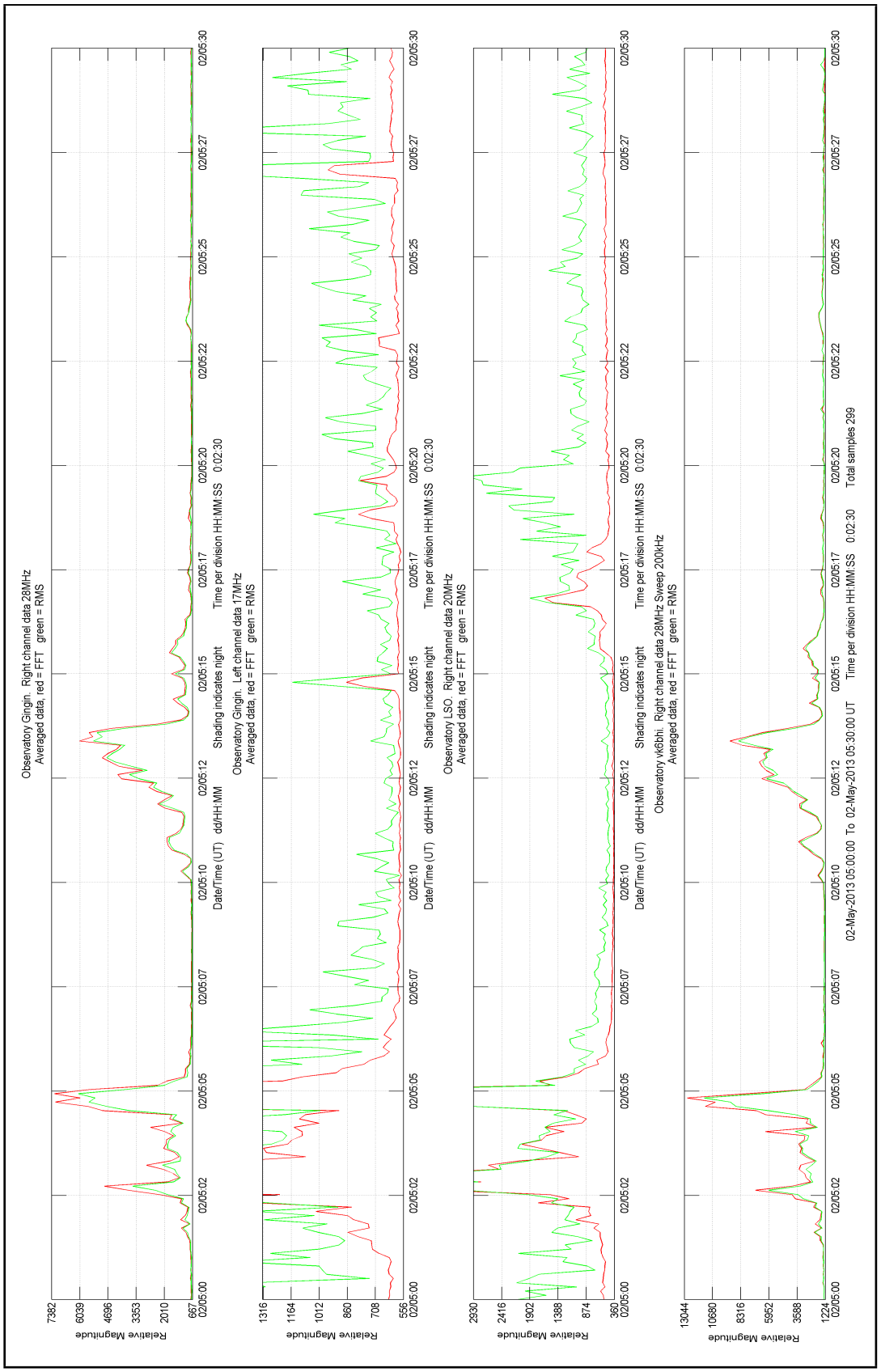


Figure 7.15: A group of TypeIII flares and a TypeV ends at approximately 0506UT and precedes the TypeII flare which begins at 0510UT at 28 MHz. The TypeII flare appears later in the LSO 20 MHz data at approximately 0517UT and in the Gingin 17 MHz data approximately one minute later.

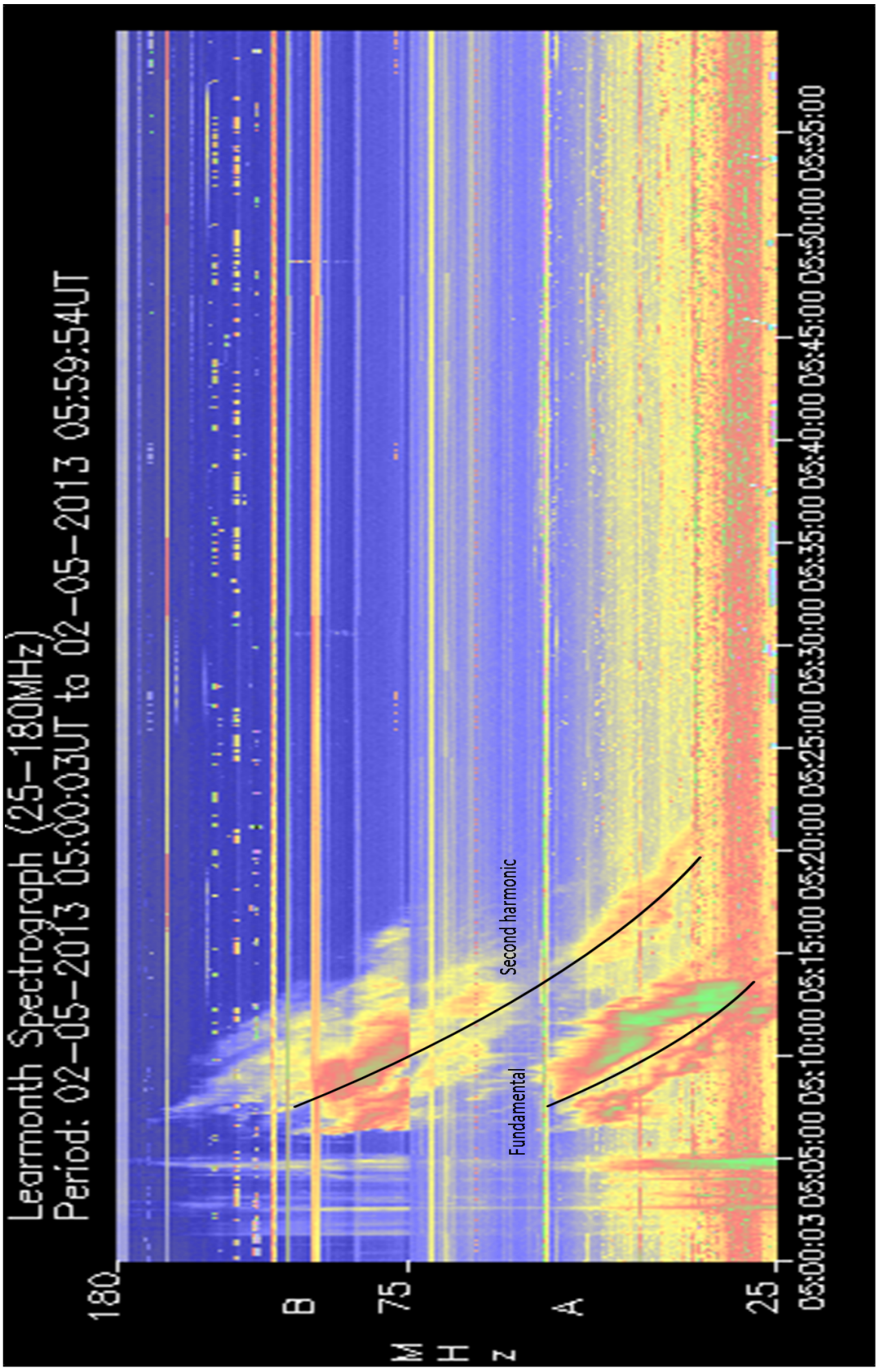


Figure 7.16: A group of TypeIII flares ends at approximately 0504UT followed by a TypeV at 0505UT. The TypeII flare starts at approximately 0507UT and is lost in RFI at approximately 0522UT. The fundamental and second harmonic frequency groups are indicated by the black lines.

The Gingin 17 MHz data and LSO data are both affected by narrow-band RFI which is shown in the green RMS trace (Figure 7.15). However, it was possible to magnify the y-axis in these plots to reveal the low-level progression of the fundamental down in frequency. It can be seen that the narrow-band RFI diminishes significantly for the duration of the TypeII flare and for a short period thereafter. The LSO SRS (Figure 7.16) also shows a reduction in RFI for this period.

Figure 7.17 shows the Geostationary Operational Environmental Satellite (GOES) X-ray data peaking at M1 during the TypeII flare and returning gradually to its pre-flare level over the next 20 minutes or so. The high level of X-ray radiation causes increased absorption in the D layer of the ionosphere resulting in the observed reduction in propagated RFI. This subject is discussed in more detail in the next section on solar X-ray flares.

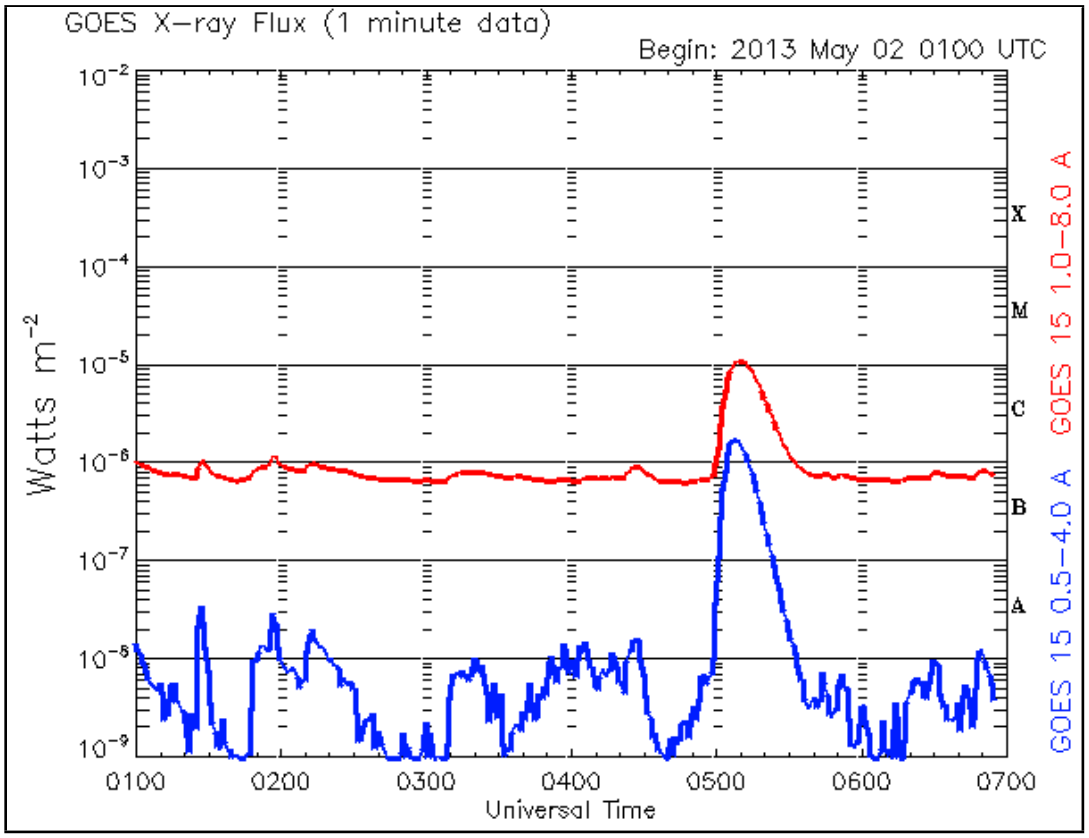


Figure 7.17: M1 X-ray flare satellite data (GOES15). The peak in X-rays coincides with the TypeII flare and a decrease in propagated RFI.

## 7.4 Solar X-ray Flares (SXF)

Solar X-ray flares are probably the most energetic events that occur on the Sun. Fortunately, the Earth's atmosphere absorbs extreme ultraviolet (EUV) and X-ray radiation, providing protection from its harmful effects and therefore this radiation is not directly detectable here on Earth.

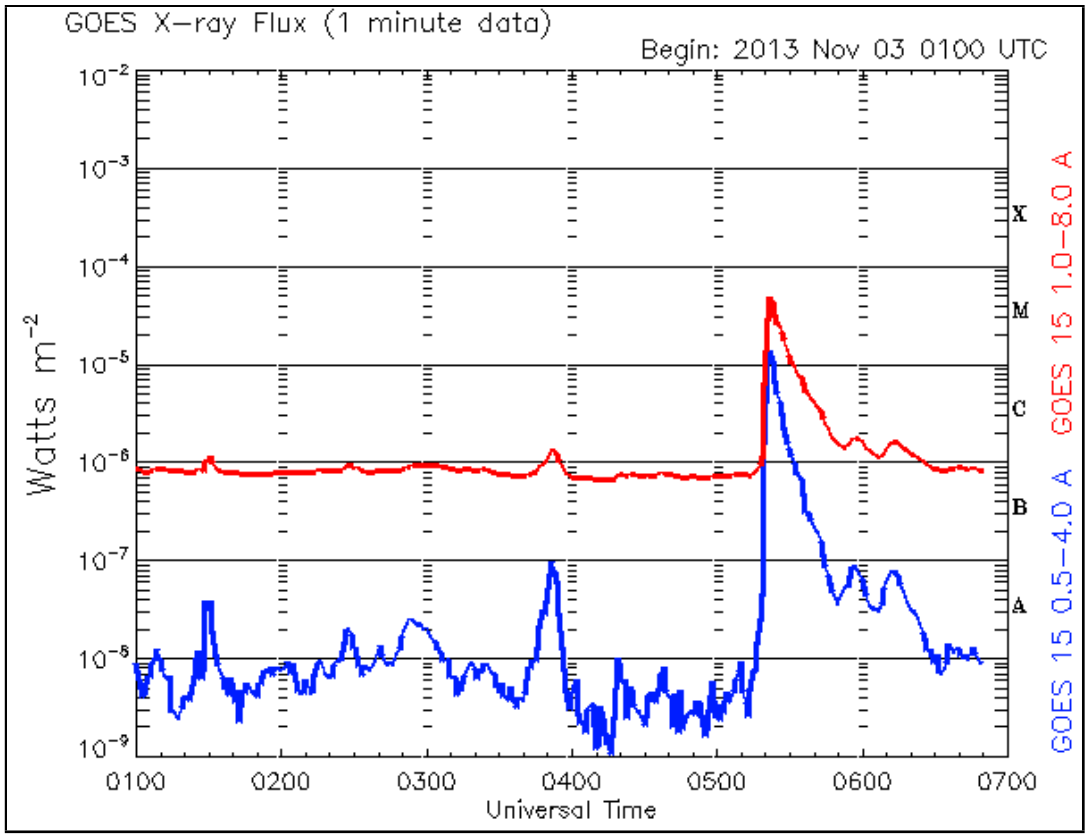


Figure 7.18: The M5 X-ray flare satellite data (GOES15). The flare strength classification letters A, B, C, M and X are shown on the vertical axis to the right and apply to the 1.0 to 8.0 Angstrom (red) data.

At present, GOES15 monitors the Sun in two wavebands: 0.5 to 4.0 Angstroms (0.05 to 0.4 nm); and 1.0 to 8.0 Angstroms (0.1 to 0.8 nm). These data are updated at one and five minute intervals and are available as graphs from `http://www.swpc.noaa.gov/rt_plots/xray_5m.html`. Some of these graphs are included here as supporting evidence for the effects of X-ray flares in the SRTs' data. The strength of X-ray flares are classified by the letters A, B, C, M, and X which relate to the order of magnitude of the peak burst intensity in Watts $m^{-2}$ measured in the 0.1 to 0.8 nm band. See Figures 7.18, 7.19 and `http://www.swpc.noaa.gov/info/glossary.html#x`.

X-ray flares produce intense ionising radiation which passes through the ionosphere and is absorbed by the atmosphere (Kraus, Fleisch, & Russ, 1999, p. 335). When this occurs, the D layer of the ionosphere (approximately 60 to 90 km above the Earth's surface) becomes ionised to an extent that causes high absorption of radio waves passing through it (Donnelly, 1976; Mitra, 1951). This results in the diffuse galactic background and propagated radio signals being absorbed before they reach the SRTs' antennas and is called a high-frequency (HF) fade out or sudden ionospheric disturbance (SID) (Itkina, 1979; Schetgen, 1996).

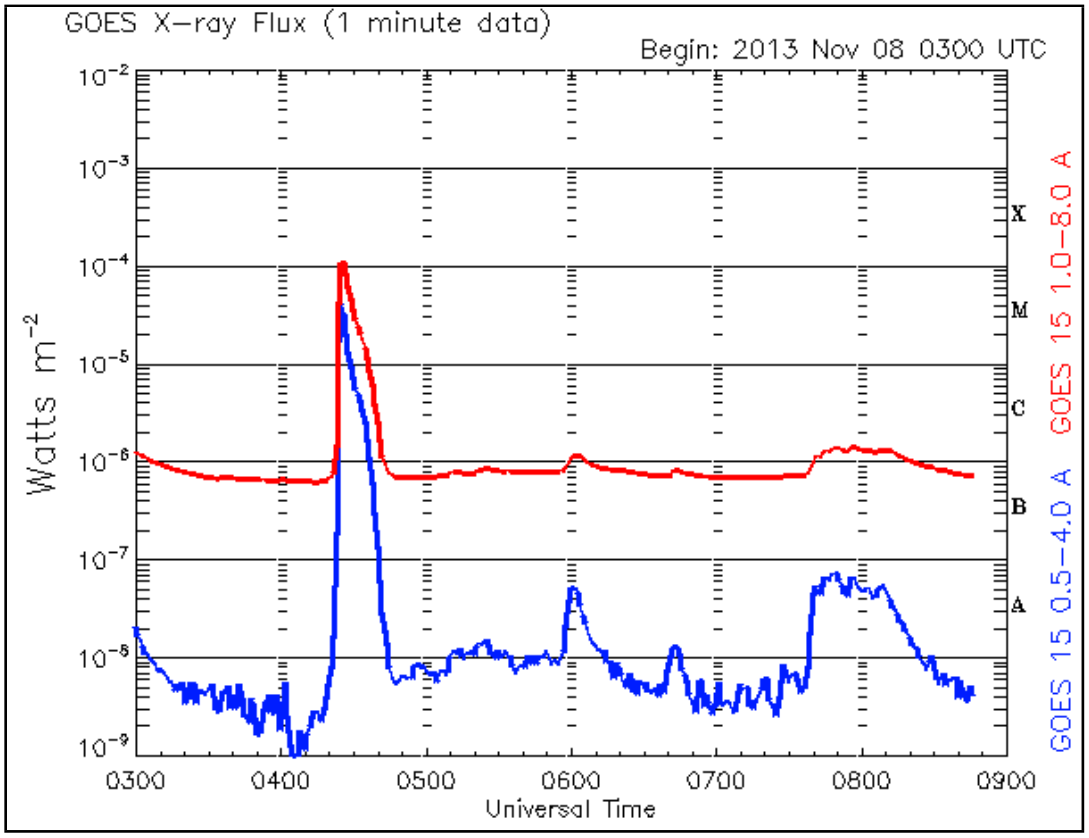


Figure 7.19: The X1 X-ray flare satellite data (GOES15) which caused a deep HF fade out and produced radio emission over a wide frequency range.

Figure 7.18 shows the GOES15 data for an M5 class X-ray flare which caused significant ionisation of the D layer and in Figure 7.20 (particularly the Gingin 17 MHz data) can be seen the dramatic effect of the increased ionospheric absorption on the propagated RFI (green trace) and the galactic background emission (red trace). Also of note, from an RFI point of view, is the fact that the green trace in the LSO data does not fall to meet the red trace. This indicates that the source of this RFI is local and probably located within the observatory complex.

Figure 7.21 shows the same data as Figure 7.20 but with an expanded y-axis to

better show the drop in galactic background emission. Due to the high particle density in the D layer, the lifetime of free electrons is short (Brodrick et al., 2005) and the recovery of the galactic background emission back to normal levels follows quite closely the decay of the X-ray flare as shown in the GOES15 data of Figure 7.18. The LSO solar radio spectrograph (SRS) data in Figure 7.22 shows the widespread effect of the X-ray flare on the HF spectrum below approximately 40 MHz.

This particular X-ray flare is unusual in that it does not have any detectable accompanying solar radio emissions. However, this is not a strong X-ray flare at class M5 ($5 \times 10^{-5}$ Watts $m^{-2}$) and in Figure 7.19 can be seen a class X1 flare that does have solar radio emissions. The SRTs' data (Figures 7.23 and 7.21 respectivly) show that this X-ray flare produced a deeper HF fade out than that of the M5 X-ray flare and yet the solar radio emission is clearly visible. This suggests that the SRF associated with the X1 flare must have been very strong in order to penetrate the ionised D layer and that there was either no SRF associated with the M5 flare, or it was very weak. These two X-ray flares occur five days apart and within one hour of each other, and therefore the galactic background emission has not changed in sidereal time significantly between the two. The SRTs' data once again show a close relationship between the recovery from the HF fadeout and the decline from peak intensity back to normal shown in the GOES data of Figure 7.19.

The TypeIII SRF at the peak of the X-ray flare is just visible in the LSO SRS data of Figure 7.24, which also shows extensive radio emission at very high frequencies (VHF) and a clear TypeII during the period of the HF fade out. The TypeII is at too high a frequency, even at the fundamental, for the SRTs to detect. The LSO SRS data of Figures 7.22 and 7.24 suggest that recovery from the HF fade out occurs first at the lower frequencies. This can also be seen in the SRTs' data, especially in the Gingin Observatory data of Figure 7.20. Since absorption increases at lower frequencies (Straw, 1994, p. 23-19) the rate of recovery is faster at lower frequencies and the data confirm this. It also appears that the galactic background emission returns at the same rate for 17 and 28 MHz. However, the galactic background emission passes through the D layer once only, whereas the propagated RFI may reflect several times between the earth and the upper layers of the ionosphere, suffering multiple D layer absorption events. A more thorough evaluation of the galactic emission data is required to determine the extent to which the 17 and 28 MHz data differ in recovery time.

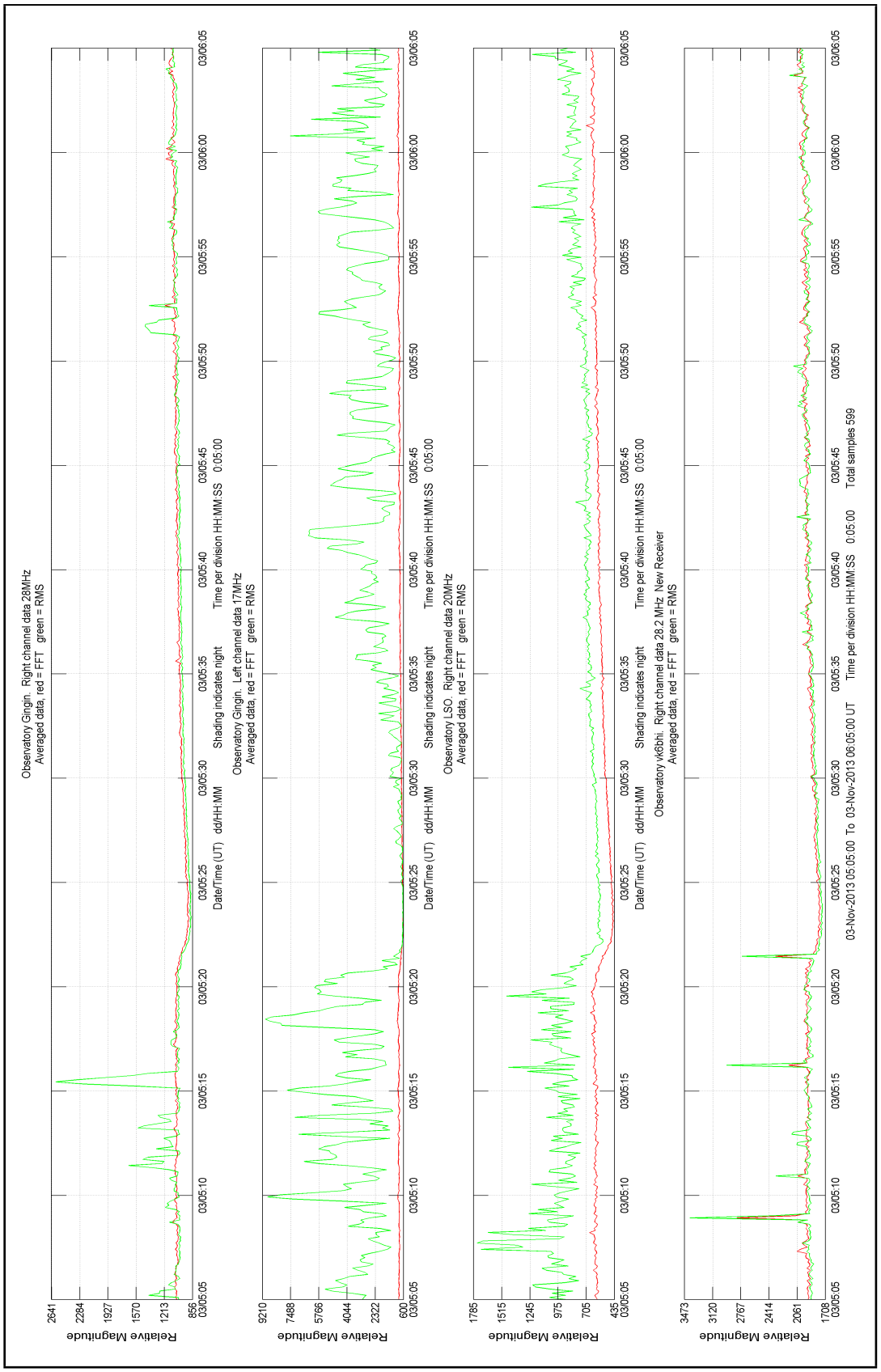


Figure 7.20: HF fade out due to an M5 X-ray flare. The green traces show a steep decline in propagated RFI at the time of the flare and a gradual recovery as the flare subsides.

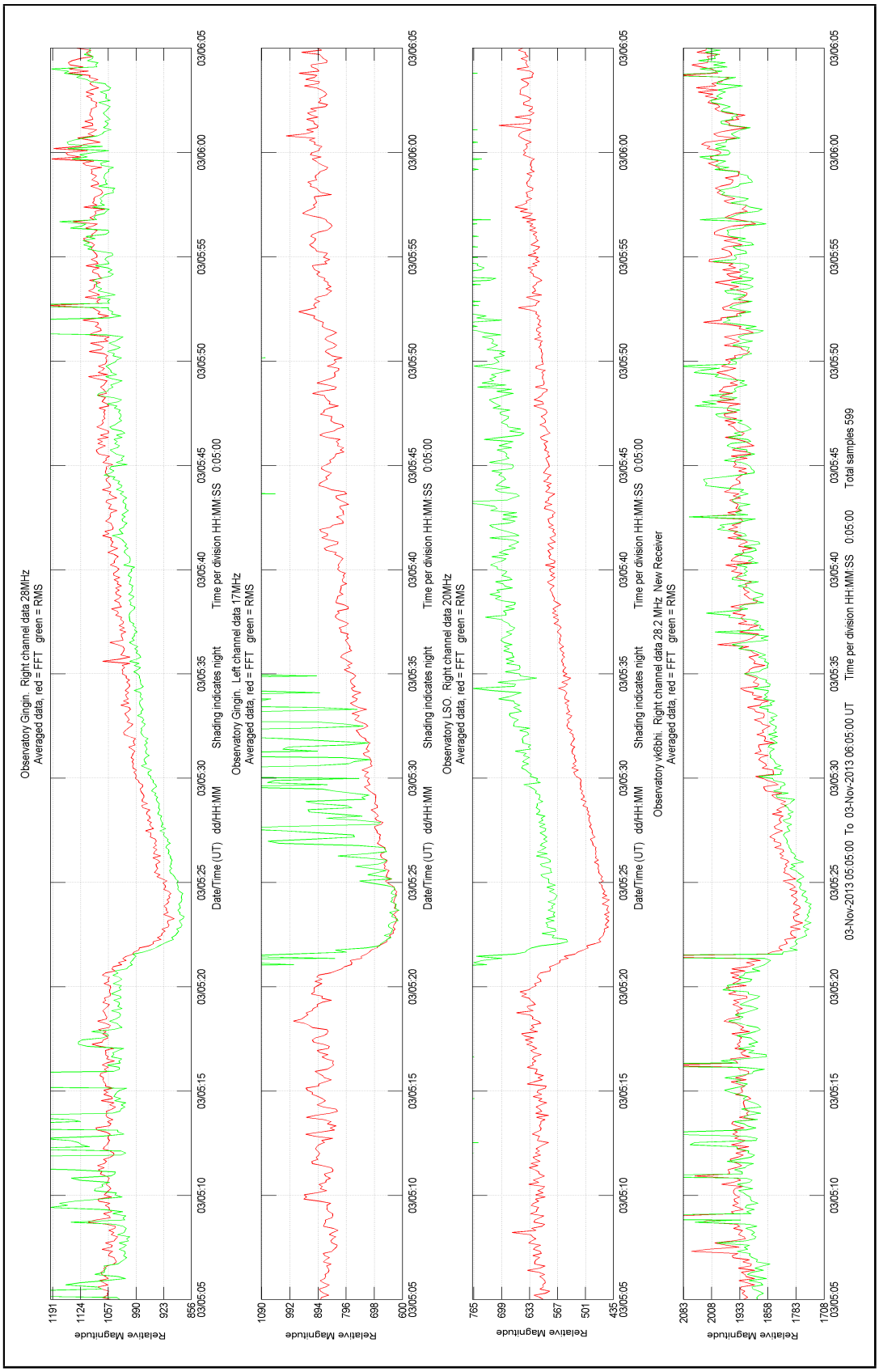


Figure 7.21: The M5 X-ray flare HF fade out showing a magnified view of the broadband galactic background noise (red) and narrow-band RFI (green).

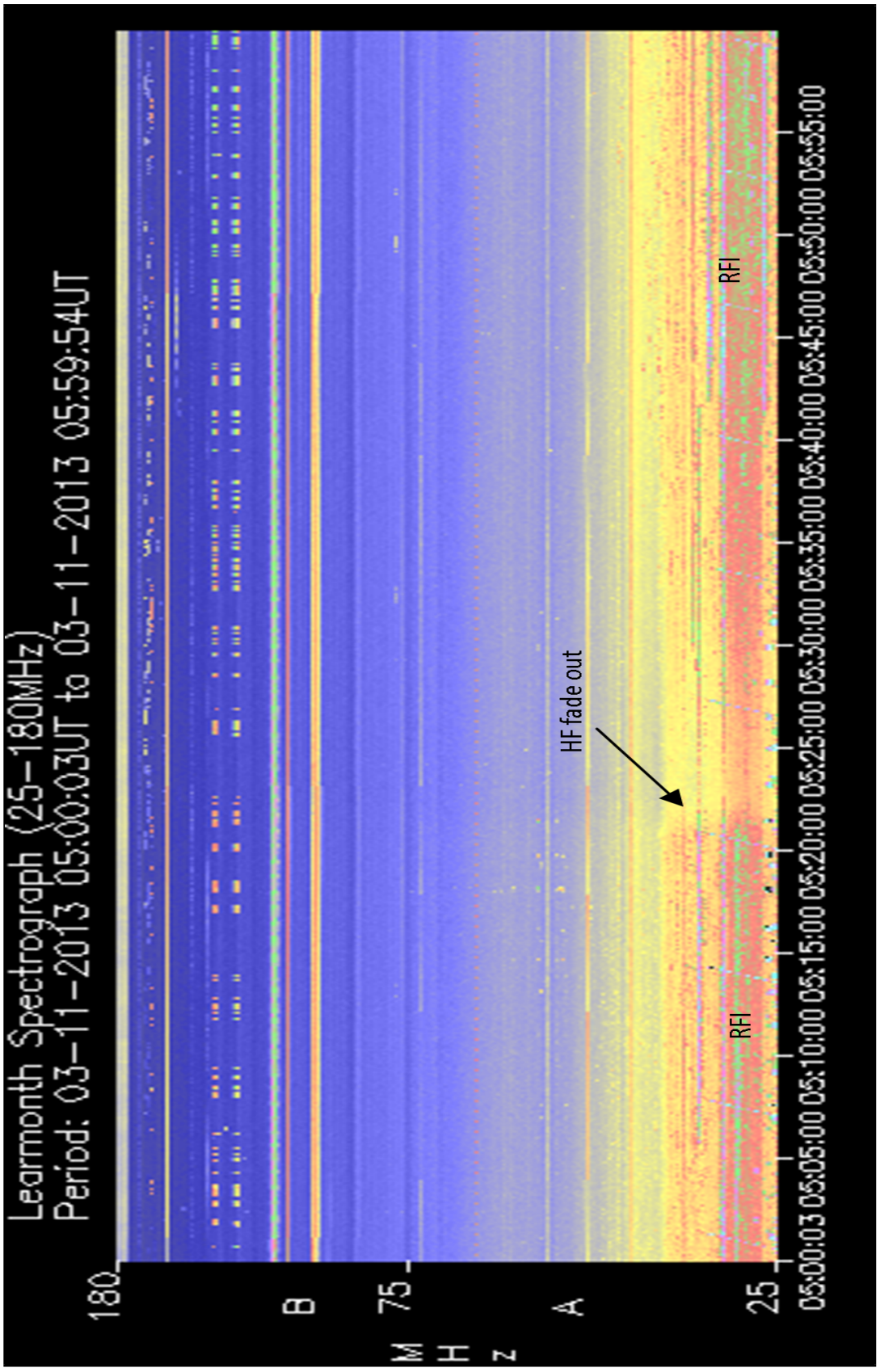


Figure 7.22: The M5 X-ray flare HF fade out showing the sudden drop in signal strength for frequencies below approximately 40 MHz at 0522UT.

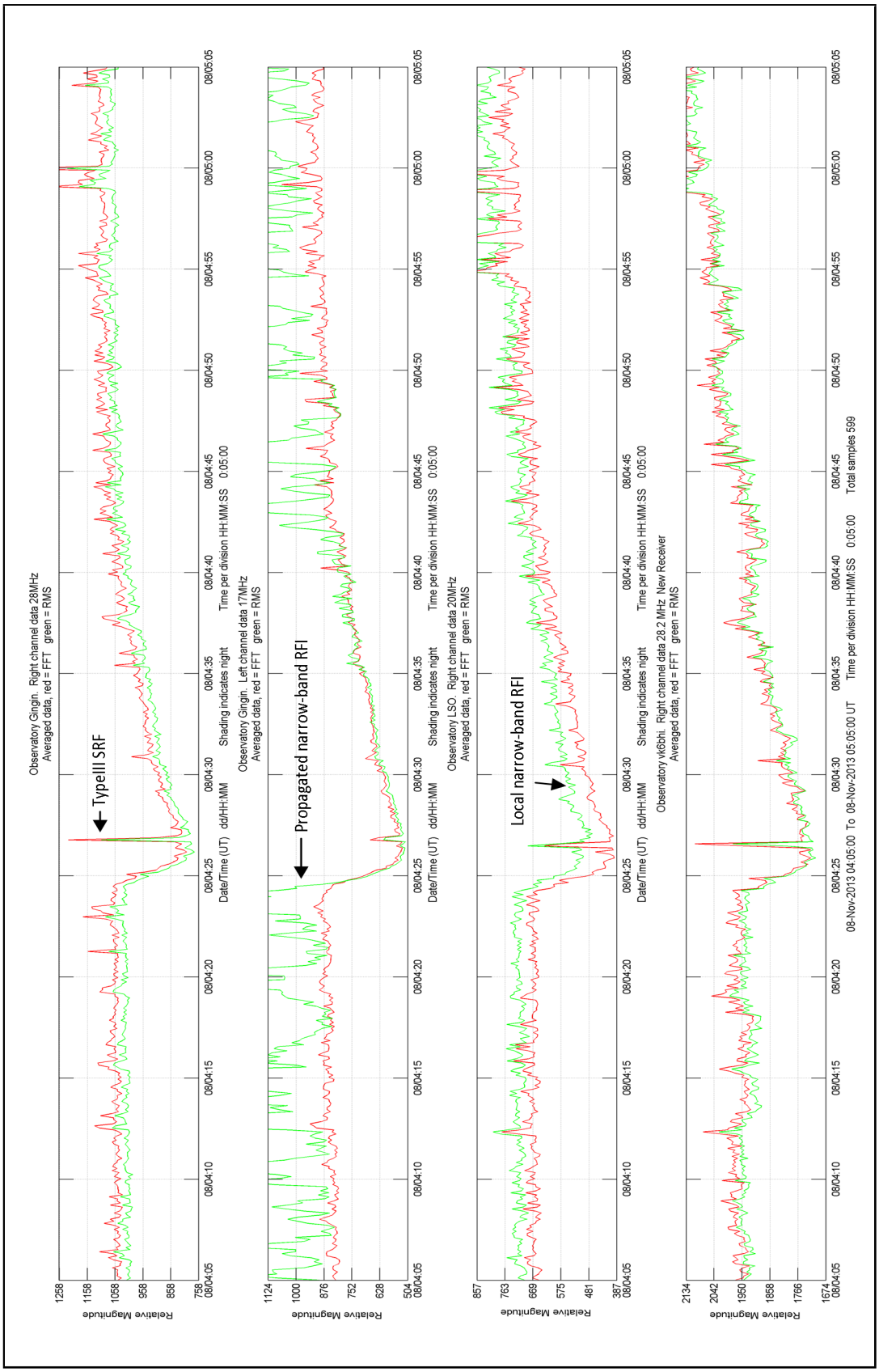


Figure 7.23: HF fade out due to an X1 X-ray flare, with a TypeIII SRF at approximately 0427UT.

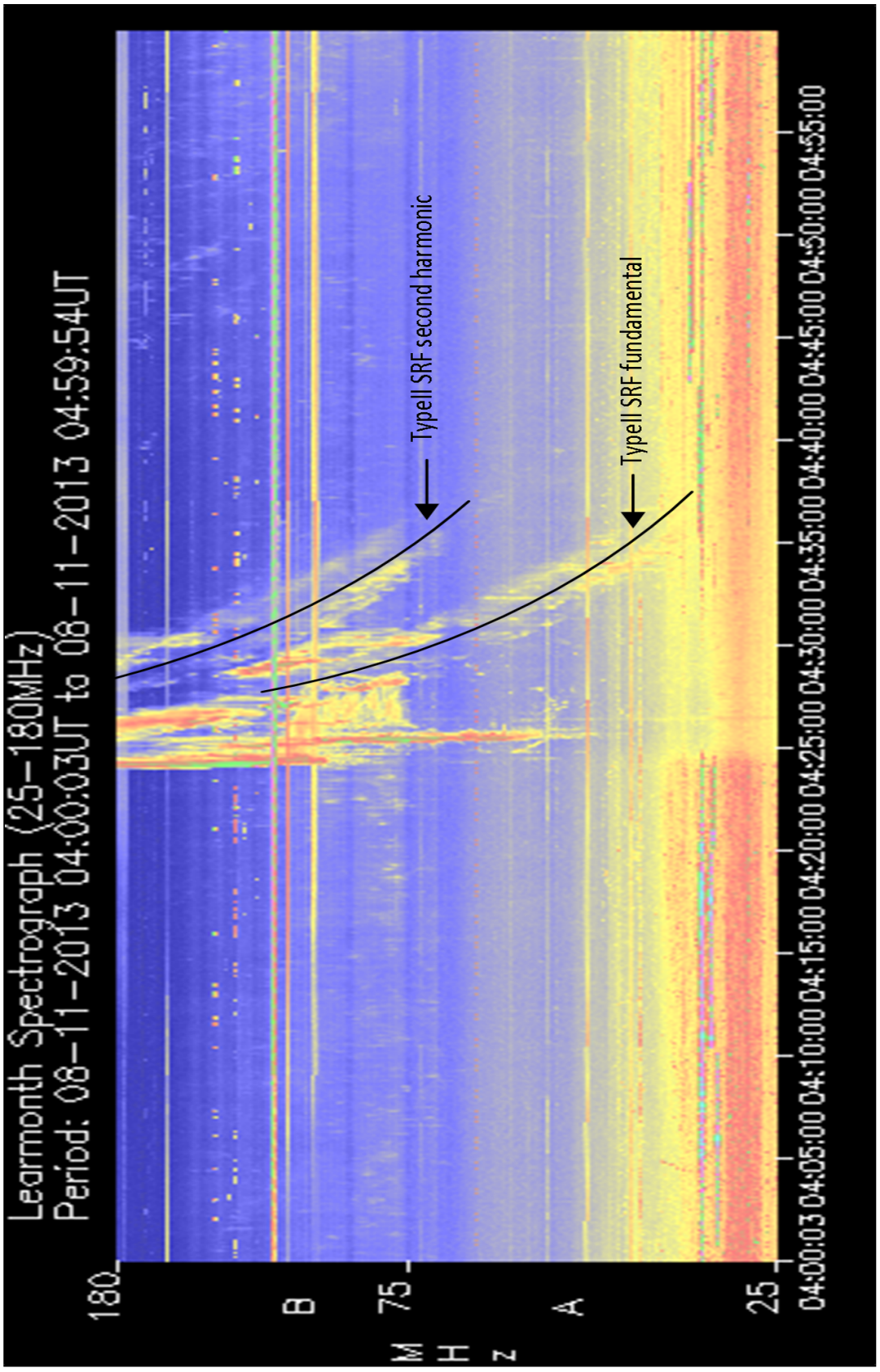


Figure 7.24: The X1 X-ray flare HF fade out and TypeII SRF. The weak TypeIII SRF is just visible at the lower frequencies at 0427UT.

## 7.5 Summary

In general the results from all three observatories have shown that the SRTs are sensitive enough to record the diurnal variation of the diffuse galactic background emission whilst having sufficient dynamic range to record the much stronger solar radio bursts and the ability to reject a significant amount of RFI. There have been periods of higher than usual local RFI which has spoiled some data but fortunately many interesting events were captured. Luck played a significant role when capturing the more rare events such as TypeII solar radio flares and solar X-ray flares. RFI could easily have spoiled the data for these events and had the X-ray solar flares occurred at a time of year when the galactic background is at a minimum during the day, then the associated HF fade-outs would not have been well observed. The HF fade-out data are particularly interesting because it may be possible to determine the strength of the related X-ray flare inferred from the galactic background emission (Brodrick et al., 2005). Also of interest would be a comparison of the GOES X-ray data with the galactic background data to measure the response and recovery times of the galactic background emission at 17, 20 and 28 MHz.

Gingin Observatory continues to record excellent data at 28 MHz, and apart from the roof motor control system, has quite low-levels of local RFI. Propagated RFI affects 17 MHz and without the ability to continually adjust the tuning of the receiver, spoils most of the data recorded during daylight hours. This is also true to a lesser extent at 20 MHz for LSO. Local RFI at LSO has increased since the original installation of the SRT and the antenna performance appears to have deteriorated. Due to distance and other factors, maintenance on the antenna by the author and local RFI mitigation measures have not been possible. Local RFI at the author's home observatory has also increased and appears to emanate from beyond the boundaries of the observatory.

Solar radio flares were quite readily detected, despite the generally low solar activity for the period of this project and there are far more good examples of solar radio flares than there is space for them in this work. Analysis of the ionosphere through the use of the diffuse galactic background does, however, present more of a challenge, since changing levels of RFI tend to mask any underlying variations in the opacity of the ionosphere. Some success was had in generating quiet day curves for the three observatories, by being very selective with the data used. This has enabled the identification of some major sources of the diffuse galactic background emission with an accuracy commensurate with that of the SRT.

No data have been presented for Jupiter noise. However, there are some data

that suggest an incidence of Jupiter noise which occurred late in the evening, when it is unlikely that solar emissions would propagate via the ionosphere. More work is required to verify the position of Jupiter relative to the SRTs' antennas and to find other reports that support the data. Since the SRTs' antennas are directed towards zenith rather than Jupiter, it is not expected that anything other than the strongest of Jupiter's emissions are likely to be detected. Identifying potential Jupiter noise within the SRTs' data is another area where further work is required. Extending the capability of the sunrise and sunset software to include Jupiter would greatly facilitate this process.

All the data presented were selected visually based on generated plots. The IPS spectrographs (mainly the LSO SRS) and GOES data from `http://www.spaceweather.com` were checked daily by the author and plots of significant events saved. Data from the SRTs were downloaded and processed weekly to identify significant events. Since there are over four years of data, it may be useful if the data could be transcribed into a standard data format (FITS[4], CASA[5]) that would enable the use of automated searches. However, such software is likely to be complex and difficult to learn, whereas the SRT software is more suitable for amateur use.

[4] `http://fits.gsfc.nasa.gov/fits_home.html`
[5] `http://casa.nrao.edu`

# Chapter 8

# Conclusions

## 8.1 Summary of Developments and Results

In this project an array of simple radio telescopes (SRTs) was developed for the study of the ionosphere and solar phenomena. These radio telescopes were installed at three sites starting with the author's home observatory, followed by Gingin Observatory and Learmonth Solar Observatory. Data were collected from these sites for a period in excess of four years and graphs produced showing a range of interesting solar radio emissions and associated effects on the ionosphere. From these data it was possible to see some of the characteristics of the behaviour of the ionosphere and relate the behaviour to solar X-ray flares that would otherwise be unobservable here on Earth. Observation of the diffuse galactic background noise has enabled the identification of, with reasonable precision for the SRTs, the major sources within our galaxy.

The development of the SRT started in chapter 2 with an analysis of the antenna system as used by NASA's Radio JOVE project. Their antenna system is optimised for observing radio noise from Jupiter and therefore needs the antenna beam focused with a declination suitable for Jupiter. For this project, an antenna directed towards zenith was required. This gives maximum gain in the direction of the galactic centre while retaining sufficient off-axis gain to pick up the much stronger solar radio flares. An in-depth analysis of the various components of the antenna system was made to ensure optimum performance in both its ability to receive the wanted signals and to reject RFI.

The design and performance of NASA's Radio JOVE receiver, which forms the basis of the SRT, was examined in chapter 3 and some improvements were made for this application. Since RFI is a major problem at the frequencies used, it helps to have as wide a bandwidth as possible and remove the RFI using DSP

in software. A significant modification for the JOVE Receiver was to increase its bandwidth from 3.5 kHz to 22 kHz, thereby making full use of a PC audio system. Other modifications were tested that delivered a reduction in noise output and more selective tuning.

Chapter 4 described the radio telescope installation at the three sites, each of which has a slightly different arrangement of antennas and frequencies of observation. Local RFI mitigation efforts and the sources of such RFI were described in some detail.

Testing of the JOVE Receiver showed that an improved receiver would be required to overcome some of its limitations. The improved receiver design and development was presented in chapter 5. A major limitation of the JOVE Receiver, for continuous observation and remote use, is its manual tuning control. A means of adjusting the receiver tuning over a wide range, with high precision, using software is required. It is then possible to select a band of frequencies for observation and the software is able to adjust the receiver tuning to avoid as much RFI as possible. The improved receiver design addresses these issues and performance data were presented for the prototype.

The radio telescope software, described in chapter 6, is in two main parts: the data recording program and the data analysis program. The data recording program (RioMeter.exe) controls the sampling and processing of data from the receiver and storage to hard disk on the PC. It also holds the observatory configuration details such as name, location coordinates and receiver frequency etc. If enabled, the RioMeter program can also send data to an e-mail address at specified intervals. The data analysis program (RioPlot.exe) provides facilities for finding, collating and displaying the recorded data. Data are displayed as graphs for single or multiple observatories and quiet day curves (QDC) generated if required.

The results of over four years of observations were presented in chapter 7. Several types of human-made RFI were identified, so that it would not be confused with the natural phenomena. The natural phenomena fall into three main categories: the diffuse galactic background (DGB); solar radio flares (SRF); and solar X-ray flares (SXF). Data plots of several types of phenomena from each category were presented, along with supporting evidence from Learmonth Solar Observatory's SRS and the GOES15 X-ray satellite data. Also presented were QDC plots of the DGB and from these plots some major components of the DGB within our galaxy were identified.

## 8.2 Future Developments

Future extensions to this work include further development of the prototype improved receiver and the RioMeter/RioPlot software. This will deliver a flexible radio astronomy receiver system suitable for serious amateur radio astronomers and educational purposes. However, the improved receiver is essentially an improved JOVE Receiver, having a direct digital synthesiser (DDS) derived local oscillator to control the tuning. Further development of the receiver, with a much wider bandwidth and built in analogue to digital conversion, will allow more advanced digital signal processing (DSP) to be carried out in the receiver. The bulky audio-frequency analogue filters can then be replaced by DSP filters, where the bandwidth is controlled by the firmware in the receiver and ultimately by the host PC. The programmable interface controller (PIC) and firmware already established provides the basis for significant development of the receiver, while rapidly advancing DDS technology will allow future receiver development to extend to many hundreds of MHz.

The receiver can be developed into a stand-alone receiver that only requires a power supply and internet connection. This may be achieved by replacing the PIC with a single board computer such as the Raspberry Pi[1]. However, the Raspberry Pi does not have a real time clock or audio analogue to digital converters, so additional hardware would be required. Also the Raspberry Pi operating system is based on Linux and it is not certain that the RioMeter program, written and compiled in Matlab, can be adapted for Linux on Raspberry Pi. The Ettus Research universal software radio peripheral (USRP) demonstrates that such a system is possible, but the USRP is expensive and over specified for the SRT.

The software defined radio (SDR)[2,3] is now well established and further development of the RioMeter program logically moves it in that direction. The look and feel of the RioMeter program needs to reflect the requirements of the radio astronomy user rather than that of a communications or broadcast receiver. There is, therefore, plenty of scope for the development of features such as spectrograph displays, RFI filters and multi-frequency data recording. Development of the RioPlot program will see it become part of, and accessed from, the RioMeter program. Extensions to the RioPlot program will include the ability to scroll through recorded data, and predict where Jupiter emissions might be found.

With the availability of internet-based data storage such as DropBox[4] it should

[1] `http://http://www.raspberrypi.org`
[2] `http://www.softrockradio.org/softrock/models-through-time/softrock40`
[3] `http://sdr-radio.com/`
[4] `https://www.dropbox.com`

be possible to share data between a large group of SRT systems using the existing RioMeter and RioPlot data structures. Some modification to the programs would be required, but once done the RioPlot program would be able to plot data from single or multiple observatories selected from the group. This opens up the possibility of developing software for analysing the data sets for correlated events with minimal false alarms due to RFI. Such software could run on a dedicated PC to give real time detection of solar events and determine their emission type.

A lot of data were collected over the period of this project and much of this remains to be thoroughly analysed. Future work may include a search for Jupiter emissions and the measurement of the strength of solar emissions as described by Dulk, Erickson, Manning, and Bougeret (2001) using the diffuse galactic background (DGB) as a calibration reference. One or two of the X-class X-ray flares may also lend themselves to analysis by the method of Brodrick et al. (2005) for comparison with the GOES15 X-ray satellite data.

## 8.3 Final Remarks

Despite its deficiencies, the JOVE Receiver is still a useful tool for teaching the basics of radio receiver design and is simple enough to be built from a kit. Assembling the kit shows how the individual component parts work together to make a radio receiver: it is no longer just a 'black box'. For those who built their JOVE Receivers from the kit, making the modifications to improve its performance will add to their construction experience and for the others, should not prove too difficult. However, without suitable software to make use of the increased bandwidth of the modified receiver, the overall performance of the radio telescope could be worse, since it will be more difficult to find an interference free frequency. A solution to this problem is to make available a kit of parts for the modifications and include the RioMeter and RioPlot software or other suitable free software. The cost of such a kit would be relatively small compared with the cost of the original kit and would allow dual use of the receiver with the original software. For future Radio JOVE project kits, the ideal solution is: a re-worked PCB to include the modifications and components; improved frequency stability; and updated software to make use of the increased bandwidth.

There is little doubt that the improved receiver could be developed into a sophisticated radio astronomy receiver. However, can the cost of this development be justified? And, who would use it? The answer to the first question lies in the answer to the second: since it is unlikely (but not impossible) that a single

receiver with limited antenna inputs can do any serious science, it is most likely to find application as an educational tool and for public use in the amateur radio astronomy fraternity and the cost would be justified in sales to those areas. The improved receiver is not seen as a replacement for the JOVE Receiver and it is not suitable for kit assembly. Rather, it provides an upgrade path for Radio JOVE users and amateur radio astronomers wanting more advanced capabilities. Unfortunately, radio astronomy does not have the immediate 'Wow' factor of looking through a good quality, commercially available, optical telescope and therefore is likely to have a more limited market. However, one can never be sure of what is around the corner, with continuing technological developments and improved connectivity via the internet, it may be possible to connect large numbers of these receivers around the world for an entirely different picture of radio astronomy.

It has been suggested[5] that the Australian Seismometer in Schools[6] program could serve as a model for a "Radio Astronomy in Schools" program. This is entirely feasible and may be something that could be coordinated through the International Centre for Radio Astronomy Research (ICRAR)[7] Outreach and Education department. Such activity will increase the engagement of school children in science and technology, leading to an increase in enrolments of undergraduate and postgraduate students and greater viability of ICRAR and its joint venture partners into the future. International sales of an ICRAR branded SRT to schools and the amateur radio astronomy market will increase public awareness of the ICRAR brand and possibly provide a useful revenue stream.

[5]By examiner 1 of this thesis.
[6]`http://ausis.edu.au`
[7]`http://www.icrar.org`

# Appendix A

# Combiner Analysis

The following analysis shows that with suitable ferrite material for transformers T1 and T2, resistor R1 ('R int' in the Mini-Circuits data sheet) is not required.

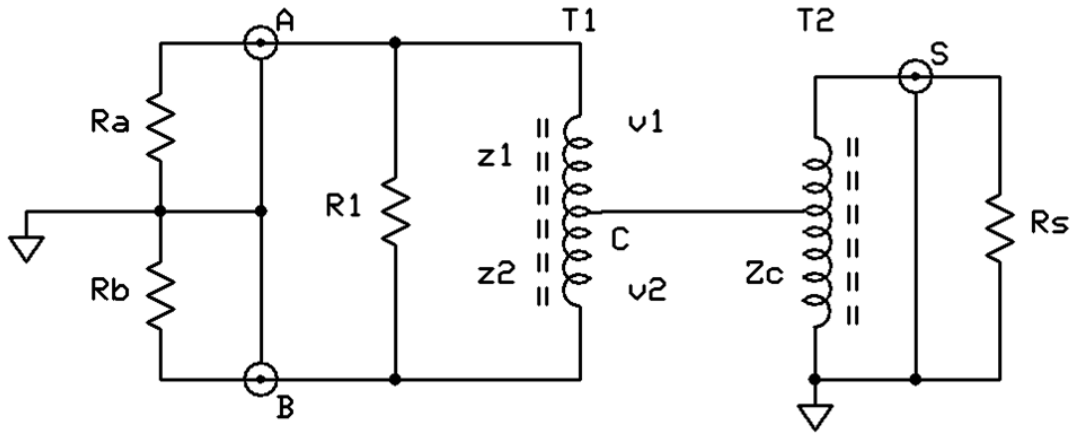


Figure A.1: Simplified combiner/splitter schematic.

The wire tapping point on T1 and T2 determine their transformation ratios; for T1 (centre tap) the impedance ratio is 4:1 and the voltage ratio is 2:1 and for T2 the impedance ratio is 2:1 and the voltage ratio is $\sqrt{2}$:1. For Rs = Ra = Rb then Zc = Rs/2, and z1 = z2 = Ra/2. The type and size of ferrite core, the properties of the ferrite and the number of turns govern the impedance of T1 and T2. For T1 the total impedance $Z_{T1}$ is made equal to Ra plus Rb, but for T2 the total impedance $Z_{T2}$ is made about four times that of Rs, which is the normal procedure for this type of transformer, see Schetgen (1996, p. 6.48). More information on ferrite materials vs frequency vs impedance can be found at: `http://www.amidoncorp.com/product_images/specifications/2-15.pdf`.

When used as a combiner, Ra and Rb are the external source resistances: either the source resistance of the test generator or the impedance of the coax to

the dipoles, which when correctly matched appear as a resistance of 75 Ohms. Rs is the external load resistance presented by the coax feeder to the receiver.

If port A is driven with port B open and port S is terminated with Rs, then $V_C = V_A/2$ and $V_{Rs} = \sqrt{2}V_C$. The current from port A into T1 generates $v1 = V_C$ and the back emf[1] of T1 generates $v2 = -v1$ with respect to C. Since $V_A = v1 + V_C$ and the circuit is symmetric. Therefore

$$\begin{aligned} V_B &= v2 + V_C \\ &= (-v1) + V_C \\ &= -V_C + V_C = 0 \ . \end{aligned} \tag{A.1}$$

Since there is no voltage on port B, Rb has no effect on the circuit and the isolation from port A is theoretically infinite.

The Mini-Circuits data sheet[2] states that:

"As a power combiner, an input signal applied to port A will cause a current to flow through the transformer and experience a 180° phase shift by the time it arrives at port B. Similarly, a current will also flow through the resistor, R int and will not experience a phase shift by the time it arrives at port B. When R int equals the impedance value across the transformer ends then, the currents appearing at port B will be equal in amplitude but opposite in phase and cancel. The net result is that no voltage appears at port B from the input signal applied at port A. Thus, there is theoretically infinite isolation between the ports."

However, the above quotation ignores the fact that an input signal applied to port A causes a voltage at the transformer centre tap C in Figure A.1 and it is this voltage that cancels the voltage at port B, not the current through 'R int'.

Since $V_C = V_A/2$ by virtue of the voltage transformation ratio of T1, it is also true that

$$V_C = V_A \frac{Zc}{z_1 + Zc} \ . \tag{A.2}$$

Now from (A.2) it can be seen that if $Zc = 0$ (Rs is short circuit) then $V_C = 0$ and from (A.1), $V_B = -V_A$. For $Zc = \infty$ (Rs is open circuit), $V_C = V_A$ and $V_B = V_A$, remembering that port B is open circuit and ideal components are assumed.

[1] Back emf (electromotive force) is a property of inductors, see Haliday, Resnick, and Walker (1997, p. 754) and Schetgen (1996, pp. 6.14 - 6.50) for more information on inductors and transformers.

[2] `http://www.minicircuits.com/app/AN10-006.pdf`

# Appendix B

# Resources

## B.1 Software

### B.1.1 Matlab

The RioMeter and RioPlot programs were written and compiled using Matlab R2008b (`http://www.mathworks.com.au`) with licence authentication via a virtual private network (VPN) connection to Curtin University.

`https://sslvpn.curtin.edu.au`

### B.1.2 Microchip MPLAB

The firmware for the PIC was developed using the Microchip MPLAB v8.92 IDE and compiled with the MPLABC18 v3.46 compiler.

`http://www.microchip.com/MPLAB`

### B.1.3 B2Spice

Electronic circuit simulations were carried out using B2Spice A/D 5.2.3 licensed to the author.

`http://www.beigebag.com`

### B.1.4 Express Schematic

Schematic diagrams were drawn using ExpressSCH, free download from

`http://www.expresspcb.com`

### B.1.5 Antenna Simulation

Antenna simulations were carried out using NEC.xls running under Windows XP, it is not compatible with Windows 7. This program, written by Peter Ward, was a free download (no longer available) that combined the flexibility of the Microsoft Excel spreadsheet with the NEC2 (numerical electromagnetics code) adapted to run under MSDOS (Microsoft disk operating system). NEC2 is still available for free download from `http://www.nec2.org`. The author added some new features to NEC.xls, with the permission of Peter Ward, some of which were used in this work.

## B.2 Hardware

### B.2.1 Microchip PICkit3

Microchip PICkit3 in-circuit debugger.

### B.2.2 Fluke 8060A

Fluke 8060A true RMS 4.5 digit multimeter. `http://www.fluke.com`

### B.2.3 Tektronix 2465B

Tektronix 2465B DV 400 MHz Oscilloscope. `http://www.tek.com/`

### B.2.4 TTi TG230

TTi TG230 0.02 Hz to 2 MHz Sweep/Function Generator.

`http://www.tti-test.com`

### B.2.5 RigExpert AA-200

RigExpert AA-200 0.1 MHz to 200 MHz Handheld Antenna Analyser.

`http://www.rigexpert.com`

### B.2.6 Agilent U1732C

Agilent U1732C Handheld LCR Meter.

`http://www.home.agilent.com/agilent/home.jspx?cc=AU&lc=eng`

### B.2.7 Yaesu Transceivers

- Yaesu FT100D Mobile Amateur Radio Transceiver.
- Yaesu FT101E Amateur Radio Transceiver.
- Yaesu FT900 Amateur Radio Transceiver.

`http://www.yaesu.com`

# References


Appleton, E. V., & Barnett, M. A. F. (1925). Local reflections of wireless waves from the upper atmosphere. *Nature*, *25*, 333-334.

Barnbaum, C., & Bradley, R. F. (1998, November). A NEW APPROACH TO INTERFERENCE EXCISION IN RADIO ASTRONOMY: REAL-TIME ADAPTIVE CANCELLATION. *The Astronomical Journal*, *115*, 2598-2614.

Behnke, P., Soberal, D., Bredeweg, S., Dunne, B., Sterian, A., & Furton, D. (2013, March). Senior capstone: A software defined radio design for amateur astronomy. *2013 3rd Interdisciplinary Engineering Design Education Conference*, 104-111.

Bibl, K. (1998, November-December). Evolution of the ionosonde. *Annali di Geofisica*, *41*(5-6).

Bowman, J., Cairns, I., Kaplan, D., Murphy, T., Oberoi, D., Staveley-Smith, L., ... Wyithe, J. (2013, January). Science with the Murchison Widefield Array. *Publications of the Astronomical Society of Australia*, *Vol.30(1)*. (`http://journals.cambridge.org`)

Breit, G., & Tuve, M. A. (1925). A radio method of estimating the height of the conducting layer. *Nature*, *116*, 357.

Brodrick, D., Tingay, S., & Wieringa, M. (2005). X-ray magnitude of the 4 November 2003 solar flare inferred from the ionospheric attenuation of the galactic radio background. *Geophysical Research*, *110*.

Cane, H., Erickson, W., & Prestage, N. (2002). Solar flares, type III radio bursts, coronal mass ejections, and energetic particles. *Journal of Geophysical Research*, *107*(0), SHP X1 - X19.

Cane, H., & Reames, D. (1990). THE RELATIONSHIP BETWEEN ENERGETIC PARTICLES AND FLARE PROPERTIES FOR IMPULSIVE SOLAR FLARES. *The Astrophysical Journal*, *73*, 253-258.

Carlson, G. E. (1998). *Signal and Linear System Analysis* (2nd ed.). John Wiley & Sons Inc.

Castelli, J. P., Aarons, J., Guidice, D. A., & Straka, R. M. (1973, September). The Solar Radio Patrol Network of the USAF and Its Application. *Proceedings of the IEEE*, *61*(9).

Chow, W. F., Ghandhi, S. K., Keonjian, E., Mathis, V. P., Paynter, D. A., Raper, J. A. A., ... Suran, J. J. (1963). *Transistor Circuit Engineering* (R. F. Shea, Ed.). New York: John Wiley & Sons, Inc.

Donnelly, R. F. (1976). Empirical Models of Solar Flare X Ray and EUV Emission for Use in Studying Their E and F Region Effects. *Journal of Geophysical Research*, *81*(25), 4745-4753.

Dulk, G. A., Erickson, W. C., Manning, R., & Bougeret, J.-L. (2001). Calibration of low-frequency radio telescopes using the galactic background radiation. *Astronomy & Astrophysics*(365), 294-300.

Dulk, G. A., Leblanc, Y., & Bougeret, J.-L. (1999, August). Type II shock and CME from the corona to 1 AU. *Geophysical Research Letters*, *26*(15), 2331-2334.

Everard, J. (2002). *Fundamentals of RF Circuit Design with Low Noise Oscillators*. Chichester, England: John Wiley & Sons Ltd.

Flag, R. S. (2012). *JOVE RJ1.1 Receiver Kit Assembly Manual*. Retrieved from `http://radiojove.gsfc.nasa.gov/telescope/rcvr_manual.pdf`

Fridman, P. A. (2001). Rfi excision using a higher order statistics analysis of the power spectrum. *Astronomy & Astrophysics*(368), 369-376.

Fridman, P. A., & Baan, W. A. (2001). Rfi mitigation methods in radio astronomy. *Astronomy & Astrophysics*(378), 327-344. (`http://www.aanda.org/articles/aa/full/2001/40/aah2928/aah2928.html`)

Gopalswamy, N. (2003). Coronal mass ejections: initiation and detection. *Advances in Space Research*, *31*(4), 869-881.

Gopalswamy, N. (2004). Recent advances in the long-wavelength radio physics of the Sun. *Planetary and Space Science*, *52*, 1399-1413.

Haliday, D., Resnick, R., & Walker, J. (1997). *Fundamentals of Physics Extended* (Fifth Edition ed.). New York: John Wiley & Sons, Inc.

Haynes, R. (1996). *Explorers of the Southern Sky: A History of Australian Astronomy*. New York : Cambridge University Press.

Huelsman, L. P. (1993). *Active and Passive Analog Filter Design an Introduction* (International Edition ed.). New York: McGraw-Hill, Inc.

Ingle, V. K., & Proakis, J. G. (2000). *Digital Signal Processing using MATLAB*. Bill Stenquist.

Itkina, M. A. (1979). Intensity of x-ray solar radiation and the value of the anoma-

lous absorption of radio waves during periods of sudden ionospheric disturbances. *Scientific-Research Radiophysical Institute.*, *21*(11), 1558-1562. (Translated from Izvestiya Vysshikh Uchebnykh Zavedenii, Radiofizika, Vol. 21, No. 11, pp. 1558-1562, November, 1978. Original article submitted October 25, 1977.)

Kathiravan, C., Ramesh, R., & Subramanian, K. R. (2002, March). Metric Radio Observations and Ray-Tracing Analysis of the Onset Phase of a Solar Eruptive Event. *The Astrophysical Journal*, *567*, L93-L95.

Kesteven, M., Hobbs, G., Clement, R., Dawson, B., Manchester, R., & T., U. (2005). Adaptive filters revisited: Radio frequency interference mitigation in pulsar observations. *Radio Science*, *40*(RS5S06).

Kraus, J. D. (1986). *Radio Astronomy* (2nd ed.). Cygnus-Quasar Books.

Kraus, J. D., Fleisch, D. A., & Russ, S. H. (1999). *Electromagnetics with Applications* (Fifth ed.). Singapore: McGraw-Hill Book Co.

Kundu, M. R., & Stone, R. G. (1984). Observations of solar radio bursts from meter to kilometer wavelengths. *Advances in Space Research*, *4(7)*, 261-270.

Little, C. G., & Leinbach, H. (1959). The Riometer - A Device for the Continuous Measurement of Ionospheric Absorption. *Proceedings of the IRE*.

Mathewson, D. S., Broten, N. W., & Cole, D. J. (1965). A Survey of the Southern Sky at 30 Mc/s. *Australian Journal of Physics*, *18(6)*, pp.665.

Meeus, J. (1991). *Astronomical Algorithms* (First English ed.). Willmann-Bell, Inc.

Mitra, A. P. (1951). The D-Layer of the Ionosphere. *Journal of Geophysical Research*, *56*(3), 373-402.

Mitra, A. P., & Shain, C. A. (1953). The measurement of ionospheric absorption using observations of 18.3 Mc/s cosmic radio noise. *Atmospheric and Terrestrial Physics*, *4*, 204 to 218.

Oberoi, D., Matthews, L. D., Cairns, I. H., Emrich, D., Lobzin, V., Lonsdale, C. J., ... Whitney, A. R. (2011). First Spectroscopic Imaging Observations of the Sun at Low Radio Frequencies with the Murchison Widefield Array Prototype. *Astrophysics*. (arXiv:1101.0620v1 [astro-ph.SR] 3 Jan 2011. `http://arxiv.org/abs/1101.0620`)

Oberoi, D., Sharma, R., Bhatnagar, S., Lonsdale, C. J., Matthews, L. D., Cairns, I. H., ... Williams, C. L. (2014). Observing the Sun with the Murchison Widefield Array. *Astrophysics*. (arXiv:1403.6250v1 [astro-ph.IM] 25 Mar 2014. `http://arxiv.org/abs/1403.6250`)

Offringa, A. R., De Bruyn, A. G., Biehl, M., Zaroubi, S., Bernardi, G., & Pandey, V. N. (2010). Post-correlation radio frequency interference classification methods. *Monthly Notices of the Royal Astronomical Society*, *405(1)*, 155-167.

Offringa, A. R., De Bruyn, A. G., & Zaroubi, S. (2012). Post-correlation filtering techniques for off-axis source and RFI removal. *Monthly Notices of the Royal Astronomical Society*, *422*, 563-580.

Oppenheim, A. V., Willsky, A. S., & Hamid Newab, S. (1997). *Signals & Systems* (Second ed.). Prentice-Hall International, Inc.

Pick, M., & Trottet, G. (1988). Past, present and future of solar radioastronomy. *Advances in Space Research*, *8*(11), 21-32.

Prestage, N. P. (1995). Recent radiospectrograph observations at Culgoora. *Journal Of Atmospheric And Terrestrial Physics*, *57(14)*, 1815-1820.

Prestage, N. P., Luckhurst, R. G., Paterson, B. R., Bevins, C. S., & Yuile, C. G. (1994). A New Radiospectrograph at Culgoora. *Solar Physics*, *150(1-2)*, 393-396.

Proakis, J. G., & Manolakis, D. G. (1996). *Digital Signal Processing Principles, Algorithms, and Applications* (Third ed.). Upper Saddle River, New Jersey 07458: Prentic-Hall International, Inc.

Schetgen, R. (Ed.). (1996). *The ARRL Handbook for Radio Amateurs* (73rd ed.). Newington, CT 06111 USA: The American Radio Relay League.

Sheridan, K. V., Labrum, N. R., & Payten, W. J. (1973, September). Three-Frequency Operation of the Culgoora Radioheliograph. *Proceedings of the IEEE*, *61(9)*, 1312-1317.

Shkarbalyuk, M. E., Kosolapenko, V. I., & Vasil'ev, A. N. (2012). Use of the WiNRADiO G305e Scanning Receiver in the Riometer for Measuring the Anomalous Absorption of Cosmic Radio Radiation. *Instruments and Experimental Techniques*, *55*(5), 596-600.

Straw, D. R. (Ed.). (1994). *The ARRL Antenna Book* (17th ed.). Newington, CT 06111 USA: The American Radio Relay League.

Thompson, R. J., Kennewell, J. A., & Prestage, N. P. (1996). A comparison of type II shock speeds. *Solar Physics*, *166(2)*, 371-378.

Tingay, S. J., Oberoi, D., Cairns, I., Donea, A., Duffin, R., Arcus, W., ... Wyithe, J. S. B. (2013). The Murchison Widefield Array: solar science with the low frequency SKA Precursor. *Journal of Physics*, *Conference Series*(440).

Tiuri, M. E., & Raisanen, A. V. (1986). Radio-Telescope Receivers. In *Radio Astronomy* (2nd ed.). Durham, N.H. 03824: Cygnus-Quasar Books.

Tonne, J. L. (2013). *Tonne Software.* Retrieved from `http://www.tonnesoftware.com/`

Van Haarlem, M., Wise, M., Gunst, A., Heald, G., McKean, J., Hessels, J., ... van Zwieten, J. (2013). LOFAR: The LOw-Frequency ARray. *Astronomy & Astrophysics*, *556*.

Wild, J. P. (1969). Observation of the magnetic structure of a type IV solar radio outburst. *Solar Physics*, *9(2)*, 260-264.

Wild, J. P., & Smerd, S. F. (1972). Radio Bursts from the Solar Corona. *Annual Review of Astronomy and Astrophysics*, *101(1)*, 159-196.